Summer 2021

Trans-Axonal Signaling and Activity-Dependent Mechanisms Of Topographic Mapping and Refinement in Vivo

Olivia Marie Spead

TRANS-AXONAL SIGNALING AND ACTIVITY-DEPENDENT MECHANISMS OF TOPOGRAPHIC MAPPING AND REFINEMENT IN VIVO

by

Olivia Marie Spead

Bachelor of Science
University of South Carolina, 2015

Submitted in Partial Fulfillment of the Requirements

For the Degree of Doctor of Philosophy in

Biological Sciences

College of Arts and Sciences

University of South Carolina

2021

Accepted by:

Fabienne E. Poulain, Major Professor

Jeff Twiss, Committee Chair

Sofia Lizarraga, Committee Member

Katie Kathrein, Committee Member

Norma Frizzell, Committee Member

Tracey L. Weldon, Interim Vice Provost and Dean of the Graduate School

DEDICATION

This work is dedicated to my parents, John and Eva, who have shaped me into the person I am today while always encouraging me to pursuit my goals and dreams.

To my three sisters, Monica, Katie, and Leah, who have been there for me from the start of it all and always offer a shoulder to lean on when I need it.

And finally, to my amazing little furbaby, Sassafras, who never fails to brighten my day.

ACKNOWLEDGEMENTS

I am incredibly fortunate to have been surrounded by a remarkable support group throughout my graduate career.

I would first like to thank my mentor, Dr. Fabienne Poulain, for the mentorship you have provided for me. You set the standards for the type of scientific integrity that I always want to strive for and encouraged me to achieve my full potential. I will always look up to you, not just as a great mentor in science, but also as an inspiring, supportive leader, both at and away from the bench.

I would also like to thank my committee – Drs. Jeff Twiss, Sofia Lizarraga, Katie Kathrein, and Normal Frizzell. Each member of my committee provided insightful feedback for my projects, pushed me to continue to learn and grow, and offered guidance for my graduate career and future. Additionally, I would like to thank Dr. Troy Herter for allowing me to experience the research process during undergrad, ultimately sparking my passion for biomedical research.

The members of my lab, both past and present, have greatly contributed to my growth as a scientist. Drs. Cory Weaver and Tine Verreet are exceptional scientists who not only helped teach me techniques and work through ideas and experiments, but also taught by simply being great examples of scientists and mentors. I would also like to thank a few of our rotation students, Irene Dalla Costa and Trevor Moreland, for aiding me in different aspects of my projects and for bringing new and exciting ideas to the lab.

Thank you to our lab technician Quill Thomas for keeping the fish room up and running and making sure we never had to worry. Your dedication to the lab, fresh take into our projects, and overall support has been invaluable.

Thank you, of course, to my amazing friends and the community I have been lucky to be a part of during this journey. Grace Jones, Dr. Johnie Hodge, Olivia Manley, and Byron Dooley – you have been there for me every step of the way. Thank you for always being there for me, in good times and bad, and for making me laugh but also letting me cry when I need it. You have truly been my lifeline these past several years. And thank you to my friends and fellow scientists – Dr. Sam Burnett, Dr. Crystal Hankin Burnett, Dr. Kristen Hogan, Drew Hogan, Dr. Timothy Hines, Jake Massey, Lindsay Sanchez, Dr. Matt Strauss, Caroline Strauss, Grace Hollenbeck, Stephanie Ackerson, and Matt Zdradzinski – for providing me with constant support and feedback at every milestone I have encountered. And to my friends, both near and far – Madison Lambert, Benton Reed, Katie Smith, Paige Gowen, Elena Lunn, Connor Donahue, Alex Guaraldi, and Samuel Hughes – for always being just a phone call away.

And finally, I want to thank Zachary Wayne Bishop. You have been my rock and have offered constant support and encouragement since the day I met you. Thank you for loving me. Thank you for being there for me. Thank you for listening to me and making me smile every single day. You truly are amazing and I am grateful to have you as my person.

ABSTRACT

Brain connectivity and function depend on the precise formation of neuronal connections during development. In the central nervous system, most axonal projections are organized into topographic maps according to the spatial organization of the neurons they originate from or the type of stimulus they respond to. Topographic mapping is in large part established by interactions between axons and their target as well as by activity-dependent pruning of mistargeted or excessive arbors. Another important mechanism contributing to topographic map formation is pre-target axon sorting, where axons become pre-ordered en route to their destination. Both topographic mapping and pre-target sorting involve the pruning and refinement of mistargeted axons and arbors, however the mechanisms underlying these processes have yet to be elucidated.

In the visual system, retinal axons are topographically sorted along the dorso-ventral axis in the optic tract before reaching the optic tectum. Previous studies in zebrafish have shown that optic tract sorting is achieved through the selective degeneration of missorted dorsal axons that have erroneously misrouted along the dorsal branch of the tract. Heparan sulfate (HS), a type of sugar chains carried by core proteins known as heparan sulfate proteoglycans (HSPGs), acts non-cell-autonomously along ventral axons to regulate the degeneration of these missorted dorsal axons. How HSPGs act to regulate pre-target sorting and the pruning of missorted axons still remains unknown. Here, we have identified the HSPG Glypican-3 (Gpc3) as specifically

expressed in ventral retinal ganglion cells (RGCs) throughout development. Using CRISPR/Cas9 genome editing, we have generated several *gpc3* mutant alleles encoding a truncated, non-functional protein. Analysis of retinal axon sorting in *gpc3* mutants reveals that some dorsal retinal axons are missorted along the dorsal branch of the optic tract, demonstrating a novel function for Gpc3 in axon-axon interactions. Interestingly, Gpc3 seems to genetically interact with Tenm3, a transmembrane protein that is also expressed in the ventral retina. *Tenm3* mutants also display missorted dorsal retinal axons as do embryos that are heterozygous for both *gpc3* and *tenm3*. Overall, our study unravels a novel function for both Gpc3 and Tenm3 in trans-axonal signaling and developmental axon pruning during neural circuit formation.

The refinement of mistargeted axonal arbors is another crucial step for topographic mapping and maturation. Unfortunately, our understanding of topographic map formation and refinement has been limited by our inability to observe these mechanisms directly in vivo. To overcome that challenge, we used Cre-mediated recombination of a new colorswitch reporter to generate a transgenic model that allows for the analysis of retinotopic map formation and maturation in vivo. We found that while the antero-posterior retinotopic map forms early in development, it remains dynamic with nasal and temporal retinal arbors expanding their projection domains over time. While temporal retinal axons seem to arborize directly at their proper target in the anterior tectum, nasal projections initially arborize in the anterior tectum as well as the posterior tectum. Over time, mistargeted nasal projections in the anterior tectum refine in an activity-dependent process, driving the sharpening of the antero-posterior map. With our novel line, we provide the first unbiased and quantitative analysis of topographic

mapping and refinement in real time in vivo. Altogether, our studies unraveled novel mechanisms of axonal pruning during neural circuit development and provide a solid platform for futures studies to determine the signaling pathways and complex mechanisms governing these processes.

TABLE OF CONTENTS

LIST OF FIGURES

LIST OF ABBREVIATIONS

AC ..... Adenylate Cyclase

Adgrl ..... Adhesion G-Protein Coupled Receptor L

A-P ..... Anterior-Posterior

ATP ..... Adenosine Triphosphate

Bim ..... Bcl2-Interactomg Member Protein

BMP ..... Bone Morphogenetic Protein

CAM ..... Cell Adhesion Molecule

cAMP ..... Cyclic Adenosine Monophosphate

CARD ..... Caspase-Recruitment Domain

Casp ..... Caspase

CNS ..... Central Nervous System

Cntn ..... Contactin

Co-IP ..... Co-Immunoprecipitation

Conn ..... Connectin

CYFIP ..... Cytoplasmic FMR1-Interacting Protein

dak ..... Dackel

DED ..... Death Effector Domain

DIG ..... Dioxigenin

dLGN ..... Dorsal Lateral Geniculate Nucleus

DLK ..... Dual Leucine Zipper Kinase

D-N ..... Dorso-Nasal

dpf ..... Days Post Fertilization

DREZ ..... Dorsal Root Entry Zone

DRG ..... Dorsal Root Ganglion

DSCAM ..... Down Syndrome Cell Adhesion Molecule

D-V ..... Dorsal-Ventral

ECM ..... Extracellular Metrix

EGFP ..... Enhanced Green Fluorescent Protein

En ..... Engrailed

Fmi ..... Flamingo

Gogo ..... Golden Goal

Gpc ..... Glypican

Gpc ..... Glypican

GPCR ..... G-Protein Coupled Receptor

GPI ..... Glycophosphatidylinositol

gRNA ..... Guide RNA

GSK3β ..... Glycogen synthase Kinase 3β

hpf ..... Hours Post Fertilization

HRMA ..... High Resolution Melting Analysis

HS ..... Heparan Sulfate

HSPG ..... Heparan Sulfate Proteoglycan

HST ..... Heparan Sulfate Sulfotransferase

ISH ..... In Situ Hybridization

ISN ..... Intersegmental Nerve

lak ..... Lakritz

LAMP ..... Limbic-system-associated protein

lHb.....Lateral Habenula

LMP .....Low Melting Point

Lpd .....Lamellipodin

Lphn .....Latrophilin

MAPK ..... Mitogen-Activated Protein Kinase

MLF ..... Medial Longitudinal Fascicle

nAChR .....Nicotinic Acetylcholine Receptor

NCAM..... Neural Cell Adhesion Molcule

NGF.....Neurotrophic Growth Factor

NMDAR.....*N*-Methyl-*D*-Aspartate Type Glutamate Receptor

NrCAM .....Neuron-Glia Related Cell Adhesion Molecule

Nrg .....Neuroglian

Nrp ..... Neuropilin

N-T .....Nasal-Temporal

OB ..... Olfactory Bulb

OE ..... Olfactory Epithelium

OR .....Olfactory Receptor

OSN..... Olfactory Sensory Neuron

OT ..... Optic Tectum

Pbl .....Pebble

PBS .....Phosphate Buffer Saline

Pcdh.....Protocadherin

pg..... Picogram

PKA.....Protein Kinase A

PSA .....Polysialic Acid

PTU 1-Phenyl-2-Thiourea

PYR ..... Pyrin

rdr ..... Radar

RFP ..... Red Fluorescent Protein

RGC ..... Retinal Ganglion Cell

RGM ..... Repulsive Guidance Molecule

RT-PCR ..... Reverse Transcription Polymerase Chain Reaction

SC ..... Superior Colliculus

Sdc ..... Syndecan

Sdc ..... Syndecan

SEM ..... Standard Error of the Mean

Sema ..... Semaphorin

Shh ..... Sonic Hedgehog

SN ..... Segmental Nerve

TBS ..... Tris Buffer Solution

Tenm ..... Teneurin

Tg ..... Transgenic

TNF ..... Tumor Necrosis Factor

Traf ..... TNF Receptor Associated Factor

TTX ..... Tetrodotoxin

TZ ..... Termination Zone

UTR ..... Untranslated Region

VBA ..... Visually-mediated Background Adaptation

V-T ..... Ventro-Temporal

VTA ..... Ventral Tegmental Area

WRC ..... WAVE Regulatory Complex

WT ..... Wild Type

CHAPTER 1

GENERAL INTRODUCTION

1.1 General Principles of Neural Circuit Wiring

The precise formation of neural circuits during development is a complex process that is essential for a properly functioning brain. Within these circuits, neurons are connected via projections called "axons", allowing these cells to communicate with one another. Most neural circuits in the central nervous system (CNS) are wired using four common mechanisms: axon guidance to the proper target, pre-target axon sorting along tracts, topographic mapping at the target, and the refinement of mis-targeted or unnecessary axonal branches [1]. Axons navigate along specific pathways to their final target by responding to attractive or repulsive cues present in the environment. Several families of guidance factors have been well-established in their roles for governing circuit development by providing long-range and/or contact-mediated signals. These include the classical "canonical" guidance cues Ephrins, Slits, Netrins, and Semaphorins [2]; adhesion molecules [3]; neurotrophic and growth factors [4]; and morphogens such as Sonic Hedgehog (Shh), Bone morphogenetic proteins (BMPs), and Wnts [5-7] . Once at their target, axonal projections are organized into maps according to the spatial orientation of the neurons they originate from or the type of stimulus they respond to. By preserving the organization of neurons between two brain regions, these topographic maps mediate an efficient transfer of information, allowing our brains to perceive the outside world and process information accurately [1, 8-11]. In most circuits, axons pre-sort into distinct bundles before reaching their topographic position at their brain target. This topographic organization is also based on the spatial orientation of the neurons the axons originate from or the type of stimulus they respond to. The precise ordering of axons before reaching their target strongly suggests that this mechanism is required for proper

topographic mapping [12, 13], however this has not yet been demonstrated outside of the olfactory system.

Over the past several decades, our understanding of the molecular mechanisms guiding axons to their target has grown immensely. To date, the majority of these findings have focused on axon-target and axon-extracellular interactions. However it has recently been discovered that trans-axonal signaling – i.e. signaling between axons that come into contact with one another – is a critical part of neural circuit development [14]. The main purpose of my thesis is to better understand how trans-axonal signaling dictates visual system development, focusing mostly on how axons communicate to regulate the refinement of mistargeted projections through both molecular and activity-based mechanisms. This chapter will present an overview of the molecular mechanisms underlying key steps of neural circuit wiring in the visual system. The rationale for undertaking the research described in this thesis will also be presented.

1.2 Neural Circuit Development in the Visual System

The visual system has been a predominant model for studying neural circuit development over the past several decades because it is experimentally accessible and connectivity can be analyzed anatomically and functionally [15-18]. While the development of the mammalian and chick visual system differs slightly from that of the frog and fish, many of the molecular mechanisms governing axonal processes are highly conserved between vertebrate species. In non-mammalian vertebrates, axons from retinal ganglion cells (RGCs) exit the eye, extend along the optic nerve, cross the midline at the chiasm, elongate along the optic tract, and topographically project to the contralateral optic

tectum (OT) in the midbrain (**Figure 1.1A**). Mammals undergo a similar process with the majority of axons crossing the midline at the chiasm to project to the contralateral superior colliculus (SC) in the midbrain and the dorsal lateral geniculate nucleus (dLGN) in the thalamus, however a subset of retinal axons do not cross the chiasm and instead project to the ipsilateral SC. In all vertebrates, once retinal axons have reached their target, they map topographically along both the anterior-posterior (A-P) axis and the dorsal-ventral (D-V) axis based on the position of the RGC they originate from in the retina (**Figure 1.1A**). Retinal axons originating from RGCs in the nasal retina project specifically to the posterior half of the tectum while axons from temporal RGCs project to the anterior tectum. Similarly, along the D-V axis, axons from dorsal RGCs project to the ventral half of the tectum while ventral RGCs project their axons to the dorsal tectum. The topographic mapping along the D-V axis is further facilitated by the sorting of retinal axons into distinct bundles of the optic tract before reaching their target. Axons originating from the dorsal retina sort along the ventral branch of the optic tract while ventral retinal axons sort along its dorsal branch. [19]. While several aspects of retinotopic mapping have been determined in recent years, the molecular mechanisms underlying pre-target sorting are still poorly understood.

1.3 Pre-Target Topographic Retinal Axon Sorting

Pre-target axon sorting and axon-axon interactions are important and underappreciated aspects of neural circuit development. Pre-target axon sorting is a critical step in the organization of axons within their circuits and is thought to be necessary for topographic mapping at the target in both the visual system and other circuits as well [12, 13, 20]. In the retinotectal system, the first axons to exit the retina and

elongate towards the tectum, known as “pioneer axons”, guide follower axons as they elongate along the optic nerve, cross the chiasm, and elongate along the optic tract [21, 22]. While many aspects of retinotopic axonal order are the same across all vertebrates, there are a few slight differences between species, especially during early development. In mammals, while retinal axons do tend to concentrate towards one half of the optic nerve depending on RGC position in the retina, retinotopic order is virtually nonexistent in the optic nerve [23, 24]. In zebrafish and xenopus, retinotopic order along the optic nerve is dependent on the axis being analyzed. Along the A-P axis, nasal and temporal retinal axons appear segregated along the optic nerve but this separation is lost along the optic tract as axons become intermixed [25, 26]. Along the D-V axis, dorsal and ventral axons remain fairly segregated along their respective halves of the optic nerve. In all vertebrates, this order flips after crossing the optic chiasm. Once retinal axons cross the midline and enter the optic tract, they become pre-ordered along the dorsal and ventral parts of the tract, with dorsal axons elongating along the ventral tract and ventral axons along the dorsal tract [12, 23, 25, 27, 28]. Interestingly, crossing at the optic chiasm is not necessary for the proper sorting of retinal axons. Indeed, in *belladonna* zebrafish mutants, axons project directly to the ipsilateral tectum, however they maintain their proper topographic projections [29]. In all species, it is known that retinal axons take incredibly precise routes along the optic tract, but how they do so remains largely unknown to this day.

Pioneer axons in most vertebrate species, including chick, frog and mammals, originate from the dorso-central part of the retina [26, 30-32], however in zebrafish, ventro-nasal axons are the first to exit the retina and elongate along the tract [25, 33]. Follower

axons then fasciculate and elongate along the pioneers. Interestingly in zebrafish embryos, several dorsal retinal axons initially misroute along the D-V axis of the optic tract and elongate along the dorsal branch instead of the proper ventral branch. These misrouted axons then selectively degenerate, leaving a properly sorted tract in place [34]. The signaling mechanism triggering the degeneration of missorted axons has yet to be elucidated, however it has been established that heparan sulfate (HS) somehow regulates this process [19, 34]. In embryos lacking HS due to mutations in either glycosyltransferase Ext2 or Ext3 [19, 34, 35], the missorted dorsal axons do not degenerate and remain improperly sorted as they elongate along the dorsal tract to their proper location in the ventro-lateral tectum.

Heparan sulfate proteoglycans (HSPGs) comprise a large family of core proteins carrying highly variable HS sugar chains covalently attached to them [36]. The membrane-bound HSPGs consist of transmembrane Syndecans (Sdcs) and glycophosphatidylinositol- (GPI) anchored Glypicans (Gpcs). During their synthesis, core proteins undergo a number of posttranslational modifications in the Golgi apparatus including the addition of HS chains as well as modifications of the HS chains such as sulfation, epimerization, and de-acetylation. These multiple enzymatic changes generate a vastly diverse number of HS structures and therefore functions carried out by HSPGs [37]. The sulfation patterns of HS guide several aspects of retinal axon guidance. For example, HS sulfation is needed for retinal axons to properly navigate to the tectum in Xenopus [38-40]. Additionally, mutations in two heparan sulfate sulfotransferases (HSTs) cause distinct guidance defects at the optic chiasm [41]. In *Hs2st* mutants, the optic chiasm is disorganized, with retinal axons growing up the ventral midline. In *Hs6st1* mutants, some

retinal axons enter the contralateral optic nerve and grow towards the contralateral eye, instead of entering the contralateral tract. These studies indicate that the sulfation pattern on HS chains is instructive for proper axon navigation at important choice points, potentially through functional interactions with guidance molecules such as Slits or Netrins.

While the importance of HS in the early steps of retinotectal development has been fairly well established, its role in the selective degeneration of missorted retinal axons was novel finding [34]. Beyond the role of HS in pre-target retinal axon sorting, very little is known about the signaling mechanism regulating sorting. Signaling through Neuropilin-1 (Nrp1), a receptor to the guidance cues Semaphorin-3s, has been suggested [42]. Knockdown of the RNA-binding protein Hermes leads to the missorting of dorsal retinal axons at least in part through an upregulation of Nrp1 expression, which suggests that Nrp1 may be involved in optic tract sorting. In vitro studies analyzing axon-axon interactions between dorsal and ventral retinal axons have discovered a range of growth cone behaviors upon axon contact, most notedly axon crossing and/or fasciculation between homotypic axons (dorsal-dorsal or ventral-ventral interactions) and axon stalling and/or retraction between heterotypic axons (dorsal-ventral interactions) [43]. Both of these interaction types appear to be regulated by the cytoplasmic FMR1-interacting protein 2 (CYFIP2) and in vivo, CYFIP2 is required for proper sorting of dorsal axons along the tract [44]. While these studies provide insight into the regulation of pre-target sorting in the visual system, the ligand-receptor interactions needed for triggering the degeneration of missorted axons have yet to be determined. One of the main goals of my thesis was to elucidate the signaling mechanism initiating that selective degeneration.

1.4 Molecular Mechanisms of Retinotopic Mapping

In 1963, Sperry hypothesized that complementary gradients of guidance molecules at the brain target and their receptors expressed by elongating axons is what determines the topographic mapping of neural circuits such as the retinotopic map [45]. In the visual system, topographic mapping occurs along the A-P and D-V axes, with both axes being established largely independently of each other [46]. Since Sperry's hypothesis was first formulated, several classes of guidance receptors and their ligands have been identified as the molecular tags regulating axon guidance and topographic mapping. The Eph receptor tyrosine kinases and their Ephrin ligands are some of the most well-characterized of these guidance cues in the context of topographic mapping. Members of the Ephrin-A family and the EphA3 receptor were the first molecular candidates discovered to be expressed in a graded manner in RGCs [47-49] and were later found to be required for topographic mapping at the tectum/SC [50-52]. Interestingly, both Ephrins and Eph receptors are membrane-bound proteins and thus require cell-cell contact in order to signal (**Figure 1.1B**) [1].

The graded expression of Ephrins, Ephs and other guidance factors in the retina is induced during early eye development by various spatiotemporally regulated morphogens and transcription factors that establish and maintain retinal polarity along the nasal-temporal (N-T) and D-V axes [53]. Proper patterning of the retina is thus absolutely required for the expression of topographic molecules, such as Ephrins and Ephs that are needed for the targeting and mapping of retinal axons [54-56]. Two classes of Eph receptors and Ephrin ligands are known to specifically regulate retinotopic mapping along the A-P or D-V axis. Along the A-P axis, multiple EphA receptors are expressed in a high-

temporal to low-nasal gradient in the retina and in a high-anterior to low-posterior gradient in the OT/SC while Ephrin-A ligands are expressed in a complementary gradient (**Fig. 1.1C**) [1, 47, 49, 50, 57]. In vitro experiments have revealed that Ephrin-As act as a repellent guidance factor to retinal axons [50-52]. Specifically, temporal axons expressing EphA receptors are repelled by the posterior tectum expressing high levels of Ephrin-A ligands, thus restricting temporal axons to the anterior part of the tectum [58, 59]. Conversely, nasal retinal axons with low levels of EphAs are not repelled by the Ephrin-As in the posterior OT/SC and so they terminate specifically at that posterior target. Interestingly, several studies have shown that it is the relative and not absolute levels of EphA expressed between neighboring RGCs that regulates topographic mapping along the A-P axis of the tectum [60-62]. Increasing EphA expression in just a subset of RGCs creates two intermixed populations of RGCs with differing EphA gradients [60]. The two populations of corresponding retinal axons produce separate maps at the SC, indicating that the maps form due to the EphA receptor level that a given axon expresses relative to that of its neighboring axons. Additionally, when Ephrin-A is inactivated only in the SC, temporal axons are properly targeted to the anterior SC, however when Ephrin-A is removed from both the SC and RGCs, the temporal axons project to the posterior SC [63]. Ephrin-A/EphA signaling can function bi-directionally – Ephrins can induce signaling through Ephs (forward signaling) or Ephs can induce signaling through Ephrins (reverse signaling) (**Figure 1.1B**). Since Ephrin-As are GPI-anchored proteins and thus lack the ability to transduce an intracellular signal, reverse signaling requires a co-receptor in order to generate a repulsive signal necessary for mapping [64]. Indeed, in mice lacking EphA7 (which is expressed in an anterior to posterior gradient at the SC but is not

expressed in the retina), both temporal and nasal retinal axons form extended termination zones at the SC [58]. Altogether, these studies indicate that signaling between axons contributes to topographic mapping and suggest that other mechanisms beyond molecular graded signals are necessary to this developmental process.

Additional molecules also contribute to A-P mapping at the tectum. In Xenopus and chick, the transcription factor Engrailed-2 (En-2) is expressed in anterior-to-posterior gradient in the tectum and acts to repel temporal retinal axons while attracting nasal axons [65, 66]. In vitro studies suggest En-2 acts to modulate the sensitivity of axons to Ephrin-As at the tectum. Repulsive guidance molecule (RGM) and its receptor neogenin are expressed in complementary gradients in the OT and retina of the chick [67, 68]. RGM is highly expressed in the posterior tectum and neogenin is expressed in a high-temporal to low-nasal gradient in the retina. In vitro stripe assays demonstrated that temporal retinal axons avoid stripes expressing RGM while nasal axons do not. Additionally, knockdown of RGM disturbs the topographic mapping at the tectum in chick. Interestingly, in mice, RGM is expressed by the SC but not in a graded manner and *RGM* mutants do not display mapping defects [69]. Other in vitro studies have suggested that Semaphorins (Sema) can also repel retinal axons expressing the co-receptors, Nrps and Plexins [70]. Nrp2 is expressed in an increasing nasal to temporal gradient in the retina of mice and its ligand, Sema3F is expressed in an increasing anterior to posterior gradient in the SC [71]. Collapse assays revealed that temporal retinal growth cones expressing high levels of Nrp2 collapse when presented with Sema3F while nasal retinal growth cones do not. These data suggest a potential role for semaphorin signaling in retinotopic mapping at the SC.

Early studies in several vertebrate species discovered that EphBs and Ephrin-Bs are also expressed in complementary gradients in the retina, but along the D-V axis instead of the N-T. Ephrin-Bs are expressed in a high-dorsal to low-ventral gradient in the retina while EphB receptors are distributed in a complementary gradient (**Figure 1.1C**) [72-76]. However, these molecules are not as obviously graded at the SC/OT. Ephrin-B1 in the mouse and the chick displays a dorsal-high to ventral-low gradient in the SC/OT [72, 73] but the gradient is restricted to the ventricular zone of the SC and the radial glia in the OT. EphBs are expressed in an overall dorsal-high to ventral-low gradient of the OT in Xenopus and zebrafish [75, 77, 78]. Mutants with disrupted Ephrin-B/EphB signaling display mapping defects along the D-V axis [73, 79] indicating the importance in Ephrin/Eph signaling in D-V mapping. Interestingly, Ephrin-B/EphB signaling in retinotopic mapping is bifunctional (i.e. it can be either attractive ore repulsive depending on the levels of Ephrin-B relative to that of EphB) and bidirectional (forward signal from Ephrin-Bs to EphBs or reverse signaling from EphB to Ephrin-Bs) [17]. For example, in the mouse, Ephrin-B1 is expressed in a ventral-low to dorsal-high gradient in the SC while EphB2/B3 are expressed by RGCs in a dorsal-low to ventral-high gradient. EphB1 is expressed uniformly throughout the RGC layer, giving the retina an overall dorsal-low to ventral-high gradient [73, 79]. EphB2/EphB3 double mutants display topographic mapping defects along the D-V axis of the SC with ventral axons projecting into an expanded region of the ventral SC. Additionally, blocking the ability of EphB to initiate a reverse signal through Ephrin-B1 also results in similar defects. Mutants lacking the C-terminal of Ephrin-B2 (i.e. mutated Ephrin-B2 unable to transduce reverse signaling but capable of forward signaling) also display mapping defects at the SC, demonstrating a role for

EphB/Ephrin-B reverse signaling in mapping [79]. Assessing different combinations of EphB1, EphB2, and EphB3 nulls demonstrated that while each individual EphB null mouse displays similar defects in D-V mapping at the SC, the frequency and severity of mapping errors increases with the number of null alleles (i.e. in double and triple mutants), indicating that the overall level of EphBs is what mediates proper signaling [80].

Along with Ephrin-Bs and EphBs, a few other molecules have been implicated in the regulation of retinotopic mapping along the D-V axis. Indeed, Wnt3 and its receptors Ryk and Frizzled were also found to regulate D-V topographic mapping [81]. Wnt3 is expressed in a dorsal-high to ventral-low gradient in the chick OT and mouse SC while its receptor, Ryk, is expressed in a ventral-high to dorsal-low gradient in the retina. In vitro assays showed that Wnt3 repulsion is mediated by high levels of Ryk, whereas axon attraction is mediated by activating the Wnt3 receptor Frizzled. Since ventral RGCs express more Ryk than dorsal RGCs, ventral axons are repelled by the high expression of Wnt3 in the medial OT while the dorsal axons expressing an overall higher level of Frizzled are attracted to the medial OT. In vivo studies confirmed that ectopic expression of Wnt3 in the tectum or of a dominant negative Ryk in RGCs both caused mapping defects along the D-V axis of the OT. Additionally, the cell adhesion molecules L1CAM and ALCAM contribute to proper D-V mapping [82-84]. L1 is known to interact with ankyrin, a scaffolding protein that links membrane-bound proteins to the cytoskeleton. A point mutation in L1 abolishing L1's interaction with ankyrin causes ventral retinal axons to map to abnormally ventral zones in the SC [82]. Interestingly, EphB phosphorylates L1 at the ankyrin binding motif to promote its binding to ankyrin, thereby directing ventral axons towards the high expression of Ephrin-B in the dorsal SC [84]. Additionally, retinal

axons in ALCAM null mice project to the proper dorsal zone in the SC but also mis-project to the ventral SC as well, similar to L1CAM mutants [82] and EphB2/B3 null mice. ALCAM is expressed in retinal axons along the optic nerve, but once axons cross the chiasm, ALCAM is no longer present while L1 remains strongly expressed along the length of the retinal axons. ALCAM is also strongly expressed in the SC. Thus, these studies provide a scenario in which ALCAM acts as a substrate to guide L1-expressing axons. Another member of the L1 family, neuron-glia related cell adhesion molecule (NrCAM), is uniformly expressed in the developing retina but also needed for proper D-V mapping [85]. NrCAM null mice displayed laterally displaced projections from the ventro-temporal retina. Like L1, NrCAM is also phosphorylated by EphB, but this time, the phosphorylation decreases its ability to bind ankyrin. In this model, EphB phosphorylation of NrCAM would promote attraction of retinal axons toward the dorsal-high concentration of Ephrin-B1 at the SC [86].

Finally, the adhesion molecule Teneurin-3 (Tenm3) has been shown to specifically regulate the topographic mapping of ipsilaterally projecting axons along both the A-P and D-V axes of the mouse SC and dLGN [86, 87], potentially through interactions with EphAs and EphBs along their corresponding axes [88]. Tenm3 is specifically expressed in the ventral retina and the dorsal part of the SC and dLGN – areas where ipsilateral retinal projections originating from in the ventro-temporal retina terminate [86, 87]. In Tenm3 knockout mice, ipsilaterally but not contralaterally projecting ventral axons erroneously terminate into the ventral SC/dLGN. Tenm3 is a type II transmembrane protein known to typically promote homophilic interactions between cells, suggesting that it might regulate the guidance of ventral retinal axons by promoting an attractive and

adhesive signal from the dorsal SC/dLGN. Interestingly though, in Tenm3 knockout mice, *EphA7* expression is downregulated while *EphB1* is upregulated [88]. In these mice, the ipsilateral axons extending from RGCs in the ventro-temporal retina project to the ventral part of the dLGN, where they are normally excluded from because of repulsive Ephrin-Eph signaling. These data suggest a model in which Tenm3 may interact with Eph/Ephrin signaling to mediate proper topographic mapping. While evidence supports a role for Tenm3 in topographic mapping at the target, whether it is involved in pre-target sorting has yet to be tested.

1.5 Neural Activity and the Refinement of Mistargeted Projections

Along the A-P axis of the visual system of amphibians and fish, retinal axons project and halt at their posterior-most position at, or just past, the proper termination zone in the OT [89, 90] with mistargeted branches refining after initial mapping [91-95]. Meanwhile in birds and mammals, the majority of RGC projections overshoot their termination zone and then are pruned back during a refinement process [24, 96, 97]. In all vertebrate species, the posterior-most extension of retinal arbors is largely regulated by repellent Ephrin-A/EphA signaling along the A-P axis [48, 50-52, 90, 98]. However, the remodeling that occurs after the initial overshoot of the termination zone (TZ) depends on spontaneous neuronal activity. Indeed, the correction and reorganization of retinal arbors in mammals [99-102], as well as the refinement of proximal branches in fish [103], occur during developmental time periods when spontaneous retinal waves occur and is prevented when neuronal activity is blocked [103, 104].

While blocking global neuronal activity does not affect the crude mapping of retinal arbors at their target, it does alter the refinement of mistargeted axonal branches and the creation of a precise map [95, 105-108]. Several early studies utilized tetrodotoxin (TTX) to block global activity during retinotectal development. TTX is a neurotoxin that blocks sodium channels and therefore the firing of action potentials. TTX application in developing chick embryos prevents the refinement of retinal fibers that overshoot their termination zone at the tectum [105]. In frogs, application of TTX increases branch dynamics and arbor size at the tectum [109, 110]. In zebrafish, blocking neural activity with TTX also leads to a more diffuse projection field of retinal arbors [95, 106-108]. Specifically blocking the activity of either single or a subset of RGCs by overexpressing the inward-rectifying potassium channel Kir2.1 also leads to a larger and more diffuse arborization field at the tectum of zebrafish and SC of mice [111, 112]. Interestingly, several of these studies indicate that even though the arborization field was larger in zebrafish embryos lacking activity, the number of terminal branches and total branch length was unchanged while the number of transient filopodia increased [95, 106-108, 111] providing more questions about how neuronal activity and arbor dynamics exactly contribute to map formation and refinement.

The formation of the retinotopic map is an incredibly dynamic process. In both mice and zebrafish, spontaneous retinal waves originate in the temporal retina and travel towards the nasal retina with neighboring cells having the same synchronous pattern of activity. These waves then propagate to the anterior OT/SC, carrying patterned activity that governs activity-dependent mechanisms during visual system development [103, 104]. During zebrafish retinotectal development, axons continuously add and retract branches,

elongating through selective branch stabilization [113, 114]. At their target, axons continue to add and retract branch tips and filopodia with only a small fraction being maintained as mature arbors [91, 92, 94, 115-117]. Blocking either presynaptic activity in RGCs or postsynaptic activity in tectal cells greatly affects those arbor dynamics [109, 118-120]. *N*-methyl-D-aspartate type glutamate receptors (NMDARs) are ion channels that allow the influx of Calcium (Ca^{2+}) when activated by glutamate. Blocking NMDAR activity in postsynaptic tectal cells of Xenopus abolishes the preferential elimination of mistargeted retinal branches [120] and similarly, in zebrafish global pharmacological blockade of NMDARs causes larger retinal arbors [121]. Synchronous firing, i.e. neurons firing at the same time and with the same frequency, through NMDAR activity creates fewer and more stable new branches by suppressing the exploratory behavior of axons as they innervate the tectum [93]. Intriguingly, pre- and postsynaptic NMDAR activities act to counterbalance morphology and synaptic maturation in the developing Xenopus retinotectal system [119]. When postsynaptic NMDARs are knocked down in tectal cells, increased spontaneous events in RGCs occur and retinal axonal arbor complexity increases. When presynaptic NMDARs are knocked down in RGCs, retinal axons display larger evoked responses and decreased axonal complexity. These results indicate that postsynaptic activity contributes to synaptic maturation and the morphology of retinal arbors while presynaptic activity guides the strength of retinotectal inputs while counterbalancing postsynaptic activity to direct axonal arbor morphology.

An elegant in vivo study in Xenopus demonstrated the importance of synchronous activity and found that patterned retinal activity is required for the elimination of branches whose firing pattern does not match that of its neighbors. Interestingly, the

temporal order of activity regulates arbor dynamics and position [122]. When a sequential stimulus is presented in the nasal-to-temporal direction of the retina, retinal arbors are refined. However, this refinement does not occur when the stimulus is presented in the opposite direction, further indicating the importance of the spatiotemporal pattern of activity in driving mapping mechanisms. Studies in mammals have also highlighted the importance of activity pattern in refining maps. Mice lacking the β2 subunit of the nicotinic acetylcholine receptor (nAChR) have altered spatiotemporal dynamics of spontaneous retinal waves compared to wild type (WT) mice. Indeed, correlated retinal activity in β2-/- mice occurs much less frequently than in WT and the retinal waves are much more brief, are of low amplitude, and display a larger wave size [123]. In contrast to WT mice, whose retinorecipient projections remodel into a refined map with neighboring axons forming overlapping but focal TZs, β2 knockout mice display larger TZs with broadly distributed axonal arbors in both the SC and the dLGN [124-127]. While pharmacologically restoring the frequency of spontaneous neuronal activity in β2 knockout mice fails to restore refined retinotopy [123], restoring the β2 subunit in RGCs, which restores some correlation in the pattern of firing, is sufficient to restore the refinement of retinal fibers at the SC [128, 129]. Additionally, when β2-nAChR is knocked out specifically in RGCs, similar defects in retinal wave activity patterns and in the refinement of retinal axon projections at the SC are observed [123]. However, spontaneous activity and retinotopic mapping is unaltered when β2 is specifically knocked out of SC neurons. Overall, these studies indicate that it is the pattern of spontaneous activity in presynaptic RGCs that is needed for proper refinement of the retinotopic map. Indeed, studies manipulating the firing patterns of RGCs indicate that asynchronous firing

weakens synaptic inputs and destabilizes branching while coincident bursts of activity and synchronous firing leads to a decreased exploratory branch remodeling of retinal fibers at the OT and dLGN and therefore promotes the maintenance of synaptic integrity [130-132]. Together, these studies indicate that it is the spatiotemporal pattern of neural activity that instructs the refinement of arbors and therefore the formation of a precise retinotopic map.

Evidence strongly points to a mechanism whereby molecular guidance by Ephrin-A/EphA first regulates topographic map formation along the A-P axis of the OT/SC and neural activity is then needed for the refinement of mistargeted projections. Several studies have further indicated that molecular- and activity-dependent mechanisms may act synergistically to regulate mapping. For example, BMP is expressed in the dorsal retina and transgenic mice overexpressing BMP display topographic mapping defects with ventral axons projecting more laterally in the SC than in WT siblings [127]. Interestingly, BMP transgenic mice in a β2-/- background have a significantly larger target zone filling nearly the entire SC compared mice only overexpressing BMP, indicating that molecular signaling and neuronal activity have a cumulative effect on map formation. Ephrin-A signaling also works in concert with spontaneous retinal activity [133, 134]. Ephrin-A2/A3/A5 triple knockout mice have severe A-P mapping defects at the SC with arbors diffusely spreading through the anterior SC while β2-/- mice have normal topography but lack refinement. Mice lacking both Ephrins-A2/A5 and β2 displayed a much more severe disruption of A-P mapping. Interestingly, ectopic expression of EphA6 and simultaneous overexpression of Kir2.1 on retinal axons did not alter the termination zone of retinal fibers, indicating that EphA signaling can occur in the absence of neuronal

activity [112]. These studies support a model in which Ephrin-A signaling guides the formation of a coarse A-P map at the SC and then neuronal activity clusters axonal arbors based on the patterns of their firing activity, thus refining the map.

The biochemical pathway downstream of neuronal activity, and therefore how exactly neuronal activity mediates refinement of mistargeted projections, is poorly understood. Many of the molecular signals and activity-dependent mechanisms of neural circuit development depend on both cyclic adenosine monophosphate- (cAMP-) dependent upstream signaling at the level of the RGC body and/or the convergence onto cAMP-dependent downstream signaling cascades at the level of the axonal terminals. For instance, the generation to retinal waves in the mammalian visual system is dependent on cAMP signaling. The spatiotemporal properties of spontaneous retinal waves is dependent on cAMP levels through the activation of A2 adenosine receptors on amacrine cells and RGCs [135, 136]. Increasing cAMP levels results in increased size, speed, and frequency of retinal waves. Additionally, inhibiting adenylate cyclase (AC) activity (the enzyme that catalyzes the production of cAMP from adenosine triphosphate (ATP) in a calcium/calmodulin-dependent manner) or protein kinase A (PKA – one of the main effectors of cAMP signaling) activity prevents spontaneous retinal waves.

Signaling downstream of neural activity is also dependent on cAMP signaling through adenosine. Several studies have sought to assess the pre- vs. postsynaptic contribution of cAMP signaling and the function of AC activity in retinotopic mapping. At least ten ACs are expressed in the brain and of those ten, only AC1 and AC8 are directly modulated by calcium and calmodulin while the others are typically modulated by G-proteins [137], making them particularly interesting in the context of neural plasticity.

AC1 is highly expressed in RGCs of developing mice and AC8 is expressed in the SC [138]. In mice carrying an inactivating mutation of the AC1 gene, Ca^{2+}-stimulated AC activity is decreased 40-60% and topographic defects in the confinement of axonal arbors to their appropriate domains can be detected at the SC and dLGN. Conditional knockout of AC1 in RGCs mimics this refinement defect in the dLGN [139]. In addition, in an organotypic co-culture system that reproduces the topographic mapping along the A-P axis of the SC by enabling the elimination of exuberant retinal axon branches [140], excess axonal branches are maintained in explants from AC1 deficient mice. Ephrin-A5 signaling blockade in WT co-cultures results in a similar phenotype, with axonal branches failing to undergo refinement. AC1 mutant retinal axons have modified responses to Ephrin-A5, with growth cones collapsing but failing to retract backwards as seen in WT axons. The response to Ephrin-A is enabled by neuronal activity and Ca^{2+} in that system- when either are blocked, the growth cone fails to collapse in response to Ephrin-A [141]. Periodic oscillations of cAMP in the retinal growth cone is able to rescue the activity blockade, but stable increases or decreases in cAMP levels are not able to do so, suggesting that cAMP oscillations generated by the activity of retinal waves is needed for refinement of axonal arbors. Interestingly, it is likely that cAMP modulation near lipid rafts regulates the pruning of excess axonal branches [142]. Lipid rafts are plasma membrane domains enriched with cholesterol, glycosphingolipids, and GPI-anchored proteins. Ephrin-As are GPI-anchored proteins and are thus likely to be localized in lipid rafts. Accordingly, Averaimo and colleagues presented a role for lipid raft-specific cAMP signaling in regulating both Ephrin-A-induced axon retraction and the pruning of retinal arbors at the SC.

Spontaneous oscillations in PKA activity, one of the main effectors of cAMP signaling, are temporally correlated with spontaneous depolarizations associated with retinal waves and PKA activity is preceded by Ca^{2+} transients in rat retinal explants [143, 144]. Neural activity causes an increase in both cAMP levels and PKA activity and removal of extracellular Ca^{2+} blocks its activity. Together, these studies designate cAMP/PKA signaling as a link between neuronal activity and the restructuring of retinal arbors at their target. The biochemical pathway downstream of cAMP/PKA signaling has yet to be elucidated in the context of retinal axon refinement. However, it has been hypothesized that this signaling could involve small GTPases such as Rho, Rac, and Cdc42 – all of which have been involved in growth cone collapse in response to Ephrin-As [141, 145, 146].

1.6 Project Summary

Axon-target and axon-environment interactions have long been studied in the context of brain development, however very little is known about how axons interact with one another in order to maintain precise spatiotemporal organization during circuit development. Additionally, selective degeneration during neural circuit development is a poorly understood field and very little is known about the underlying mechanism for such a process. Zebrafish are a unique and powerful model system for studying retinotopic formation during development –embryos are transparent, allowing for a direct visualization of retinal projections through high-resolution confocal microscopy and timelapse imaging; the zebrafish genome has been sequenced and fully annotated, providing us with information needed for genetic manipulation and analysis; and the zebrafish visual system development is fairly rapid [16]. First retinal axons exit the retina around 32 hours post fertilization (hpf), arrive at the tectum by 48 hpf, and innervate the

tectum around 72 hpf [25], with pre-target sorting along the tract occurring between 48 and 72 hpf [34]. My project employed the unique advantages of zebrafish embryos to analyze two aspects of neural circuit development in vivo – pre-target topographic sorting along the optic tract and topographic mapping along the A-P axis of the tectum.

In **Chapter 2**, I first include a survey of the literature to address the role of axon-axon interactions in neural circuit wiring. While axon-target and axon-environment interactions have long since been of interest in the field of developmental neurobiology, the communication between axons themselves has only recently emerged as crucial mechanism for proper circuit development. Earlier studies provided insight into trans-axonal signaling mediating the fasciculation of axonal tracts for proper guidance to their target and for the defasciculation of axonal bundles at important choice points. However, it is now known that axon-axon interactions govern almost every aspect of circuit development including repulsion along and within tracts needed for proper target selection, repulsion at the target mediating precise synaptic connectivity, and potentially even selective degeneration for circuit refinement.

Chapter 3 focuses on the trans-axonal signaling mechanism mediating pre-target topographic sorting of retinal axons. Given the underappreciated field of trans-axonal signaling, there are many open questions that need to be answered in order to fully understand neural circuit development. Studies from our lab have shown that HS functions non-cell-autonomously, either in the environment around the optic tract or in the pioneer ventral axons signaling to missorted dorsal axons, to regulate pre-target retinal axon sorting. However, the specific components of this signaling complex have yet to be identified. The first part of my project focused on determining the trans-axonal

signaling mechanism triggering the selective degeneration of missorted dorsal axons. Understanding the signaling mechanism by which selective degeneration enables the formation of a precise circuit can provide broader insight into proper circuit formation and potentially into neurodevelopmental and degenerative disorders. In this study, I found that Glypican-3 (Gpc3) is the only membrane-bound HSPG to be expressed specifically by ventral RGCs. Like mutants lacking HS [19, 34], *Gpc3* mutants have missorted dorsal axons along the dorsal optic tract, indicating that Gpc3 is the main HSPG regulating the degeneration of missorted retinal axons. Surprisingly, *Tenm3* mutants also display a similar phenotype and interestingly, Gpc3 and Tenm3 interact, at least genetically, to mediate pre-target sorting of retinal fibers. These results are the first to determine a role for Gpc3 in neural circuit wiring along with a novel role for Tenm3 in axon pruning.

Chapter 4 includes a study on the unbiased analysis of retinotopic mapping and refinement in vivo. Previously, the only approach to study these processes was injecting lipophilic fluorescent dyes into specific quadrants of the retina. Retinal axons elongating from these topographic locations are then labeled as the dyes diffuse along them. While informative, this method does not allow for consistent live imaging and for the genetic manipulation of different RGC populations. It therefore restricts us in the types of questions we would like to answer, in particular how axon-axon interactions contribute to retinotopic mapping and the refinement of mistargeted axons during visual system development. We have developed a novel transgenic line that allows for visualization of the A-P retinotopic map, and used that line for the unbiased and quantitative analysis of retinotopic map development and maturation. I discovered that map development is a

dynamic process. Initially, nasal retinal axons project and arborize within the anterior tectum and to the posterior half of the tectum. As development continues, the mistargeted nasal projections in the anterior half of the tectum undergo an activity-dependent refinement to create a more precise retinotopic map. I was able to, for the first time, analyze the dynamicity of map formation in a quantitative and impartial manner, thereby paving the way for future studies on activity-dependent and molecular mechanisms of retinotopic mapping.

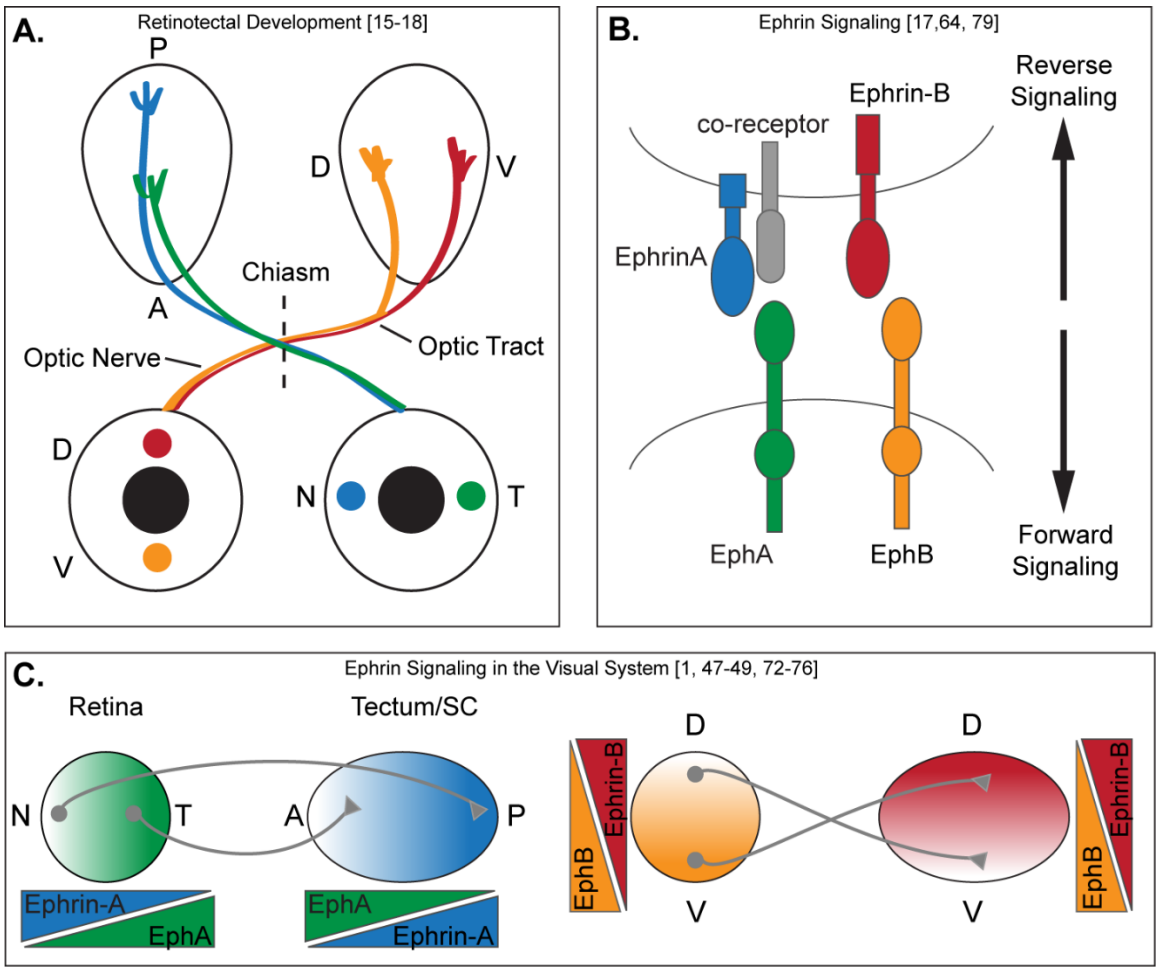

Figure 1.1: Retinotectal development and topographic mapping. (**A**) During visual system development, RGC axons exit the eye, elongate along the optic nerve, cross the midline at the chiasm, and project along the optic tract to the optic tectum. At the optic tectum, retinal axons arborize in distinct termination zones depending on the position of their cell body along the A-P and D-V axes in the retina. Axons originating from RGCs in the nasal retina project to the posterior tectum and axons from temporal RGCs project to the anterior tectum. Along the D-V axis, dorsal RGCs project their axons to the ventral tectum and ventral RGCs project to the dorsal tectum. (**B**) Ephrin/Eph signaling can function bi-directionally. Forward signaling occurs when Ephrins induce a signal through Eph receptors and reverse signaling occurs when Ephs induce a signal through Ephrins. Class A Ephrins are GPI-anchored proteins and thus require a co-receptor to transduce a reverse signal. (**C**) EphA receptors are expressed in a high-temporal to low-nasal gradient in the retina and in a high-anterior to low-posterior gradient in the tectum. Ephrin-As are expressed in complementary gradients in the retina and tectum. Similarly, EphBs are expressed in a high-ventral to low-dorsal gradient in the retina and tectum while Ephrin-Bs are expressed in a high-dorsal to low-ventral gradient in the retina and tectum.

CHAPTER 2

TRANS-AXONAL SIGNALING IN NEURAL CIRCUIT WIRING[1]

[1] Spead O and Poulain FE. 2020. *International Journal of Molecular Sciences* 21(14):5170.
Reprinted here with permission from the publisher.

2.1 ABSTRACT

The development of neural circuits is a complex process that relies on the proper navigation of axons through their environment to their appropriate targets. While axon-environment and axon-target interactions have long been known as essential for circuit formation, communication between axons themselves has only more recently emerged as another crucial mechanism. Trans-axonal signaling governs many axonal behaviors, including fasciculation for proper guidance to targets, defasciculation for pathfinding at important choice points, repulsion along and within tracts for pre-target sorting and target selection, repulsion at the target for precise synaptic connectivity, and potentially selective degeneration for circuit refinement. This review outlines the recent advances in identifying the molecular mechanisms of trans-axonal signaling and discusses the role of axon-axon interactions during the different steps of neural circuit formation.

2.2 INTRODUCTION

The formation of neural circuits is a complex developmental process that gives rise to intricate and precise networks essential for brain function [1, 147]. Defects in axonal connectivity have been associated with a number of neurological disorders including Autism Spectrum Disorders [148, 149], congenital mirror movements [150, 151], horizontal gaze palsy with progressive scoliosis [152], and others [153-155], making it crucial to better understand the mechanisms governing axon guidance and neural circuit wiring.

During development, axons navigate along precise pathways to reach their final target by responding to attractive or repulsive guidance cues present in their environment. This navigation is ensured by motile structures at their leading ends, the growth cones, which possess numerous receptors at their surface allowing them to respond to the various

extra-cellular signals they encounter [156, 157]. A panoply of factors are known to provide long-range and/or contact-mediated signals, including the classical guidance cues Ephrins, Slits, Netrins, and Semaphorins [2], adhesion molecules [3, 158], neurotrophic and growth factors [4], or morphogens such as Sonic Hedgehog (Shh), Bone morphogenetic proteins (BMPs), and Wnts [5, 6]. The activity of these signaling factors has mostly been studied in classical model systems for axon guidance such as the sensory and motor innervation of the limb [159], the midline [160, 161], and the retinotectal and olfactory systems [17, 18, 162, 163]. These models have been instrumental in defining the general rules of axon navigation and targeting. For instance, studying the formation of retinotectal maps in the frog led Sperry to formulate his chemoaffinity hypothesis [45], whereby retinal axons with a unique profile of receptors interpret guidance cues distributed in a gradient at their target. While axon-target and axon-extracellular environment interactions have been widely recognized as essential for the formation of circuits, communication between axons themselves has recently emerged as another crucial, yet understudied, mechanism [164, 165].

The first indication for a role of axon-axon communication, or trans-axonal signaling, in circuit wiring came from early experiments in chick, amphibians and mice showing that sensory projections in the limb were disturbed following motor neuron ablation [166-168], or that retinal and olfactory axons were still able to order themselves in the absence of their respective target [169, 170]. Additional studies in vertebrates and invertebrates have highlighted the importance of neuronal birth timing and age-related axonal elongation in axon-axon communications, with early-born pioneer axons often dictating the trajectory of later-born axons that follow them [171, 172]. In the retinotectal system, for instance, pioneer retinal axons guide follower axons out of the eye, at the

midline and along the optic tract [21, 22]. In addition to the temporal control of axon outgrowth, the temporal regulation of receptor availability at the surface of axons is critical in determining the sensitivity of axons to signals presented by other axons. It also allows axons to change their responsiveness to a cue in a precise spatial and temporal manner [156, 173]. While homotypic and heterotypic interactions between axons have been recognized as essential for proper neuronal connectivity for more than four decades, our understanding of the cellular and molecular mechanisms at play has only more recently progressed. In this review, we describe specific examples that highlight the importance of trans-axonal signaling in circuit wiring during development, focusing on the mechanisms underlying selective fasciculation and adhesion, repulsion, and selective defasciculation.

2.3 Axon Fasciculation and Adhesion

Homotypic and heterotypic fasciculation between axons facilitates and coordinates the formation of tracts en route to a common target or between inter-connected brain regions. Early studies demonstrating the importance of pioneer-follower axon interactions in neural circuit formation have suggested a crucial role for adhesion and fasciculation between axons as they navigate towards their target. For example, in the Drosophila olfactory system, ablation of early-born olfactory receptor neurons, whose axons act as pioneers, prevents the targeting of later-born axons to the antennal lobe structure [174]. Similarly, ablation of early-born pioneer neurons in the olfactory [175] or visual [21] systems in zebrafish causes later-born follower axons to misroute on their way to their target and fail to establish proper connections. Interestingly, in the zebrafish forebrain commissure, leading and following commissural axons show a difference in kinetics at the midline: while leading axons pause slightly before speeding back up to

cross the midline, followers do not slow down and continue across the midline at a constant speed [176]. Follower axons notably change their kinetics at the midline and adopt a leader behavior upon ablation of leading axons, suggesting a direct interaction between leading and following axons, with follower axons fasciculating and navigating along the pioneering axons. Interestingly, axon fasciculation can not only occur after a growth cone encounters the shaft of a neighboring axon and moves along it, but also through a "zippering" mechanism involving direct interactions between axonal shafts [177]. Overall, interactions between axons are facilitated by cell birth order, expression of adhesion molecules, and conserved signaling pathways that mediate proper fasciculation as axons elongate to their target.

2.3.1 Homotypic Fasciculation

Cell adhesion molecules (CAMs) are highly conserved across species and have been found to regulate both homotypic and heterotypic axon-axon interactions in several circuits (**Figure 2.1**) [3, 158, 178]. For example, Neuroglian (Nrg), the Drosophila orthologue of L1-CAMs in vertebrates, is required for the fasciculation between axons projecting to the peduncle of the mushroom bodies [179]. Two intracellular adaptor proteins, Ankyrin-2 and Moesin, interact with Nrg to cluster it along the axonal surface, thereby allowing for stable homophilic Nrg complexes to form between axons as they elongate (**Figure 2.1A**). Similarly, the adhesion molecule L1 facilitates fasciculation between sensory axons during hindlimb development in chick, allowing them to form bundles important for the guidance of later-growing axons [180]. Indeed, injecting an anti-L1 antibody into the chick hindlimb at a timepoint when all motor axons, but only a few sensory axons, have reached the plexus, causes sensory axons to defasciculate and fail to navigate along their

proper peripheral nerve [181]. While injecting an antibody against the neural cell adhesion molecule NCAM does not alter sensory axon projections, the enzymatic removal of polysialic acid (PSA) from NCAM causes an increase in sensory axon fasciculation, demonstrating that post-translational modifications of CAMs can modulate axon-axon interactions. Similar observations have been made in the neuromuscular and visual systems: in ovo injection of an anti-L1 or an anti-NCAM antibody directly into the iliofibularis muscle in chick leads to the defasciculation of motor axons, while removal of PSA from NCAM increases their fasciculation [182]. Likewise, injecting an anti-NCAM antibody into the developing chick retina causes a disorganization of the optic nerve suggestive of retinal axon defasciculation [183].

Along with L1 and NCAM, early studies in the chick and goldfish retinotectal systems indicate that the adhesion molecule ALCAM (also called BEN, DM-GRASP, SC1, or Neurolin) is also necessary for the proper bundling of retinal axons into fascicles [184, 185]. Adding an antiserum against ALCAM to chick retinal explants in culture blocks the elongation of retinal axons on other retinal axons, but not on laminin [184]. Similarly, injecting an anti-ALCAM antibody into the eyes of growing goldfish causes retinal axons to defasciculate, leading to disorganized optic nerves [185]. Interestingly, *ALCAM* mRNA is locally translated in growth cones of retinal axons, and reducing ALCAM local translation in chick retinal axons in culture prevents axons from elongating on ALCAM, but not laminin, coverslips [186]. Retinal axons also show fasciculation defects in *Alcam* knock-out mice [187], indicating that ALCAM's function in mediating adhesion between axons is conserved across species.

Other members of the immunoglobulin superfamily of CAMs are also known to regulate axon fasciculation. In the mouse visual system, DSCAM (Down Syndrome Cell Adhesion Molecule) is necessary for the fasciculation of retinal axons along the optic tract [53]. Retinal axons defasciculate in *Dscam* mutants, causing them to stray from their normal path. In the chick peripheral system, the Synaptic cell adhesion molecules SynCAMs were found to regulate axon-axon contacts between afferent fibers as they enter the dorsal root entry zone (DREZ) of the spinal cord [188]. Both overexpression and knockdown of SynCAMs lead to disorganized axon-axon contacts between sensory afferents. In particular, knockdown of SynCAM2 and SynCAM3 leads to the segmentation of axon bundles and mistargeting of axons to the dorsal part of the spinal cord as well as aberrant pathfinding at the DREZ. Finally in the mouse motor system, Contactin-2 (also known as TAG-1) has been detected in the distal segment of motor axons as they elongate into the periphery [189]. Specific inactivation of *TAG-1* in motor neurons causes a thickening of the ventral root of the spinal cord and a defasciculation of motor axons in vitro.

In addition to the immunoglobulin superfamily of CAMs, members of the cadherin superfamily form another class of CAMs that mediate neural circuit formation through axon-axon interactions. In *C. elegans, fmi-1*, the ortholog of vertebrate Celsr and Drosophila *flamingo*, is needed for adhesion between pioneer and follower axons that form the ventral nerve cord [190]. More recently in the mouse, Protocadherin-17 (Pcdh17) has been shown to be required for growth cone migration at axon-axon contact sites between amygdala axons as they extend to the hypothalamus and ventral striatum [191]. Pcdh17 accumulates at homotypic contacts between cells, and growth cones lacking

Pdch17 are no longer able to migrate properly along other axons both in vivo and in vitro. Conversely, ectopic expression of Pcdh17 in axons that do not normally express Pcdh17 causes these axons to mix with axons expressing endogenous Pcdh17. Elegant live imaging and biochemical experiments further showed that Pcdh17 recruits the WAVE complex and the actin-associated proteins Lamellipodin (Lpd) Ena/VASP to axon-axon contact sites, thereby promoting the motility of growth cones as they make contact with other axons of the same tract.

The function or abundance of adhesion molecules at the axonal surface is tightly regulated by classical guidance cues (**Figure 2.1AIV-VII**). In particular, Semaphorins have been identified as major regulators of axon fasciculation. In the Drosophila visual system, transmembrane Sema1a and PlexA are both expressed on the surface of photoreceptor axons that project to the medulla of the optic lobe. While Semaphorins usually act as ligands activating Plexin receptors [192, 193], in this system Sema1a reverse signaling mediates axonal adhesion as photoreceptor axons extend through intermediate target zones to the lamina of the optic lobe [194, 195]. Interestingly, Sema1a reverse signaling increases the adhesive function of Fascilin 2 (Fas2) at the surface of photoreceptor axons by down-regulating the activity of the small GTPase Rho1 [195]. This is in sharp contrast to its role in the Drosophila motor system, where Sema1a reverse signaling activates Rho1 to promote axon-axon repulsion, thus balancing the adhesive activity of Fas2 and another CAM, Connectin (Conn), for proper motor axon targeting [196]. A similar mechanism whereby Semaphorin signaling regulates the expression of an adhesion molecule has been described in zebrafish [197]. Knockdown of both Sema3D and L1-CAM leads to a loss of adhesion between medial longitudinal fascicle (MLF) axons. Importantly, Sema3D

regulates the axonal levels of L1: Sema3D overexpression increases L1 protein levels, whereas Sema3D knockdown decreases them. Which signaling pathway is activated by Sema3D to regulate L1 protein levels remains unclear, but it could involve the Semaphorin-3 receptor Neuropilin-1 (Nrp1). Interestingly, Nrp1 and L1 were found to associate via their extracellular domains [198], and Nrp1 is known to be required for proper homotypic fasciculation of both motor and sensory axons in the developing limb in mice [199]. Altogether, these different studies highlight the control of adhesion molecules by Semaphorin signaling as a key conserved mechanism for regulating homotypic axon fasciculation.

Other classical guidance cues have been shown to mediate homotypic fasciculation, however it remains unknown whether they do so directly or by regulating adhesion molecules (**Figure 2.1AVIII-X**). For example, fasciculation in the sensorimotor system of mice is, at least in part, mediated through Ephrin-B/EphB signaling [200]. Ephrin-B1 is present on developing sensory axons as well as in the surrounding limb bud mesenchyme while its receptor, EphB2, is expressed on both sensory and motor axons. Mice lacking Ephrin-B1 exhibit defasciculated sensory and motor axons, supporting a model whereby Ephrin-B1 signaling from the mesenchyme maintains the fasciculation of peripheral projections through a surround-repulsion mechanism. However, defasciculation appears more robust in full knock-out embryos compared to conditional knock-outs lacking Ephrin-B1 from the mesenchyme, suggesting that Ephrin-B1 might also promote the fasciculation of sensory axons via a distinct mechanism involving axon-axon communication [200]. In addition to EphB2, the guidance cue Slit2 and its receptors, Robo1 and Robo2, are expressed by motor neurons in mice as well. Inactivation of any of

these three proteins causes motor axons to prematurely defasciculate before reaching their muscle target at the diaphragm [201]. While it remains unclear how Slit2, a secreted factor, promotes motor axon fasciculation, signaling could possibly involve N-cadherin, whose distribution at the surface of placodal cells in chick is increased by Slit/Robo signaling [202]. Finally, another classical guidance pathway that has recently been implicated in mediating axon fasciculation involves the secreted factors Netrin and Draxin and their receptor DCC [203]. Draxin was first identified as a repulsive guidance cue that also promotes homotypic fasciculation between commissural axons in the mouse corpus callosum [204]. A screen for large extracellular protein interactions and immunoprecipitation assays later demonstrated that Draxin interacts with both DCC and Netrin [205, 206]. Crystal structures of Draxin/DCC and Draxin/Netrin-1 complexes were recently analyzed and suggest that Draxin tethers Netrin-1 and DCC together to promote axon fasciculation [207].

Along with classical guidance cues, other signaling molecules regulate axon fasciculation in addition to their other better-known functions. Endocannabinoids, for instance, have been identified as guidance cues regulating axon pathfinding and elongation in mouse and xenopus [208], and deletion of the cannabinoid receptor CB_1R from mouse cortical neurons in vivo causes a defasciculation of their axons [209]. A recent study reported that Kinesin-1 regulates the trafficking and sub-cellular localization of CB_1R in mouse cortical neurons, thereby modulating endocannabinoid signaling and axon fasciculation [210].

2.3.2 HETEROTYPIC FASCICULATION

The nervous system comprises many axonal tracts formed by different neuron types. Selective heterotypic fasciculation between different axon types coordinates the development of these tracts into neural circuits (**Figure 2.1B**). For example, in the developing cerebral cortex, pioneer axons that form the corpus callosum originate from neurons in the cingulate cortex and guide follower axons arising from the neocortex. While cingulate axons are guided toward and across the midline by cues present in the environment, neocortical axons fasciculate with pioneer axons and use them as a guide [211]. Innervation of the habenula is another developmental process that relies on heterotypic axon fasciculation. The habenula includes the lateral habenula (lHb) that projects axons to monoaminergic nuclei, including dopaminergic nuclei, in the ventral tegmental area (VTA). Conversely, the lHb receives reciprocal dopaminergic inputs from the VTA [212-214]. Interestingly, the genetic ablation of the habenula in the mouse leads to the loss of dopaminergic projections to the lHB [81]. Furthermore, physically preventing the outgrowth of habenular axons from the lHb also inhibits the elongation of dopaminergic axons to the lHb in mouse brain hemisections, indicating that lHb axons extending to the ventral midbrain sort and guide afferent dopaminergic axons to the lHb [215]. This pre-target reciprocal trans-axonal signaling is mediated by the adhesive molecule Limbic-system-associated protein (LAMP) present at the surface of lHb axons. LAMP likely engages in homophilic interactions to mediate adhesion, as it is also expressed by dopaminergic neurons projecting to the lHb.

Another example of interactions between reciprocal, afferent and efferent axons involves thalamocortical and corticothalamic axons that meet in the subpallium to form

the internal capsule before projecting to their respective targets [216]. Several studies have suggested that cortical and thalamic axons may rely on each other for proper guidance in the internal capsule. Mutations affecting thalamic axons were shown to alter cortical axons, and conversely [217]. Further studies later confirmed that reciprocal interactions between thalamocortical axons and pioneer cortical axons that are generated by cells in the subplate are required for the guidance of both thalamocortical and corticothalamic projections in the subpallium and within the neocortex. Genetically ablating the thalamus in vivo causes corticothalamic axons to be misguided along a different trajectory towards the cerebral peduncle. The interaction between thalamocortical axons and pioneer cortical axons in the subpallium is required for proper guidance but relies on a tight temporal control of axon elongation [218]. Pioneer cortical axons indeed reach the lateral subpallium before thalamic axons and must halt their elongation and pause until thalamic axons reach the proper location in order to guide them. This waiting period is triggered by the transient expression of PlexinD1 by pioneer cortical axons that allows them to pause in response to Sema3E secreted by the radial glia. Conversely in the neocortex, cortical efferent axons are required for thalamic axons to cross the pallial-subpallial boundary [219].

In the peripheral nervous system, sensory and motor axons also use heterotypic interactions to extend to their appropriate targets. Along with mediating homotypic fasciculation of motor and sensory axons, Nrp1 regulates heterotypic fasciculation between motor and sensory axons in the developing limb of the mouse [199]. Specific ablation of Nrp1 from sensory axons causes not only sensory but also motor axons to defasciculate. This observation suggests a model whereby Nrp1 acts with a yet unidentified ligand on sensory and motor axons to mediate their fasciculation.

Interestingly, Nrp1 and Sema3A are both expressed by motor and sensory neurons, suggesting that motor axons might also defasciculate in response to increased extra-cellular levels of Sema3A that would occur upon Nrp1 ablation from sensory axons. Additional studies in the chick hindlimb have further demonstrated that motor axons extend first and provide a guiding path for the follower sensory axons [167]. It was later found in vertebrates that earlier-projecting motor neurons express EphA3 and EphA4, while sensory axons express Ephrin-A [220]. Inactivation of EphA3 and EphA4 in mouse motor neurons leads to the loss of sensory axon projections. Moreover, the EphA3 ectodomain was shown to promote sensory axon elongation in an Ephrin-A-dependent manner in vitro, suggesting that Ephrin-A reverse signaling mediates interactions between sensory and motor axons. Altogether, these studies highlight the importance of heterotypic axon-axon fasciculation in the establishment of peripheral nerves.

2.4 TRANS-AXONAL REPULSION

As important as selective homotypic and heterotypic fasciculation, trans-axonal repulsive interactions mediate the segregation of axons within a tract or the dissociation of axons into distinct tracts forming different circuits. Typically, repulsion between homotypic axons leads to their segregation and sorting en route to or at their target, while heterotypic repulsion generates independent axonal tracts [165]. Repulsion between axonal arbors from same-type neurons also leads to the formation of separate projection fields at the target, thereby ensuring optimal spatial coverage required for efficient connectivity [164, 221].

2.4.1 Repulsion and Selective Defasciculation at Choice Points

As they navigate to their final destination, axons often encounter several successive choice points where intermediate targets such as guidepost cells steer them along the proper path. Interestingly, axons themselves also provide directional information to other axons at choice points (**Figure 2.2A**). In the mouse visual system, axons from retinal ganglion cells (RGCs) either cross the midline at the optic chiasm to project contralaterally to the opposite optic tract or do not cross and project ipsilaterally. A recent study demonstrated that contralateral retinal axons that reach the chiasm first transport and secrete Shh at the optic chiasm, thereby repelling later-extending ipsilateral axons that express the receptor Boc (**Figure 2.2AI**) [222]. Thus, in this system, trans-axonal repulsive signaling between contralateral and ipsilateral axons provides a spatiotemporal regulation of axon segregation at the optic chiasm that ensures proper subsequent axonal targeting.

Axon-axon repulsion and selective defasciculation at choice points also allow a subgroup of axons to segregate from the main bundle to navigate to an independent target. Periphery muscle innervation by motor axons, for instance, requires selective axon defasciculation. It has been extensively studied in Drosophila, where motor axons initially exit the central nervous system (CNS) as the intersegmental nerve (ISN) and segmental nerve (SN) before further dividing into five distinct motor branches – the ISN, ISNb, ISNd, SNa, and SNc [223]. Each of these five bundles defasciculates again, so that motor axons innervate individual muscle targets. Sema1a signaling has been shown to regulate the defasciculation of motor axons at specific choice points [224]. Both Sema1a and its receptor PlexA are expressed by motor neurons, and ISN and ISNb axons fail to

defasciculate from each other and project to improper targets in *sema1a* and *plexA* mutants. Interestingly, forward and reverse signaling are both required for motor axon defasciculation, with Sema1a reverse signaling being modulated by two counteracting Rho1 GTPase regulators [225]. In particular, the Rho guanine nucleotide exchange factor Pebble (Pbl) acts downstream of Sema1a to promote the defasciculation of ISNb axons at their choice points (**Figure 2.2AII**). In absence of Pbl, ISNb motor axons become hyperfasciculated, leading to improper targeting. What mechanism could control the specific activation of Sema1a signaling at choice points? Interestingly, a secreted member of the heparan sulfate proteoglycan (HSPG) family, Perlecan, is found at higher levels in the extracellular matrix (ECM) at defasciculation choice points and appears to be expressed by a subset of motor neurons [226]. Like in *sema1a* and *plexA* mutants, motor axons fail to defasciculate in *perlecan* mutants, and re-expressing *perlecan* in neurons rescues axon fasciculation defects. Whether Perlecan is selectively secreted by motor axons at choice points to regulate Sema1a/PlexA signaling and motor axon defasciculation remains to be established.

Complementary to Semaphorin signaling, the cell adhesion receptors Integrins have also been reported to regulate motor axon defasciculation in Drosophila [227]. Mutants lacking Integrin α1 or Integrin α2 have increased fasciculation of ISNb and SNa axons that causes a lack muscle innervation. Interestingly, DCas, the Drosophila member of the Crk-associated substrate (Cas) family known to act downstream of Integrins, is highly detected in developing motor axons [227]. Like in *Integrin* mutants, ISNb axons fail to defasciculate from the ISN bundle in *DCas* mutants and double *Dcas*/+;*Integrin*/+ heterozygotes, suggesting that Integrin signaling through Dcas is needed for proper motor

axon defasciculation. Surprisingly, overexpressing DCas in neurons causes a similar hyperfasciculation defect in an Integrin-dependent manner, suggesting that Integrin/DCas signaling regulates both axon-axon and axon-ECM interactions at choice points. How integrin signaling and other pathways co-regulate axon-axon repulsion to direct defasciculation has yet to be determined.

2.4.2 Axon-Axon Repulsion between and within Tracts

Trans-axonal repulsive signaling between heterotypic tracts allows axons to form distinct bundles and take different trajectories towards their respective targets. In the sensorimotor system, for instance, motor and sensory axon bundles elongate closely to each other in a coordinated manner but remain physically segregated through contact-dependent repulsive interactions as they elongate to the muscle and dermis, respectively [167, 180]. Interestingly in mice, EphA3 and EphA4 are present at the surface of motor axons while DRG sensory neurons express high levels of Ephrin-A. Disrupting Ephrin signaling by selectively inactivating EphA3 and EphA4 in motor neurons leads to the intermingling of adjacent motor and sensory axons [228], indicating that Ephrin-A/EphA trans-axonal signaling mediates the repulsion between motor and sensory axons required for their segregation.

Similar trans-axonal repulsive interactions are observed in the developing corpus callosum, where axons from the medial and lateral regions of the cortex project to the contralateral medial and lateral cortical regions, respectively. As they elongate across the midline, medial and lateral cortical axons are organized into separate bundles, with medial axons passing through the dorsal part of the corpus callosum and lateral axons elongating through its ventral part. EphA3 is expressed on lateral-projecting axons and

repels medial-projecting axons upon contact, thereby ensuring the segregation of the two axonal tracts [229]. Interestingly, Sema3A-Nrp1 signaling also regulates the topographic ordering of callosal axons [230]. Axons extending from the motor and sensory cortex are spatially segregated into distinct bundles in the corpus callosum. Selectively inactivating Nrp1 or Sema3A in neurons from the motor or sensory cortex, respectively, causes defects in axon segregation, with motor and sensory cortical axons intermixing within the corpus callosum. Disruption of callosal axon organization further leads to subsequent defects in contralateral projections and mapping, highlighting the importance of pre-target topographic ordering of axons for proper brain wiring.

Outside of the corpus callosum, pre-target topographic axon sorting has been observed in many other systems and shown indeed to be an essential step for map formation. For example, thalamocortical axons originating from distinct thalamic nuclei are already ordered in the subpallium before reaching the cortex [231]. Selectively disturbing subpallium development without affecting the thalamus or cortex causes thalamocortical axons to intermix en route to their target and subsequently fail to form functional topographic maps in the cortex [20]. Similarly, pre-target axon sorting is critical for the formation of a functional topographic map in the vertebrate olfactory system [13]. In the mouse olfactory system, about one thousand types of olfactory sensory neurons (OSNs) convey odor information perceived in the olfactory epithelium (OE) to the olfactory bulb (OB). Each OSN expresses a single type of G protein-coupled odorant receptor (OR), and same-type OSNs expressing the same OR extend axons that converge onto common individual target sites called glomeruli in the olfactory bulb [232]. As the organization of glomeruli does not correlate with the position of the OSNs in the OE,

convergence of olfactory axons onto specific glomeruli along the antero-posterior axis is ensured by pre-target axon sorting (**Figure 2.2B**). Interestingly, ORs themselves have an instructive role in the sorting and targeting of axons that is independent of their odor ligand specificity [233, 234]. The spontaneous activity of each OR generates a unique level of cyclic adenosine monophosphate (cAMP) that in turn, initiates signal transduction cascades activating the transcription of specific genes [235, 236]. cAMP notably positively regulates the expression of Nrp1, causing OSNs to express variable Nrp1 levels. Interestingly, Nrp1 and Sema3A are expressed in a complementary manner in the olfactory nerve. Axons with high levels of Nrp1 elongate along the outer, lateral part of the bundle, while axons with high levels of Sema3A are confined within its center [13]. Specific inactivation of Nrp1a or Sema3A in OSNs causes axons to intermingle and lose their topographic order within the nerve, indicating that repulsive trans-axonal signaling mediated by Sema3A/Nrp1 determines the relative positioning of olfactory axons. A similar repulsive signaling mediated by Eph-Ephrin has been suggested to regulate the segregation of olfactory receptor cell axons in the moth [237].

Pre-target axon sorting has also been extensively studied in the visual system. In vertebrates, retinal axons are preordered along the dorso-ventral axis in the optic tract before reaching the tectum, with dorsal and ventral axons elongating along the ventral and dorsal branches of the tract, respectively [12, 23, 25, 27, 28]. As in the olfactory and thalamocortical systems, pre-target ordering of retinal axons is thought to facilitate proper topographic mapping at the target [12]. The signaling mechanism mediating optic tract sorting has not yet been determined, but several studies in zebrafish have highlighted an essential role for heparan sulfate (HS) [19, 34, 238]. In embryos lacking HS due to mutations

in the glycosyltransferases Ext2 and Extl3, pre-target sorting is disrupted, with several dorsal axons misrouting along the dorsal part of the optic tract. Although the mechanism by which HS regulates retinal axon sorting is not well understood, it might involve Nrp1 signaling [42]. Indeed, knockdown of Hermes, an RNA-binding protein expressed in RGCs, leads to partial missorting of dorsal axons through the upregulation of Nrp1 expression, suggesting that Nrp1 levels must be temporally regulated for proper sorting. Interestingly, a micro-RNA, miR-124, indirectly regulates the onset of Nrp1 expression in retinal axons in Xenopus, thereby controlling the sensitivity of retinal growth cones to Sema3A [239]. While Sema3A, Nrp1 and several Plexins are known to be expressed in RGCs, their contribution to retinal axon sorting, and possibly trans-axonal signaling in that system, remains to be tested. Additional studies in Xenopus have highlighted the role of axon-axon interactions in optic tract sorting [43]. In vivo, growth cones of dorsal and ventral axons show a range of behavior upon contact with other axons along the tract, including crossing over the contacted axon, fasciculating with it, or following it at a distance. Further experiments in vitro revealed that homotypic contacts between either dorsal or ventral axons usually lead to axon crossing or fasciculation, while heterotypic contacts are usually followed by axon crossing, stalling or retraction. Interestingly, both homotypic fasciculation and heterotypic repulsion appear to be regulated by the cytoplasmic FMR1-interacting protein 2 (CYFIP2). CYFIP2 translocates to the growth cone periphery upon axonal contact, where it interacts with members of the WAVE regulatory complex (WRC) to regulate actin dynamics. Knockdown of CYFIP2 reduces homotypic fasciculation events and increases axonal stalling and retraction after a growth cone contacts an axon in vitro. In vivo, interaction between CYFIP2 and the WRC is

required for the sorting of dorsal axons along the tract, which is disrupted in *cyfip2* zebrafish mutants [44]. While the role of CYFIP2 provides insight into the regulation of heterotypic and homotypic axonal interactions during optic tract sorting, the ligands and receptors upstream of CYFIP2 that would mediate trans-axonal signaling in that system remain unidentified. The importance of axonal birth order and the potential role of pioneer vs. follower axon interactions for the segregation of ventral and dorsal axons have also yet to be addressed.

2.4.3 Axon Repulsion at the Target

Axon-axon interactions continue to dictate the pathway taken by axons as they reach their target and subsequently arborize. In the mouse olfactory system, for instance, olfactory axons are segregated along the dorso-ventral axis and maintain their relative position from their exit from the OE to their entry of the OB. Axons from the dorsomedial zone of the OE project to the dorsal part of the OB first and are followed by axons from the ventrolateral zone that project to the ventral OB [8, 232, 240]. Interestingly, Sema3F and its receptor Neuropilin-2 (Nrp2) are expressed in a complementary graded manner along the dorso-ventral axis in OSNs. Early-arriving dorsomedial axons exhibit high levels of Sema3F, and later-arriving ventrolateral axons express high levels of Nrp2 [241]. Selective inactivation of Sema3F in OSNs does not affect the sorting of dorsomedial and ventrolateral axons en route to the OB, but it causes Nrp2-expressing axons to mistarget to the dorsal region of the OB upon arrival. The detection of Sema3F protein, but not of *Sema3F* transcript, in the outer nerve layer of the dorsal OB suggests an "indirect" trans-axonal signaling model, whereby pioneer dorsomedial axons produce and deposit Sema3F in the dorsal OB, which in turn repels ventrolateral axons and restricts

them to the ventral OB [242]. A similar trans-axonal signaling mechanism between early- and later-arriving axons has been described in the Drosophila olfactory system, where antennal ORN axons expressing high levels of Sema1A reach the peripheral antennal lobe first and repel later-arriving maxillary palp olfactory axons, constraining them to central glomeruli [243].

Trans-axonal signaling also dictates the fine mapping of axons at their final destination. Once axons have elongated and reached their target, they form elaborate axonal arbors within specific territories or termination zones, establishing precise synaptic connections essential for an efficient transfer of information. Several studies have demonstrated that competitive axon-axon interactions facilitate different steps of circuit development, including topographic order and mapping [17]. Repulsive interactions between axons at the target regulate the size and shape of individual axonal arbors, thereby restricting them to precise termination zones. In zebrafish, for instance, interactions between sensory axon arbors limit the size of individual arbors and confine them to restricted territories. In the absence of neighboring neurons, sensory axon arbors continue to grow without restriction [244]. Similarly, retinal axons form larger and more complex arbors at the tectum in the absence of neighboring axons [245, 246]. Consequently, disturbing axon-axon interactions independently of the target modifies the formation of precise topographic maps at the target. In the mouse visual system, for instance, trans-axonal signaling between nasal and temporal retinal axons contributes to retinocollicular mapping along the antero-posterior axis (**Figure 2.2CI**) [63]. Temporal retinal axons that express high levels of EphA project to the rostral superior colliculus (SC) that expresses Ephrin-As at low levels. Conversely, nasal retinal axons with low levels of EphA project

to the caudal SC that expresses high levels of Ephrin-As. Interestingly, the targeting of temporal axons is not affected after selectively inactivating EphrinA5 in the SC, but becomes altered and posteriorly shifted to the caudal SC (that is, the area targeted by nasal axons), upon EphrinA5 ablation in both the SC and the retina. Thus, target-independent trans-axonal signaling prevents temporal and nasal axons from forming overlapping termination zones, thus ensuring proper mapping.

Homotypic axon-axon repulsive interactions finally ensure that axonal arbors from neurons sharing the same function do not overlap with each other and are properly spaced. This "tiling" mechanism allows axons to maximize the coverage of an area while minimizing redundancy of targeting [221]. Interestingly, different types of neurons that innervate a common target tile independently of one another, implicating a specificity of signaling and suggesting an essential role for contact-mediated repulsion. Live imaging studies of trigeminal and spinal cord sensory neurons in zebrafish have indeed confirmed that axons repel each other and limit the size of their arborizations through direct contact-mediated repulsion [244]. Several studies in Drosophila have highlighted the role of adhesion molecules in mediating proper spacing between axonal arbors (**Figure 2.2CII**). In the visual system, for instance, the atypical cadherin Flamingo (Fmi) enables proper spacing between R8 photoreceptor axons in the medulla by facilitating competitive interactions between adjacent R8 axonal arbors [247]. When *fmi* is mosaically knocked out in R8 cells, growth cones become irregularly spaced and often overlap, suggesting that Fmi mediates repulsive interactions between R8 cells in a cell-autonomous manner. Interestingly, aggregation assays in vitro and clonal analyses in vivo have recently revealed that Fmi interacts *in cis* with another transmembrane receptor, Golden goal

(Gogo). Like Fmi, Gogo mediates repulsive axon-axon interactions between R8 axons [248], and *fmi* and *gogo* genetically interact to regulate R8 axon targeting in the medulla [249]. As both Fmi and Gogo colocalize at cell-cell contacts when expressed in cultured cells [249], the formation of Fmi-Gogo complexes might be needed for the proper spacing of R8 axonal arbors. Along with photoreceptor cells, L1-L5 neurons in the lamina also project axons to spatially restricted columns in the medulla, with each column containing only one axon of each neuron type [250]. Homophilic binding between Dscam2, a member of the DSCAM family, mediates repulsion between L1 axonal arbors, thereby restricting them to specific columns. In *dscam2* mutants, L1 axons still target the correct layer of the medulla but are no longer restricted to a single column.

In addition to mediating the correct spacing of axonal arbors in the Drosophila visual system, atypical cadherins have recently emerged as regulators of axonal tiling in vertebrates [251, 252]. Among the 70 different protocadherins (Pcdh) identified in mammals, PcdhαC2 is the only Pcdhα isoform expressed in serotonergic neurons. While serotonergic axon terminals are precisely ordered and evenly spaced in their target fields in the basal ganglia and hippocampus, they appear disorganized, tangled and clumped together in mice lacking PcdhαC2. This phenotype could also be observed upon specific ablation of PcdhαC2 in serotonergic neurons [241], suggesting that Pcdhαc2 mediates homophilic repulsive interactions to promote tiling between serotonergic axon terminals. Interestingly, the Pcdhα gene cluster has been associated with schizophrenia and autism spectrum disorders, suggesting the possible involvement of defective trans-axonal signaling in the etiology of these neurodevelopmental disorders.

2.5 Concluding Remarks and future perspectives

Trans-axonal signaling regulates a striking number of developmental processes that are essential for neural circuit wiring. Both homotypic and heterotypic axon-axon interactions not only mediate axon adhesion and bundling for guidance to the proper target, but also defasciculation for pathfinding at important choice points, repulsion within and between tracts for pre-target sorting and target selection, and repulsion at the target for precise synaptic connectivity. Interestingly, one axonal behavior that is notably lacking from this list is selective axon degeneration. Local axon degeneration refine nervous system connectivity in many species, for instance by remodeling axonal projections during metamorphosis in insects, or by pruning mistargeted axons or axonal branches in vertebrates [253]. In the zebrafish visual system, for example, some dorsal retinal axons initially misroute along the dorsal branch of the optic tract, indicating that pre-target sorting of retinal axons is not precisely established during initial pathfinding. Topographic order is eventually achieved through the selective degeneration of these missorted dorsal axons [34]. The observations that axon-axon interactions participate in the segregation of retinal axons along the tract [43] and that ventral axons elongate along the tract first in zebrafish [33], raise the intriguing possibility that ventral axons might trigger the selective degeneration of missorted dorsal axons. As HS functions non-cell-autonomously to trigger this degeneration [34], testing its role in trans-axonal signaling between ventral and dorsal axons might provide clues about the molecular mechanism involved.

While many studies have highlighted the importance of axon-axon interactions, the signaling mechanisms and cellular dynamics governing trans-axonal communication

are only beginning to emerge in vivo. The recent development of innovative genetic, molecular and imaging techniques will undoubtedly open new avenues of research by enabling the molecular profiling of single neurons, the selective manipulation of specific axons, and the visualization of axon-axon dynamics at high resolution. Characterizing the molecular and cellular mechanisms by which axons communicate with each other remains a key question to address for better understanding how precise and efficient neural circuits are formed and maintained.

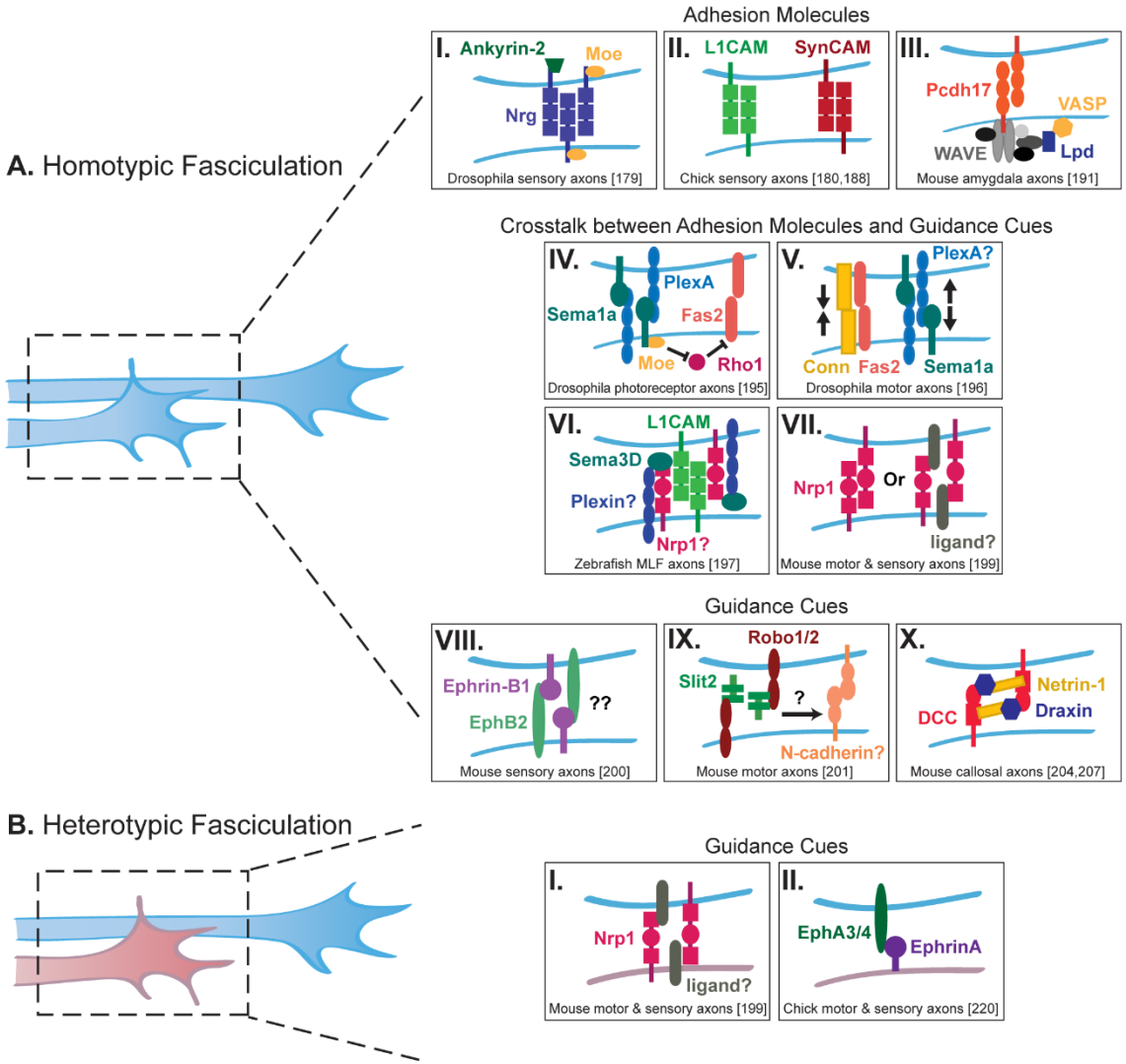

Figure 2.1: Trans-axonal signaling mediates homotypic and heterotypic fasciculation. (AI-III) CAMs regulate homotypic axon-axon fasciculation. (AI) Nrg is clustered along the

Figure 2.1 (Continued): surface of Drosophila sensory axons to mediate homotypic fasciculation [179]. (AII) L1CAM and SynCAM both mediate homotypic fasciculation of chick sensory axons [180,188]. (AIII) Pcdh17 facilitates trans-axonal homotypic fasciculation in mouse amygdala axons by recruiting the WAVE complex, Lpd, and VASP [191]. (AIV-VII) Crosstalk between CAMs and classical guidance cues regulate homotypic axon-axon interactions. (AIV) Sema1a reverse signaling increases the adhesive function of Fas2 in Drosophila photoreceptor axons [195], while it balances the adhesive functions of Conn and Fas2 in motor axons (AV) [196]. (AVI) Sema3D signaling likely involving Nrp1 and Plexin co-receptors regulates the expression levels of L1CAM to mediate homotypic fasciculation of zebrafish MLF axons [197]. (AVII) In mouse motor and sensory axons, Nrp1, either on its own or with an unknown ligand, facilitates homotypic axon-axon fasciculation[199]. (AVIII-X) Other classical guidance cues also mediate homotypic trans-axonal signaling. (AVIII) Ephrin-B1 and EphB2, expressed on mouse sensory axons, may regulate homotypic axon fasciculation by binding in *trans* [200]. (AIX) Slit/Robo signaling mediates homotypic fasciculation of motor axons, possibly by regulating the surface levels of N-cadherin [201]. (AX) Interactions between Netrin-1, Draxin and DCC facilitate fasciculation of mouse callosal axons [204,207]. (BI-II) Classical guidance cues also mediate heterotypic trans-axonal signaling. Nrp1, through an unknown ligand, as well as Ephrin-A/EphA signaling, mediate trans-axonal heterotypic fasciculation of motor and sensory axons [299,220.]

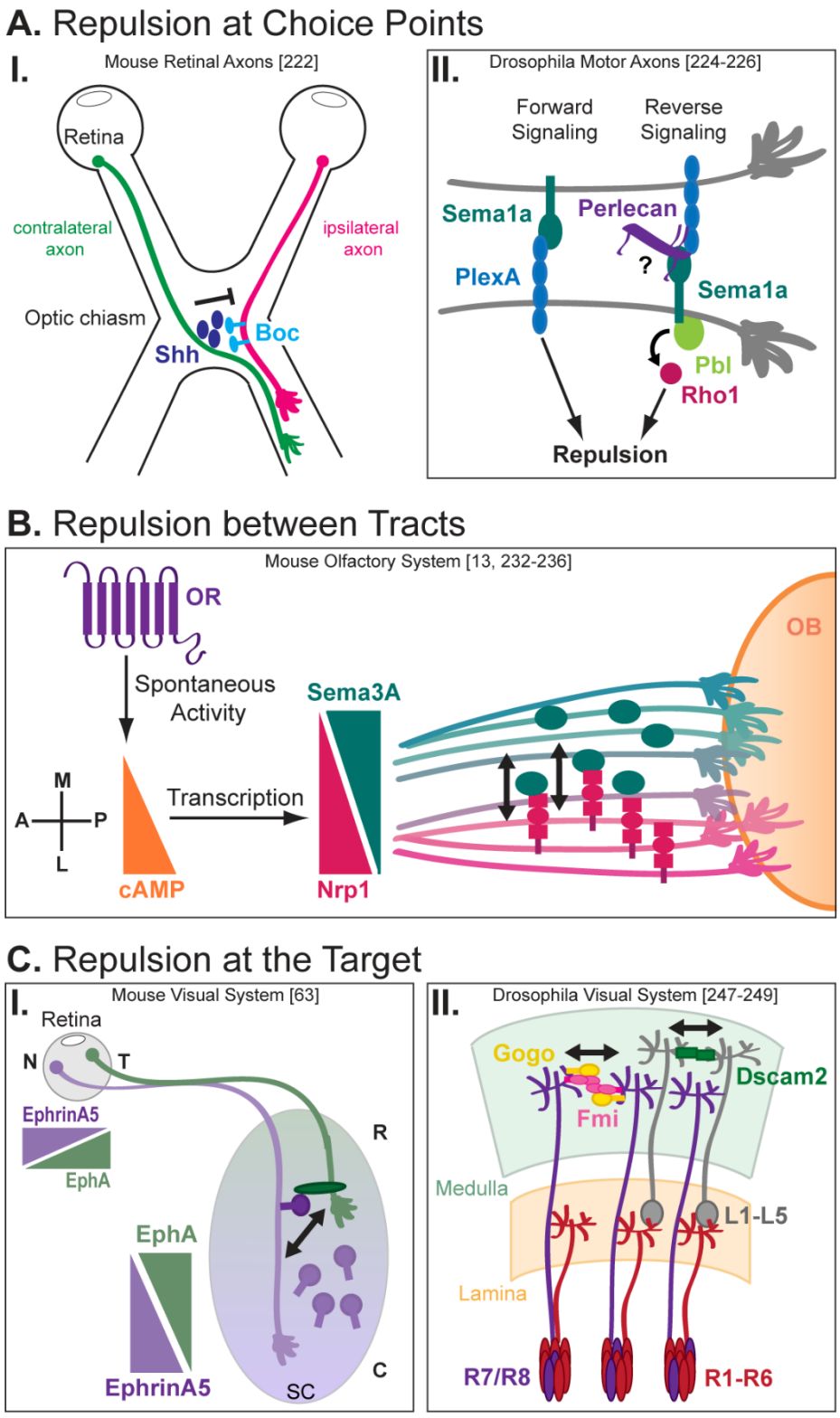

Figure 2.2: **Axon-axon interactions regulate axonal repulsion during neural circuit wiring**. (AI) In the mouse visual system, contralateral retinal axons arriving early at the optic chiasm secrete Shh, which repels

Figure 2.2 (Continued): later-arriving ipsilateral axons that express the Shh receptor Boc [222]. (AII) Both forward and reverse Sema1a signaling regulate motor axon repulsion in Drosophila. Reverse signaling relies on the activation of Rho1 by Pbl, and possibly secreted Perlecan [224-226.] (B) In the mouse, axon-axon repulsion establishes pre-target axon sorting of olfactory sensory axons. ORs produce patterns of spontaneous activity that generate different levels of cAMP. cAMP then activates transcription of Nrp1, which is expressed in a complementary manner to its ligand, Sema3A, in the olfactory nerve. Repulsive signaling between Nrp1- and Sema3A-expressing axons sorts axons as they extend to the OB [13,232-236]. (CI) Repulsion between nasal and rostral retinal axons at the SC contributes to topographic mapping. EphrinA5 is highly expressed by nasal retinal axons while EphA is high on temporal retinal axons. Temporal axons are repelled from the caudal SC by EphrinA5 present in both the environment and at the surface of nasal axons [63]. (CII) In the Drosophila visual system, Dscam2 interactions mediate repulsion and proper spacing of L1-L5 axon arbors in the medulla. Spacing of R7/R8 axon arbors is mediated by Fmi and Gogo interactions [247-249].

CHAPTER 3

GPC3 MEDIATES TENM3 TRANS-AXONAL SIGNALING TO PRUNE TOPOGRAPHIC SORTING ERRORS[2]

[2] Spead O, Weaver CJ, and Poulain FE. To be submitted Fall of 2021.

3.1 ABSTRACT

An important mechanism contributing to topographic map formation and neural circuit development is pre-target axon sorting, during which axons become pre-ordered en route to their destination. A salient example is the visual system, where retinal axons are topographically sorted along the dorso-ventral axis in the optic tract before reaching the optic tectum. While optic tract sorting contributes to the topographic fidelity of retinotectal connections, little is known about how it is established. Our previous studies in zebrafish have shown that optic tract sorting is achieved through the selective degeneration of missorted dorsal axons that have erroneously misrouted along the dorsal branch of the tract. Heparan sulfate (HS), a type of sugar chains carried by core proteins known as heparan sulfate proteoglycans (HSPGs), acts non-cell-autonomously along ventral axons to induce the degeneration of these missorted dorsal axons. We have now identified Glypican-3 (Gpc3) as the only HSPG specifically expressed in ventral retinal ganglion cells (RGCs) at the time of pre-target retinotectal sorting. Analysis of retinal axon sorting in *gpc3* mutants reveals that some dorsal retinal axons are missorted along the dorsal branch of the optic tract, demonstrating a novel function for Gpc3 in the nervous system. Interestingly, the adhesion molecule Tenm3 is also found in the ventral RGC layer, and *tenm3* mutants also display defasciculated and missorted dorsal axons. We provide evidence that *gpc3* and *tenm3* genetically interact to mediate the degeneration of missorted dorsal retinal axons. Overall, our study unravels a novel function for Gpc3 and Tenm3 in trans-axonal signaling and developmental axon degeneration during neural circuit formation.

3.2 INTRODUCTION

During nervous system development, axons elongate and take complex routes in order to form proper connections at their target. In the central nervous system, most circuits are organized into topographic maps that maintain the neighboring relationship of axons from their origin to their target. For example, in the visual system, the retinotopic map develops depending on the position of the retinal ganglion cells (RGCs) in the retina – RGCs from the nasal retina project axons to the posterior tectum while temporal RGCs project to the anterior tectum; similarly along the dorsal-ventral axis, dorsal RGCs project axons to the ventral tectum and conversely [17].

Axon-target interactions have been widely recognized as the main contributor to the formation of topographic maps. However, studies have more recently realized the importance of communication between axons themselves as they traverse their environment. Trans-axonal signaling appears especially important for pre-target axon sorting, a process whereby axons become pre-ordered before reaching their destination [14]. Pre-target axon sorting occurs within several circuits and is necessary for the proper mapping of axons at their target [13, 20, 231]. For example, olfactory system neurons (OSNs) express specific odorant receptors (ORs). OSN axons form distinct bundles along the olfactory nerve depending on the type of OR they express and this pre-ordering is necessary for their mapping at the olfactory bulb [13, 254, 255]. In the visual system, RGC axons are pre-ordered along the optic tract according to the D-V position of the RGCs they originate from in the retina [12, 25, 27, 28]. Dorsal retinal axons elongate along the ventral branch of the optic tract to reach the ventral tectum while axons from ventral RGCs navigate along the dorsal tract. The pre-ordering of axons within these circuits is highly

conserved among vertebrates and relies on mechanisms that are independent of the target – pre-target sorting remains intact in both the olfactory system and visual system when the olfactory bulb and tectum are removed, respectively [13, 169, 170].

Pre-target sorting has been extensively studied in the visual system, however the molecular signaling pathway regulating this process still remains elusive. One interesting study suggested that Semaphorin-Neuropilin (Sema-Nrp) signaling may mediate retinal axon sorting [42]. Knockdown of the RNA binding protein Hermes results in an upregulation of Nrp1 expression and partial missorting of dorsal retinal axons [42]. Sema3A-Nrp1 signaling also regulates the topographic ordering of axons in the corpus callosum [230]. Indeed, when Nrp1 and Sema3A are inactivated in motor and sensory cortical neurons, respectively, axons intermix within the corpus callosum instead of forming distinct axonal tracts and do not map properly at the contralateral cortex. Additionally, in the olfactory system, complementary expression of Nrp1 and Sema3A along the olfactory nerve contributes to proper pre-target axon sorting and topographic mapping at the olfactory bulb [13]. Axons with high levels of Nrp1 elongate along the outer, later part of the olfactory nerve while axons expressing high levels of Sema3A are confined to the center part of the bundle. When Nrp1 or Sema3A are inactivated in OSNs, olfactory axons become intermixed along the olfactory nerve, indicating that repulsive trans-axonal signaling mediates pre-target sorting in the olfactory system. While it is known that Sema3A, Nrp1, and several Plexins are expressed in RGCs, a direct role for Sema-Nrp signaling has yet to be tested in retinal axon sorting.

However, several studies have shown an essential role for heparan sulfate (HS) in pre-target sorting along the optic tract in zebrafish [19, 34]. In embryos lacking HS due to

mutations in the glycosyltransferases Ext2 and Ext3l (*dak* and *box* mutants, respectively), dorsal retinal axons misroute along the dorsal branch of the optic tract [19]. Interestingly, in WT embryos, several dorsal axons missort along the dorsal optic tract early on but then selectively degenerate, leading to a properly sorted tract [34]. HS actually functions non-cell-autonomously to trigger the selective degeneration of these missorted dorsal axons. HS chains are attached to the core proteins of heparan sulfate proteoglycans (HSPGs) and HSPGs are largely known to regulate signaling pathways during many aspects of neurodevelopment [37]. For example, many guidance cues require HS during axon elongation and guidance. The guidance molecules Netrin, Slit, and Sonic Hedgehog (Shh) all require HS at the midline for proper signaling through their respective receptors – Dcc, Robo, and Patched [256-262]. HS also regulates Sema-Nrp signaling in several systems. Secreted Sema3A interacts with HS with high affinity [263] and this interaction has been shown to promote Sema3A binding to Nrp1, leading to growth cone collapse [264, 265]. In these systems, HSPGs regulate well-known signaling pathways either directly by acting as co-receptors or indirectly by modulating the expression of the guidance molecule and/or receptor. While HS regulates pre-target retinal axon sorting[19, 34], the molecular signaling pathway that triggers the degeneration of missorted dorsal axons is still unknown and many questions remain unanswered. Which HSPG is mediating pre-target sorting in the visual system? What are the other molecular players regulating the selective degeneration of missorted axons?

Several molecules involved in visual system development show restricted expression patterns along the D-V axis and therefore may be important for pre-target sorting and/or topographic mapping. Ephrin-Bs are expressed in a high-dorsal to low-

ventral gradient in the retina while their receptors EphBs are expressed in an opposing gradient [266, 267]. However, while Ephrin-B/EphB signaling does indeed play a role in topographic mapping at the tectum, it does not appear to regulate retinal axon sorting along the optic tract [268]. Additionally, the Wnt receptor Ryk, is expressed in a high-ventral to low-dorsal gradient in the retina [81]. Wnt signaling has been shown to have a neuroprotective role during developmental pruning in both the olfactory system of Drosophila [269] and in the C. elegans [270]. However it has also recently been shown that Wnt signaling can mediate neurite pruning [271], providing a potentially interesting signaling pathway in pre-target retinal axon sorting. While Wnt signaling has been shown to regulate topographic mapping, its function in pre-target sorting has not been tested. Another interesting molecule, Teneurin-3 (Tenm3) has more recently been discovered to be expressed specifically in the ventral retina [87, 272, 273]. Teneurins are a family of type II transmembrane proteins which typically mediate homophilic recognition and adhesion [274]. Studies have provided evidence of a diverse number of roles teneurins have in nervous system development including synaptic partner matching [275, 276], the specification and mapping of ipsilaterally projecting retinal axons [87, 273, 277], and topographic circuit assembly in the hippocampus [278]. The involvement of teneurins in the developing visual system and the specific expression of Tenm3 in the ventral retina lead us to hypothesize that Tenm3 signaling could be involved in pre-target retinotopic axon sorting.

In this study, we report that *glypican-3 (gpc3),* a member of the HSPG family attached to the plasma membrane by a glycophosphatidylinositol- (GPI-) anchor, is specifically expressed by ventral RGCs. Embryos with non-functional *gpc3* display missorted dorsal axons along the dorsal branch of the optic tract, a phenotype that

resembles that in *dak* mutants. *Gpc3* mutants do not display retinal patterning defects along the D-V axis, indicating that Gpc3 is directly involved in the signaling pathway that regulates the degeneration of missorted dorsal retinal axons. Interestingly, *tenm3* is also expressed in the ventral retina and *tenm3* mutant embryos also have missorted and defasciculated axons. We further show that *gpc3* and *tenm3* genetically interact to regulate retinal pre-target sorting. Considering the known roles for Teneurins in mediating cell adhesion and stabilizing synapses [43], it is surprising that Tenm3 is necessary for the pruning of missorted axons. However, given these data, we propose a model in which Gpc3 regulates Tenm3 signaling to trigger the degeneration of missorted dorsal retinal axons, ensuring the development of a properly sorted optic tract. This study provides the first evidence for a role of Gpc3 in CNS development and reveals a novel function for Tenm3 in developmental axon pruning.

3.3 METHODS

Zebrafish Husbandry

This research was approved by the University of South Carolina IACUC Committee. Embryos were obtained from natural matings, raised at 28.5°C in E3 medium (5 mM NaCl, 0.17 mM KCl, 0.33 mM $CaCl_2$, and 0.33 mM $MgSO_4$) in the presence of 150 mM of 1-phenyl-2-thiourea (PTU) (Sigma) to prevent pigment formation, and staged by age and morphology [279]. WT embryos were from Tubingen or AB strains. *Tenm3* mutants were a generous gift from Dr. R. Hindges (Kings College, London, UK) and *lakritz (lak)* mutants were a generous gift from Dr. F. Del Bene (Institut Curie, Paris, France). Embryos were anaesthetized in tricaine (Western Chemicals) before fixation or

imaging. Zebrafish larvae and young fish were nurtured using rotifer suspension and dry food (Gemma). Adult fish were fed with dry food (Gemma).

Cloning & In Situ Hybridization

cDNA templates cloned into pCRII-TOPO were amplified by PCR using M13fw and M13rv primers and were purified on gel. *In vitro* transcription of dioxigenin-labeled probes was performed using the RNA Labeling Kit (Roche Diagnostics Corporation) according to manufacturer's instructions to generate antisense and sense probes for *gpc3, tbx5a, vax2,* and *tenm3*. Embryos were dechorionated at the appropriate developmental stages and fixed in 4% paraformaldehyde in phosphate buffer saline (pH 7.4) for 2 hours at room temperature and then 4°C overnight. Whole mount in situ hybridization was performed as previously described [78]. After staining, embryos were cleared in 80% glycerol for imaging using an Olympus SZX16 stereomicroscope equipped with Olympus DP80 dual color camera and Cellsens standard software. Digital images were cropped and aligned using Adobe Photoshop.

Quantification of Retinal Gene Expression

Quantification of gene expression in the retina was carried out according to Picker & Brand, 2005 [280] with the following modifications: Eyes were dissected after in situ hybridization using a sharpened tungsten needle and imaged in 80% glycerol from a lateral view. Images were imported into Fiji ImageJ analysis software [281, 282], transformed to 8-bit grayscale images, and then inverted. An oval selection was made halfway between the lens and the RGC layer periphery and the Oval Profile Plot plugin was used to determine signal intensity along a 360ºtrajectory. Values were exported and further analyzed in Microsoft Excel. To analyze the Gene Expression Coverage (**Figure 4.9**) in

the dorsal and ventral halves of the retina, the signal intensity along a 180° radial trajectory in the dorsal retina (for *tbx5a*) and in the ventral retina (for *vax2*) was measured using Oval Profile Plot plugin as described above (at 24 hpf, the selection is made halfway between the lens and the outer edge of the eye). We determined the position (°) of maximum (Max) intensity. Then we determined the position of the minimum intensity nasal (MinN) and temporal (MinT) to the maximum value. The position halfway between the maximum and the MinN and the position halfway between the maximum and the MinT were then determined. We then defined the Gene Expression Coverage as the difference between these halfway-radial positions.

Generation of *gpc3* Mutant Lines

gRNAs were designed to target *gpc3* Exon 2 and Exon 7. The target sequences (with PAMs in brackets) used in this study were *gpc3* Exon 2: GCTTATTGCCAAACAGAATA[TGG] and *gpc3* Exon 7: GGTGCGAGAAGAAACCCATC[CGG]. Oligos were designed with an NheI restriction site followed by the sequence for the T7 promoter, the gRNA target sequence, and a HindIII restriction site. Oligos were digested and ligated into the pSMART-KJ vector using the Quick Ligation Kit (New England BioLabs). The MEGAshortscript T7 Transcription Kit (Thermo Fisher) was used to synthesize gRNAs from the plasmid templates. 500-600 ng of gRNA and 800-900 ng of Cas9 protein (PNA Bio Inc.) were co-injected at the one cell stage in WT embryos. Efficiency of CRISPR injections was analyzed on injected embryos at 28 hpf by high resolution melting analysis (HRMA) [283] with the primers 5'-ATGGAGGAGCGTTACCTG-3' and 5'-GATGATGAGCCCTTTGAGC-3' for Exon2 target and 5'-

GATGGAGGGCTCGACAAGG-3' and 5'-CCTCCTCATCCTCATCTGTCTG-3' for Exon7 target. Once adult, fish that had been injected with gRNA + Cas9 were outcrossed to WT fish and mutations in the F1 generation were detected using the described HRMA analysis. Mutated sequences detected by HRMA were further amplified using the following primers: Exon2: 5'-GCGGTCTGTTTACTTGTTTATTG-3' and 5'-GCCCAAGGGGATGCTAAAG-3'; Exon7: 5'-CCACTGGCATAGAACATTGAATC-3' and 5'-ACCTGCAAAGATGCGCAGTC-3'). Amplicons were cloned in pCRII using the TopoTA kit (Thermo Fisher) and analyzed by sequencing.

Genotyping of Mutant Lines

Lakritz (*lak*) and *dackel* (*dak*) mutants were previously described [284]. To genotype *lak*, genomic DNA was amplified by PCR using the primers: 5'-CCGGAATTACATCCCAAGAAC-3' and 5'-GGCCATGATGTAGCTCAGAG-3'. Amplicons were then digested with StuI (which cuts WT but not *lak* mutant DNA) and run on a 2% agarose gel. WT genomic profiles had bands at 200 and 100 bp while *lak* mutants had a single band at 300 bp. To genotype *dak*, the following dCAPS primers were used to amplify genomic DNA: 5'-TGGACAGGCTCATCATGTGT-3' and 5'-CGGTCCAGACTCCATTCGGCTGAAGACTT-3'. PCR products were digested with MseI (cuts *dak* but not WT) and run on a 3% Metaphor gel (Lonza). WT profiles had a band at 193 bp while mutants had a band at 163 and 30 bp. *Tenm3* mutants were genotyped by HRMA using the following primers: 5'-CAAGTTCAAGAAGTCCTCAAAG-3' and 5'-TACGGAGAGCAGTATGGAG-3'. To genotype *gpc3* Exon 2 mutants, genomic DNA was amplified using the dCAPS primers 5'-CAAAATGGAGGAGCGTTACCTGCTTATTGCCAACCCGA-3' and 5'-

CTTGACTCTAAGCATTTCAGCTTTCCGCCCAAGGGGATG-3'. Amplicons were digested with AvaI (which cuts the mutant but not WT DNA) and run on a 3% Metaphor gel (Lonza). Exon2 mutants were identified by the presence of a band at 192 bp and WT, by a band at 225 bp. *Gpc3* Exon 7 mutants were genotyped by HRMA using the following primers: 5'-GATGGAGGGCTCGACAAGG-3' and 5'-CCTCCTCATCCTCATCTGTCTG-3'.

DNA Plasmid Constructs

All expression vectors were generated using the Tol2Kit Gateway cloning system [285]. The *pME-EGFPgpc3* entry plasmid was generated by cloning EGFPgpc3 from *PCS-EGFP-GPC3* (courtesy of the Topczewski lab, Northwestern University), in which EGFP was placed at the 5'-end of *gpc3* after the sequence coding for the signal peptide. Primers were designed with att sequences for pME-entry sites [285] (fw-5'-GGGGACAAGTTTGTACAAAAAAGCAGGCTGGGCAAACATGCCAGGTTTAAAACTATATGGTGC-3' and rv-5'-GGGGACCACTTTGTACAAGAAAGCTGGGTGTCACTGAAGACCCAGTGTTATGAAG-3'). A two-step PCR was performed to generate a form of EGFPgpc3 lacking its heparan sulfate chains *(pME-EGFPgpc3ΔHS*) in which three predicted HS attachment sites coding Serines were mutated to Alanines (S489A, S503A, S516A). *pME-EGFPgpi* was generated to express only the signal peptide, EGFP, and the GPI-anchor of Gpc3 using the same forward primer mentioned above along with the reverse primer: 5'-GGGGACCACTTTGTACAAGAAAGCTGGGTGTCACTGAAGACCCAGTGTTATGAAGATGATGATGGTGATGGTGAAGATGAAGGCTGCAGTAGGAACATGTGCTGCTCCAGGTATTGATGATCCACCGTGTGCGTCTGTGGCCAGTCTGGGTAGGGCT

GCAGAATCTAGAGGCTC-3'. Since the subcellular localization and function of Ext2 are not modified by the addition of GFP to Ext2 C-terminal [286], pME-ext2-EGFP was generated by adding the EGFP coding sequence to the 3'-end of *ext2* coding sequence by PCR. A sequence encoding the flexible linker [GGGRS] was inserted between *ext2* and EGFP to ensure that the addition of EGFP did not alter Ext2 function. *pME-EGFP-gpc4* and *pME-EGFP-gpc5a* were generated using a two-step PCR that inserted the EGFP coding sequence after the sequences coding the signal peptides for *gpc4* and *gpc5a.* *pCS2+-gpc4* and *pCS2+-gpc5* plasmids (courtesy of Dr. Ken Kramer, Creighton University) were used as templates. A modified *p5E-isl2b-gata2* entry clone encoding a 7.6 kb genomic fragment upstream of the isl2b start codon fused to the 1 kb promoter of gata2a [21] was used to generate all constructs. Final plasmids (*isl2b:EGFPgpc3*, *isl2bEGFPgpc3ΔHS*, *isl2b:EGFPgpi*, *isl2b:EGFPgpc4, isl2b:EGFPgpc5a* and *isl2b:ext2EGFP*) were generated by LR reactions with the *pDestTol2pA2* backbone [285].

Generation of stable transgenic lines

Stable transgenic lines were generated using the Tol2 transposon methods as described previously [287]. 10 to 40 pg of DNA (*pTol2pA2-isl2b:EGFPgpc3*, *isl2bEGFPgpc3ΔHS*, *isl2b:EGFPgpi*, *isl2b:EGFPgpc4, isl2b:EGFPgpc5a* and *isl2b:ext2EGFP)* were co-injected with 25 pg of synthetic mRNA encoding Tol2 transposase at one-cell stage. Injected embryos with transient expression of the transgenes were raised to adulthood as the F0 generation. F0 fish were outcrossed to WT to screen for positive F1 embryos expressing the desired transgene. Transgenic F1 carriers were subsequently outcrossed to WT to generate stable lines with a single-copy insertion of the transgene.

Visualization of Optic Tract Sorting

DN and VT retinal axons were labeled as described previously (10). Briefly, glass microneedles were coated with the lipophilic dyes DiO and DiD (Molecular Probes, Invitrogen) and introduced in the ventral-temporal and dorso-nasal parts of the retina, respectively, of embryos fixed at 4 dpf. Dyes were let to diffuse overnight, and the contralateral eye was then removed for confocal imaging from a lateral view. Embryos were embedded in 1% low melting point (LMP) agarose in PBS on a membrane-bottomed petri dish and imaged using a TCS SP8X laser-scanning confocal microscope equipped with LAS X software, HyD and PMT detectors, and a 20x objective (digital zoom 1.5 for LV, 1 for DV). The entire optic tract and tectum was imaged with a Z-series interval of 1.5 μm.

Quantification of Missorting Phenotype

To quantify the missorting phenotype in *gpc3* mutants, confocal stacks were rotated along the X, Y, and Z axes in ImageJ using the TransformJ Plugin [288] so that the width of the tectum was at its widest point. Rotated stacks were maximally projected and then the Enhance Local Contrast (CLAHE) plugin was used to better detect defasciculated missorted dorsal fascicles. Max projected images of the dorso-nasal (DN) axons were then binarized using Auto Threshold, and binarized images were used for all analyses. Only embryos with a missorting phenotype were analyzed. To analyze the Displacement of missorted fascicles, measurements were taken along a line perpendicular to the entrance of the optic tract, positioned at the point where dorsal and ventral axons are entering the tectum. The distance from the ventral most point of the properly sorted dorsal axons (ventral branch of the optic tract) to the furthest dorsal missorted fascicle

was measured and was then reported over the width of the properly sorted dorsal axon bundle (ventral branch). A Displacement Index greater than 1 indicates missorting while an index averaging 1 indicates no missorting. To analyze how many fascicles were missorted in each embryo, the perpendicular line was positioned across the dorsal branch of the optic tract and the Plot Profile Plugin was used to determine the number of missorted fascicles (indicated by the number of peaks in the Plot).

Statistical Analysis

Data were analyzed and graphs were produced using Microsoft Excel and Prism (GraphPad Prism 9 Software). Data are presented as the mean ± SEM (unless otherwise noted). Statistical tests were applied as indicated in the Results and Figure Legends. To compare multiple groups, we performed one-way ANOVA followed by Tukey's multiple comparisons post-hoc test. To compare mutant and WT phenotypes at the described timepoints, a Two-Sample t-Test for Equal Means was performed between mutant and WT values. For the Displacement Index, a Two-Sample t-Test for Equal means was performed between each genotype and a value of 1 (1 indicating no missorting occurs). Finally, to compare the percentage of embryos with a missorting phenotype across genotypes, a Chi-Square test with Yates' correction was performed. The number of larvae analyzed and the statistical methods used to compare groups are described in each figure legend.

3.4 RESULTS

HS functions non-cell-autonomously in ventral retinal axons to regulate axon sorting.

HS functions non-cell-autonomously in the retinotectal system to induce the degeneration of missorted dorsal retinal axons during pre-target sorting. [34]. This means HS could be functioning at the surface of the cells surrounding the optic tract or along ventral axons signaling to the missorted dorsal axons, as ventral axons are the pioneer axons elongating first along the dorsal branch of the optic tract [33]. In order to determine if HS functions along retinal axons, we generated a Tg[*isl2b:ext2EGFP*] stable transgenic line that expresses *ext2* fused to EGFP in RGCs but not in the optic tract region). We then established this line in a *dak* mutant background [19, 238]. As a control we established a Tg[*isl2b:EGFP*] stable line in a *dak* mutant background. *Dak* mutants expressing EGFP only in RGCs showed strong expression of EGFP in RGCs and along retinal axons (**Figure 4.1A**). *dak* mutants expressing *ext2* fused to EGFP in RGCs also showed strong expression in the cell bodies as well as a fainter expression along the retinal axons (**Figure 4.1B**). To analyze axon sorting along the optic tract, we injected lipophilic dyes into the dorso-nasal (DN) and ventro-temporal (VT) quadrants of the retina of *dak* mutants at 4 dpf [16]. We observed missorted DN axons in *dak* mutants expressing EGFP in RGCs (**Figure 4.1C,** yellow arrowheads). However, we did not detect any missorted dorsal retinal axons in *dak* mutants expressing *ext2* in RGCs. Indeed, 79.3% of *dak;isl2b:EGFP* embryos had missorted DN axons while only 6.5% of *dak*;*isl2b:ext2-EGFP* embryos had missorted axons. Together with our previous results demonstrating that HS acts non-cell-autonomously for proper sorting of dorsal axons[34], our results

demonstrate that HS functions along ventral retinal axons to trigger the degeneration of missorted dorsal axons during pre-target optic tract sorting.

***Gpc3* is exclusively expressed by ventral RGCs.**

Since HS is functioning along ventral retinal axons to regulate pre-target sorting, we then sought to determine whether a specific HSPG is expressed in the retina during pre-target sorting. We analyzed the expression of membrane-bound HSPGs by whole mount in situ hybridization (ISH) to assess which are expressed in the visual system at the time when pre-target sorting is occurring. Ten Glypicans [289] and three Syndecans [290] have been identified in zebrafish. Among them, we found that *gpc3* is expressed in the ventral half of the retina. At 48 hpf, when pre-target retinal axon sorting is just beginning [34], *gpc3* is highly expressed in the nervous system (**Figure 4.2A-A'**) and begins to be expressed in the ventral half of the RGC layer (**Figure 4.2A"**). By 60 hpf (**Figure 4.2B-B"**) and through 72 hpf (**Figure 4.2C-C"**), when missorted dorsal axons are actively degenerating [34], *gpc3* is strongly and specifically expressed in just the ventral half of the RGC layer (**Figure 4.2B", 2C"**). To determine if RGCs are the cells expressing *gpc3*, we repeated ISH in *lak* mutants that carry a mutation in *atoh7*, a transcription factor needed for the determination of RGC fate [284]. *Lak* mutants therefore do not have RGCs. While *gpc3* remained strongly expressed throughout the nervous system in *lak* mutants at 72 hpf (**Figure 4.2D**), it is no longer detected in the retina (**Figure 4.2D'**) while its strong ventral expression is apparent in *lak* siblings (**Figure 4.2E'**). These results indicate that *gpc3* is specifically expressed by ventral RGCs during the time missorted dorsal retinal axons degenerate.

To identify the signaling pathway restricting *gpc3* expression to ventral RGCs, we investigated the role of (bone morphogenetic protein) BMP signaling, which is known to mediate the dorsalization of the retina [53, 291, 292]. Gdf6a, a member of the BMP family, regulates the polarized expression of known axon guidance molecules, such as EphBs and Ephrin-Bs along the D-V axis of the retina [292]. We therefore tested the role of BMP signaling by analyzing *gpc3* expression in the *gdf6a* mutant, *radar (rdr),* by ISH at 72 hpf. As expected, WT embryos displayed *gpc3* expression only in the ventral half of the RGC layer (**Figure 4.2F'**). In contrast, *rdr* embryos had *gpc3* expressed throughout the entire retina (**Figure 4.2F**), indicating that *gdf6a* is required for restricting *gpc3* expression to ventral RGCs during retinal development. We further quantified *gpc3* expression intensity along a 360° radius (**Figure 4.2G**), half-way between the outer RGC layer and the lens (**Figure 4.9A**) at 48, 60 and 72 hpf. In WT embryos, *gpc3* is highly expressed only in the ventral retina and is absent in the dorsal retina at all stages. *Radar* showed high expression of *gpc3* throughout the retina and the expression profile looks similar to that of *isl2b*, which is known to be expressed throughout the RGC layer [21]. On the other hand, *lak* mutants did not display any expression of *gpc3* in the retina.

Gpc3 is required for the degeneration of missorted dorsal retinal axons.

Given its selective expression in ventral RGCs, we hypothesized that Gpc3 might be needed for proper retinotopic sorting along the optic tract. To test its role in retinotectal development, we generated *gpc3* mutants using CRISPR-Cas9-mediated mutagenesis [293, 294]. We designed two independent gRNAs (**Figure 4.3A,** red bars) to target Exon 2, which encodes part of Gpc3's large globular domain, and Exon 7, right upstream the sequences coding for Gpc3's HS attachment sites (blue triangles on

schematic). We obtained two mutant alleles, one with a two nucleotide insertion followed by a mismatch in Exon 2 (+2MM) that leads to the addition of several missense amino acids before a premature stop codon, and the other with a 4-nucleotide deletion in Exon 7 (Δ4) that leads to a truncated protein without any HS attachment site (**Figure 4.3A-B**). To test whether *gpc3* is required for optic tract sorting, we injected the lipophilic dyes DiD and DiO in the DN and VT quadrants of the retina at 4 dpf in *gpc3* mutants and WT siblings (**Figure 4.3C-E**). Both *gpc3* mutants had missorted dorsal retinal axons along the dorsal tract (**Figure 4.3C-D,** yellow arrowheads) while WT embryos had properly sorted dorsal axons (**Figure 4.3E**). 55% of +2MM mutant embryos and 65% of Δ4 mutant embryos had missorted dorsal retinal axons while only 7% of WT embryos showed this phenotype (**Figure 4.3F**). To further analyze the extent of missorting in *gpc3* mutants, we developed two quantifications. We first quantified the number of missorted dorsal fascicles in mutants that had a missorting phenotype (**Figure 4.3G**). +2MM embryos had an average of 3.7 ± 0.3 missorted fascicles and Δ4 mutants had an average of 4.6 ± 0.4 missorted fascicles while WT had an average of 0.5 ± 0.2 missorted axons. We then calculated a Displacement Index (**Figure 4.3H**) that corresponds to the distance between the furthest missorted dorsal fascicle and the ventral tract over the width of the properly-sorted dorsal axon bundle. A value close to 1 indicates that there are no "displaced" dorsal axons while a value above 1 indicates missorted fascicles. +2MM and Δ4 mutant embryos with missorted dorsal axons have a Displacement Index of 2.62 ± 0.15 and 2.83 ± 0.39, respectively, both showing a significant displacement of dorsal fascicles. WT embryos have a Displacement Index of 1.25 ± 0.1, indicating that WT embryos do not

have missorted dorsal axons. Altogether, our results indicate that Gpc3 is required for the proper sorting or dorsal axons during pre-target optic tract sorting.

Sorting defects observed in *gpc3* mutants could be caused by either disrupted D-V patterning of the retina or disrupted signaling between ventral axons and missorting axons during pre-target sorting. To determine if *gpc3* mutants have altered D-V retinal patterning, we analyzed the expression of *tbx5a,* a transcription factor required for the expression of dorsal-specific genes [53, 295], and of *vax2*, a homeodomain transcription factor required for ventralization of the retina [53, 55], in WT and *gpc3-/-* embryos. Like WT embryos, *gpc3-/-* showed *tbx5a* expression in the dorsal part of the retina at 24, 48, and 72 hpf (**Figure 4.4A**). We quantified the Gene Expression Coverage of *tbx5a* in the dorsal retina (**Figure 4.9B)**, which showed no significant difference between WT and *gpc3-/-* at 24, 48, or 72 hpf (**Figure 4.4B**). Similarly, *gpc3-/-* had ventral-specific *vax2* expression in the retina, much like WT embryos, at 24, 48, and 72 hpf (**Figure 4.4C**). The Gene Expression Coverage of *vax2* (**Figure .4D**) also showed no significant difference between WT and *gpc3-/-* at these three time points. Therefore, *gpc3* mutants do not have altered D-V patterning, suggesting that Gpc3 plays a direct role in pre-target axon sorting along the optic tract.

Altering HS levels in RGCs disrupts retinal axon sorting along the tract.

Since *gpc3* is restricted to ventral RGCs, we then wanted to determine if levels of HS across the D-V axis of the retina are important in the regulation of pre-target sorting. To test whether expressing *gpc3* throughout the entire RGC layer causes missorting along the tract, we generated several stable transgenic lines that express transgenes in all RGCs thanks to the RGC-specific *isl2b* promoter [21]. The first line, *Tg[isl2b:EGFPgpc3]*,

expressed EGFP fused to *gpc3* (**Figure 4.5A**). These embryos, with *gpc3* now expressed in the dorsal retina and also over-expressed in the ventral retina, had missorted dorsal retinal axons (yellow arrowheads). We also expressed *gpc4* and *gpc5a* in a similar manner – compared to Gpc3, Gpc4 has a very different HS chain pattern along its core protein, whereas Gpc5a is the most closely related glypican and therefore has a similar HS attachment pattern [289]. Furthermore, neither *gpc4* nor *gpc5a* are expressed in RGCs in WT embryos (data not shown). Expressing *gpc4* and *gpc5a* (**Figure 4.5B-C**) in all RGCs also caused missorted dorsal retinal axons. However, embryos expressing a form of *gpc3* in which the Serine residues to which HS chains are attached [296] were mutated to Alanines (*Tg[isl2b:EGFPgpc3ΔHS])* had properly sorted dorsal axons (**Figure 4.5D**), indicating that HS at the surface of Gpc3 is required for its effect along the tract. As a control, we generated a line expressing only EGFP fused to the glycophosphatidylinositol- (GPI-) anchor of Gpc3 (*Tg[isl2b:EGFPgpi]*). These embryos also had properly sorted dorsal retinal axons (**Figure 4.5E**). Altogether, these data suggest that the levels of HS across the D-V axis of the retina is important for the degeneration of missorted dorsal axons and altering these levels likely interferes with the signaling needed for retinotopic axon sorting along the tract. It is therefore important for *gpc3* to be restricted to ventral RGCs in order for it to function in pre-target axon sorting. However, our data, also suggest that the nature of the core protein itself presenting HS is not that important for activating the signaling pathway mediating selective degeneration. It is likely that *gpc3* is expressed at the right place and at the right time to mediate pre-target sorting in the visual system.

Gpc3 genetically interacts with Tenm3 to regulate pre-target retinal axon sorting.

Glypicans are known to regulate various signaling pathways in several ways, mainly by acting as co-receptors, regulating receptor trafficking, or by controlling the secretion of ligands into the extracellular space [37]. To test whether Gpc3 regulates the signaling pathway required for pre-target retinotectal axon sorting, we aimed to find other molecules known to be differentially expressed along the D-V axis of the retina that could be candidates for interacting with Gpc3. Surprisingly, the adhesion molecule Teneurin-3 (Tenm3) has an extremely similar expression pattern to that of *gpc3* in the retina at 72 hpf [272, 297]. We confirmed *tenm3* expression in the ventral RGC layer at 72 hpf by ISH in WT embryos (**Figure 4.6A**), indicating that Tenm3 might regulate the sorting of dorsal retinal axons. To determine if *tenm3* is required for sorting along the optic tract, we injected DiD into the DN quadrant of the retina of *tenm3-/-* embryos [298] fixed at 4 dpf. *Tenm3-/-* embryos lacking functional Tenm3 (**Figure 4.6B**) displayed severely defasciculated dorsal axons that missort along the dorsal branch of the optic tract (yellow arrows) (**Figure 4.6C-C'**), while WT embryos have properly sorted dorsal axons (**Figure 4.6D**). Thus, Tenm3 is required for proper sorting of dorsal retinal axons along the tract.

As with *gpc3-/-,* the missorting phenotype in *tenm3-/-* could be a result of disrupted D-V patterning in the retina or disrupted signaling between ventral axons and missorted dorsal axons. To determine if *tenm3*-/- have altered D-V retinal patterning, we again assessed the Expression Coverage of *tbx5a* and *vax2* in WT and *tenm3-/-* embryos. *Tbx5a* was expressed specifically in the dorsal retina at 24, 48, and 72 hpf of *tenm3-/-* and WT embryos (**Figure 4.7A**) and there was no significant difference between the Gene

Expression Coverage at any of these timepoints (**Figure 4.7B**). Similarly, *vax2* was expressed in the ventral retina in *tenm3 -/-* and WT embryos (**Figure 4.7C**), and its expression coverage did not significantly differ between mutants and WT at any of the three timepoints (**Figure 4.7C**). Thus, the axon sorting defects seen in *tenm3-/-* do not result from disrupted D-V patterning of the retina, indicating that *tenm3* must be directly involved in the signaling pathway mediating axon sorting.

We then assessed whether *gpc3* and *tenm3* act in the same pathway by analyzing retinotopic sorting in double heterozygous embryos (*tenm3-/+;gpc3-/+*). Embryos heterozygous for only *tenm3* (**Figure 4.6E**) or only *gpc3* (**Figure 4.6E'**) showed properly sorted dorsal axons. However *tenm3-/+;gpc3-/+* embryos had missorted dorsal axons (**Figure 4.6E"**, yellow arrowheads), much like the phenotype seen in *gpc3-/-*, indicating that *gpc3* and *tenm3* genetically interact to regulate pre-target retinal axon sorting along the optic tract. We then ensured that the missorting phenotype observed is not due to altered *gpc3* expression in *tenm3-/-* or altered *tenm3* expression in *gpc3-/-* (**Figure 4.7E**). *Tenm3-/-* embryos at 72 hpf express *gpc3* in the ventral retina and this expression pattern is unaltered from that seen in WT embryos. Conversely, *gpc3-/-* embryos do not have altered expression of *tenm3* compared to WT. Therefore, Gpc3 and Tenm3 do not affect each other's expression pattern in the ventral retina and the missorting phenotype seen in *gpc3-/-* and *tenm3-/-* is not due to altered retinal expression.

3.5 DISCUSSION

Pre-target axon sorting and the elimination of mistargeted axons via pruning are crucial steps to neural circuit development, however the molecular mechanisms mediating these processes are still not well understood. We previously discovered a non-cell-autonomous

role for HS in triggering the selective degeneration of missorted dorsal retinal axons during pre-target retinotopic sorting [34]. We then confirmed that HS functions specifically in RGCs to regulate this process, suggesting a mechanism in which HS-dependent trans-axonal signaling from pioneer ventral retinal axons to missorted dorsal axons mediates the degeneration of dorsal retinal axons. Here, we discovered that Gpc3 is the only HSPG that is expressed specifically by ventral RGCs, and that Gpc3 is required for the degeneration of missorted dorsal retinal axons. Tenm3 is also expressed specifically in the ventral RGC layer at the time of pre-target retinotectal axon sorting. *Tenm3-/-* embryos have severely defasciculated and missorted dorsal retinal axons. In addition, embryos that are heterozygous for both *gpc3* and *tenm3* also display missorted dorsal retinal axons, proving a genetic interaction between *gpc3* and *tenm3* that is necessary for the degeneration of missorted dorsal retinal axons. Our results lead us to propose a model in which Gpc3 and Tenm3 are likely to interact as a complex on the surface of ventral retinal axons (**Figure 3.8**), positioning Tenm3 so that it can interact with its unknown ligand at the surface of the missorted dorsal retinal axons.

The most well-characterized role for Gpc3 in vivo has been its regulation of Hedghog (Hh), Wnt, BMP, and fibroblast growth factor (FGF) signaling [299-305]. In particular, Gpc3-null mice have altered Hh and Wnt signaling [301, 306]. Gpc3 knockout in mice leads to the inhibition of non-canonical Wnt/JNK signaling while in parallel activating canonical Wnt/β-catenin signaling [301]. These mice also have increased Hh signaling [306] and display developmental overgrowth [307]. This phenotype is characteristic of that seen in patients with Simpson Golabi Behmel Syndrome (SGBS), who carry mutations or duplications in *gpc3* [308, 309]. Along with pre- and post-natal overgrowth,

SGBS patients exhibit a myriad of other symptoms including mild to moderate intellectual disability. However how Gpc3 directly contributes to this neurological disability is unknown. Here we have described a first role for Gpc3 in the nervous system by demonstrating its requirement in pre-target retinal axon sorting, which highlights the importance of Gpc3 in circuit wiring.

The requirement of Tenm3 for the pruning of missorted retinal axons came as a surprise given that Teneurins are mostly known for mediating cell-cell adhesion during synaptic partner matching [275, 276, 310]. However, recent studies are unveiling other functions that Teneurins can carry out in the nervous system. Along with adhesion during synapse formation, Teneurins have also been implicated in axon fasciculation during neurite outgrowth and axon pathfinding in both invertebrate and vertebrate species [311, 312]. In the zebrafish visual system, Tenm3 is needed for proper RGC dendrite stratification in the retina as well as laminar arborization at the tectum [272]. Knockdown of Tenm3 leads to RGC and amacrine cell dendrite stratification defects in the inner plexiform layer as well as in the outer retina. In the mouse visual system, Tenm3 is required for the proper topographic mapping of ipsilaterally projecting retinal axons [87, 273]. Tenm3 also guides the proper topographic mapping of proximal CA1 hippocampal axons to the distal subiculum [278]. While the full understanding of how Tenm3 is mediating topographic mapping and the laminar distribution of axons at the target in these systems is still unknown, it is likely that axon targeting is established through homophilic Tenm3 adhesion as Tenm3 is expressed in a complementary manner along axons and at their target in these circuits [87, 272, 273, 278, 298].

Along with homophilic interactions in *trans*, Teneurins interact in *trans* with Latrophilins (Lphns), a group of adhesion G-protein-coupled receptors (GPCRs) [313-317]. The classically viewed role for Teneurins is in synaptic partner matching and *trans*-synaptic adhesion during synapse development which has been demonstrated in both *Drosophila* and mammals [275, 276, 314-316]. An interaction between Teneurin and Latrophilin has also been shown to mediate axon attraction in vitro [317]. In this system, Tenm2 is proteolytically released into the intercellular space where it binds to Lphn1 on axonal growth cones to induce axon attraction and fasciculation. While all of the aforementioned functions for Tenm3 are in synaptic partner matching or possibly as attractive cues during axon guidance, Tenm3 might also provide a signal for other cellular functions. Indeed, a recent study discovered that Tenm2 is needed for proper cortical neuron migration via a contact-mediated repulsion mechanism [318]. Teneurins are expressed in migrating cortical neurons while Lphn1 is expressed in radial glial cells of the developing cortex. Tenm2 and Lphn1 interact, initiating a repulsive signal from radial glial cells to the migrating cortical neurons (so in that case, Tenm2 transduces a signal from Lphn1). This recent study shows that Teneurins can function in other roles besides adhesion and therefore it is possible that Tenm3 regulates other developmental processes such as pre-target sorting and pruning during visual system development.

How can Teneurins have such a diverse repertoire of functions during nervous system development? Teneurins are large type II transmembrane glycoproteins that are composed of an N-terminal intracellular domain, a hydrophobic transmembrane region, and a large extracellular domain [319, 320]. The interactions and therefore cellular responses mediated by Teneurins depends on the binding domains involved. Indeed, alternative

splicing of Teneurins regulates Teneurin interactions. For example, Tenm2 contains a seven-residue region in its extracellular domain that acts as a switch to regulate trans-cellular adhesion between Tenm2 and Lphn [321]. The splice variant lacking the seven amino acids binds full-length Lphn and activates trans-cellular signaling while the splice variant without those seven amino acids fails to do so. Interestingly, the same splice variant lacking the seven amino acids cannot mediate trans-homodimerization while the other variant can [278]. The members of the Teneurin family are highly conserved within and between species. Tenm3 has also been identified as having alternatively spliced isoforms in mice and chicken [278, 322]. One isoform differs by the inclusion or exclusion of exon 12, encoding 9 amino acids in the EGF-like region of the extracellular domain. The other isoform differs in the inclusion/exclusion of exon 20 which encodes 9 amino acids in the NHL region of the extracellular domain. These regions are both highly conserved in zebrafish and therefore it is possible that zebrafish express different isoforms of Tenm3. Discovering which splice variants of Tenm3 are expressed in the zebrafish retina would allow us to further understand the signaling mechanism regulating this process.

It is possible that the unknown ligand binding to Tenm3 could trigger the endocytosis of the Gpc3-Tenm3- receptor complex in the ventral axons, thereby leading to the destabilization of the contacts between ventral and missorted dorsal axons and allowing for missorted axons to degenerate. Such mechanism has been seen in Ephrin-B/ EphB signaling [323, 324]. Upon contact between EphB-expressing cells and Ephrin-B-expressing cells, Ephrin-B is trans-endocytosed into the EphB-expressing cell [324]. The internalization of the receptor-ligand complex leads to the destabilization of cell-cell contacts. A similar phenomenon is seen in the reverse direction with the trans-endocytosis of the Ephrin-B/EphB complex into the Ephrin-B-expressing cell, again

aresulting in axon withdrawal and growth cone collapse [323]. In this model for pretarget sorting, once Tenm3 binds its ligand (presumably Lphn), the complex of Gpc3-Tenm3-Lphn would become endocytosed, allowing for the retraction and degeneration of the missorted dorsal axons. Alternatively, and most likely, the Tenm3-Lphn interaction could directly initiate a transduction signal for the missorted dorsal axons to degenerate. Recent studies in *C. elegans*, *Drosophila*, and in vitro studies in mammalian cells have provided evidence supporting a role for Lphn in modulating intracellular cAMP signaling during different developmental processes [321, 325-327]. Interestingly, in the mouse visual system, cAMP modulation downstream of Ephrin-A signaling controls the pruning of ectopic retinal axonal branches [142]. These cAMP signals are restricted to the lipid rafts along retinal growth cones and are required for Ephrin-A induced axon retraction and the pruning of mistargeted projections at the superior colliculus (SC). This offers an intriguing pathway to investigate in pre-target retinotectal axon sorting in zebrafish. Upon Gpc3-Tenm3 interacting with Lphn, Lphn could modulate cAMP signaling in the missorted dorsal axons, leading to their degeneration. While both presented hypotheses are intriguing, the ligand on the missorted dorsal axons first needs to be defined. Zebrafish express a member of the Latrophilin family, *adgrl3.1* in the RGC layer during development [328, 329] and therefore is an interesting candidate for Tenm3's ligand during pre-target retinotopic sorting. Futures studies will evaluate the expression and function of *adgrl3.1* in pre-target retinal axon sorting and determine if it indeed interacts with Gpc3/ Tenm3.

Although our data indicate a genetic interaction between Gpc3 and Tenm3, how Gpc3 regulates Tenm3 signaling during pre-target retinotopic sorting remains unanswered. Gpc3 is attached to the plasma membrane by a GPI anchor and depending

on the context, glypicans can stimulate or inhibit signaling pathways [37, 330]. Many in vitro studies have been conducted to better understand how Gpc3 interacts with Wnt and Hh signaling pathways. Gpc3 stimulates Wnt signaling by binding Wnt at the plasma membrane while simultaneously interacting directly with the Wnt receptor, Frizzled [331]. The binding of Gpc3 to Wnt triggers the endocytosis of the Gpc3/Wnt/Frizzled complex which then stimulates Wnt signaling. A similar phenomenon has been shown for the interaction between Gpc3 and Hh, however this mechanism acts to inhibit Hh signaling [306, 332]. Gpc3 competes with Patched (Ptc), a receptor for Hh, for binding with Hh [306]. When Gpc3 and Hh bind, the Gpc3/Hh complex is endocytosed and subsequently degraded [306, 332]. While informative on the mechanistic function of Gpc3, the majority of these studies have been conducted in vitro and the in vivo studies have only scratched the surface at understanding the signaling pathways mediated by Gpc3. Glypicans typically interact with other proteins to sequester and present those proteins along the cell surface[37] however they can also act to aid in the trafficking of receptors at the membrane[306, 333, 334]. Interestingly, Tenm1 has been shown to interact with heparin via its C-terminal extracellular YD-repeat domain [335]. Plating dorsal root ganglion (DRG) neurons on substrates containing recombinant proteins mimicking the YD-repeat domain of Tenm1 induced neurite fasciculation and outgrowth. However, addition of heparin to these cultures caused the neurites in direct contact with the YD-repeat substrate to retract. As Teneurins are highly conserved within and between species [322], it is probable that Gpc3 and Tenm3 interact through the C-terminal domain of Tenm3 and the HS chains on Gpc3. Gpc3 would then act to present Tenm3 along the plasma membrane, thus

presenting Tenm3 to its unknown ligand on the missorted dorsal axons. Future studies will focus on determining the ligand expressed in missorted dorsal retinal axons as well as the intracellular signaling pathway needed for the degeneration of missorted dorsal retinal axons.

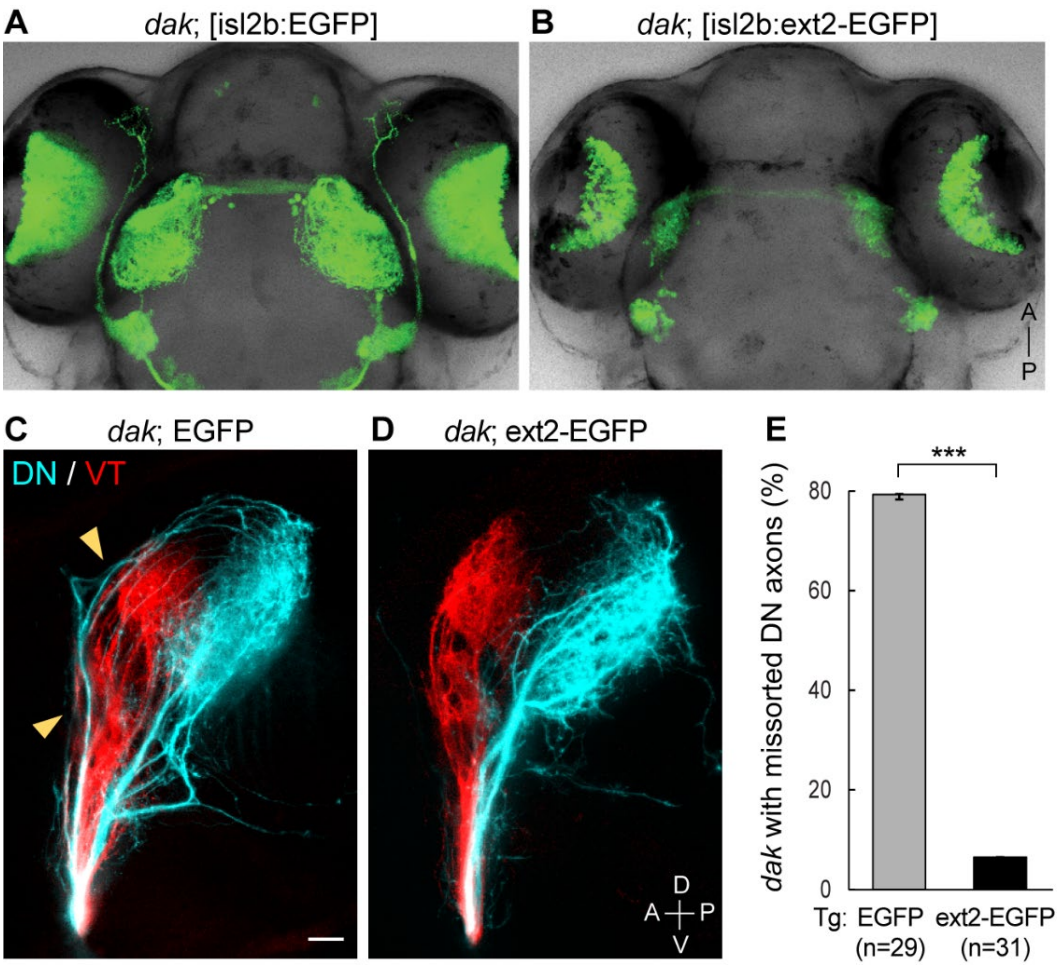

Figure 3.1: Ext2 is required in RGCs to regulate pre-target sorting. (**A**) Dorsal view of a *dak* mutant embryo expressing *EGFP* under the control of the RGC-specific promoter *isl2b*. (**B**) Dorsal view of a *dak* mutant embryos expressing *ext2-EGFP* in RGCs. (**C**) *dak* mutants expressing EGFP in RGCs have missorted dorso-nasal axons (yellow arrowheads). (**D**) *dak* mutants expressing *ext2*-EGFP in RGCs do not have missorted dorsal axons. Confocal microscopy, scale bar: 50 µm. (**E**) 79.3% of *isl2b:EGFP;dak* mutant embryos displayed missorted DN axons while only 6.5% of *dak*;*isl2b:ext2-EGFP* embryos had missorted DN axons. Statistical analysis: Chi-square test with Yates' correction showed a significant difference between the two groups. $X2$ (1, N = 47) = 20.72, $p < 0.001$.

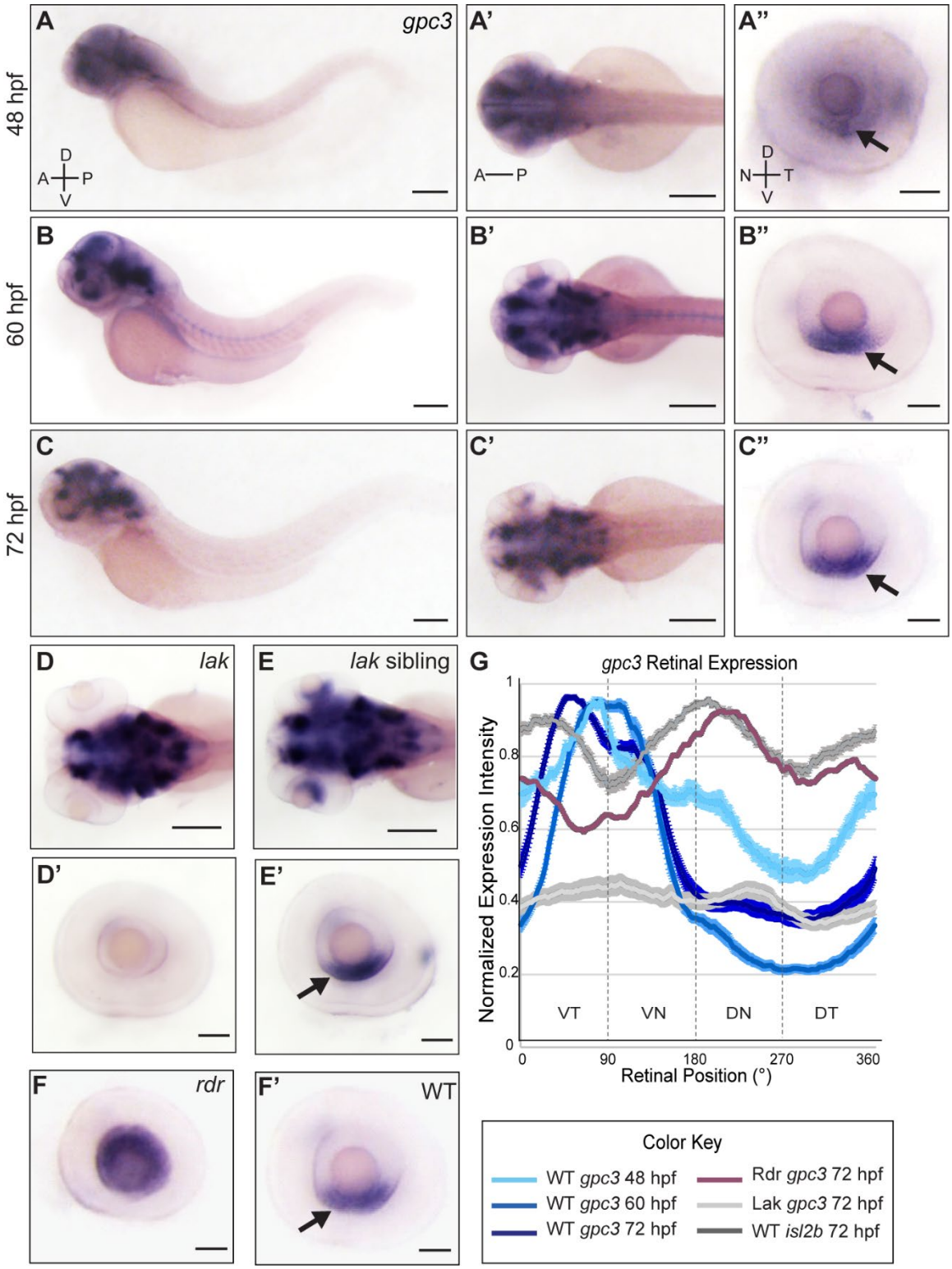

Figure 3.2: *gpc3* is expressed specifically by ventral RGCs. (**A-A"**) WT embryos stained for *gpc3* by ISH at 48 hpf from a lateral view (**A**), dorsal view (**A'**) and a dissected eye (**A"**). *gpc3* is strongly expressed in the nervous system and expression starts to be detected in the retina at 48 hpf (arrow). (**B-B"**) WT embryos at 60 hpf show strong signal for *gpc3* in the nervous system and in the ventral RGC layer in the retina (arrow). (**C-C"**) *gpc3*

Figure 3.2 (Continued): continues to be strongly expressed in the nervous system and ventral RGC layer at 72 hpf (Arrow). (**D-E'**) *gpc3* expression in *lak* mutants and siblings at 72 hpf. *gpc3* is expressed in the nervous system of *lak* mutants but no expression is detected in the eye (**D'**) whereas it is strongly expressed in the ventral RGC layer in *lak* siblings (**E'**). (**F-F'**) *gpc3* expression in *rdr* mutants and WT at 72 hpf. *gpc3* is expressed throughout the entire retina in *rdr* mutants (**F**) while it is expressed in only the ventral RGC layer in WT (arrow) (**F'**). (**G**) Quantification of signal intensity along a 360° trajectory shows that *gpc3* expression is restricted to the ventral RGC layer during retinotectal development. *gpc3* is not expressed in *lak* mutants at 72 hpf and its expression becomes dorsalized in *rdr* mutants at 72 hpf. Dissected WT retinas stained by ISH for *isl2b* were quantified as a positive control. See **Figure S1** for description of quantification method. Scale bars: 200 µm in A-C' and D-E, 50 µm in A"-C" and D'-E'.

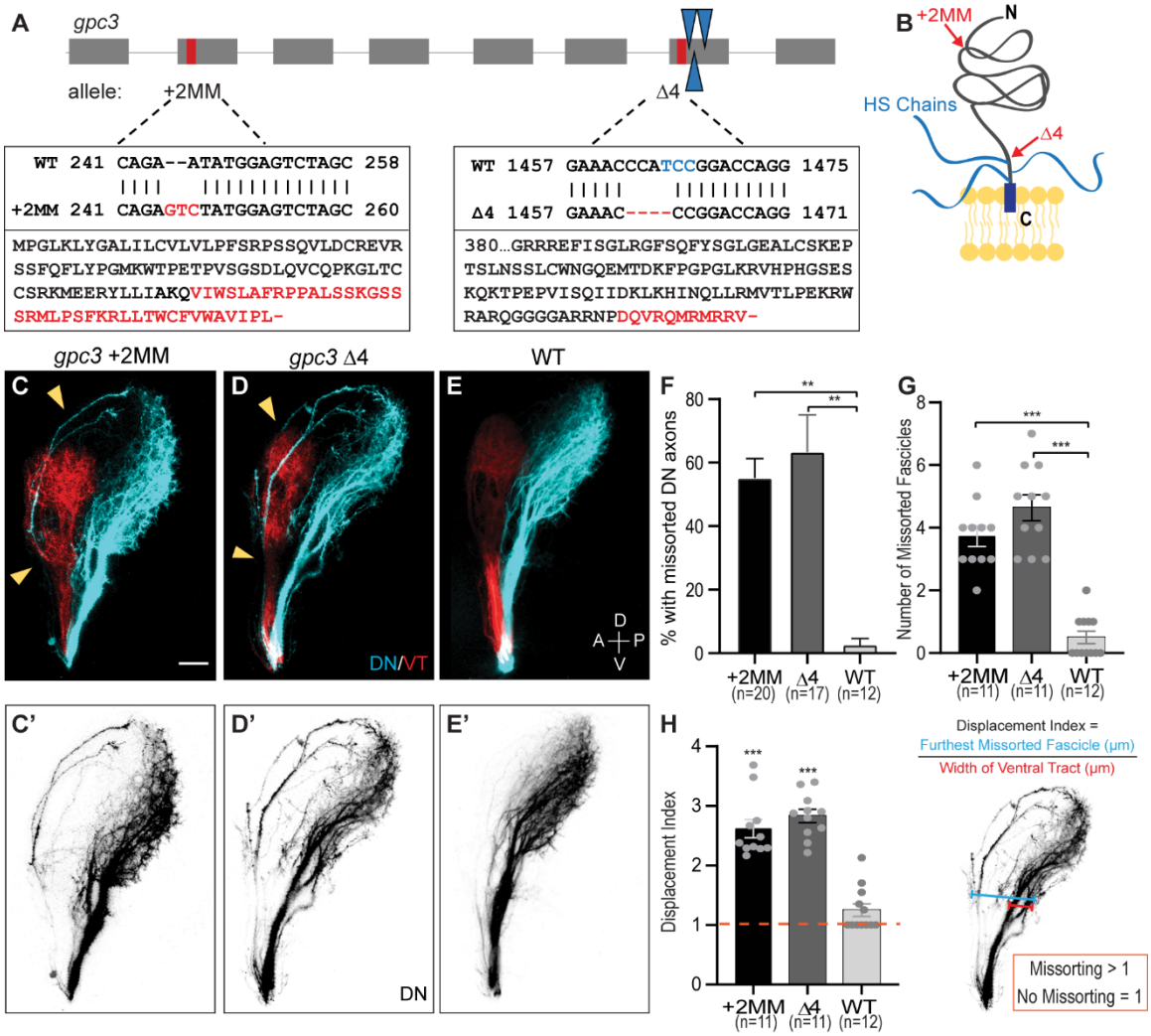

Figure 3.3: Gpc3 is required for proper sorting of dorsal retinal axons. (**A**) Schematic of *gpc3* gene. *Gpc3* contains 7 Exons. CRISPR gRNAs were designed to target sites (red bars) in Exon 2 and in Exon 7, just upstream codons encoding the HS attachment sites (indicated by blue arrows). Two mutants were analyzed in this study: mutants with the (+2MM) allele have a two-nucleotide insertion followed by a mismatch in Exon 2. Mutants with the (Δ4) allele have a four-nucleotide deletion in Exon 7 located just upstream of the codon encoding the first HS attachment site. The corresponding amino acid sequences for each allele are shown below the mutations: +2MM leads to the addition of 40 amino acids (in red) followed by a premature stop codon, and the Δ4 mutation leads to the addition of 11 amino acids and a premature stop that remove the first HS attachment site. (**B**) Schematic of Gpc3 protein structure. Gpc3 is a GPI-anchored protein with a large globular domain at the N-terminus and three HS attachment sites in its C-terminal region. Red arrows indicate regions corresponding to the CRISPR target sites. (**C-E'**) VN and DN retinal axons along the optic tract were labeled by topographic injections of DiD in the DN retina (blue) and DiO in the VT retina (red) of embryos fixed at 4 dpf. Confocal microscopy, maximal projections. (**C'-E'**) DN retinal axons labeled with DiD. (**C-D'**) *Gpc3* mutants have missorted dorsal axons along the dorsal branch of the optic tract

Figure 3.3 (Continued): (yellow arrowheads) while WT embryos have properly sorted dorsal axons (**E-E'**). Confocal microscopy, scale bar: 50 µm. (**F**) 55% of (+2MM) and 65% of (Δ4) *gpc3* mutants have missorted DN axons, compared to only 7% of WT embryos (n = 20 +2MM embryos, 17 Δ4 embryos, 12 WT embryos). (**G**) Number of missorted dorsal fascicles along the dorsal bundle of the axon tract. +2MM mutant embryos with a missorting phenotype have an average of 3.73 ± 0.33 missorted fascicles, Δ4 mutants have an average of 4.64 ± 0.39 missorted fascicles, and WT have an average of 0.5 ± 0.19 missorted fascicles (n = 11 +2MM embryos, 11 Δ4 embryos, 12 WT embryos). (**H**) The Displacement Index corresponds to the distance between the furthest missorted fascicle and the ventral tract (blue bar) over the width of the properly sorted dorsal axon bundle along the ventral tract (red bar). A Displacement Index of one indicates no missorting. +2MM mutants with a missorting phenotype have a Displacement Index of 2.62 ± 0.15 and Δ4 mutants have a Displacement Index of 2.83 ± 0.11 while WT embryos have an index of 1.25 ± 0.11 (n = 11 +2MM embryos, 11 Δ4 embryos, 12 WT embryos). Statistical Analysis: (**F**) Chi-square test with Yates' correction showed a significant difference between the two groups. $X2$ (2, N = 34) = 11.58, $p < 0.01$; (**G**) One-Way ANOVA with Tukey's posthoc test (**H**) Two-sample t-test compared to a control value of 1 (1 indicating no missorting); ** $p < 0.01$, ***$p < 0.001$.

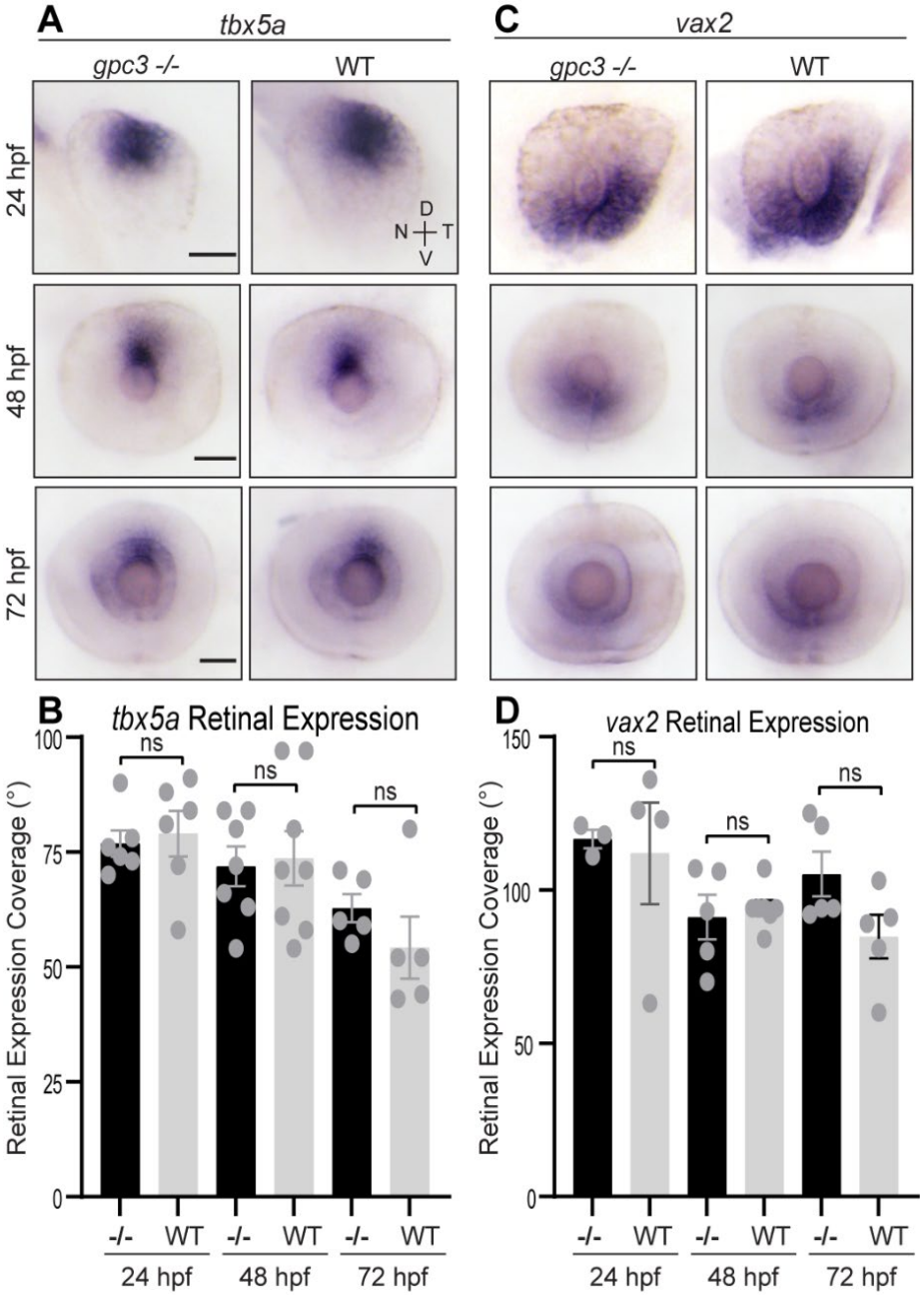

Figure 3.4: *Gpc3* mutants do not have retinal patterning defects along the D-V axis. (**A**) Dissected eyes of *gpc3-/-* (+2MM allele) and WT embryos stained for *tbx5a* by ISH at 24, 48, and 72 hpf. In both WT and mutants, *tbx5a* is expressed in the dorsal retina at all timepoints and becomes more restricted throughout development. (**B**) Quantification of tbx5 expression coverage in the dorsal retina. See **Figure S1** for description of quantification method. The expression coverage of *tbx5* is not changed in *gpc3-/-* compared to WT. (**C**) Eyes of *gpc3-/-* and WT embryos stained for *vax2* by ISH at 24, 48, and 72 hpf. *vax2* is highly expressed in the ventral eye at 24 hpf. Its expression decreases but remains specific to the ventral retina at 48 and 72 hpf. (**D**) Quantification

Figure 3.4 (Continued): of *vax2* expression coverage in the ventral retina. The expression coverage is unchanged in *gpc3-/-* compared to WT embryos. Scale bars: 50 μm. Statistical analysis: Two-Sample t-Test between mutant and WT at each timepoint.

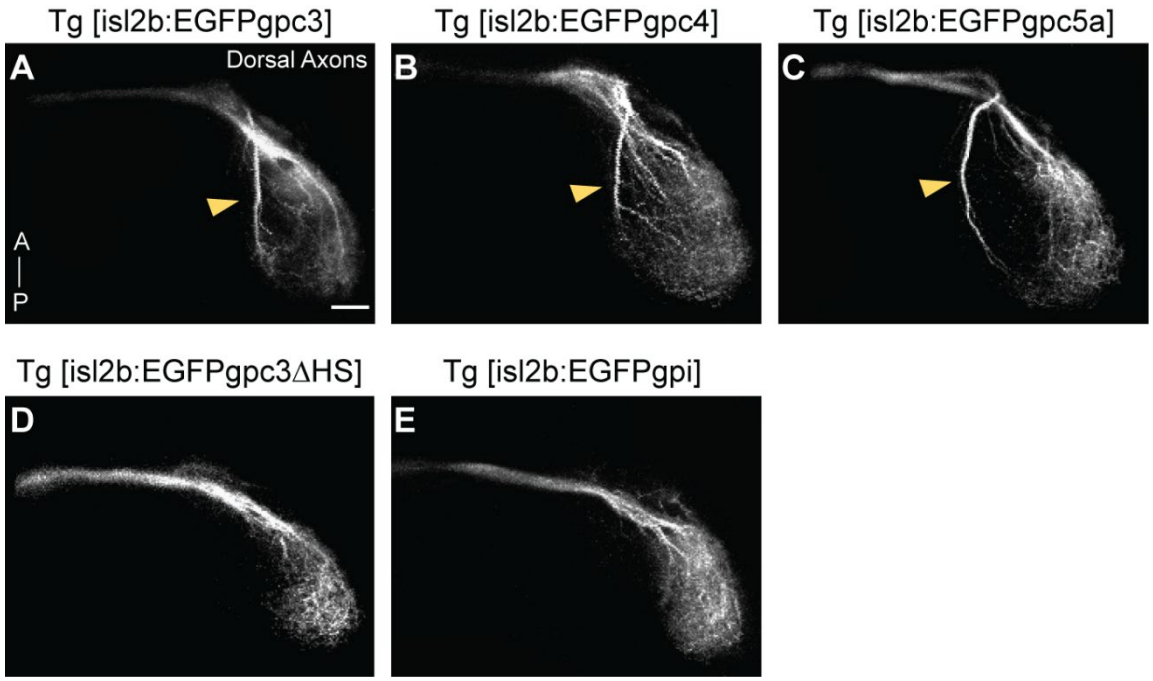

Figure 3.5: Altering HS levels in RGCs disrupts retinal axon sorting along the tract. DN retinal axons were labeled by topographic injection of DiD in the DN retina of embryos fixed at 4 dpf. WT embryos expressing *gpc3* (**A**) *gpc4* (**B**) or *gpc5* (**C**) fused to EGFP in all RGCs have missorted dorsal axons (yellow arrowhead). (**D**) WT embryos expressing *gpc3* with mutated HS attachment sites have properly sorted dorsal axons. (**E**) Control WT embryos expressing EGFP fused to the GPI anchor of *gpc3* also have properly sorted dorsal axons. Dorsal views, confocal microscopy, maximal projections. Scale bar: 50 µm.

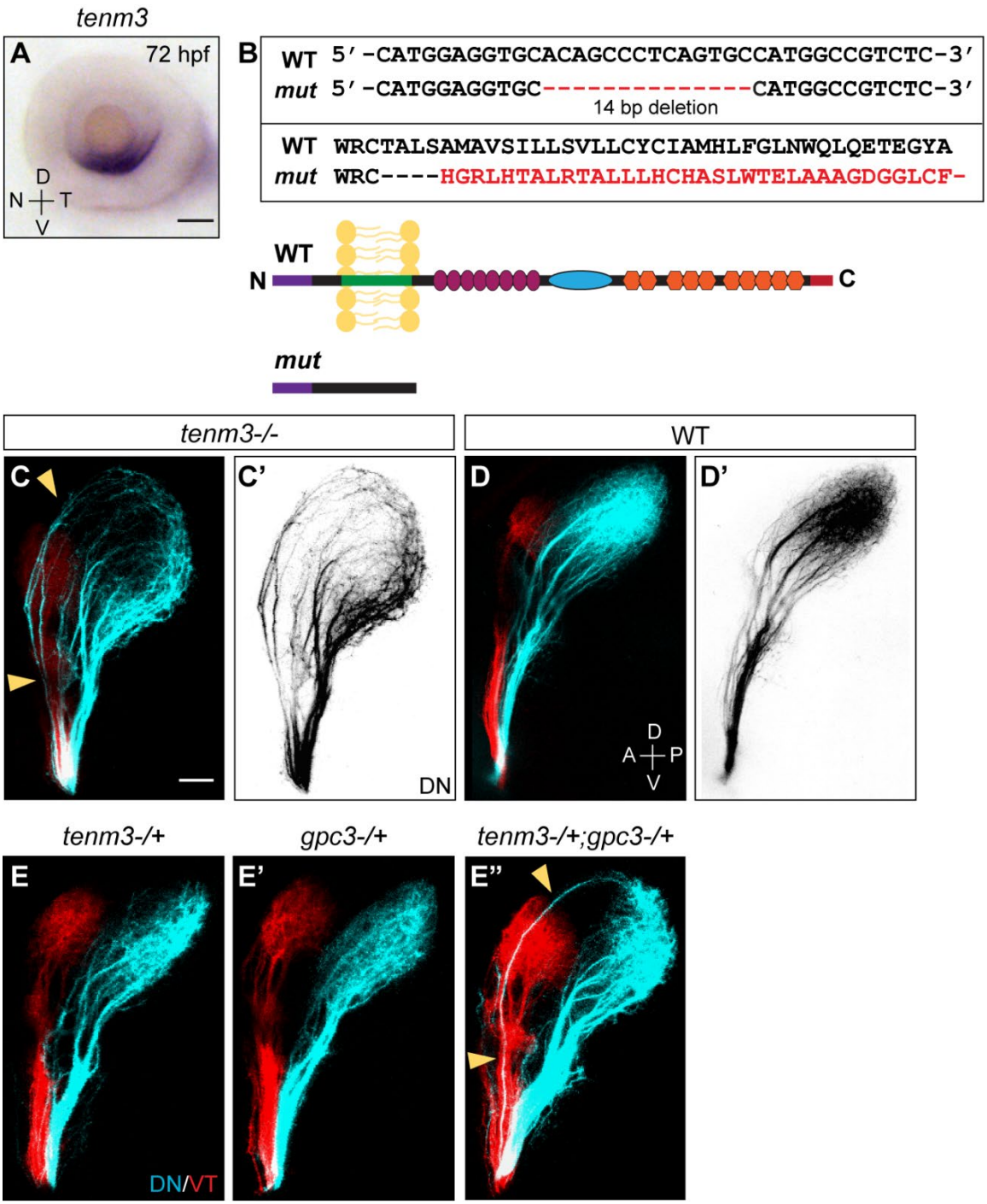

Figure 3.6: Tenm3 and Gpc3 genetically interact for proper retinal axon sorting. (**A**) Dissected WT eye at 72 hpf stained for *tenm3* by ISH. *Tenm3* is expressed specifically in the ventral RGC layer. (**B**) Schematic of the 14 base pair deletion present in the *tenm3* gene in *tenm3-/-* [298], and leading to structural changes in the Tenm3 protein. Since Tenm3 is a type II transmembrane protein, the 14 base pair deletion creates a truncated protein lacking the entire extracellular domain. (**C-C'**) Topographic injections of lipophilic dyes show missorted dorsal axons (arrowheads) in *tenm3 -/-* mutants compared to WT embryos (**D-D'**) that have properly sorted dorsal axons. (**E-E"**) *tenm3* and *gpc3* genetically interact to

Figure 3.6 (Continued): regulate sorting. *Tenm3-/+* (**E**) and *gpc3-/+* (**E'**) have properly sorted dorsal axons, whereas *tenm3-/+;gpc3-/+* embryos have missorted dorsal axons (arrowheads). Confocal microscopy. Scale bars: 50 μm.

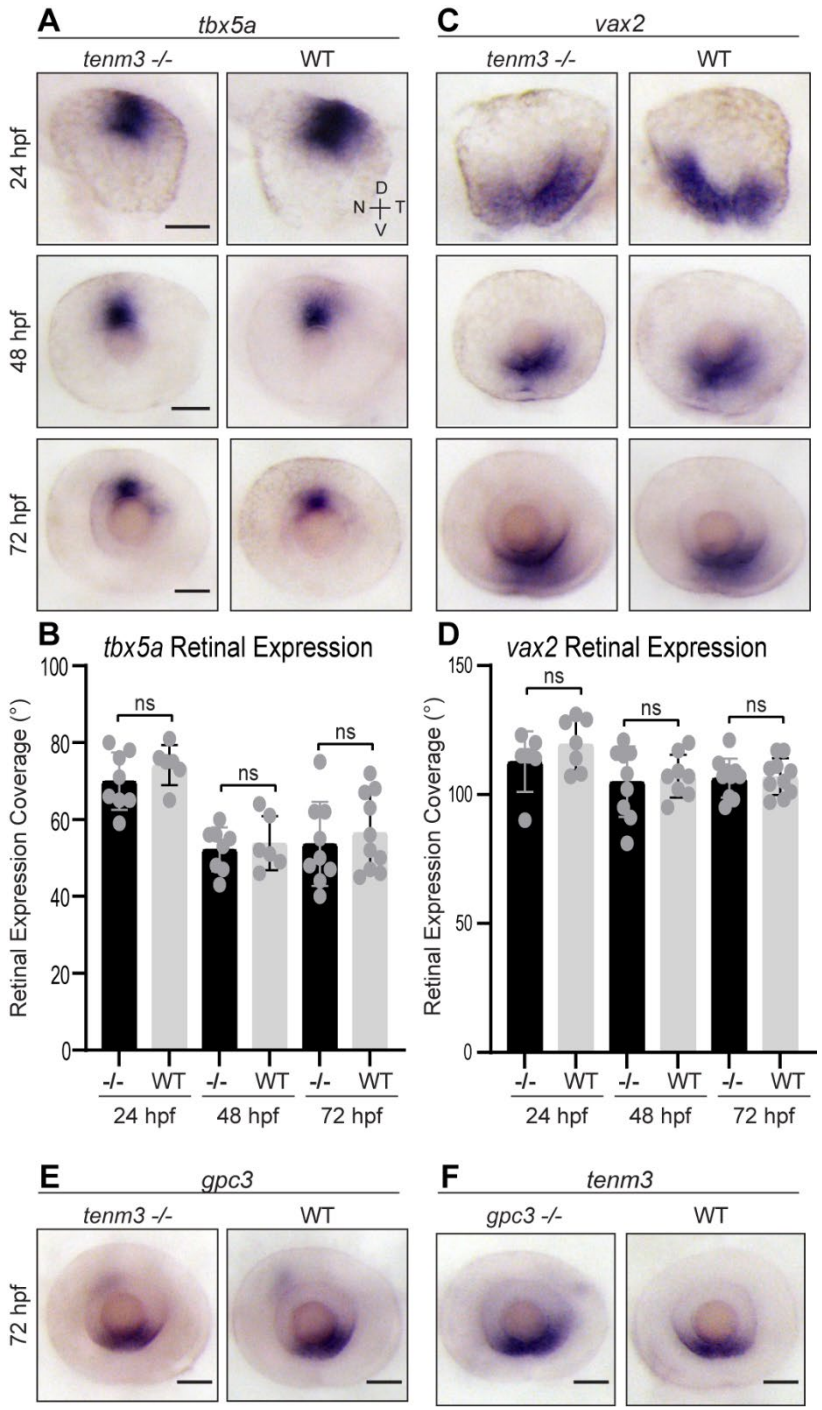

Figure 3.7: *Tenm3* mutants do not have retinal patterning defects along the D-V axis. (**A**) Dissected eyes of *tenm3-/-* and WT embryos stained for *tbx5a* by ISH at 24, 48, and 72 hpf. *tbx5a* is expressed in the dorsal retina at all timepoints and becomes more restricted throughout development. (**B**) Quantification of *tbx5* expression coverage in the dorsal retina, which is not changed in *tenm3-/-* compared to WT. (**C**) Dissected eyes of ISH staining for *vax2* in *tenm3-/-* and WT

Figure 3.7 (Continued): embryos at 24, 48, and 72 hpf. *vax2* is highly expressed in the ventral eye at 24 hpf. Its expression remains specific to the ventral retina at 48 and 72 hpf. (**D**) Quantification of *vax2* expression coverage in the ventral retina, which is unchanged in *tenm3-/-* compared to WT embryos. (**E**) Eyes dissected from *tenm3-/-* and WT embryos at 72 hpf and stained for *gpc3* by ISH. *gpc3* expression is highly expressed in the ventral RGC layer and is not altered in *tenm3-/-*. (**F**) Eyes dissected from *gpc3-/-* and WT embryos and stained for *tenm3* by ISH at 72 hpf. *tenm3* is expressed specifically in the ventral RGC layer and is not altered in *gpc3-/-*. Scale bars: 50 μm. Statistical tests: t-test between mutant and WT at each time point. Statistical analysis: Two-Sample t-Test between genotypes at each timepoint.

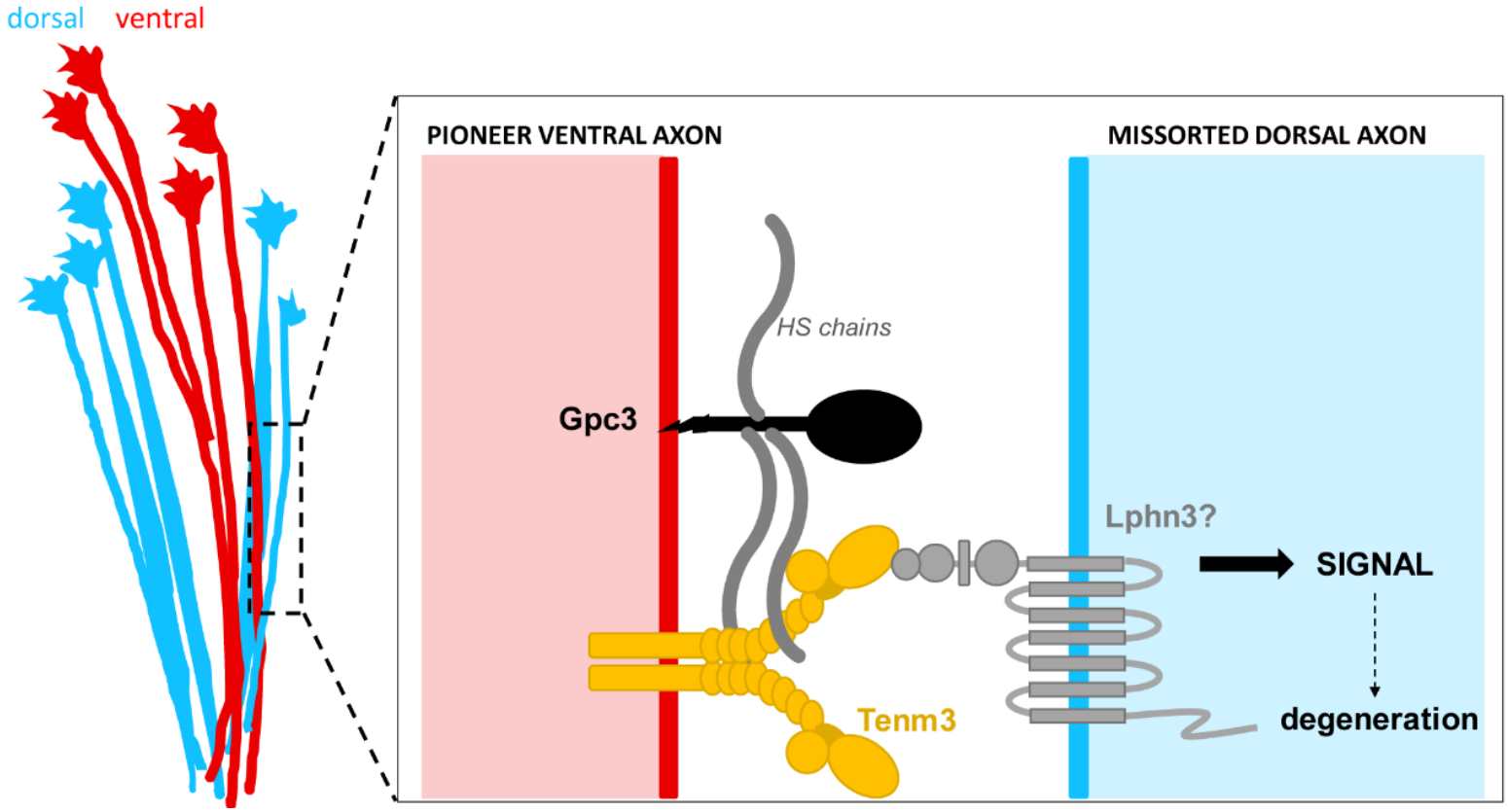

Figure 3.8: Trans-axonal signaling mediates the selective degeneration of missorted dorsal axons. Schematic of the potential signaling mechanism regulating the sorting of retinal axons along the optic tract. Gpc3 and Tenm3 are both present at the surface of pioneer ventral retinal axons. Gpc3 may interact with Tenm3 through its HS chains, presenting Tenm3 to its receptor on the missorted dorsal axons and initiating a signal for the missorted axon to degenerate. While the receptor has yet to be identified, Tenm3 is known to interact with Lphn3, which is also expressed in the retina at the time of pre-target sorting.

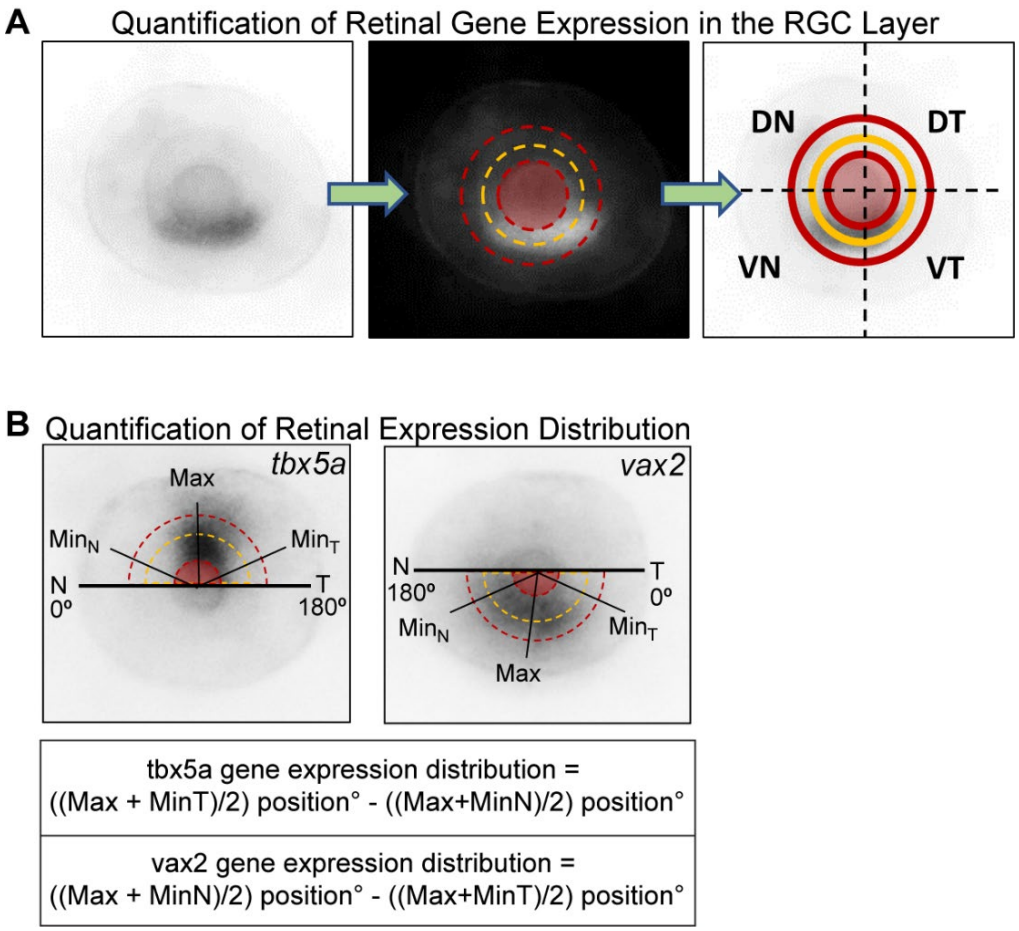

Figure 3.9: Quantification of gene expression in the retina. (**A**) Quantification of gene expression in the RGC layer along a 360° trajectory. Grayscale images of dissected eyes are first inverted in Fiji. Then an oval selection half-way between the lens and the outer-most point of the RGC layer (yellow dashed lines) is selected and the Oval Profile plugin is run along 360°. Oval Profile gives an expression profile based on pixel intensity. We can then analyze where in the axis a gene is expressed. (**B**) Quantification of retinal expression coverage for patterning experiments. All quantifications were performed on inverted grayscale images as described above. The signal intensity along a 180° radial trajectory in the dorsal retina (for *tbx5a*) and in the ventral retina (for *vax2*) was measured using Oval Profile Plot plugin. We determined the position (°) of maximum (Max) intensity. Then we determined the position of the minimum intensity nasal (MinN) and temporal (MinT) to the maximum value. The position halfway between the maximum and the MinN and the position halfway between the maximum and the MinT were then determined. We then defined the Gene Expression Coverage as the difference between these halfway-radial positions.

CHAPTER 4

ACTIVITY-MEDIATED REFINEMENT OF NASAL RETINAL PROJECTIONS DRIVES TOPOGRAPHIC MAP SHARPENING IN THE TELEOST VISUAL SYSTEM[3]

[3] Spead O and Poulain FE. 2020. Available on *bioRxiv* doi: 10.1101/2020.12.14.422653. Reprinted here with permission from the publisher.

4.1 Abstract

Topographic maps in the brain are essential for processing information. Yet, our understanding of topographic mapping has remained limited by our inability to observe maps forming and refining directly in vivo. Here, we used Cre-mediated recombination of a new colorswitch reporter in zebrafish to generate the first transgenic model allowing the dynamic analysis of retinotopic mapping in vivo. We found that the antero-posterior retinotopic map forms early but remains dynamic, with nasal and temporal retinal axons expanding their projection domains over time. Nasal projections initially arborize in the anterior tectum but progressively refine their projection domain to the posterior tectum in an activity-dependent manner. This activity-dependent refinement drives retinotopic map sharpening along the antero-posterior axis. Altogether, our study provides the first analysis of a topographic map maturing in real-time in a live animal and opens new strategies for dissecting the intricate mechanisms of precise topographic mapping in vertebrates.

4.2 Introduction

Organization of neuronal connections into topographic maps is essential for the efficient transfer of information between brain regions. In the visual system, retinal projections transmit a precise and continuous representation of the external world by maintaining the neighboring relationship of the neurons they originate from in the retina [1, 9, 11, 336]. Along the antero-posterior axis, retinal ganglion cells (RGCs) in the nasal retina project axons to the posterior tectum (or superior colliculus -SC- in mammals), whereas temporal RGCs innervate the anterior tectum. As Sperry first postulated in his chemoaffinity hypothesis [45], studies in mouse, chick, xenopus and fish have demonstrated

that this precise retinotopic map is first established by specific axon-target interactions, whereby axons with a specific set of receptors interpret guidance cues distributed in a gradient at the target. The repellent cues ephrin-As, for instance, are the main factors mediating topographic mapping along the antero-posterior axis. Subsequently to this guidance process, retinotopic projections are refined by activity-dependent mechanisms triggered by spontaneous waves of retinal activity or visual experience [337-340].

It is now well accepted that both guidance cues at the target and patterned retinal activity act together in an instructive manner to establish a precise retinotopic map [112, 133, 134]. However, increasing evidence also implicates additional mechanisms in the establishment of retinotopy. Repulsive, competitive and stabilizing interactions among axons themselves are thought to play an important role in both initial mapping and refinement [14, 63, 111, 131, 245, 341-343]. Yet, our understanding of how and when trans-axonal signaling contributes to retinotopic map formation and maturation has remained limited by our inability to selectively manipulate RGCs in a topographic and reproducible manner. It also remains unclear how the retinotopic map becomes sharper as a whole, as we currently lack the ability to observe the map forming and refining over time in the same embryo in vivo. Fourier optical imaging of intrinsic signals allows for the visualization of functional collicular maps in the mouse but can only be employed once animals have developed vision, well after the retinotopic map has formed and refined [133]. On the other hand, retinotopy can be analyzed at earlier stages by injecting lipophilic dyes or electroporating DNA plasmids in specific retinal quadrants. However, both approaches often require fixing specimen for analysis and have some degree of

variability, which precludes the study of mapping dynamics and the detection of subtle topographic changes between times or conditions.

Because of its rapid external development and transparency, the zebrafish larvae has become a model of choice for the study of retinotopy [113, 344, 345]. Injections of lipophilic dyes in opposite regions of the retina have been used extensively to label retinotopic projections at different stages of development or regeneration and identify mutants with retinotopic defects [25, 35, 346-348]. Using that approach, early studies have shown that nasal and temporal retinal axons are localized at retinotopic sites as early as 3 days-post-fertilization (dpf), with temporal and nasal axons innervating the anterior and posterior tectum, respectively [25, 108]. Labeling a subset of RGCs in larvae fixed at 4 and 6 dpf has also revealed that projections cover a smaller territory at later stages, suggesting a refinement of the retinotopic map over time [107]. That reduced coverage is not observed in embryos treated with the voltage-gated sodium channel blocker tetrodotoxin (TTX), indicating a role for neuronal activity in retinotopic map maturation. While these observations highlight similar mechanisms underlying precise retinotopy in zebrafish and other species, we still do not know exactly when and how the retinotopic map refines and matures in teleosts. Advances in molecular genetics have allowed the generation of multiple transgenic lines for analyzing the lineage and functions of neuronal populations in zebrafish [349-351], but the lack of enhancer driving transgene expression in specific retinal quadrants has precluded a similar unbiased analysis of retinotopic mapping over time in vivo.

Here, we report the generation of the first genetic model allowing the dynamic and quantitative analysis of retinotopic map formation and refinement directly in vivo.

We show that an enhancer located up-stream of *hmx1* and *hmx4* genes on chromosome 14 drives selective transgene expression in the nasal retina. We used Cre-mediated recombination of an *RGC:colorswitch* reporter to specifically label nasal and temporal retinal axons in vivo and image their projection domains at the tectum from 3 to 6 dpf by live confocal microscopy. Our analysis reveals that while the antero-posterior retinotopic map is formed at early developmental stages, it remains dynamic, with nasal and temporal axons expanding their projection domains over time. We further show that nasal retinal projections initially arborize in the anterior half of the tectum but progressively refine and condense their projection domain to the posterior tectum in an activity-dependent manner from 4 to 5 dpf. We finally demonstrate that the refinement of nasal projections drives the sharpening of the antero-posterior retinotopic map, and that both are prevented by genetically blocking neuronal activity in RGCs.

4.3 Materials and Methods

Zebrafish Husbandry and Maintenance

All experiments and procedures were approved by the Institutional Animal Care and Use Committee of the University of South Carolina. Zebrafish WT, mutant and transgenic embryos were obtained from natural matings, raised at 28.5°C in E3 medium (5 mM NaCl, 0.17 mM KCl, 0.33 mM $CaCl_2$, and 0.33 mM $MgSO_4$) in the presence of 150 mM of 1-phenyl-2-thiourea (PTU) (Millipore Sigma, Burlington, MA) to prevent pigment formation, and staged by age and morphology [279]. WT embryos were from the Tübingen or AB strains. *Maco* ^{tt261} heterozygous fish (generous gift from Dr. A. Ribera, University of Colorado School of Medicine) were identified by high-resolution melting analysis (HRMA) [283] using the following primers: *maco-hrma-fw*: 5'-

TTGTACCGGTGACGAACG-3', *maco-hrma-rv*: 5'-AACAGAAGAAGGCATGAATACAC-3'. *Maco* mutant embryos were identified based on their lack of touch response at 48 hours post-fertilization (hpf) [352]. Embryos were anaesthetized in tricaine-S (Western Chemicals, Ferndale, WA) before fixation or imaging. Zebrafish larvae and young fish were nurtured using rotifer suspension and dry food (Gemma 75 and 150, Skretting USA, Westbrook, ME). Adult fish were fed with dry food (Gemma 300, Skretting USA).

Cloning of *hmx* cDNAs and putative enhancers

For cloning *hmx1* and *hmx4* cDNAs, zebrafish mRNA was isolated from embryos at 24 and 48 hpf, respectively, using Trizol and the RNeasy mini kit (Qiagen, Hilden, Germany), and cDNA was prepared from RNA using the SuperScriptIII First-Strand Synthesis system (Invitrogen, Carlsbad, CA). *Hmx1* and *hmx4* cDNAs were amplified using the following full length primers: *hmx1-fw*: 5'-ATGCATGAAAAAAGCCAG-CAACAGC-3', *hmx1-rv:* 5'-TCAGACAAGGCCTGTCATCTGC-3', *hmx4-fw:* 5'-ATCTAACGGAGAATATGAG-CAAGGAG-3', *hmx4-rv*: 5'-TCATATATCTCCATCAAACAGGCTGAAATAC-3'. Amplicons were subcloned into PCRII-TOPO (Invitrogen) and sequenced to verify gene identity and confirm sequence orientation. *Hmx1* putative enhancer elements were amplified by PCR from total genomic DNA using the LA Taq PCR kit v2.1 (TaKaRa, Mountain View, CA) and the following primers: *hmx1-En1-fw:* 5'-ACCGCACCACTAAA- GAGTCACAG-3', *hmx1-En1-rv:* 5'-GGGTGATACGTGAATACCTCTAAGCA-3', *hmx1-En2-fw:* 5'-GAGGGTGCCAGATGGAGATACAC-3', *hmx1-En2-rv:* 5'-ACTGGCTCTGCTATGCTTCTGTTTC-3', *hmx1-En2s-fw:* 5-

GAACGGTACCGAACCGTCTATTAAAAGATTACACTAC-3' (KpnI restriction site added in primer), *hmx1- En2s-rv:* 5'-GAACGGATCCAATAAACAAGGGACTAATAATTCAAGG-3' (BamHI restriction site added in primer), *hmx1-En3-fw:* 5'-GAACGGTACCTCTTTGGAGACTGGCTGAACTGAC-3' (KpnI restriction site added in primer), *hmx1-En3-rv:* 5'-GAACGGATCCATTCTCCGTTAGATGCGGGTCC-3' (BamHI restriction site added in primer). Amplicons were purified on gel using the Qiaquick gel extraction kit (Qiagen), subcloned into PCRII-TOPO (Invitrogen) and sequenced before being digested and ligated into the Gateway *p5E-MCS* entry vector [285] using the following restriction endonucleases: XhoI / BamHI (for *hmx1- En1*), DraII (for *hmx1-En2*), and KpnI / BamHI (for *hmx1-En2s* and *hmx1-En3*).

Generation of transgenesis vectors

All transgenesis constructs were generated using the Tol2kit Gateway cloning system [285]. To generate *hmx1* reporter constructs, *p5E-hmx1-En1*, *p5E-hmx1-En2*, *p5E-hmx1-En2s, p5E-hmx1-En3, pME-EGFPCAAX* and *p3E-polyAv2* were recombined into the *pDestTol2pA2* destination vector using a Gateway Multisite LR reaction [285] (Invitrogen). *p5E-hmx1-En2*, *pME-iCre* and *p3E-polyAv2* were recombined into *pDestTol2CR3* (*pDestTol2pA3* with *myl7:TagRFP* transgenesis marker) to generate the *hmx1-En2:iCre* construct. The sequence encoding *loxP-TagRFPCAAX-polyA-loxP* was amplified by PCR, purified on gel using the Qiaquick gel extraction kit (Qiagen), and recombined into the pDONR221 destination vector to generate the *pME-loxP-TagRFPCAAX-polyA-loxP* entry vector. A modified *p5E-isl2b-gata2a* entry clone encoding a 7.6 kb genomic fragment upstream of the *isl2b* start codon fused to the 1 kb

promoter of *gata2a* [21, 95], *pME-loxP-TagRF- PCAAX-polyA-loxP, and p3E-EGFPCAAX-polyA* were recombined into the *pDestTol2pA2* destination vector to generate the *isl2b:loxP-TagRFPCAAX-loxP-EGFPCAAX* (*RGC:colorswitch*) reporter construct. *p5E- isl2b-gata2a*, *pME-gal4VP16* [285], and *p3E-polyAv2* were recombined into *pDestTol2CG2* to generate the *isl2b:gal4* construct. The sequence encoding *Kir2.1-2A-mKateCAAX* flanked by FseI and DraI restriction sites was amplified by PCR using *pME-Kir2.1-2A-mGFP* [353] (generous gift from Dr. J. Fetcho, Cornell University) and *p3E-mKate2CAAX-polyA* as templates, purified on gel and recombined into pDONR221 to generate the *pME-Kir2.1-2A-mKateCAAX* entry vector. A non-conducting version of Kir2.1, KirMUT, was constructed similarly to generate the *pME-KirMUT-2A-mKate- CAAX* entry vector. *p5E-UAS* [285], *pME-Kir2.1-2A-mKateCAAX* (or *pME-KirMUT-2A-mKate- CAAX),* and *p3E-polyAv2* were recombined into *pDestTol2pA2* to generate the *UAS:Kir2.1/KirMUT-2A- mKate2CAAX* construct.

Generation of stable transgenic lines

Stable transgenic lines were generated using the Tol2 transposon method as described previously [287]. 10 to 40 pg of purified DNA (*pTol2pA2-hmx1-En1:EGFPCAAX, pTol2pA2-hmx1- En2:EGFPCAAX, pTol2pCR3-hmx1-En2:iCre, RGC:colorswitch, pTol2CG2-isl2b:gal4)* were co-injected with 25 pg of synthetic mRNA encoding Tol2 transposase at one-cell stage, and injected embryos with transient expression of transgenes were raised up to adulthood as F0 generation. F0 fish were then out- crossed to WT to screen for positive F1 embryos expressing the transgenes. Expression of EGFP and TagRFP driven in the heart by the *myl7* promoter was used to

identify *isl2b:gal4* and *hmx1-En2:iCre* carriers, respectively. Transgenic F1 carriers were subsequently out-crossed to WT to generate stable lines with a single-copy insertion.

Transient expression of Kir2.1 and Kir2.1MUT

For transiently expressing Kir2.1 or KirMUT together with mKate2CAAX in RGCs, 40 pg of *UAS:Kir2.1-2A- mKate2CAAX* or *UAS:KirMUT-2A-mKate2CAAX* were co-injected with Tol2 transposase mRNA at one cell stage in zygotes obtained from a cross between [*isl2b:gal4*] and [*hmx1:iCre; RGC colorswitch*] stable transgenic lines. Triple transgenic embryos identified by the expression of both TagRFP and EGFP in the heart and RGCs were selected for imaging and quantification. As reported in other systems [354-356], about 5% of [*hmx1:iCre; RGC colorswitch*] double transgenic embryos showed aberrant Cre-mediated recombination that was first observed in the trigeminal at 24 hpf. These embryos were discarded from our analysis.

Whole-mount In Situ Hybridization

For making ISH probes, cDNA templates cloned into pCRII-TOPO were amplified by PCR using M13fw and M13rv primers and purified on gel.
In *vitro* transcription of digoxigenin-labeled probes was performed using the DIG RNA Labeling Kit (Millipore Sigma) according to manufacturer's instructions. Embryos were dechorionated at the appropriate developmental stages and fixed in 4% paraformaldehyde in phosphate buffered saline (pH 7.4) for 2 hours at room temperature and overnight at 4°C. Whole-mount in situ hybridization was performed as previously described [78]. After staining, embryos were cleared in 80% glycerol for imaging. Sense probes were used as controls and did not reveal any staining. Images were acquired using an Olympus SZX16

stereomicroscope equipped with an Olympus DP80 dual color camera and Cellsens standard software. Digital images were cropped and aligned using Adobe Illustrator.

Quantification of retinal gene expression

Quantification of gene expression in the retina was carried out according to [280] with the following modifications. Eyes were dissected from embryos stained by ISH using a sharpened tungsten needle and imaged in 80% glycerol in a lateral view as described above. Images were imported into Fiji ImageJ analysis software [281, 282], transformed to 8-bit grayscale images, and inverted. An oval selection was applied half-way between the lens and the RGC layer periphery, and signal intensity was measured along a 360º trajectory using the Oval Profile Plot plugin. Values were exported and analyzed in Microsoft Excel.

Immunolabeling

Embryos were fixed in 4% PFA in Phosphate-buffered saline (PBS) for two hours at room temperature and then overnight at 4°C. Embryos were washed three times in PBT (PBS + 0.5% Triton X-100). Antigen retrieval was done in 150 mM Tris, pH 9 for 5 minutes at room temperature followed by 20 minutes at 70°C. Embryos were then permeabilized at room temperature for 15 minutes in water first, and then for 30 minutes in PBS with 1% Triton and 0.1% collagenase. Embryos were blocked for one hour at room temperature with blocking buffer (PBS with 0.5% Triton, 1% DMSO, 1% BSA, and 2% normal goat serum). Primary anti-EGFP (ab290, Abcam, Cambridge, UK) and anti-TagRFP (M204-3, MBL International, Woburn, MA) antibodies were applied at 1:500 dilution in PBT supplemented with 1% DMSO and 1% BSA overnight for 4°C. Embryos were washed three times in PBT. Secondary Alexa Fluor 488 Goat anti-Rabbit

(111-545-003, Jackson Immuno Research, West Grove, PA) and Alexa Fluor 594 Donkey anti-Mouse (715-585-150,Jackson Immuno Research) antibodies were diluted 1:500 in PBT with 1% DMSO and 1% BSA and applied together with TO-PRO-3 (T3605, Thermo Fisher, Waltham, MA) diluted 1:1000 over- night at 4°C. Embryos were washed five times in PBT and mounted in 1% ultrapure low melting point (LMP) agarose (16520050, Thermo Fisher) for confocal imaging.

Confocal Microscopy

For time-course imaging of live embryos from 3 to 6 dpf, embryos were anesthetized in 0.015% tricaine- S and embedded dorsally in 1% LMP agarose in E3 medium + PTU in a lumox membrane-bottomed dish (Greiner Bio-one, Monroe, NC). Images were acquired on a Leica TCS SP8X laser-scanning confocal microscope equipped with LASX software, HyD detectors, and a 20X objective. Z-series of the entire retinotectal system were acquired at 512 × 512 pixel resolution with a zoom of 1 and Z-intervals of 1.5 µm. After imaging, embryos were kept individually in a 12-well dish and allowed to recover for 24 hours before being re-anesthetized and mounted dorsally for the next day of imaging. Maximal and sum intensity projections were compiled at each time point in ImageJ software.

For high resolution imaging of the retinotectal system at 4 dpf, immunolabeled embryos were mounted either laterally after removing the contralateral eye or dorsally in 1% LMP agarose and imaged as described above with a Z-interval of 1 µm. 3D reconstructions of the retinotectal system were generated using FluoRender [357, 358].

Quantification of Topographic Mapping at the Tectum

All quantitative analyses of topographic mapping were conducted using ImageJ software. For unbiased analysis, dorsal view Z-series were consistently rotated along the X, Y, and Z-axes using the TransformJ Plugin [288], so that the left and right tecta were aligned horizontally, both optic tracts intersected at an angle of 60°, and the roundness of the right tectal neuropil was equal to 1. To analyze the area of coverage, rotated images were maximally projected and binarized using a threshold of 80 for TagRFP and of 75 for EGFP. Thresholds were chosen to best represent the raw images acquired. Using the TagRFP channel, we delineated the anterior tectal boundary as the anterior line where retinal axons enter the tectum, and the TagRFP posterior boundary. Using the EGFP channel, we delineated the posterior tectal boundary as the caudal-most border where retinal axons arborize at the tectum. We defined the Equator (E) as ½ the length of the tectum measured along the antero-posterior axis between the anterior and posterior tectal boundaries. We used the Analyze Particles tool in ImageJ to measure the tectal coverage (area) of the TagRFP-positive temporal axons, of the EGFP-positive nasal axons in the anterior half of the tectum (rostral to the Equator), and of the EGFP-positive nasal axons in the posterior half of the tectum (caudal to the Equator). We calculated The Total Tectal Coverage as the sum of the TagRFP and posterior-EGFP axonal coverages.

To further analyze retinotopic mapping along the antero-posterior axis, we defined an Equatorial Alignment Index as the ratio between the antero-posterior length (l) of the TagRFP coverage (measured between the anterior tectal boundary and the TagRFP boundary) and the Equator. We established a Nasal Axon Mistargeting Index as the ratio between the EGFP area of coverage in the anterior half of the tectum and the EGFP area

of coverage in the posterior half of the tectum. We calculated a Refinement Index as the ratio change of the Nasal Axon Mistargeting Index between two consecutive days.

To quantify the sharpness of the boundary between the TagRFP and EGFP projection domains, rotated images were sum-projected for measuring the mean fluorescence intensity of the TagFRP and EGFP signals. We divided the antero-posterior length of the tectum into 10 bins of equal height on merged images using the Polygon Selection tool in ImageJ, and measured the mean fluorescence intensity of each channel in each bin using the Measurement function in ImageJ. Bin1 was defined as the anterior-most tectal bin and Bin10, as the posterior-most tectal bin. Intensity values were normalized to the maximum value for each channel and plotted along the antero-posterior axis. We determined the point at which fluorescence intensity reached 50% of its normalized maximum value for each channel, and defined the Sharpness Index as the absolute distance between the $EGFP_{50\%}$ and $TagRFP_{50\%}$ positions at 4 and 5 dpf. (See **Figure 4.7** for a detailed illustration of our quantifications).

For analyzing retinotopic mapping in *maco* mutants, we imaged embryos from a *maco*/+ incross in blind conditions and genotyped embryos after imaging. Only mutants and WT siblings were kept for quantification. A few *maco* mutants developed periocular edema by 5 dpf and were discarded from our analysis.

For analyzing retinotopic mapping in embryos expressing Kir2.1 or KirMUT in RGCs, we imaged mKate2CAAX at the tectum of injected embryos (see previous section on transient expression of Kir2.1 transgene) at 4 dpf using an excitation wavelength shifted to 615 nm to prevent any bleed-through of the TagRFP signal. We measured the mean fluorescence intensity of mKate2CAAX over the total tectal area and selected

embryos with an average intensity over 400 for our analysis (referred to as "high mKate2" embryos). Of note, mKate2CAAX could be visualized along the optic tracts in "high mKate2" embryos but not in "low mKate2" embryos with these imaging conditions.

Visually-mediated Background Adaptation (VBA) Assay

Larvae were exposed to bright illumination from the bottom for 30 minutes to light-adapt and then imaged from a dorsal view at 5 dpf. Images were binarized using a threshold of 40, and pigmentation of larvae was assessed by measuring the area of melanophore coverage in a region caudal to the eyes and rostral to the medulla oblongata (See **Figure 4.12**).

Western Blotting

Embryos were anaesthetized at 5 dpf and lysed in RIPA buffer (Millipore Sigma). Protein concentrations were measured using a Pierce BCA Protein Assay Kit (Thermo Fisher), and 50 µg of denatured proteins were run on a 12% acrylamide gel and transferred to a 0.2 µm nitrocellulose membrane (BioRad, Hercules, CA). We blocked membranes in 5% Milk in TBST (Tris Buffer Solution + 0.1% Tween) and applied primary antibodies overnight at 4°C. Secondary antibodies were applied for 1.5 hours at room tempera- ture, and proteins were detected using Amersham Western Blotting Detection Reagent (GE Healthcare, Chicago, IL). Western blot membranes were probed with mouse anti-RFP (RF5R Invitrogen, 1:500 dilution), rabbit anti-Kir2.1 (APC-026, Alomone Labs, Jerusalem, Israel, 1:500 dilution), and rabbit anti-GAPDH (14C10, Cell Signaling Technology, Danvers, MA, 1:2000 dilution). Secondary HRP-conjugated

horse-anti-mouse (7076S, Cell Signaling Technology) and goat-anti-rabbit antibodies (7074S, Cell Signaling Technology) were used at a 1:2000 dilution.

Statistical Analysis

All statistical analyses were performed with GraphPad Prism 9 software (GraphPad, San Diego, CA). We define biological replicates as individual larvae from a mixed clutch born from pairings of at least two males and two females. Each experiment was repeated at least three times under similar experimental conditions. Sample size was decided was based on the low variability detected in pilot studies. Data are presented as mean ± SEM. For better communicating variability across samples and experimental reproducibility, graphs are represented as "SuperPlots" [359], in which biological replicates representing independent experiments are color-coded, with circles representing individual embryos tested and triangles representing averages. To compare groups with repeated measures over time, we performed repeated measures one-way ANOVA followed by Tukey's multiple comparisons post-hoc test. To compare data with both "within-subjects" and "between-subjects" factors (i.e. *maco* and Kir2.1 data), we performed mixed effects one-way ANOVA followed by Tukey's multiple comparisons post-hoc test. The number of larvae analyzed and the statistical methods used to compare groups are described in details in each figure legend.

4.4 RESULTS

hmx1 is expressed in the nasal retina throughout development

With the aim of identifying potential enhancers that would drive specific expression in the nasal or temporal retina throughout development in zebrafish, we first

assessed genes that were previously described as selectively expressed in the nasal or temporal retinal half in vertebrates. Among them, the transcription factor *hmx1* has been specifically detected in the nasal retina of zebrafish, chick, and mice and was reported to regulate the retinal expression of EphA receptors [56, 360-364]. Given its role in retinal patterning, we decided to further analyze and quantify *hmx1* expression throughout retinotectal development by in situ hybridization (ISH). At 24 hpf, when optic cup morphogenesis is complete [365], *hmx1* was strongly expressed in the nasal retina and the lens and was also faintly detected in the otic vesicle (**Figure 4.1A, A'**). At 48 hpf, when first retinal axons elongate along the tract and reach the tectum [25, 33], *hmx1* remained strongly expressed in the nasal retina and otic vesicle and could also be detected in the pharyngeal arches (**Figure 4.1B, B', E**). Interestingly, while *hmx1* expression remained stable in the otic vesicle and pharyngeal arches over time, it became restricted to the RGC layer in the nasal retina at 72 hpf (**Figure 4.1C, C', F**) and 96 hpf (**Figure 4.1D, D', G**). Hmx1 expression could also be detected at lower levels in the nasal inner nuclear layer at both stages (**Figure 4.1F, G**). We further quantified the expression levels of *hmx1* along a 360° clockwise trajectory in the RGC layer at 48, 72, and 96 hpf (**Figure 4.1H**) and found a sharp gradient of expression along the nasal-temporal axis, with *hmx1* being highly expressed in the nasal half of the retina but absent from the temporal half at all three stages (**Figure 4.1I**). Since *hmx1* and its paralog *hmx4* arose from tandem duplication and are tightly linked on the same chromosome in chick and zebrafish [366, 367], we also analyzed the expression of *hmx4* during retinal development (**Figure 4.2**). As previously described in chick [56, 368], *hmx4* had a similar expression to that of *hmx1* and

was strongly detected in the nasal retina, otic vesicle and pharyngeal arches from 24 to 96 hpf.

A distal *hmx1* enhancer drives selective expression in nasal progenitors and RGCs

The restricted expression of *hmx1* and *hmx4* in the nasal retina prompted us to search for potential enhancers regulating their expression. Transcriptional enhancers are cis-regulatory elements containing short DNA sequences bound by specific transcription factors. Their activity has been correlated with the enrichment of specific post-translational modification of histones, allowing the prediction of their position in the genome. Active enhancers are notably associated with the presence of histone H3 lysine 4 monomethylation (H3K4me1) and H3K27 acetylation (H3K27ac), while H3K4me3 is predictive of active promoters [369-372]. We thus analyzed the genomic tracks of H3K4me3, H3K4me1, and H3K27ac modifications previously generated by [373] to identify putative distal regulatory elements in the *hmx1/4* locus region. *Hmx1* and *hmx4* are tightly linked on chromosome 14 and are both composed of two exons and one intron (**Figure 4.3A**). We identified two regions upstream *hmx1* that were characterized by the genomic co-localization of H3K4me1 and H3K27ac marks at 24 (data not shown) and 48 hpf (**Figure 4.3A**). We delineated a first putative element, *hmx1-En1,* as a 7 kb region right upstream the *hmx1* gene, and a second putative element, *hmx1-En2*, as a 7 kb region located more distally. A third putative regulatory element of 1.8 kb, *hmx1-En3*, was located in-between *hmx1* and *hmx4* genes. We tested the enhancer activity of these potential elements by generating stable transgenic lines expressing EGFP targeted to the plasma membrane by the CAAX prenylation motif of Ras [374] under the control of each of these elements. While *hmx1-En3* did not exhibit any enhancer activity, *hmx1-E*n1 and *hxm1-*

En2 drove EGFPCAAX expression in specific and partially overlapping regions at 96 hpf. Both enhancers were active in the pharyngeal arches and lips, but only *hmx1-En2* drove EGFP expression in the nasal retina and lens (**Figure 4.3B-C'**). Since developmental enhancers can be found in evolutionary conserved regions [375, 376], we used a multi-species alignment (visualized in UCSC genome browser) to identify conserved domains within *hmx1-En2.* We delineated a 3 kb region, *hmx1-En2s*, that was conserved across teleosts and amphibians. However, that region did not exhibit any enhancer activity despite its location within *hmx1-En2*.

As *hmx1-En2* was the only enhancer driving expression in the nasal retina at 96 hpf, we analyzed its activity throughout retinal development in more detail (**Figure 4.4**). At 24 hpf, before RGCs differentiate [377-379], EGFP expression was strongly detected in the nasal retina and lens of Tg[*hmx1-En2:EGFPCAAX*] transgenic embryos (**Figure 4.4A, A').** This restricted expression was maintained at 48 and 96 hpf, with EGFP remaining selectively expressed in the nasal half of the retina at both stages (**Figure 4.4D-E'**). Interestingly, while *hmx1* transcripts were only detected in the RGC layer at 72 and 96 hpf (**Figure 4.1F, G**), EGFP remained visible in the entire nasal retina, likely because of its lasting stability in vivo. Like *hmx1* transcripts, EGFP was also found in several other structures including the pharyngeal arches at 48 and 96 hpf. It was also noticeably detected in the midbrain at 96 hpf (**Figure 4.4E, E'**). To determine whether *hmx1-En2* could drive transgene expression in nasal RGCs, we crossed our Tg[*hmx1-En2:EGFP*CAAX] transgenic line to Tg[*isl2b:TagRFP*] transgenic fish that express TagRFP under the control of the RGC-specific *isl2b* promoter [21, 34]. Confocal analysis of double transgenic embryos at 96 hpf revealed that EGFP partially overlapped

with TagRFP in the nasal retina (**Figure 4.4G-H'**). Importantly, we could also detect EGFP in nasal retinal axons innervating the posterior half of the optic tectum in the midbrain (**Figure 4.4G, G'**), indicating that *hmx1-En2* is effective in driving selective expression in nasal RGCs at late stages of retinotectal development.

***Hmx1:cre*-mediated recombination of an *RGC:colorswitch* reporter enables the visualization of the antero-posterior retinotopic map in vivo**

Since the entire nasal retina and several brain structures beside the optic tectum were labeled in Tg[*hmx1-En2:EGFPCAAX*] transgenic larvae, we next sought to generate a stable transgenic line that would allow the direct visualization of the antero-posterior retinotectal map in vivo. The *Cre/loxP* system has been employed extensively in zebrafish for conditional expression and lineage tracing analyses using single-insertion loxP cassettes generated through Tol2-mediated transgenesis [380-382]. We thus took advantage of that system to restrict transgene expression to nasal or temporal RGCs only. We generated a Tg[*hmx1-En2:cre*] stable transgenic line that expresses *cre* in the nasal retina, and a Tg[*isl2b:loxP-TagRFPCAAX-loxP-EGFPCAAX*] stable reporter line that expresses a switch transgene in RGCs (hereafter referred to as Tg[*RGC:colorswitch*]). To ensure that the *RGC:colorswitch* reporter transgene has integrated in an optimal genomic location for Cre-dependent recombination and to eliminate any functional positional effect, we established three independent Tg[*RGC:colorswitch*] stable transgenic lines and tested their responsiveness to Cre by crossing them to Tg[*hsp70l:cre*] transgenic fish (data not shown). We selected the Tg[*RGC:colorswitch*] reporter line whose progeny showed complete change of fluorescence in all RGCs following heat shock at 24 hpf (data not shown). We then crossed that line to generate a Tg[*hmx1-En2:Cre;*

RGC:colorswitch] double transgenic line, and analyzed double transgenic embryos by immunolabeling for EGFP and TagRFP at 4 dpf (**Figure 4.5**).

High resolution confocal imaging and 3D-rendering of double transgenic embryos revealed a bi-colored retinotectal map along the antero-posterior axis (**Figure 4.5**). We found that embryos had a bi-colored RGC layer in the retina, with nasal and temporal RGCs expressing EGFP and TagRFP, respectively (**Figure 4.5A, D-D"**). We confirmed by ISH that *tagRFP* was specifically expressed by temporal and not nasal RGCs at 4 dpf (**Figure 4.5D'''**). We then analyzed the projection domains of nasal and temporal retinal axons at the tectum. After elongating together along both branches of the optic tract (**Figure 4.5C**), TagRFP-positive temporal retinal axons terminated in the anterior half of the tectum (**Figure 4.5B", C'**) while GFP-positive nasal axons projected through the anterior tectum to reach the posterior tectum (**Figure 4.5B''', C"**). The sharp boundary between the nasal and temporal projection domains appeared to split the tectal neuropil into two equivalent halves (**Figure 4.5B'''**). Thus, our observations indicate that *hmx1:cre*-mediated recombination can be used to drive selective transgene expression in nasal vs temporal RGCs. Our results also establish the Tg[*hmx1-En2:Cre; RGC:colorswitch*] transgenic line as the first genetic model allowing the direct visualization of retinotopic mapping in vivo throughout development.

The antero-posterior retinotopic map is established at early developmental stages

We next analyzed retinotopic mapping in living larvae from 3 to 6 dpf (**Figure 4.6**). Like larvae fixed and immunolabeled at 4 dpf, living larvae had a bi-colored antero-posterior retinotectal map at all stages analyzed. To analyze retinotectal map development in a reproducible and unbiased manner, we established a consistent imaging

and quantification method across embryos (**Figure 4.7**). Confocal stacks of the retinotectal system taken from a dorsal view were consistently rotated along the x, y, and z axes to orient all embryos in a similar and comparable manner (**Figure 4.6A, A'; Figure 4.7).** We then used maximal projections of rotated stacks to delineate several landmarks at the tectum and analyze the projection domains of nasal and temporal retinal axons (**Figure 4.6A"**). We used binarized maximal projections of TagRFP stacks to define the anterior-most boundary of the tectal neuropil (hereafter referred to as anterior tectal boundary) and the caudal boundary of the TagRFP-positive projection domain that we named "TagRFP Boundary". We measured the distance (l) between the anterior tectal and TagRFP boundaries to determine the length of the TagRFP projection domain along the antero-posterior axis (**Figure 4.7B-B"**). We used binarized maximal projections of EGFP stacks to set the posterior-most boundary of the tectal neuropil, and measured the total length of the tectum (L) as the distance between the anterior and posterior tectal boundaries. We also defined the Equator (E) as ½L, and used it to delineate the anterior (rostral to E) and posterior (caudal to E) halves of the tectum (**Figure 4.7B-B"**).

At 3 dpf, when the retinotectal map can first be visualized in fixed embryos [25, 33], we found that EGFP-positive nasal retinal axons had already elongated through the anterior half of the tectum to innervate the posterior half (**Figure 4.6B**). Some nasal axons also seemed to arborize in the anterior tectal half, just rostral to the Equator. On the other hand, TagRFP-positive temporal retinal axons projected specifically to the anterior tectum and were not observed in the posterior half (**Figure 4.6B'**). The TagRFP Boundary was rostral to the Equator at that stage (**Figure 4.6B', B"**). From 4 to 6 dpf, the projection domain of TagRFP-positive temporal axons expanded within the anterior half

of the tectum, thereby pushing the TagRFP Boundary towards the Equator (**Figure 4.6C'-E"**). Conversely, the projection domain of EGFP-positive nasal axons appeared denser and progressively more restricted to the posterior half of the tectum (**Figure 4.6C-E**). To better analyze the dynamics of retinotopic map formation, we quantified the tectal area covered by nasal and temporal axons over time (**Figure 4.6F-I, Figure 4.7B-B"**). Overall, the total tectal coverage (area of the tectum covered by nasal and temporal axons) significantly increased from 8,578.89 ± 202.23 μm^2 at 3 dpf to 14,287.80 ± 243.06 μm^2 at 6 dpf ($p < 0.001$), indicating a continuous growth and innervation of the tectum as development proceeds (**Figure 4.6F**). The area covered by TagRFP-positive temporal axons in the anterior half of tectum also steadily and significantly increased from 3,989.22 ± 99.55 μm^2 at 3 dpf to 7,824.67 ± 130.46 μm^2 at 6 dpf ($p < 0.001$) (**Figure 4.6G**), suggesting that the increasing innervation by temporal axons greatly contributes to the tectum growth. We further quantified the expansion of the area covered by temporal axons by measuring the position of the TagRFP Boundary in relation to the Equator (**Figure 4.6J**). The Equatorial Alignment Index corresponding to the ratio of the TagRFP coverage length (l) to the Equatorial length (E) gradually increased from 79.54 ± 1.0% at 3 dpf to 94.89 ± 1.2% at 5 dpf ($p < 0.001$). It eventually reached 100 ± 0.9% at 6 dpf, indicating that the TagRFP boundary progressively shifts posteriorly until its position matches that of the Equator. Finally, the area covered by EGFP-positive nasal axons in the posterior half of tectum also steadily and significantly increased from 4,589.66 ± 135.87 μm^2 at 3 dpf to 6,381.07 ± 134.64 μm^2 at 5 dpf ($p < 0.001$), but then remained stable from 5 to 6 dpf (**Figure 4.6H**). Thus, our results demonstrate that the antero-posterior retinotopic map is formed early on during development but remains

dynamic, with the projection domains of both nasal and temporal axons expanding over time.

Nasal retinal projections refine over time and generate a more precise map

In contrast to temporal axons that reach the anterior tectum immediately, nasal retinal axons must navigate through the anterior half of the tectum to reach their correct target in the posterior half. Interestingly, we noticed that some nasal axons seemed to arborize in the anterior tectal half just rostral to the Equator at 3 and 4 dpf (**Figure 4.6B, C**). However, these arborizations were not as clearly observed at 5 dpf, as shown by the apparent decrease in EGFP fluorescence intensity between 4 and 5 dpf (arrows in **Figure 4.6C, D**). We analyzed in more detail the tectal coverage of EGFP-positive nasal axons in the anterior half of the tectum. Strikingly, the area covered by nasal axons in the anterior tectum significantly decreased between 3 and 4 dpf (from 3,668.46 ± 119.45 μm^2 to 3,175.32 ± 146.91 μm^2, $p < 0.001$) and between 4 and 5 dpf (from 3,175.32 ± 146.91 μm^2 to 2,840.33 ± 108.94 μm^2, $p < 0.001$), but remained stable between 5 and 6 dpf (**Figure 4.6I**). While the values obtained at 6 dpf likely represent fluorescence from the nasal axonal bundles that have extended through the anterior tectum, the significant decreased in tectal coverage observed from 4 to 5 dpf suggests that nasal retinal projections in the anterior tectal half might refine during that time period. We thus calculated a Nasal Axon Mistargeting Index as the ratio between the anterior and posterior tectal areas covered by EGFP-positive nasal axons (**Figure 4.6K**). That index significantly decreased between 3 to 4 dpf (from 80.34 ± 1.93% to 56.76 ± 2.58%, $p < 0.001$) and between 4 to 5 dpf (from 56.76 ± 2.58% to 44.76 ± 1.72%, $p < 0.001$), but remained stable between 5 and 6 dpf (46.93 ± 1.83%). We also established a Refinement

Index corresponding to the change in the Nasal Axon Mistargeting Index between two consecutive days (**Figure 4.6L**). The Refinement Index was superior to one between 3 and 4 dpf and 4 and 5 dpf (1.48 ± 0.07 and 1.27 ± 0.03, respectively), indicating a refinement of nasal retinal projections between these stages. In contrast, it averaged a value of 1 between 5 and 6 dpf (0.97 ± 0.04), indicating that no change or refinement occurred during that time period. Thus, our results indicate that nasal retinal axons refine and condense their projection domain to the posterior tectum from 3 to 5 dpf.

To determine the effect of that refinement on the retinotopic map, we decided to analyze the sharpness of the map at 4 and 5 dpf. We used sum projections of rotated stacks to measure the mean fluorescence intensity of EGFP and TagRFP in bins of equal height distributed along the antero-posterior axis of the tectum (**Figure 4.7C-C"**). Interestingly, the mean EGFP intensity significantly decreased between 4 and 5 dpf in bins 3 and 4 in the anterior tectal half while it significantly increased in bins 6-9 in the posterior tectum (**Figure 4.6M**). We further analyzed the sharpness of the EGFP-TagRFP boundary by normalizing fluorescence intensities to their maximum values at 4 and 5 dpf, and plotting them along the antero-posterior axis of the tectum (**Figure 4.6N, O**). We then determined the distance from the anterior tectal boundary at which EGFP and TagRFP intensities reached 50% of their maximal value (dashed lines in **Figure 4.6N, O**). Interestingly, $EGFP_{50\%}$ shifted from an averaged position of 40.73 ± 13.16 µm at 4 dpf (anterior region of Bin 3) to 53.45 ± 9.92 µm (Bin 4) at 5 dpf. In contrast, $TagRFP_{50\%}$ kept a similar location between Bins 4 and 5 from 4 to 5 dpf (54.76 ± 5.22 µm and 59.76 ± 5.15 µm, respectively). We next calculated a Sharpness Index corresponding to the absolute value of the distance between $EGFP_{50\%}$ and

$TagRFP_{50\%}$ (double arrows in **Figure 4.6N and O**). That index significantly decreased between 4 and 5 dpf (from 16.56 ± 1.95 μm to 9.63 ± 1.30 μm, $p < 0.001$) (**Figure 4.6P**), demonstrating that the boundary between nasal and temporal projection domains sharpens during that interval. Thus, our results demonstrate for the first time that the zebrafish retinotectal map sharpens and becomes more precise as nasal retinal projections refine and disappear from the anterior tectum.

Maco mutants have retinotopic mapping and refinement defects

Previous studies have demonstrated a role for neural activity in regulating retinal axon arbor size and dynamics [93, 95, 107, 111, 113, 120]. We thus decided to test whether neural activity was required for the refinement of nasal axons in the anterior tectum by analyzing the retinotopic map of *macho* (*maco*) mutants at 4 and 5 dpf [29, 35, 346]. *Maco* mutants harbor a mutation in the *pigk* gene that encodes a glycosylphosphatidylinositol (GPI)-anchor transamidase involved in GPI anchor synthesis and attachment to nascent proteins [383, 384]. That mutation also causes a down-regulation of voltage-gated sodium channels leading to a lack of neural activity in peripheral sensory neurons and RGCs [107, 352, 385]. Both *maco* mutants and their wild-type (WT) siblings had a bi-colored antero-posterior retinotectal map at 4 and 5 dpf (**Figure 4.8A-D"**), with EGFP-positive nasal axons innervating the posterior tectal half (**Figure 4.8A-D**) and TagRFP-positive temporal axons, the anterior half (**Figure 4.8A'-D'**). However, we noticed differences in the anterior tectal coverage of nasal axons between WT and mutants. While nasal retinal projections seemed to disappear from the anterior tectum at 5 dpf in WT, they did not in *maco* mutants (**Figure 4.8C, D**). We quantified the tectal coverage of nasal and temporal axons at 4 and 5 dpf. While *maco* had a

significantly smaller tectal neuropil than their WT siblings, the total tectal coverage significantly increased in both mutants and WT (**Figure 4.8E**). The area covered by EGFP-positive nasal axons in the posterior half of the tectum also significantly increased between 4 and 5 dpf in both *maco* and WT, although it was overall smaller in *maco* mutants (**Figure 4.8G**). In contrast, the area covered by nasal axons in the anterior half of the tectum significantly decreased from 4 to 5 dpf in WT but remained constant in *maco* mutants (**Figure 4.8H**). The Nasal Axon Mistargeting Index similarly decreased in WT (from 0.60 ± 0.02 at 4 dpf to 0.48 ± 0.02 at 5 dpf) but not in *maco* (0.60 ± 0.03 at both 4 and 5 dpf) (**Figure 4.8J**), demonstrating that the refinement of nasal projections does not occur in *maco* (**Figure 4.8H**). Lack of refinement was further confirmed by the Refinement Index that averaged 1 in *maco* (**Figure 4.8K**). Since we have shown that the refinement of nasal projections correlates with a sharpening of the retinotopic map (**Figure 4.6**), we next examined how the refinement defects observed in *maco* mutants might affect topographic mapping. Analysis of the EGFP-TagRFP boundary sharpness at 4 and 5 dpf revealed that the distance between $EGFP_{50\%}$ and $TagRFP_{50\%}$ did not change in *maco* mutants (**Figure 4.9**). The Sharpness Index even slightly increased in *maco* (from 20.11 ± 1.97 μm at 4 dpf to 21.85 ± 2.05 μm at 5 dpf) instead of decreasing like in WT siblings (from 19.01 ± 1.75 μm to 15.13 ± 2.04 μm, $p < 0.05$) (**Figure 4.8L**). Thus, our results demonstrate that the lack of refinement of nasal retinal projections in *maco* prevents the sharpening of the retinotopic map over time.

In addition to the refinement defects affecting nasal axons, we unexpectedly observed subtle defects in the TagRFP-positive temporal projections in *maco*. We noticed that temporal axons arborized in a larger area in *maco* mutants than in WT siblings and

expanded their area of coverage beyond the Equator (**Figure 4.8A'-D'**). We calculated a Temporal Arborization Field index as the ratio of the TagRFP area of coverage to the total tectal area, and found that it was indeed significantly higher at 4 and 5 dpf in *maco* compared to WT siblings (58.15 ± 0.77% vs 52.57 ± 0.51% at 4 dpf, and 58.80 ± 0.62% vs 53.44 ± 0.5% at 5 dpf) (**Figure 4.8F**). Moreover, the Equatorial Alignment Index exceeded 1 in *maco* at both 4 and 5 dpf (1.05 ± 0.2 and 1.09 ± 0.02, respectively) while remaining inferior to 1 in WT siblings at both stages (0.93 ± 0.01 and 0.94 ± 0.01, respectively) (**Figure 4.8I**). Our analysis thus revealed a slightly expanded mapping of temporal retinal axons in *maco* mutants. We could not observed any retinal patterning defects in *maco* (**Figure 4.10**), suggesting that this topographic mapping defect results from local guidance errors at the tectum.

Blocking neural activity in RGCs prevents the refinement of nasal retinal projections

The *pigk* mutation in *maco* not only affects other neurons besides RGCs but also likely prevents receptors other than voltage-gated sodium channels from being targeted to the plasma membrane. We thus decided to express the inward-rectifying potassium channel Kir2.1 (or a non-conducting form of Kir2.1, KirMUT, as a control) selectively in RGCs to test whether neuronal activity was required cell-autonomously for refining nasal retinal projections in the anterior tectum. We injected a *UAS:Kir2.1-2A-mKate2CAAX* or a *UAS:KirMUT-2A-mKate2CAAX* transgene in zygotes from an [*isl2b:gal4*] outcross, and analyzed whether transient expression of Kir2.1 blocked RGC activity by conducting a visually-mediated background adaptation (VBA) assay at 5 dpf (**Figure 4.12**) [386]. The VBA is a physiological response dependent on RGC function during which zebrafish

larvae adapt to changing levels of light by adjusting the distribution of melanin pigments (also known as melanosomes) in their skin [284]. During normal VBA, melanosomes aggregate in response to bright illumination, giving larvae a pale appearance. We found that larvae expressing Kir2.1 in RGCs (thereafter referred to as Kir2.1 embryos) demonstrated two levels of dark, expanded pigmentation despite bright illumination (**Figure 4.12**). Some Kir2.1 embryos retained dispersed melanosomes (embryos with "large melanophores") in response to light, indicating a lack of VBA, while others had more restricted but yet abnormally expanded melanin ("smaller melanophores"), indicating a reduced VBA. In contrast, embryos expressing KirMut and uninjected embryos showed fully aggregated melanosomes in response to bright illumination (**Figure 4.12**). We quantified the area covered by pigmented melanophores in these four groups and found that it was significantly larger in Kir2.1 embryos than in KirMUT or uninjected embryos (**Figure 4.12**). Transient expression of Kir2.1 in RGCs is thus sufficient to block neuronal activity in RGCs.

We then tested whether blocking RGC activity was sufficient to prevent the refinement of nasal retinal projections in the anterior tectal half. We selected embryos with high mKate2CAAX expression for our analysis (see Material and Methods for the definition of high mKate2 expression), and ensured by Western blot that high mKate2 expression correlated with high expression of Kir2.1 blocking RGC neural activity (**Figure 4.12**). As reported previously [108], blocking neuronal activity in RGCs did not prevent the overall formation of the retinotectal map (**Figure 4.13**). The total tectal area covered by retinal axons significantly increased between 4 and 5 dpf in Kir2.1, KirMUT and uninjected embryos, with no significant difference between groups at either time

point (**Figure 4.11A**). Similarly, no difference could be observed in the Temporal Arborization Field index (**Figure 4.11B**) or the Equatorial Alignment Index (**Figure 4.11C**). The area covered by EGFP-positive nasal axons in the posterior half of the tectum significantly increased between 4 and 5 dpf in all groups (**Figure 4.11D**). In contrast, the area covered by nasal axons in the anterior half of the tectum significantly increased from 4 to 5 dpf in Kir2.1 embryos (from 2,818.35 ± 130.98 μm^2 to 3,140.43 ± 154.2 μm^2, $p < 0.05$), while it decreased (from 2,933.79 ± 101.46 μm^2 to 2,663.95 ± 89.66 μm^2, $p < 0.05$) in uninjected embryos and tended to diminish (from 3,110.74 ± 133.37 μm^2 to 2,950.5 ± 101.25 μm^2) in KirMUT embryos. Consequently, the Nasal Axon Mistargeting Index remained constant in Kir2.1 embryos (from 0.61 ± 0.04 to 0.58 ± 0.03) instead of decreasing like in KirMut (from 0.63 ± 0.02 to 0.51 ± 0.02) and uninjected (from 0.53 ± 0.01 to 0.43 ± 0.05) control embryos (**Figure 4.11F**). Kir2.1 embryos had a Refinement Index averaging 1 (1.06 ± 0.03), demonstrating that their nasal projections did not refine in the anterior tectum between 4 and 5 dpf (**Figure 4.11G**). In contrast, KirMut and uninjected embryos had a Refinement Index of 1.24 ± 0.04 and 1.26 ± 0.04, respectively, indicating that refinement occurred during that time period. We finally examined the precision of the retinotopic map in Kir2.1, KirMUT and uninjected embryos (**Figure 4.13**). While the Sharpness Index significantly decreased between 4 and 5 dpf in KirMUT (from 26.14 ± 1.72 to 17.82 ± 1.36 µm, $p < 0.01$) and uninjected (from 18.21 ± 1.36 µm to 11.64 ± 1.44 µm, $p < 0.05$) embryos, it remained stable (from 23.76 ± 3.31 µm to 20.19 ± 2.23 µm) in Kir2.1 embryos (**Figure 4.11H**). Thus, our results demonstrate that selectively blocking neural activity in RGCs prevents

the refinement of nasal retinal projections and the sharpening of the retinotopic map during development.

4.5 Discussion

Our understanding of topographic map development and maintenance has so far been limited by a lack of genetic models allowing the direct observation of maps over time. Here, we report the generation of a novel zebrafish transgenic line that, for the first time, allows for the unbiased and quantitative analysis of retinotopic map formation and refinement directly in vivo. Using live confocal imaging of transgenic larvae from 3 to 6 dpf, we show that the antero-posterior retinotopic map is formed at early developmental stages but remains dynamic as both retina and tectum grow, with the projection domains of nasal and temporal axons expanding over time. We further demonstrate that nasal retinal projections initially arborize in the anterior half of the tectum but progressively refine and condense their projection domain to the posterior tectum in an activity-dependent manner from 4 to 5 dpf. We finally show that the refinement of nasal retinal projections mediates the sharpening of the antero-posterior retinotopic map, and that both are prevented by blocking neuronal activity in RGCs.

In agreement with previous studies in zebrafish and other species [56, 360, 364, 368, 387-389], our data reveal that the homeobox transcription factors *hmx1* and *hmx4* are expressed in a sharp nasal-high to temporal-low gradient in the retina throughout development (**Figure 4.1, 4.2**). The detection of *hmx1* and *hmx4* throughout the nasal retinal neuroepithelium at early stages indicates that both genes are expressed in proliferating neuroblasts and might regulate their positional identity and differentiation. Supporting that hypothesis, reduced *hmx1* expression has been shown to block retinal cell

differentiation in zebrafish [360, 387] and cause microphthalmia in mouse [390] and human [387, 391, 392]. Although zebrafish embryos injected with *hmx1* morpholino oligonucleotides do not exhibit any eye patterning defect [360], misexpression of *hmx1* or *hmx4* does alter the regional specification of the retina along the nasal-temporal axis in chick [56, 363], suggesting that *hmx1* and *hmx4* have redundant functions in teleosts. Interestingly, our analysis shows that the expression of both *hmx1* and *hmx4* becomes restricted to the nasal RGC and inner nuclear layers at later stages. We have also identified a distal regulatory element upstream *hmx1* and *hmx4* genes that drives expression in nasal RGCs at 4 dpf (**Figure 4.4**). Altogether, these data suggest that *hmx1* and *hmx4* are expressed by mature RGCs themselves at late stages of development. In support of that observation, recent studies using single cell profiling of the adult human retina have reported *hmx1* transcripts in RGCs as well as horizontal cells and Muller glia [393-395]. Future studies examining the effects of manipulating *hmx1* expression directly in nasal or temporal RGCs will thus be of great interest to better understand the progression of the oculoauricular syndrome caused by *hmx1* mutations in human [387, 391, 392].

Using *hmx1:cre*-mediated recombination of an *RGC:colorswitch* reporter, we have generated a novel transgenic line that enables the unprecedented visualization of the antero-posterior retinotopic map in vivo. We were able to image and analyze for the first time retinotectal map development within the same embryo over successive days. This unparalleled temporal resolution allowed us to observe dynamic changes in retinotopic mapping that could not be seen previously in fixed embryos (**Figure 4.6**). We found that while the antero-posterior retinotopic map is established early on, it progressively shifts caudally as temporal axons expand their innervation of the anterior tectum. This caudal

shift is accompanied by the progressive refinement of nasal projections that condense their projection domain to the posterior tectum. The consistent expression of *EGFP* and *tagRFP* transgenes in the nasal and temporal retina, respectively, allowed us to analyze in a reproducible manner multiple parameters of retinotopic mapping. Interestingly, these parameters did not show much variability across embryos with the same genetic background, indicating that retinotopic mapping is a robust and highly stereotyped process. That property allowed us to discover subtle phenotypes in mutants that were not detected in previous studies (**Figure 4.8**). We notably observed that temporal retinal axons arborize in a larger area and expand their coverage beyond the neuropil equator in *maco* mutants compared to WT siblings. This subtle mapping defect was not detected in embryos lacking neuronal activity in RGCs, suggesting that it might result from axon misguidance at the tectum. Interestingly, *maco* mutant harbor a mutation in Pigk, a component of the transamidase complex responsible for GPI anchor synthesis and attachment to nascent proteins [383, 384]. Although it remains unknown which GPI-anchored proteins are impaired by Pigk deficiency, ephrin-As are good candidates. Ephrin-As and their receptors EphAs are indeed expressed in counter-gradients across the nasal-temporal axis in the retina and antero-posterior axis in the tectum and SC [47, 48, 50, 51, 57, 76, 77, 396-398]. Ephrin-A2 and ephrin-A5 are notably expressed at high levels in nasal RGCs and posterior tectum, while temporal RGCs express high levels of EphA receptors. Temporal axons are repelled by ephrin-As present in the posterior tectum and project more caudally in the SC of mice lacking different combination of ephrin-As [50, 52, 134]. Temporal axons also invade the target of nasal axons when ephrin-A5 is removed from both the retina and SC but not if ephrin-A5 is only lacking in the SC, indicating that nasal

axons themselves participate in the repulsion of temporal axons from the caudal tectum [63]. A dysregulation of ephrin-A targeting to the plasma membrane at the tectum and/or along nasal axons could thus explain the subtle phenotype we observed in *maco*.

While temporal axons expand their projection domain within the anterior tectum, we found that nasal retinal projections initially covering the caudal part of the anterior tectum refine and progressively condense their domain to the posterior half between 3 and 5 dpf. This refinement is unlikely to be caused by cell death in the retina, as apoptosis in the RGC layer peaks from 1.5 to 3 dpf before sharply decreasing from 4 to 6 dpf [399, 400]. Instead, it is likely driven by the dynamic rearrangement of axonal branching pattern as nasal axons extend caudally and arborize in their final zone in the posterior tectum. In xenopus, nasal axons retract their branches from the anterior tectum after initiating branches in both anterior and posterior tectal halves [91]. While retinal axons in zebrafish were initially thought to elongate along straight trajectories and only arborize after reaching their target area [115], more recent studies using high-resolution time-lapse imaging have revealed a different mode of elongation where axons continuously extend and retract branches, and navigate by selective branch stabilization [113, 114]. Once in their termination area, axonal arbors remain highly dynamic and frequently elongate and retract filopodia and branch tips, with only a small fraction of them being maintained in the mature arbor [93-95, 117, 401, 402]. A retraction of proximal branches or filopodia that have extended in in-appropriate areas coupled with a constant remodeling of arborizing axons might thus redistribute the position of branches and cause arbors to shift caudally, leading to the progressive refinement of nasal projections we observed.

Our results demonstrate that the refinement of nasal projections requires neuronal activity in RGCs, as it does not occur in *maco* mutants lacking voltage-gated sodium channels or in embryos expressing the inward-rectifying potassium channel Kir2.1 in RGCs (**Figures 4.8 and 4.11**). Several studies have highlighted a role for neuronal activity in refining the size and morphology of terminal retinal arbors in the tectum and SC. Application of TTX increases branch dynamics and causes enlarged axonal arbors in xenopus and frog [109, 110]. TTX also prevents the refinement of retinal fibers that overshoot their termination zone in chick [105]. Similarly in the mouse, axons appear more diffuse and occupy a larger area in the SC after RGCs have been silenced by in utero electroporation of Kir2.1 [112]. Studies in zebrafish, however, have not detected any consistent changes in the size or morphology of terminal arbors after globally silencing RGCs. While the projection field of retinal axons appears more diffuse in *maco* mutants and embryos with silenced RGCs [35, 95, 107], the number of terminal branches or their total length does not appear to change at 5, 6 or 7 dpf, even though the formation of transient filopodia is increased [95, 106-108, 111]. What could explain these differences across species? First, the exact timing of analysis might have not allowed for the detection of subtle changes in arbor coverage. Analysis of retinal arbors in relation to their time of arrival at their termination zone has indeed revealed that silenced arbors continue to steadily and slowly expand their coverage after reaching their target instead of expanding and retracting like WT arbors [113]. This continued expansion leads to a significant increase in coverage that was only detectable 14 hours after axons had reached their target. Alternatively, localized changes in a subset of branch tips could lead to a spatial rearrangement of axonal arbors without modifying the average branch number and length. Several studies in xenopus and

the mouse have demonstrated that the pattern of neuronal activity has an instructive role in locally remodeling axonal arbors [93, 120, 126, 131]. Activity is notably required for the elimination of branches whose firing pattern does not match that of their neighbors. An elegant study in xenopus has further demonstrated that the temporal order of retinal axon activity also regulates arbor dynamics and position [122]. Sequentially activating RGCs by a stimulus moving in an anterior-to-posterior (RGC activity propagating from the temporal to nasal retina), but not in a posterior-to anterior direction refines the topographic distribution of retinal axons along the antero-posterior axis. Axons stimulated earlier than convergent arbors (i. e. temporal axons) shift their arbors towards the anterior tectum, while axons stimulated later (i.e. nasal axons) shift their arbors posteriorly. In both cases, arbors modify their position by structurally rearranging their branches, with the spatial distribution of branch retraction dictating the direction of the shift. Nasal arbors that are stimulated after temporal arbors in forward-moving larvae lose branches located rostrally to their center of mass. Interestingly, spontaneous waves of retinal activity that preferentially initiate in the temporal retina and propagate to the anterior SC/OT have been described in both the mouse and zebrafish [103, 104]. These directional waves are present as early as 2.5 dpf in zebrafish, suggesting that they might drive similar structural rearrangements of retinal arbors as those observed in the tadpole.

By promoting structural rearrangements of axonal arbors, spatiotemporal patterns of retinal activity drive the sharpening of visual circuits [123, 125, 127, 129, 132, 136, 403]. Our data similarly show that blocking the refinement of nasal projections prevents the sharpening of the antero-posterior retinotopic map. While a lack of neuronal activity was known to cause less defined projection fields in zebrafish [95, 107], our study provides the first

unbiased and precise quantification of topographic mapping over time in vivo, both in WT and after silencing RGCs. By analyzing the fluorescence intensity of nasal and temporal projection domains along the antero-posterior axis of the tectum, we were able to detect a gradual shift of nasal projections over time (reflected by a slope of fluorescence intensity becoming steeper) that is absent when RGCs were silenced. Overall, our observations and results from other studies suggest that the mechanisms of retinotopic map formation and refinement in teleosts and other species are more similar than previously thought. Retinal projections in mammals and chick eliminate misplaced branches in an activity-dependent manner after initially over-shooting their termination zone. Similarly, in zebrafish, nasal retinal projections initially arborizing in anterior areas refine their projection domains in an activity-dependent manner. While increasing evidence indicate that both competitive and stabilizing interactions between axons play an important role in re-shaping arbors [111, 131, 245, 341], how axons communicate and influence each other for refining their projection domains remains an important question. By enabling the selective manipulation of nasal and temporal RGCs, our new genetic model will provide new strategies for analyzing the molecular mechanisms by which axon-axon interactions contribute to precise retinotopic mapping in vertebrates.

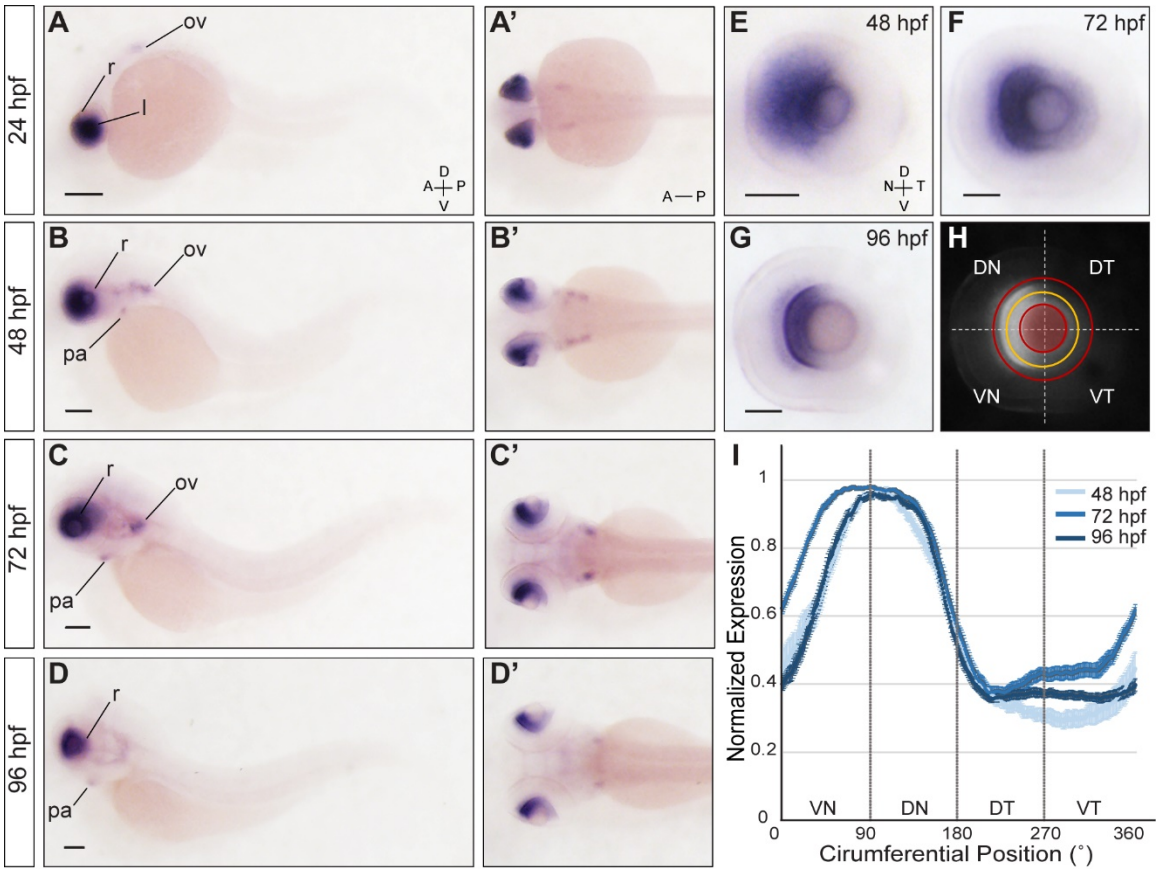

Figure 4.1: *Hmx1* is expressed in the nasal RGC layer throughout development. Lateral (**A-D**) and dorsal (**A'-D'**) views of whole embryos stained for *hmx1* by ISH. (**A, A'**) At 24 hpf, *hmx1* is strongly expressed in the anterior retina (r) and lens (l) and weakly detected in the otic vesicle (ov). (**B, B'**) At 48 hpf, *hmx1* expression remains strongly detected in the anterior retina and is also seen in the otic vesicle and pharyngeal arches (pa). (**C, C'**) *Hmx1* expression remains consistent at 72 hpf. (**D, D'**) By 96 hpf, *hmx1* remains strongly expressed in the anterior retina and is still detected in the otic vesicle, and to a lesser extent, in the pharyngeal arches. (**E-G**) Lateral views of eyes dissected from embryos stained for *hmx1* by ISH. (**E**) At 48 hpf, *hmx1* is specifically detected in the nasal half of the retina. (**F, G**) This regionalized expression becomes restricted to the anterior RGC layer, and to a lesser extent the anterior inner nuclear layer, at 72 and 96 hpf. A similar expression is observed for *hmx4* (**Figure 4.2**). (**H, I**) Quantification of *hmx1* expression in the RGC layer. (**H**) Intensity profiles of *hmx1* expression are measured on inverted grayscale images along a line (yellow) drawn half-way between the lens and the RGC layer periphery (delineated with red lines). (**I**) Quantification of signal intensity along a clockwise 360° trajectory shows that *hmx1* expression is restricted to the anterior RGC layer during retinotectal development. Means ± SEM are shown. Scale bars: 200 µm in A-D'; 50 µm in E-G. (A: Anterior, P: posterior, D: dorsal, V: ventral, N: nasal, T: temporal, VN: ventro-nasal, DN: dorso-nasal, DT: dorso-temporal, VT: ventro-temporal).

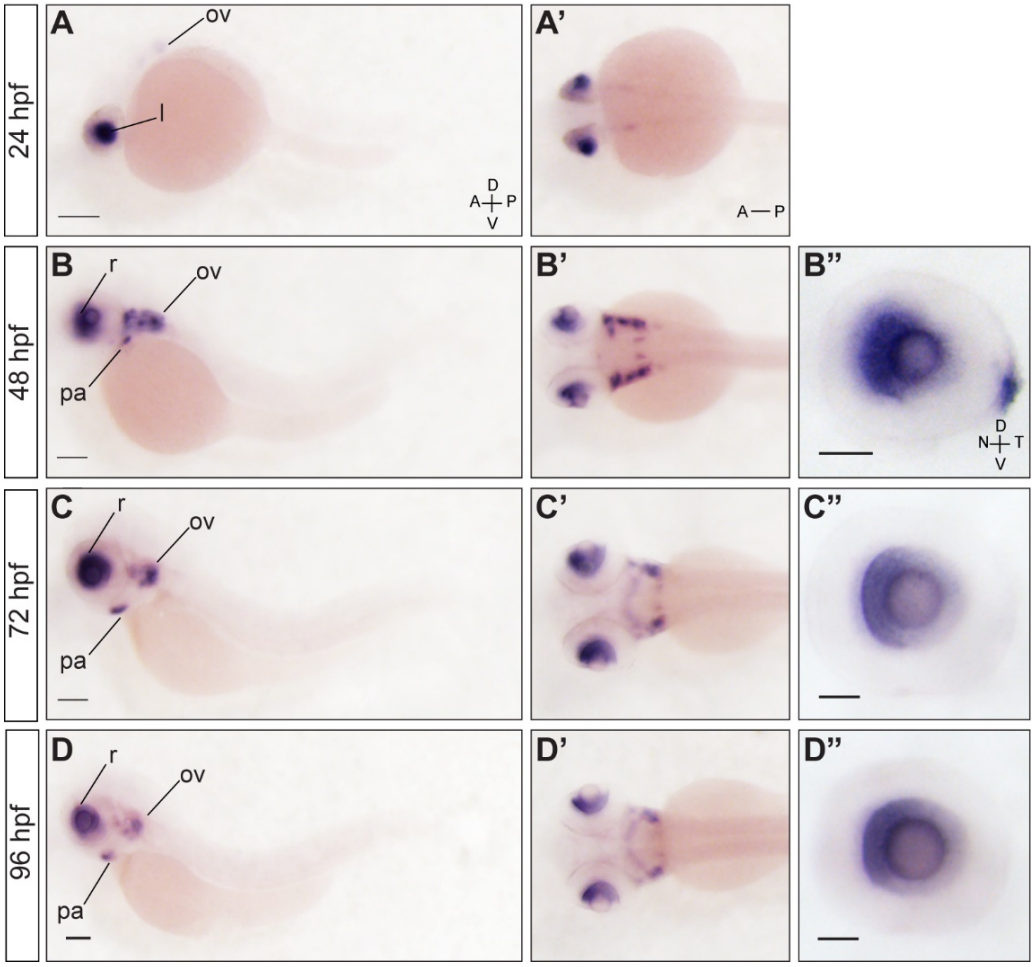

Figure 4.2: *Hmx4* is expressed in a nasal-high to temporal-low gradient in the retina. Lateral (**A-D**) and dorsal (**A'-D'**) views of whole embryos stained for *hmx4* by ISH. (**A, A'**) At 24 hpf, *hmx4* is expressed in the developing lens (l) and is also weakly expressed in the retina (r) and otic vesicle (ov). (**B, B'**) At 48 hpf, *hmx4* expression is strongly detected in the anterior retina, the otic vesicle and pharyngeal arches (pa). (**C, C'**) *Hmx4* expression remains consistent at 72 hpf. (**D, D'**) By 96 hpf, *hmx4* remains strongly expressed in the anterior retina and is still detected in the otic vesicle and pharyngeal arches, although to a lesser extent. (**B"-D"**) Lateral views of eyes dissected from embryos stained for *hmx4* by ISH. *Hmx4* has a high-nasal to low-temporal graded expression in the RGC layer of the retina at 48, 72 and 96 hpf. Scale bar: 200 µm in A-D'; 50 µm in E-F.

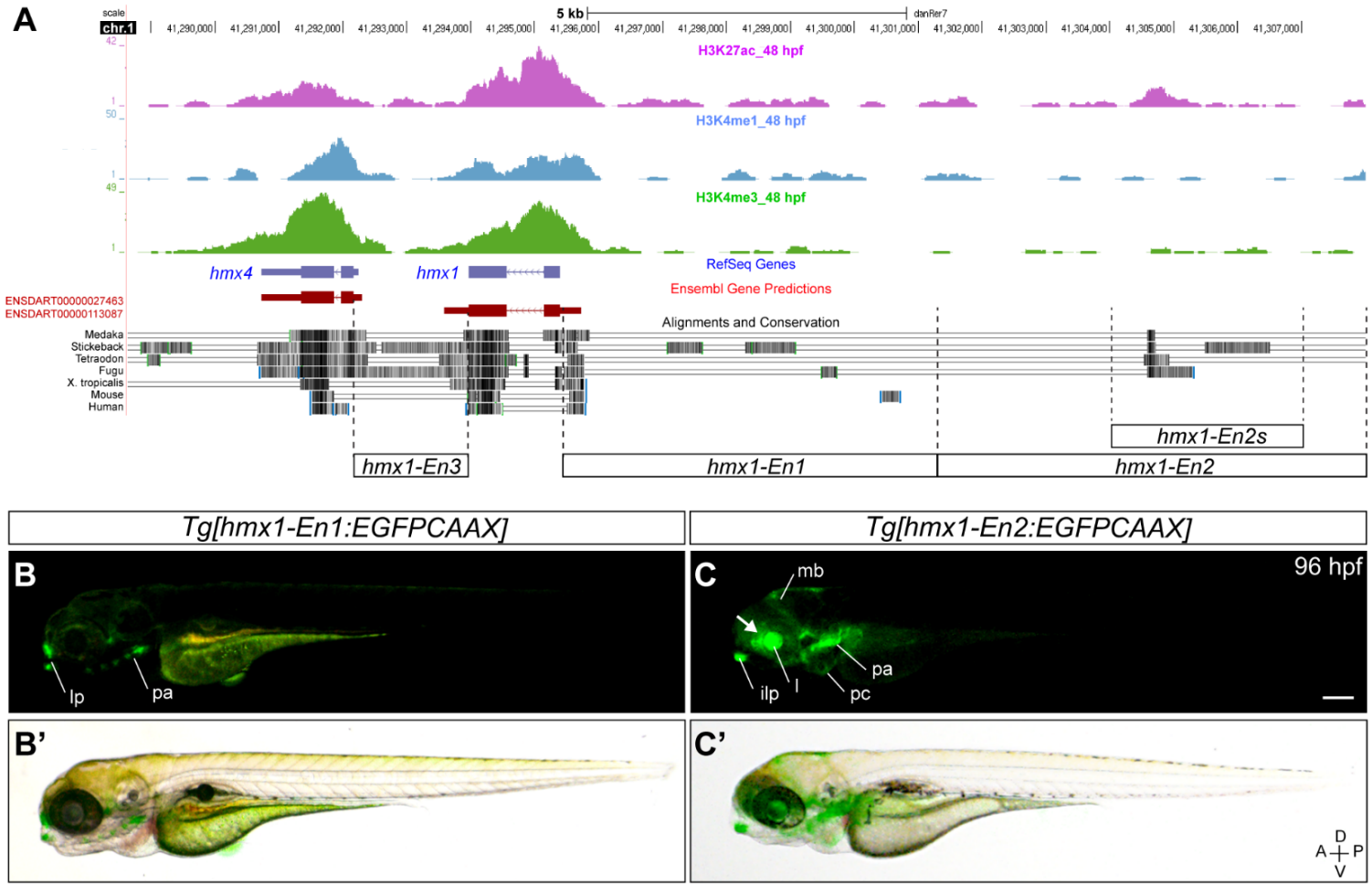

Figure 4.3: *Hmx1* enhancers recapitulate *hmx1* endogenous expression. (**A**) Schematic representation of the *hmx4* and *hmx1* genomic locus on chromosome 1 (Zv9 assembly, UCSC Genome browser) [404]. The distribution of H3K27ac, H3K4me1, and H3K4me3 modifications along 18 kb spanning the *hmx1-hmx4* locus at 48 hpf is shown (tracks from Bogdanovic et al., 2012 [373]). Four putative regulatory regions annotated as *hmx1-En1*, *hmx1-En2*, *hmx1-En2s* and *hmx1-*

Figure 4.3 (Continued): *En3* were tested for enhancer activity in stable transgenic embryos. (**B, B'**) The *hmx1-En1* enhancer drives EGFPCAAX expression in the pharyngeal arches (pa) and the lip (lp) region at 96 hpf. (**C, C'**) The *hmx1-En2* enhancer drives EGFPCAAX expression in the anterior retina (arrow), lens (l), midbrain (mb), pharyngeal arches (pa), inferior lip (ilp) and pericardic (pc) region at 96 hpf. Epifluorescence microscopy, scale bar: 200 μm.

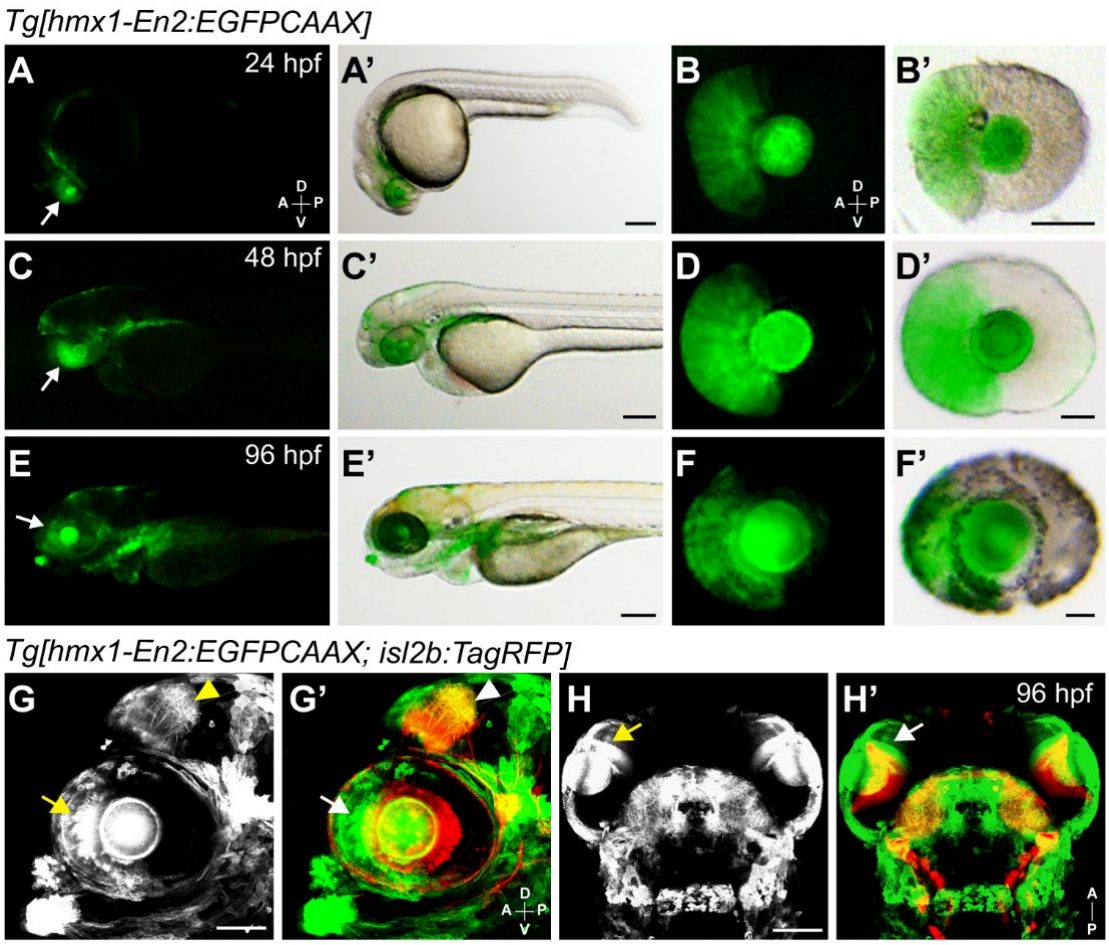

Figure 4.4: The Hmx1-En2 enhancer drives expression in the anterior retina throughout development. (**A-F'**) EGFPCAAX expression in [*hmx1-En2:EGFPCAAX*] transgenic embryos (A,C,E) and dissected eyes (B,D,F) at 24, 48 and 96 hpf. Fluorescence is detected in the anterior half of the retina (arrows) and the lens at all stages. No expression is observed in the posterior retina. Epifluorescence microscopy, scale bar: 200 µm in embryo pictures, 50 µm in eye pictures. (**G-H'**) Lateral (G, G') and dorsal (H, H') views of a double transgenic embryo expressing EGFPCAAX driven by the *hmx1-En2* enhancer and TagRFP driven by the RGC-specific *isl2b* promoter at 96 hpf. EGFPCAAX is observed in nasal RGCs (arrows) and nasal retinal axons projecting to the posterior tectum (arrowheads). Confocal microscopy, scale bar: 100 µm.

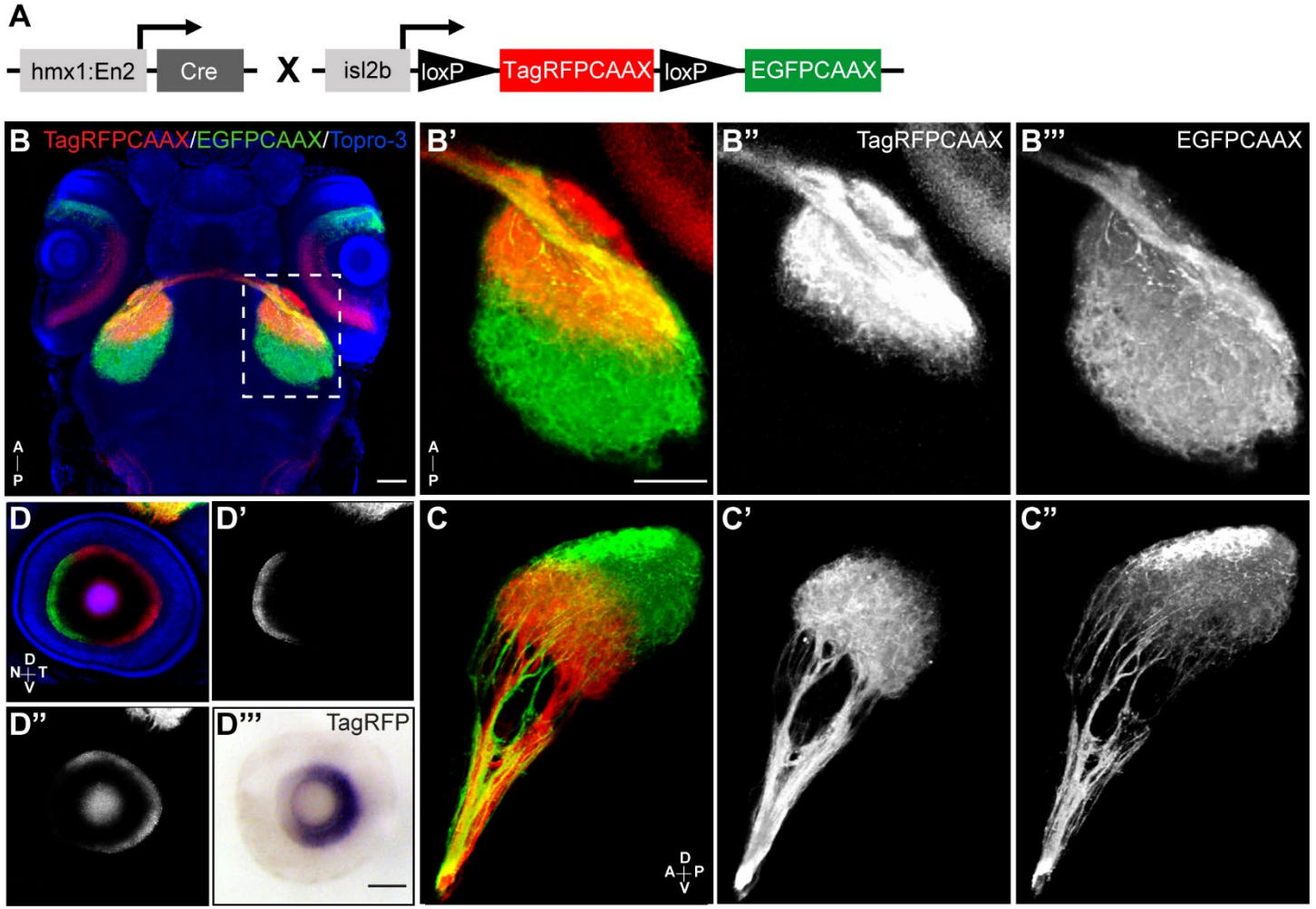

Figure 4.5: *Hmx1:cre*-mediated recombination of an *RGC:colorswitch* reporter enables the visualization of the antero-posterior retinotopic map in vivo. (**A**) Schematic of the *hmx1-En2:cre* transgene and *isl2b:loxP-TagRFPCAAX-loxP-EGFPCAAX* (*RGC:colorswitch*) reporter expressed in double transgenic embryos. (**B**) Dorsal view of a double transgenic embryo immunostained for TagRFP and EGFP at 4 dpf. ToPro-3 was used as

Figure 4.5 (Continued): a nuclear counterstain to delineate the tectal neuropil. Corresponding 3D rendered movie of the antero-posterior retinotopic map is shown in Figure 4 - supplement movie 1. (**B'-B'''**) 3D renderings of the tectum from a dorsal view. (**B"**) TagRFP-positive temporal retinal axons project specifically to the anterior half of the tectum. (**B'''**) EGFP-positive nasal retinal axons project through the anterior tectum to the posterior tectum. (**C-C"**) 3D rendering of the optic tract and tectum from a lateral view. (**C**) Nasal and temporal retinal axons intermingle within the tract but project to distinct tectal areas. (**C'**) TagRFP-positive temporal axons project to the anterior half of the tectum. (**C"**) EGFP-positive nasal axons project to the posterior tectum. (**D-D"**) Eye of a double transgenic embryo immunostained for TagRFP and EGFP at 4 dpf. (**D'**) EGFP-positive RGCs are restricted to the nasal retina. (**D"**) TagRFP-positive RGCs are observed in the temporal half of the retina. (**D'''**) Eye of a double transgenic embryo stained for *tagRFP* by ISH at 4 dpf. *TagRFP* expression remains restricted to the temporal retina. Confocal microscopy (**B-D"**), scale bar: 50 μm.

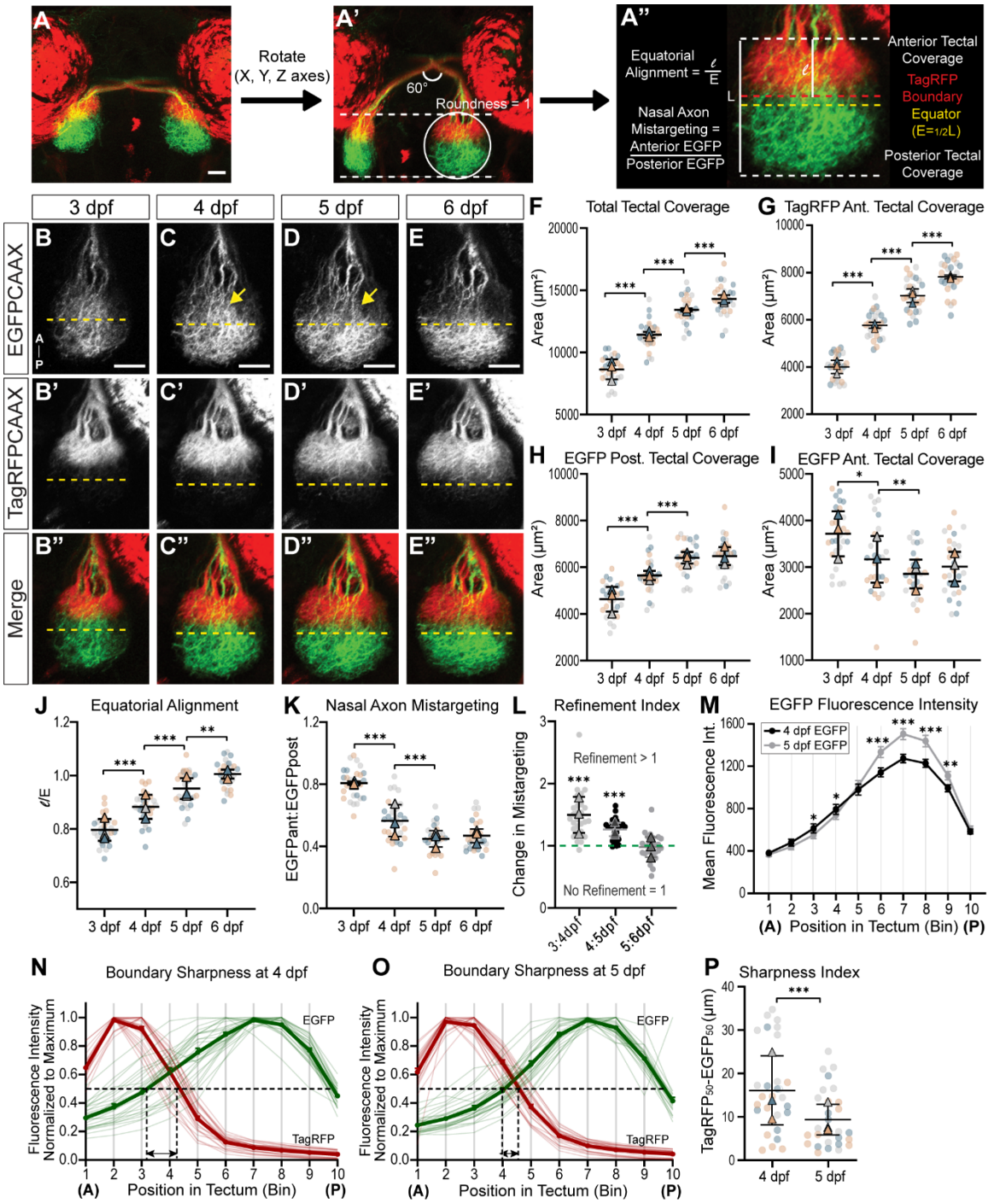

Figure 4.6: Nasal retinal axons refine their tectal projection domain between 4 and 5 dpf. (**A-A"**) Summarized quantification method to analyze retinotopic map development and refinement. A detailed description of quantification method is provided in **Figure 4.7**. (**A-A'**) Z-series were opened in ImageJ and rotated so that both optic tracts intersect at an angle of 60°, and that the tectal roundness was equal to 1. (**A"**) After rotation, TagRFP and EGFP channels were separately maximum projected and thresholded for analysis of area coverage in the tectum. Four boundaries were defined to delineate the anterior and posterior halves of the tectum, with the anterior boundary corresponding to

Figure 4.6 (Continued): the rostral limit of the tectum (line where retinal axons enter the tectum), the posterior boundary corresponding to the caudal end of the tectum, the TagRFP boundary (red dashed line) corresponding to the caudal boundary of the TagRFP signal from temporal axons, and the Equator (E; yellow dashed line) corresponding to ½ of the total tectum length (L) measured from the rostral to the caudal tectal boundary. The tectal area rostral to the Equator was defined as the anterior half of the tectum, the tectal area caudal to the Equator, as the posterior half. (**B-E"**) Development of the antero-posterior retinotopic map from 3 to 6 dpf. (**B-E**) EGFP-positive nasal axons innervate the posterior half of the tectum by progressively refining their targeting domain. Between 4 and 5 dpf, nasal axons mis-targeting to the anterior half of the tectum seem to disappear (arrows). (**B'-E'**) TagRFP-positive temporal axons specifically and precisely target the anterior half of the tectum. (**B"-E"**) The antero-posterior topographic map is established fairly early on and maintained as retinal axons continue to innervate the tectum during development. As the tectum develops, the temporal retinal arborization field expands to fill the anterior half of the tectum, reaching the Equator position (yellow dashed lines) by 6 dpf. Confocal microscopy, scale bar: 50µm. (**F**) The total area of the tectum covered by TagRFP-positive and EGFP-positive axons significantly increases from 3 to 6 dpf. (**G**) The anterior area of the tectum covered by TagRFP temporal axons also steadily increases from 3 dpf and 6 dpf. (**H**) EGFP-positive nasal axons terminating in the posterior half of the tectum cover a significantly larger area between 3 and 4 dpf, and 4 and 5 dpf, before the area of coverage stabilizes between 5 and 6 dpf. (**I**) The anterior tectal area covered by EGFP nasal axons significantly decreases between 4 and 5 dpf, indicating a refinement of the nasal projection domain. (**J**) The Equatorial Alignment Index (l/E) corresponding to the ratio of the TagRFP coverage length (l) to the Equatorial length (E) steadily and significantly increases to a value around 1 from 3 to 6 dpf, indicating that the TagRFP boundary progressively shifts posteriorly until its position matches that of the Equator. (**K**) The Nasal Axon Mistargeting Index, defined as the ratio between the anterior and posterior tectal areas covered by EGFP-positive nasal axons, shows a significant decrease between 3 and 4 dpf as well as 4 and 5 dpf. (**L**) The Refinement Index that corresponds to the change in the Nasal Axon Mistargeting Index between two consecutive days is superior to one between 3 and 4 dpf and 4 and 5 dpf, indicating a refinement of nasal projections between these stages. It averages a value of 1 between 5 and 6 dpf, indicating that no refinement occurs during that time frame. (**M**) The mean fluorescence intensity of EGFP was measured in 10 bins of equal height along the length of the tectum at 4 and 5 dpf (a detailed description of quantification method is provided in **Figure 4.7**). Bins 3 and 4 in the anterior half of the tectum show a significant decrease in signal between 4 and 5 dpf, while bins 6-9 in the posterior half of the tectum display a significant increase. (**N, O**) Normalized fluorescence intensities of EGFP and TagRFP were plotted along the antero-posterior axis of the tectum, and the distance from the anterior tectal boundary at which EGFP and TagRFP intensities reached 50% of their maximal value is marked by dashed lines. The distance between $EGFP_{50\%}$ and $TagRFP_{50\%}$ decreases between 4 and 5 dpf (double arrows), indicating that the boundary between EGFP and TagRFP projection domains becomes sharper over time. (**P**) The Boundary Sharpness Index corresponding to the absolute value of the distance between $EGFP_{50\%}$ and $TagRFP_{50\%}$ (double arrows in N and O) significantly decreases between 4 and 5 dpf. (**F-L, P**) Data represent mean ± SEM. n = 27 embryos. In each graph, three biological replicates representing independent experiments are color-

Figure 4.6 (Continued): coded in grey, teal and orange, respectively. Circle plots represent each data point, and triangle plots represent the averages of each biological replicate [359]. Statistical Analysis: (F-K) repeated measures one-way ANOVA with Tukey's posthoc test; (L) paired t-test compared to a control of 1 (1 representing no change); (M) paired t-test between 4 and 5 dpf within each bin; (P) paired t-test; *$p < 0.05$, ** $p < 0.01$, ***$p < 0.001$.

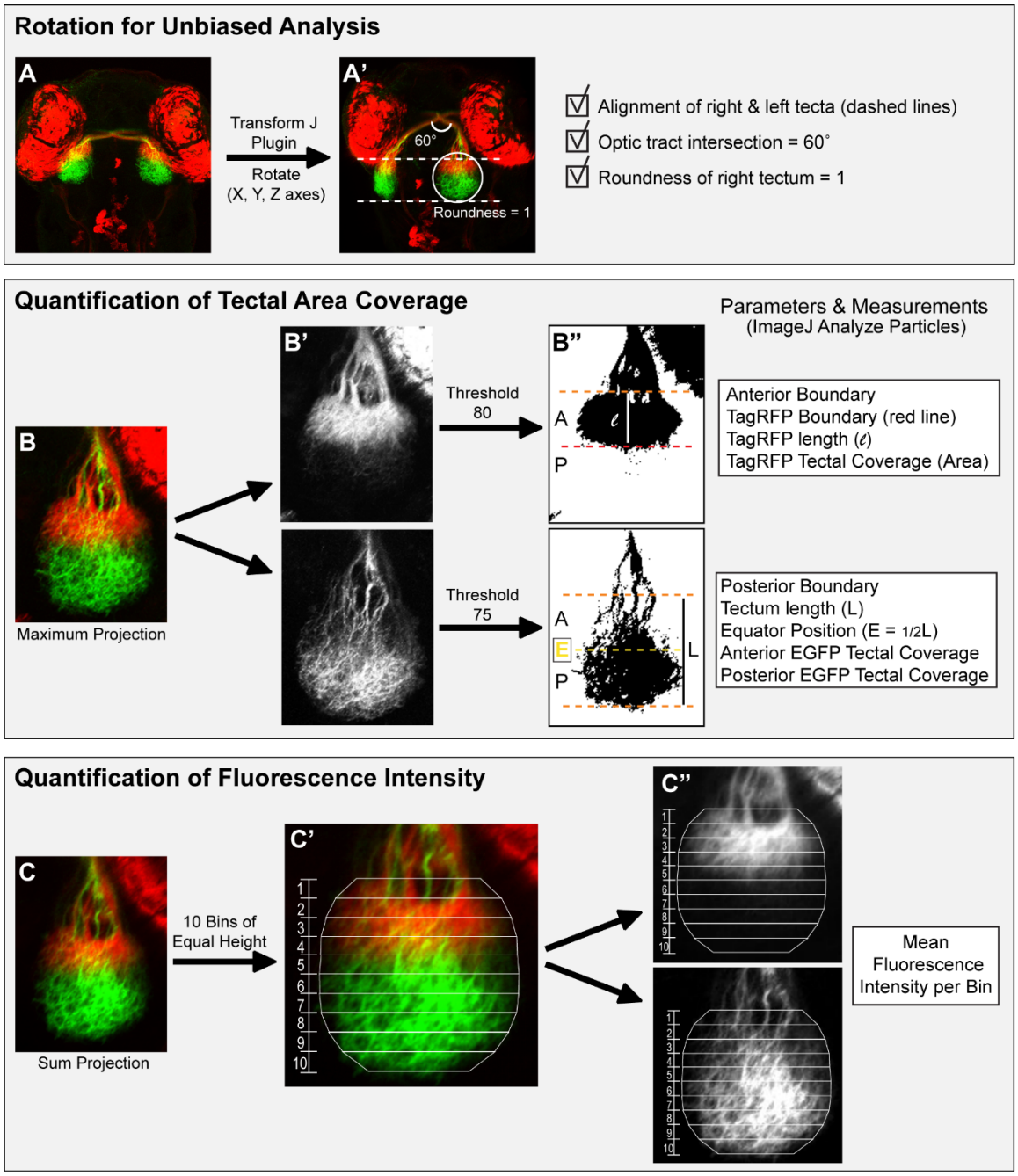

Figure 4.7: Visualization and quantification of antero-posterior retinotopic mapping. (**A, A'**) Confocal stacks taken from a dorsal view were rotated along the X, Y, and Z-axes using the TransformJ plugin in ImageJ to obtain a consistent orientation between embryos. All stacks were rotated so that the left and right tecta were aligned horizontally, both optic tracts intersect at an angle of 60°, and the tectal roundness was equal to 1. (**B-B"**) Quantification of tectal area coverage. (**B, B'**) Rotated stacks were first maximum-projected. (**B"**) TagRFP and EGFP maximal projections were binarized with a threshold of 80 and 75, respectively. The binarized TagRFP maximal projection was used to delineate the anterior tectal boundary, the TagRFP boundary position, and the distance between the anterior tectal and TagRFP boundaries (l). The tectal coverage area of TagRFP-positive

Figure 4.7 (Continued): temporal axons was measured using the Analyze Particles tool in ImageJ. The binarized EGFP maximal projection was used to delineate the posterior tectal boundary. The total tectum length (L) between the anterior and posterior tectal boundaries was measured, and the Equator (E) was set at ½ the total tectum length. The Analyze Particles tool was used to measure the tectal coverage area of the EGFP-positive nasal axons in the anterior (rostral to E) and posterior (caudal to E) halves of the tectum. (**C-C"**) Analysis of fluorescence intensity at the tectum. (**C**) Confocal stacks were sum-projected. (**C'**) The tectum was divided into 10 bins of equal height using the polygon selection tool, with Bin1 being the anterior-most bin and Bin10 being the posterior-most bin. (**C"**) The mean fluorescence intensity of TagRFP and EGFP signals was measured within each bin using ImageJ.

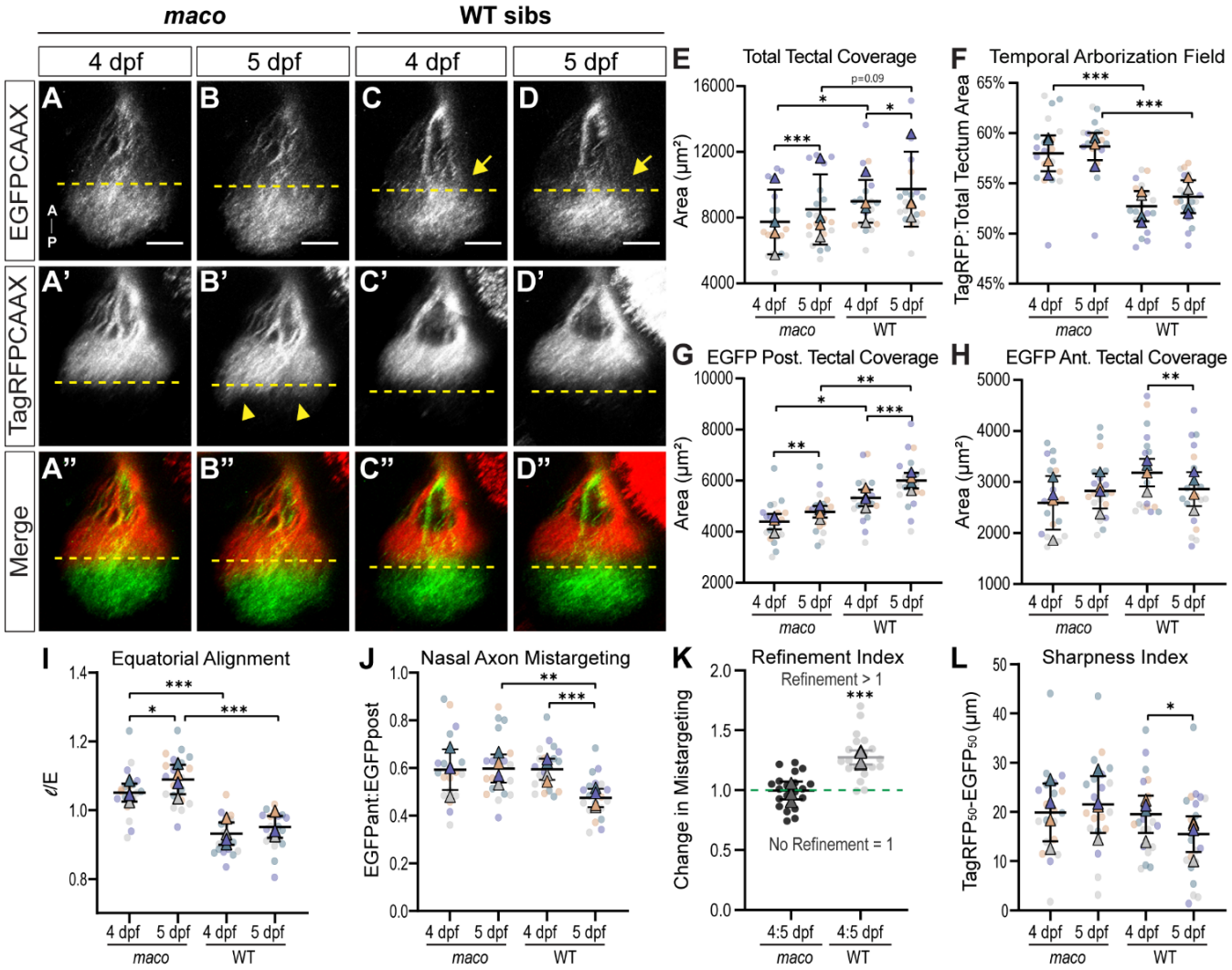

Figure 4.8: *Maco* mutants have retinotopic mapping and refinement defects. (**A-D"**) Development of the antero-posterior retinotopic map in *maco* mutants (A-B") and WT siblings (C-D") from 4 to 5 dpf.

Figure 4.8 (Continued): (**A-D**) EGFP-positive nasal axons innervate the posterior half of the tectum in both *maco* and WT. The anterior tectal area covered by nasal retinal axons does not seem to change between 4 and 5 dpf in *maco* while it appears to decrease in WT siblings (arrows). (**A'-D'**) TagRFP-positive temporal axons specifically target the anterior half of the tectum in *maco* and WT siblings, but their projection domain expands caudally beyond the Equator (dashed line) in *maco* (arrowheads). Confocal microscopy, scale bar: 50µm. (**E**) Although *maco* have a significantly smaller tectum than WT at 4 and 5 dpf, the total area of the tectum covered by nasal and temporal axons significantly increases in both *maco* and WT between 4 and 5 dpf. (**F**) The Temporal Arborization Field index, defined as the ratio of the TagRFP area of coverage to the total tectal area, is significantly higher at 4 dpf and 5 dpf in *maco* compared to their WT sibling, indicating an expanded mapping of temporal retinal axons in *maco* mutants. (**G**) The area covered by EGFP-positive nasal axons in the posterior half of the tectum significantly increases from 4 to 5 dpf in both *maco* and WT. *Maco* have however a significantly smaller area of coverage in the posterior half of the tectum than WT at both stages. (**H**) The area covered by nasal axons in the anterior half of the tectum significantly decreases between 4 and 5 dpf in WT but not in *maco,* indicating an absence of refinement of the nasal projections in the mutant. (**I**) The Equatorial Alignment Index is greater than 1 at both 4 and 5 dpf in *maco,* indicating that the TagRFP boundary extends beyond the Equator in *maco* mutants. (**K**) The Nasal Axon Mistargeting Index decreases in WT but not in *maco* between 4 and 5 dpf, indicating a lack of refinement of the nasal projections in the mutant. (**L**) While the Refinement Index between 4 and 5 dpf is superior to 1 in WT, it averages 1 in *maco,* confirming the absence of refinement of the nasal projection domain in the mutant. (**M**) The Boundary Sharpness Index significantly decreases in WT but remains constant in *maco,* indicating that the boundary between EGFP and TagRFP projection domains does not refine over time in the mutant. Graphs representing the boundary sharpness at 4 and 5 dpf in maco are provided in **Figure 4.9**. (**E-L**) Data represent mean ± SEM. n = 20 embryos per genotype. Four biological replicates representing independent experiments are color-coded in grey, teal, purple and orange, respectively. Statistical Analysis: (E-J, L) mixed-effects one-way ANOVA with Tukey's posthoc test; (K) paired t-test compared to a control of 1 (1 representing no change); *$p < 0.05$, ** $p < 0.01$, ***$p < 0.001$.

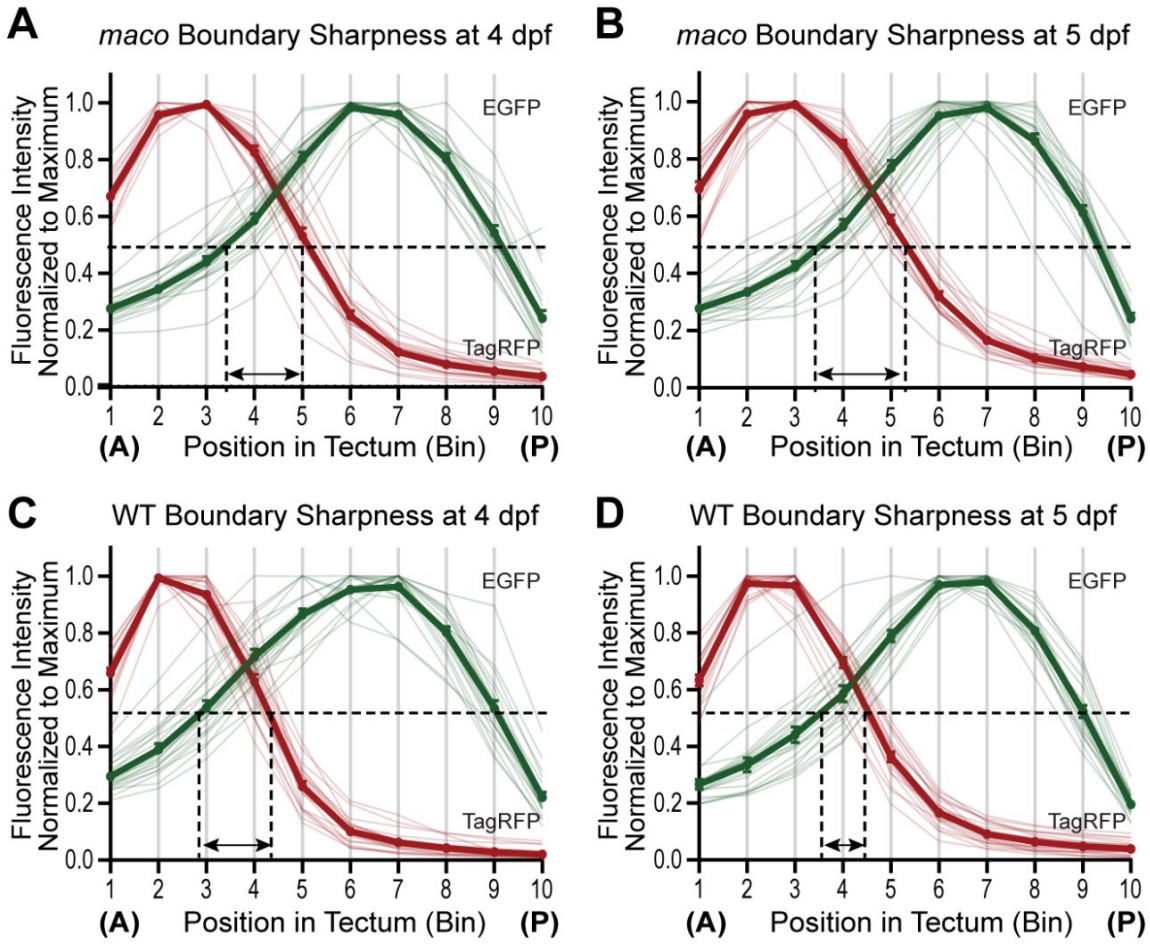

Figure 4.9: The antero-posterior retinotopic map does not sharpen over time in *maco* mutants. (**A-B**) Mean fluorescence intensities of EGFP and TagRFP were normalized to their respective maximum value and plotted along the antero-posterior axis of the tectum. The distance between $EGFP_{50\%}$ and $TagRFP_{50\%}$ does not change between 4 and 5 dpf in *maco*. (**C-D**) The distance between $EGFP_{50\%}$ and $TagRFP_{50\%}$ decreases between 4 and 5 dpf in WT siblings, demonstrating that the boundary between EGFP and TagRFP projection domains becomes more precise over time. Data represent mean ± SEM. n = 20 embryos per genotype.

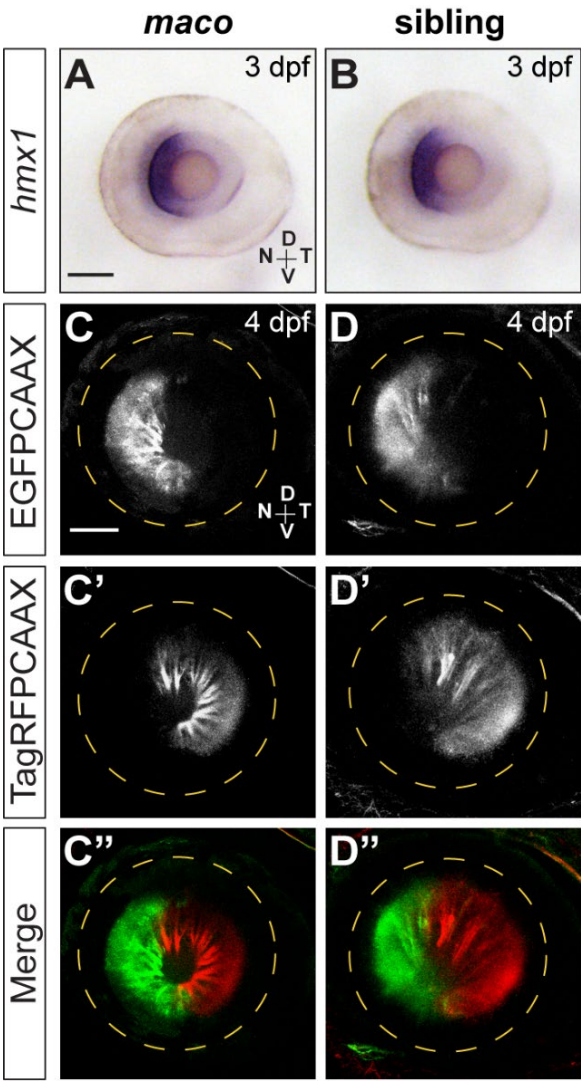

Figure 4.10: Retinal patterning is not disrupted in *maco* mutants. (**A, B**) Lateral views of eyes dissected from *maco* and sibling embryos stained for *hmx1* by ISH at 3 dpf. *Hmx1* expression is restricted to the nasal retina in both *maco* and siblings. (**C-D"**) Eye of a [*hmx1-En2:cre; RGC:col- orswitch*] double transgenic *maco* or WT sibling embryo at 4 dpf. (**C, D**) EGFP-positive RGCs are restricted to the nasal retina. (**C', D'**) TagRFP-positive RGCs are observed in the temporal half of the retina. (**C", D"**) No differences in EGFP or TagRFP expression in the retina are observed between *maco* and WT. Confocal live microscopy, maximal projections, scale bar: 50 µm.

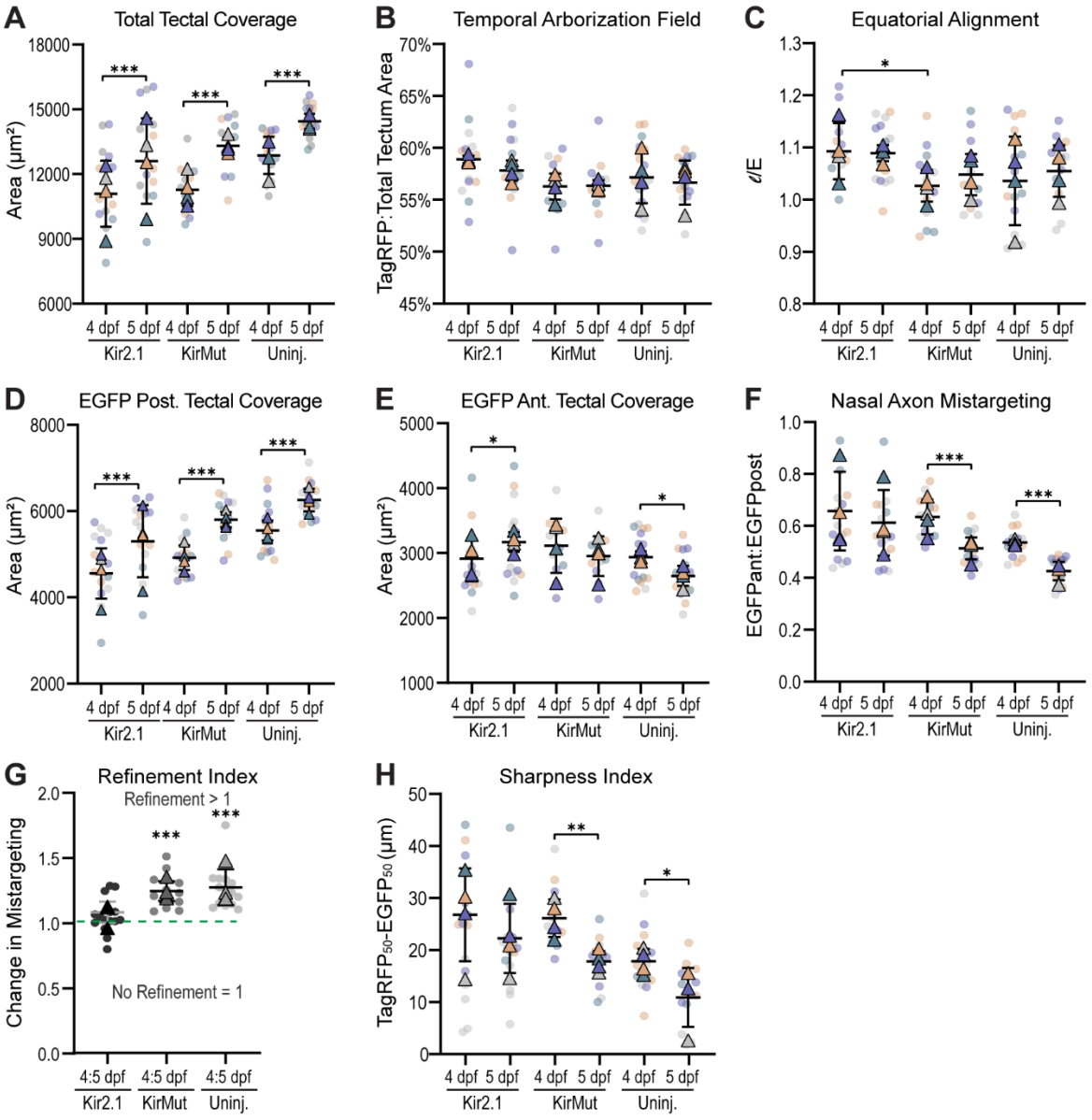

Figure 4.11: Blocking neuronal activity in RGCs prevents the refinement of nasal projections. (**A**) Like uninjected control embryos, embryos expressing Kir2.1 or KirMut in RGCs (thereafter referred to as Kir2.1 or KirMUT embryos) display an increase in total tectal coverage between 4 and 5 dpf. (**B**) The Temporal Arborization Field index is similar in Kir2.1, KirMUT and uninjected embryos at 4 and 5 dpf. (**C**) The Equatorial Alignment Index does not significantly differ between days or between experimental groups. (**D**) The area covered by EGFP-positive nasal axons in the posterior half of the tectum significantly increases between 4 and 5 dpf in Kir2.1 embryos but remains significantly smaller than that in the uninjected controls at both time points. (**E**) The anterior tectal area covered by EGFP-positive nasal axons slightly increases between 4 and 5 dpf in Kir2.1 embryos while it decreases in KirMut and uninjected embryos, suggesting a lack of refinement of the nasal projections in Kir2.1 embryos. (**F**) While the Nasal Axon Mis- targeting Index significantly decreases between 4 and 5 dpf in KirMut and uninjected embryos, it remains stable in Kir2.1 embryos, indicating a lack of refinement of the nasal projections. (**G**) While the

Figure 4.11 (Continued): Refinement Index between 4 and 5 dpf is greater than 1 in KirMut and uninjected embryos, it averages 1 in Kir2.1 embryos, confirming the absence of refinement of the nasal projection domain. (**H**) The Boundary Sharpness Index significantly decreases in KirMut and uninjected embryos but remains stable in Kir2.1 embryos, indicating that the boundary between the EGFP and TagRFP domains does not refine over time in embryos expressing Kir2.1 in RGCs. (**A-H**) Data represent mean ± SEM. n = 15 Kir2.1 embryos, 12 KirMut embryos, 15 uninjected embryos. Four biological replicates representing independent experiments are color-coded in grey, teal, purple and orange, respectively. Statistical Analysis: (A-F, H) mixed-effects one-way ANOVA with Tukey's posthoc test; (G) paired t-test compared to a control of 1 (1 representing no change); *$p < 0.05$, ** $p < 0.01$, ***$p < 0.001$.

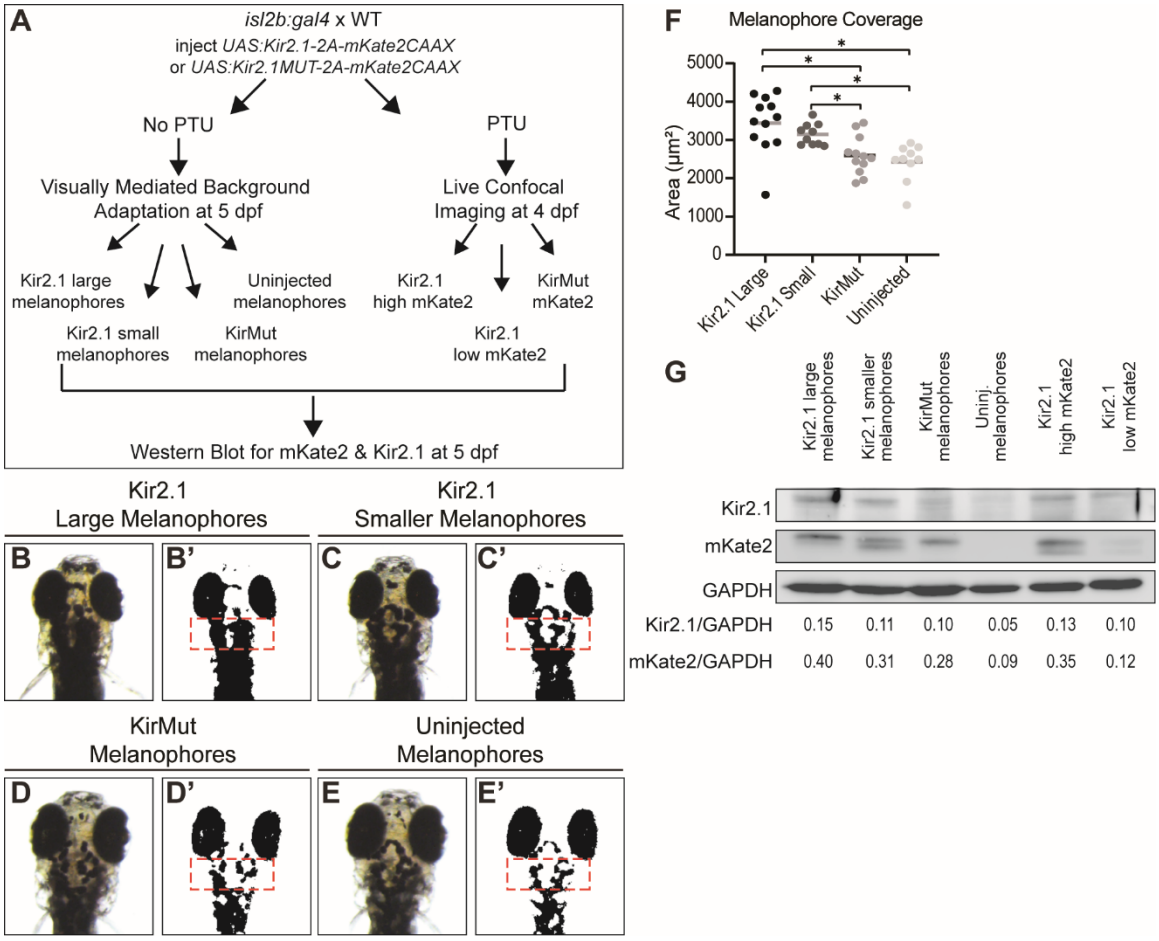

Figure 4.12: Expressing Kir2.1 in RGCs blocks larvae's visually mediated background adaptation. (**A**) Experimental work-flow to assess the functionality of Kir2.1 transgene in injected embryos. A *UAS:Kir2.1-2A-mKate2CAAX* or a *UAS:Kir2.1MUT-2A-mKate2CAAX* transgene was injected in zygotes from an [*isl2b:gal4*] outcross at one-cell stage. Embryos were divided into two groups: one raised in the absence of PTU for conducting a Visually-mediated Background Adaptation (VBA) assay at 5 dpf, and another raised with PTU for the analysis of mKate2 expression at 4 dpf by confocal microscopy. Based on the VBA assay, embryos were sorted into four groups: embryos expressing Kir2.1 that had expanded pigmentation ("large melanophores") despite bright illumination, embryos expressing Kir2.1 that had "smaller melanophores", embryos expressing KirMut, and uninjected embryos as another control group. After confocal imaging at 4 dpf, embryos were sorted into three categories based on the intensity of mKate2 expression: embryos expressing Kir2.1 that had high mKate2 expression (see Material and Methods for high mKate2 expression definition), embryos expressing Kir2.1 that had low mKate2 expression, and embryos expressing KirMut. All embryos were then used for analyzing Kir2.1/Kir2.1MUT and mKate2 expression by Western blot at 5 dpf. (**B-E'**) VBA in embryos expressing Kir2.1 or KirMut in RGCs (thereafter referred to as Kir2.1 or KirMUT embryos) and uninjected embryos. Pictures of embryos in a dorsal view (B, C, D, and E) were binarized using a threshold of 40 (B', C', D' and E'). The area covered by pigmented melanophores was measured in a region caudal to the eyes and rostral to the medulla oblongata (orange box). (**B-C'**) Kir2.1 embryos demonstrated two levels of dark, expanded

Figure 4.12 (**Continued):** pigmentation despite bright illumination. (**B, B'**) Some Kir2.1 embryos retained dispersed melanosomes ("large melanophores") in response to light, indicating a lack of VBA. (**C, C'**) Other Kir2.1 embryos had more restricted but yet abnormally expanded melanin in response to light ("smaller melanophores"), indicating a reduced VBA. (**D-E'**) In contrast to Kir2.1 embryos, KirMut and uninjected embryos showed fully aggregated melanin in response to bright illumination. (**F**) The area covered by pigmented melanophores (pigmentation measured in the region delineated by orange boxes in B'-E') is significantly larger in Kir2.1 embryos with large or smaller melanophores than in KirMUT or uninjected embryos. Statistical analysis: One-way ANOVA with Tukey's posthoc test; *$p < 0.05$, ** $p < 0.01$, ***$p < 0.001$. (**G**) Expression of Kir2.1 or KirMUT and mKate2 assessed in the different groups by Western blot at 5 dpf. High expression of Kir2.1 is detected in Kir2.1-expressing embryos with large melanophores and high mKate2 levels. Kir2.1 is also detected at lower levels in Kir2.1-expressing embryos with smaller melanophores or with low mKate2 and in KirMut-expressing embryos. Similarly to Kir2.1, mKate2 is detected in all embryos expressing Kir2.1 or KirMUT but at reduced levels in Kir2.1 embryos with low mKate2, indicating that mKate2 expression can be used as an indicator of Kir2.1 expression. Kir2.1 and mKate2 signal intensities were normalized to that of GAPDH used as a loading control. High levels of Kir2.1 expression correlate with high levels of mKate2 expression. Data represent mean ± SEM. n = 12 Kir2.1 large melanophore embryos, 10 Kir2.1 small melanophore embryos, 12 KirMut embryos, 10 uninjected embryos.

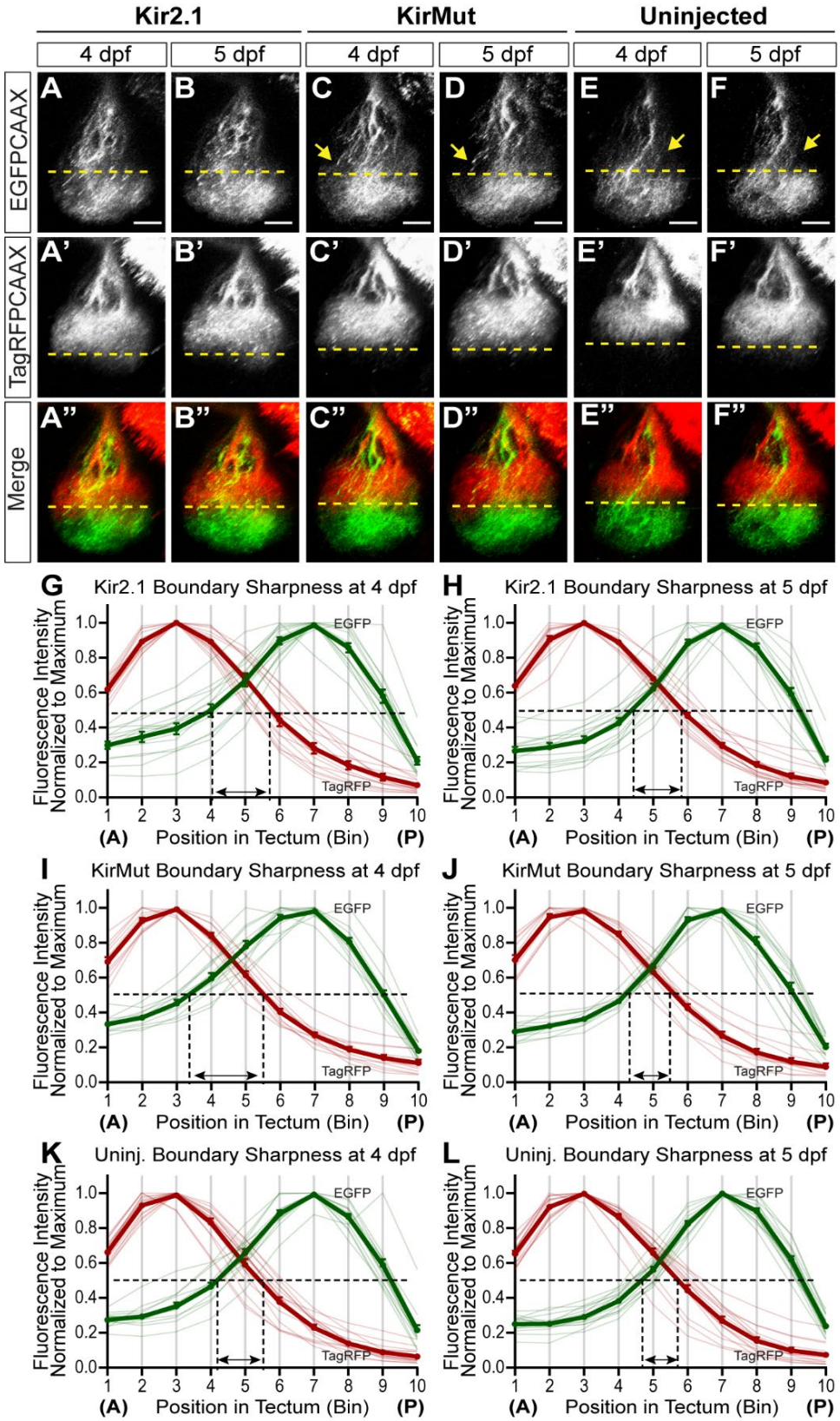

Figure 4.13: Blocking neuronal activity in RGCs prevents the sharpening of the antero-posterior retinotopic map.

Figure 4.13 (Continued): (**A-F"**) Development of the antero-posterior retinotopic map in Kir2.1 (A-B"), KirMUT (C-D"), and uninjected embryos (E-F") from 4 to 5 dpf. (**A-F**) EGFP-positive nasal axons innervate the posterior half of the tectum in all three experimental groups. The area covered by nasal axons in the anterior half of the tectum appears to decrease between 4 and 5 dpf in KirMut and uninjected embryos (arrows) but does not seem to change in Kir2.1 embryos. (**A'-F'**) TagRFP-positive temporal axons specifically target the anterior half of the tectum. Confocal microscopy, scale bar: 50 μm. (**G-H**) Mean fluorescence intensities of EGFP and TagRFP were normalized to their respective maximum value and plotted along the antero-posterior axis of the tectum. The boundary sharpness between the temporal and nasal arborization domains (shown as the distance between $EGFP_{50\%}$ and $TagRFP_{50\%}$) does not change between 4 and 5 dpf in Kir2.1 embryos. (**I-L**) The boundary sharpness between the temporal and nasal arborization domains decreases between 4 and 5 dpf in KirMUT (I, J) and uninjected (K, L) embryos, indicating the formation of a more precise antero-posterior retinotopic map. Data represent mean ± SEM. n = 15 Kir2.1 embryos, 12 KirMut embryos, 15 uninjected embryos.

CHAPTER 5

GENERAL DISCUSSION AND FUTURE DIRECTIONS

5.1 General conclusions

This dissertation focuses on the mechanisms regulating the formation of neural circuits and, in particular, how axons communicate with one another in order to establish proper connections. In **Chapter 3**, we discovered a novel role for Gpc3 and Tenm3 in pre-target retinotectal axon sorting. *Gpc3* and *tenm3* are both expressed in ventral RGCs and genetically interact to regulate the degeneration of missorted dorsal retinal axons. While many questions surrounding the signaling mechanism underlying that process have yet to be answered, this study has advanced our knowledge of the trans-axonal mechanism mediating axon degeneration during development. In **Chapter 4**, we generated a novel transgenic line that allows for the visualization of the A-P retinotopic map at the tectum. We analyzed the generation of the retinotopic map in an unbiased and quantitative manner and revealed the dynamic nature of map formation in vivo. Finally, we discovered a role for neural activity in the refinement of mistargeted axonal projections. Overall, the results from both projects described here offer novel insights into the molecular and activity-based mechanisms underlying developmental axon pruning.

5.2 Trans-Axonal Signaling during Retinotopic Pre-Target Sorting

In **Chapter 3**, we discovered a novel role for both Gpc3 and Tenm3 in retinotopic pre-target axon sorting along the optic tract. It was previously shown that HS is needed non-cell-autonomously for the selective degeneration of missorted dorsal retinal axons, leaving a properly sorted optic tract by the end of retinotopic development [19, 34].

However, which HSPG is regulating this process was unknown. Gpc3 is expressed specifically by RGCs in the ventral half of the retina and is the only HSPG with this unique expression pattern. In *gpc3-/-* embryos, missorted axons fail to degenerate, similar to the phenotype seen in *dak* in which *ext2*, a gene that encodes a glycosyltransferase necessary for HS biosynthesis, is mutated [19]. These results highlight that Gpc3 is needed for proper axon sorting and led to the first role for Gpc3 in nervous system development to be unveiled. Interestingly, *tenm3* has the same expression pattern in the retina as *gpc3* – it is expressed exclusively in the ventral RGC layer during the time when axon sorting is taking place. *Tenm3-/-* mutants also have missorted dorsal axons. Finally, we discovered a genetic interaction between *gpc3* and *tenm3* by showing that *gpc3-/+;tenm3-/+* embryos display the same phenotype as *gpc3-/-* and *tenm3-/-* embryos. While we showed this interaction on a genetic level through epistasis experiments, I have also spearheaded the implementation of biochemical techniques to test whether Gpc3 and Tenm3 physically interact in vivo. I have developed a new protocol for the immunoprecipitation (IP) of Gpc3 from RGCs of zebrafish larvae using the *Tg[isl2b:EGFPgpc3]* transgenic line I established. An early study discovered that Tenm1 interacts with heparin through the YD-repeats in the C-terminal extracellular domain and that this interaction actually inhibited neurite outgrowth in culture [335]. As Teneurins are known to be highly conserved [322], it is likely that the HS chains of Gpc3 interact with the same C-terminal domain of Tenm3. Current and future studies can use this protocol to determine whether Gpc3 interacts with Tenm3 by either co-IP or mass spectrometry analysis.

One of the most pressing questions to answer is what ligand do Gpc3 and Tenm3 interact with to initiate the degeneration of missorted dorsal retinal axons? Interestingly, an interaction between Teneurin and Latrophilin has been shown to mediate repulsion between migrating cortical neurons and radial glia. There, Lphn1 expressed on radial glial cells signals to the migrating cortical neurons expressing Tenm2 [318]. Zebrafish express a member of the Latrophilin family, *adgrl3.1*, in the retina during early development [328, 329]. We confirmed that *adgrl3.1* is strongly and uniformly expressed throughout the RGC layer during the time of retinotectal pre-target sorting (**Figure 5.1A-B**). Additionally, preliminary experiments suggest that *adgrl3.1* regulates axon sorting along the optic tract. We injected DiD in the DN retina of embryos from an *adgrl3.1*-/+ incross and observed several embryos (about 25%) that had missorted dorsal axons (**Figure 5.1C**). These data suggest that *adgrl3.1* may be the receptor that interacts with Gpc3 and Tenm3 during pre-target sorting. Future studies will analyze the presence of this phenotype in an established *adgrl3.1* mutant line and will also determine if this *adgrl3.1* genetically interacts with *gpc3* and *tenm3* through epistasis experiments. Antibodies for *adgrl3.1* can also be tested for use in zebrafish and if one is found, co-IP experiments can be performed to confirm an interaction with this complex.

Along with the abovementioned experiments, determining the domain facilitating Tenm3 signaling during optic tract sorting would also help determine its potential ligand. Teneurins are highly conserved, large Type II transmembrane glycoproteins with several different domains [319, 320, 405] (**Figure 5.2**). For example, the intracellular domain can mediate interactions with the actin cytoskeleton [406] while the extracellular domain contains a linker region that may serve as a proteolytic processing site as well as another

potential cleavage site [320, 322]. Additionally, several studies have shown that the YD-repeat domain of Teneurins (**Figure 5.2**) interacts with Latrophilin [318, 321, 407] to mediate synapse formation and repulsion during cortical neuron migration. Since Tenm3 is a Type II transmembrane protein, CRISPR genome editing can be used to target these different domains and generate mutants expressing truncated forms of Tenm3 lacking these different domains. This will allow us to better understand which domain of Tenm3 is interacting with Gpc3 and possibly Latrophilin to regulate topographic axon sorting. Additionally, Teneurins can be alternatively spliced and the splice variants have different affinities for binding in *trans* with other Teneurins or Latrophilins [407]. Analysis of *tenm3* cDNA in WT zebrafish RGCs would offer more information on the splice variants present at timepoints of retinotectal development.

Once the receptor-ligand interaction has been fully elucidated, the next question to answer would be the downstream intracellular signaling that is mediating the degeneration of missorted dorsal retinal axons. Very little is known about selective degeneration during nervous system development. While apoptotic activity via Casp3 and Casp6 regulates axon pruning in the mouse SC [408, 409], degeneration during optic tract sorting of zebrafish does not require activation of apoptotic pathways involving P53, Casp3 or Bax [34]. However an interesting study revealed that Casp6 activation can trigger axon degeneration independently from apoptosis [410], providing us with an interesting hypothesis as to whether non-apoptotic Caspase signaling could function downstream of HS-mediated retinal axon degeneration signaling pathway. Our understanding of the spatiotemporal expression and activation of Caspases in the nervous system is still lacking and as such, we sought to analyze the Caspase family in zebrafish embryos [411]

(**Appendix A**). We fully characterized the expression of the 19 zebrafish caspases from 24 – 96 hpf in zebrafish, revealing distinct expression patterns for each, providing a solid foundation for testing the role of non-apoptotic caspases in selective degeneration during retinotopic development.

While there is growing evidence suggesting that selective axon degeneration during development is independent from neuronal apoptosis, many of these studies have only been carried out in vitro [412]. If Caspase signaling is involved in retinal axon pruning, it would involve upstream effectors that would induce the Caspase signal. Several studies have suggested a role for Kinase signaling in triggering local axon degeneration. For example, dual leucine zipper kinase (DLK) is activated in cultured sensory neurons in a model of developmental axon degeneration triggered by neurotrophic growth factor (NGF) withdrawal [413, 414]. DLK activation leads to the phosphorylation of JNK which then initiates a signal for degeneration [414]. Additionally, glycogen synthase kinase 3 beta (GSK3β) is required for axonal pruning both in dorsal root ganglion (DRG) cultures and in the visual system in vivo, and GSK3β signaling most likely acts in parallel to JNK signaling to regulate pruning [415]. In addition, p38 mitogen-activated-protein-kinase (MAPK) activity has been shown to act upstream of Caspase signaling in retinal axons during both axon guidance and pruning [416, 417]. As such, investigating the role of Caspase and Kinase signaling in the degeneration of missorted axons could be an interesting pathway to investigate.

Latrophilins have recently been shown to regulate cAMP signaling [321, 325-327]. cAMP signaling regulates numerous cellular functions and has been shown to have both pro-apoptotic and anti-apoptotic functions depending on the cell type and signaling

cascades involved [418]. Additionally, cAMP signaling downstream of GPCRs activates two main effectors: PKA or Epac, a Rap1 guanine nucleotide exchange factor [419], and which pathway is activated seems to determine if elevated cAMP promotes cell survival or induces cell death. For example, increased levels of cAMP induce PKA phosphorylation of GSK3β which promotes survival of cerebellar granule cells [420]. On the other hand, cAMP signaling through Epac in cortical neurons leads to increased expression of the pro-apoptotic Bcl2-interacting member protein (Bim), inducing apoptosis [421]. Retinal axon retraction in mice is also dependent on cAMP signaling downstream of EphA/Ephrin-A [142], however the signaling cascade involved has yet to be determined. As such, cAMP signaling downstream of Latrophilin is an interesting candidate to investigate in the degeneration of missorted dorsal retinal axons during zebrafish retinotectal development.

5.3 Neural Activity and Refinement during Map Formation

In **Chapter 4**, we established a novel transgenic line that allows for the visualization of the antero-posterior retinotectal map in real time. Additionally, I developed an unbiased and quantitative method for analyzing the dynamics of map formation and refinement. Together, this provides a powerful tool that can be used to address questions that have been otherwise difficult to delve into due to a lack of approaches and techniques. Additionally, we provided a time course analysis of retinotectal formation and demonstrated that while the A-P map develops fairly early on, it remains dynamic. The temporal axons arborize in the anterior half of the tectum while the nasal axons steadily refine their projections to the posterior tectum in an activity-

dependent manner. This progressive refinement of mistargeted nasal retinal arbors in the anterior half of the tectum leads to a sharper, more precise retinotectal map.

While our study was the first quantitative assessment of topographic mapping over time in vivo, our results mostly reaffirmed previous studies assessing the role of neural activity during refinement. Several studies have shown that a lack of neural activity causes less-defined projection fields in the retinotectal system [95, 107] and that the spatiotemporal pattern of activity in the retina drives the sharpening of visual circuits [123, 125, 127, 129, 132, 136, 403]. One very interesting question that our new tool is perfectly designed to answer is how does the development of nasal arbors affect that of temporal arbors and vice versa. There is increasing evidence that both competitive and stabilizing interactions between axons play an important role in shaping arbors at the tectum [131, 245, 341], but how these axons are communicating to each other remains unknown. Our transgenic line allows for the selective manipulation of nasal vs. temporal RGCs, providing new strategies for analyzing axon-axon interactions during retinotopic mapping. For example, we can use this line to block neural activity in just the nasal RGCs or just the temporal RGCs and assess how silencing these different groups of RGCs influences map formation and refinement. While these experiments have not yet been carried out, we can expect that the initial A-P map would still form in embryos with silenced nasal or temporal RGCs, however the refinement would be similarly affected as we saw in our experiments silencing all RGCs. It is likely that silencing nasal RGCs would prevent the refinement of mistargeted nasal arbors in the anterior tectum. Without activity from neighboring RGCs, the retinal arbors would likely be larger and more complex because there would be no signal to stabilize and arrest their growth [95, 107, 111, 245]. Similarly, silencing temporal

RGCs would likely lead to an enlargement of their arborization fields as well. We can also block activity in single or a small subset of nasal- or temporal-specific RGCs and analyze the differences in arbor dynamics as these axons arborize at their targets. These experiments can be assessed as a time course, taking snapshots over time of individual embryos, or we can use high resolution timelapse imaging to see how the dynamics of nasal vs. temporal retinal arbors influence each other during retinotectal mapping.

Patterned activity and guidance cues at the target, mainly EphA/Ephrin-A signaling, act together to establish a precise retinotopic map [112, 133, 134]. However, axon-axon interactions are also beginning to emerge as an important mechanism in retinotopic map formation [14]. An in vivo study went on to demonstrate a role for Eprhin-A signaling between axons [63]. In the retina, nasal RGCs express high levels of Ephrin-As and low levels of EphAs while temporal RGCs express low levels of Ephrin-As and high levels of EphAs. During A-P mapping in the mouse visual system, temporal retinal axon expressing high levels of EphA project to the rostral SC that expresses low levels of Ephrin-As. When EphrinA5 is inactivated only in the SC, targeting of temporal axons is not affected, but temporal arbors shift posteriorly when EphrinA5 is inactivated in both the SC and the retina [63]. These results suggest that trans-axonal EphrinA5 signaling from nasal retinal axons to temporal retinal axons prevents overlapping termination zones at the SC. However, these observations were obtained indirectly by removing EphrinA5 from the entire retina as well as from the SC. Moreover, whether a converse signaling from temporal axons to nasal axons is also needed for proper targeting of nasal axons (or of temporal axons themselves) during retinotopic mapping has not yet been addressed. Our novel transgenic line offers a unique system in which we can alter expression of

guidance cues in just the nasal or temporal retina so that we can begin to address these questions.

While investigating potential mechanisms of topographic mapping and refinement, we decided to analyze the role of Contactin-2 (Cntn2). Cntn2 is GPI-anchored adhesion molecule that is known to promote axon growth and fasciculation in several neural circuits [422] and it is expressed specifically in the nasal retina of developing zebrafish [423-425] (**Figure 5.4A-B**). Despite this restriction expression, its role in the retinotectal system has been surprisingly uncharacterized to this point. We employed the two-RNA component version of CRISPR/Cas9 genome editing [426] to induce mutations in our RGC-colorswitch transgenic line at two different target sites in *cntn2* (**Figure 5.3A**). The CRISPR system proved to be highly efficient (**Figure 5.3B-C'**) and allowed us to analyze retinotectal map formation in injected "crispant" embryos alongside control embryos injected with Cas9 only.

Overall tectal coverage by nasal and temporal axons did not differ between crispants and control embryos. We also did not observe any differences in the temporal arborization field between crispants and control (**Figure 5.4G-I**) indicating that Cntn2 likely does not regulate the mapping of temporal arbors. Interestingly, we did detect differences in the mapping and refinement of nasal arbors. We observed a significant difference in the anterior tectal coverage by nasal arbors between crispants and controls (**Figure 5.4K**). While the mistargeted nasal axons in the anterior half of the tectum decreased between 4 and 5 dpf in controls, it remained constant or even slightly increased in the *cntn2* crispants (**Figure 5.4K**), revealing that refinement does not occur when *cntn2* is mutated (**Figure 5.4L**). This lack of refinement in crispant embryos was

accompanied by a lack of sharpening between the temporal and nasal arborization fields in the tectum (**Figure 5.5**). These results demonstrate that *cntn2* is necessary for the refinement and sharpening of the A-P retinotectal map.

While we have discovered a novel role for Cntn2 in the nervous system, these results only provide a foundation for understanding its role in retinotectal development and the next goal is to understand how Cntn2 is regulating the refinement of mistargeted nasal arbors. Our data confirm the expression of *cntn2* in the nasal retina at times of retinotectal development and furthermore, it has been shown that Cntn2 is expressed in nasal RGCs and along retinal axons [423]. It is therefore likely that Cntn2 is functioning cell-autonomously in nasal retinal axons to regulate the refinement of the mistargeted arbors in the anterior half of the tectum. To test this hypothesis, we could use our *hmx1-En2:Cre* transgenic line to re-express *cntn2* in just the nasal RGCs and assess if this rescues the lack of refinement in *cntn2* mutants.

Interestingly, the phenotype we observed in *cntn2* crispants is reminiscent of that seen in *maco* mutants (**Figure 4.8**). *Maco* mutants carry a mutation in *pigk* which encodes a member of the transamidase complex needed for GPI-anchor synthesis and attachment to nascent proteins [383, 384]. This mutation also causes a lack of neuronal activity in RGCs and peripheral sensory neurons due to a downregulation of voltage-gated sodium channels [107, 352, 385]. Although several studies have shown that proper GPI-biogenesis is needed for targeting sodium channels to the plasma membrane, the mechanism is still unknown [107, 352, 385, 427]. Interestingly, another member of the Contactin family, Cntn1, does indeed interact with voltage-gated sodium channels, increasing their density at the plasma membrane [428-434] and so Cntn2 could function in a similar manner

during retinotectal development showing a direct interaction between a GPI-anchored protein and sodium channels. It is therefore possible that *maco* mutants have impaired biogenesis of Cntn2 that causes the downregulation of sodium channels that subsequently leads to the lack of refinement.

The first question to address is to test whether neuronal activity in RGCs is affected when *cntn2* is mutated. To do so, we could collaborate with another lab with expertise in electrophysiology to conduct whole-cell recordings of RGCs in *cntn2* mutants. Additionally, we could produce a stable transgenic line to express a calcium indicator, GCaMP, in RGCs and in a *cntn2* mutant background. We would then perform calcium imaging to assess spontaneous neural activity in their RGCs to determine if neuronal activity is blocked in *cntn2* mutant RGCs. We could also determine if Cntn2 and sodium channels interact by performing co-IP in WT embryos. Along with our novel transgenic line and unbiased quantification method, these studies would begin to unravel that potential interactions between neuronal activity and molecular-based mechanisms regulating retinotectal map development and refinement.

Overall, these studies have provided novel mechanisms mediating the selective pruning of retinal axons both en route to their target and at their target. In **Chapter 3**, I demonstrated a novel genetic interaction between Gpc3 and Tenm3 that regulates the degeneration of missorted dorsal retinal axons, a phenomenon that is not well understood to this day. Additionally, in **Chapter 4**, I generated a novel transgenic line that allows for visualization of the A-P retinotectal map. We used this line to analyze map formation and the refinement of mistargeted retinal axons in an unbiased and quantitative way. With this line, we confirmed the activity-dependent refinement of mistargeted retinal arbors and

were able to quantitatively assess the dynamic processes of map formation for the first time. These two projects provide better understanding as well as new methods and techniques for beginning to elucidate axon-axon interactions and how they contribute to neural circuit formation.

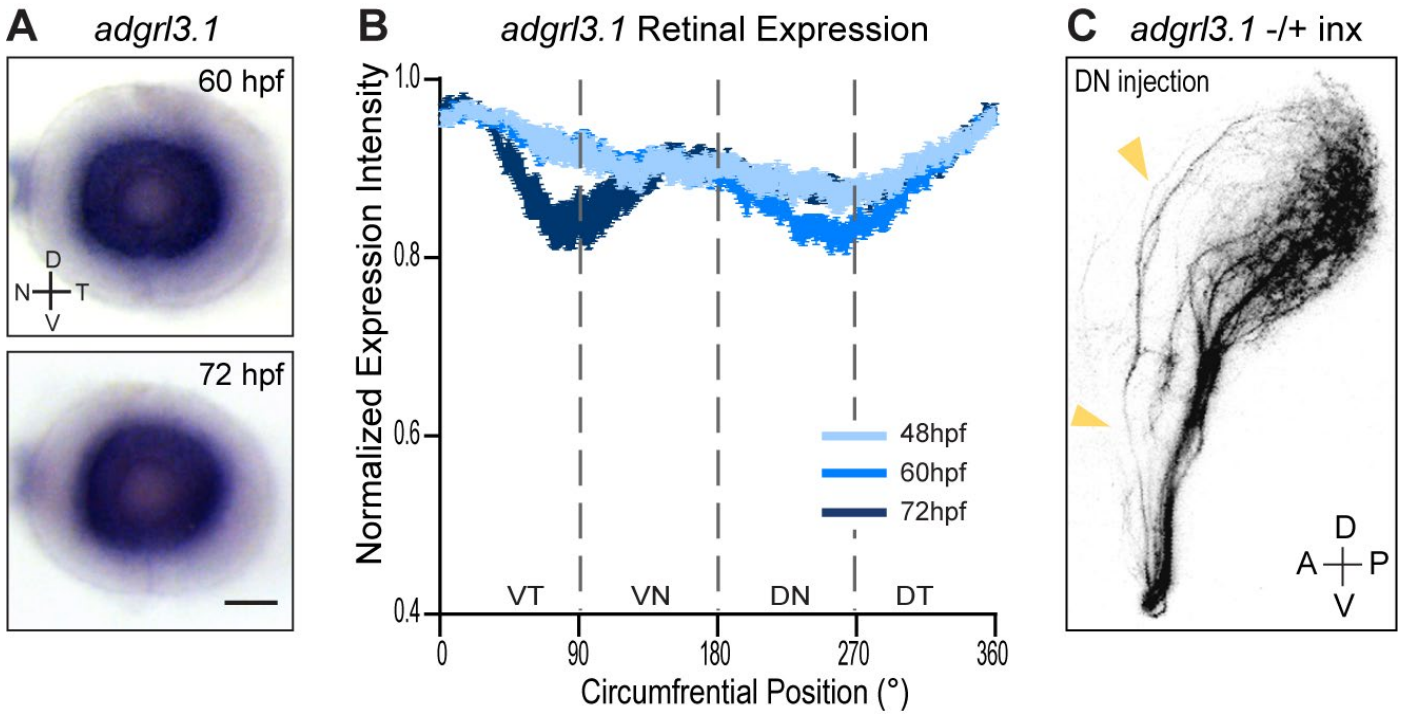

Figure 5.1 *Adgrl3.1* is expressed in the retina and may regulate pre-target retinotectal axon sorting. (**A**) Dissected eyes from WT embryos stained by ISH for *adgrl3.1* at 60 and 72 hpf. *adgrl3.1* is strongly expressed throughout the RGC layer (experiments by Trevor Moreland). (**B**) Quantification of signal intensity along a 360° trajectory shows that *adgrl3.1* is uniformly expressed throughout the RGC layer at 48, 60, and 72 hpf. (**C**) Embryos from an incross of *adgrl3.1-/+* were injected with DiD in the DN retina at 4 dpf. About 25% of embryos from the incross displayed missorted dorsal axons (yellow arrowheads).

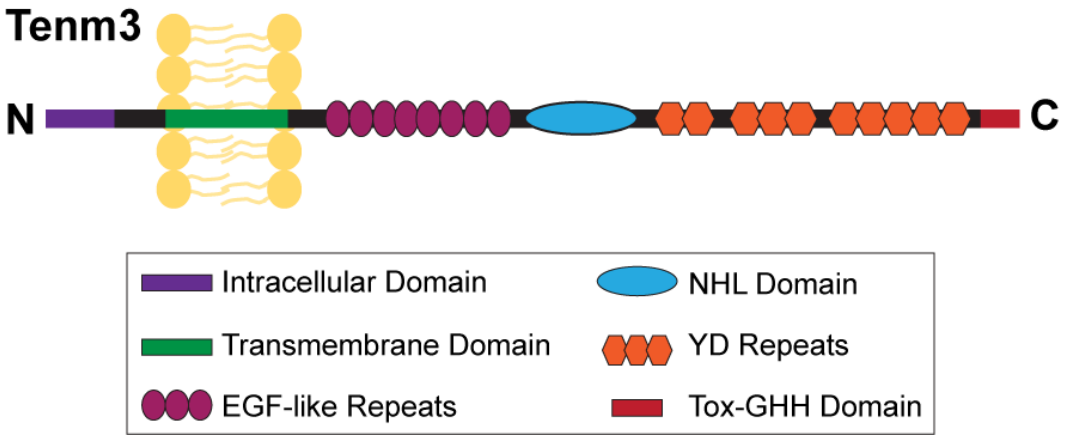

Figure 5.2 Schematic of Tenm3 protein structure. Tenm3 is a Type II transmembrane protein with the N-terminal intracellular and the C-terminal in the extracellular space. The domains include an intracellular domain, transmembrane domain, EGF-like repeats, an NHL domain, YD repeats, and a Tox-GHH Domain [322].

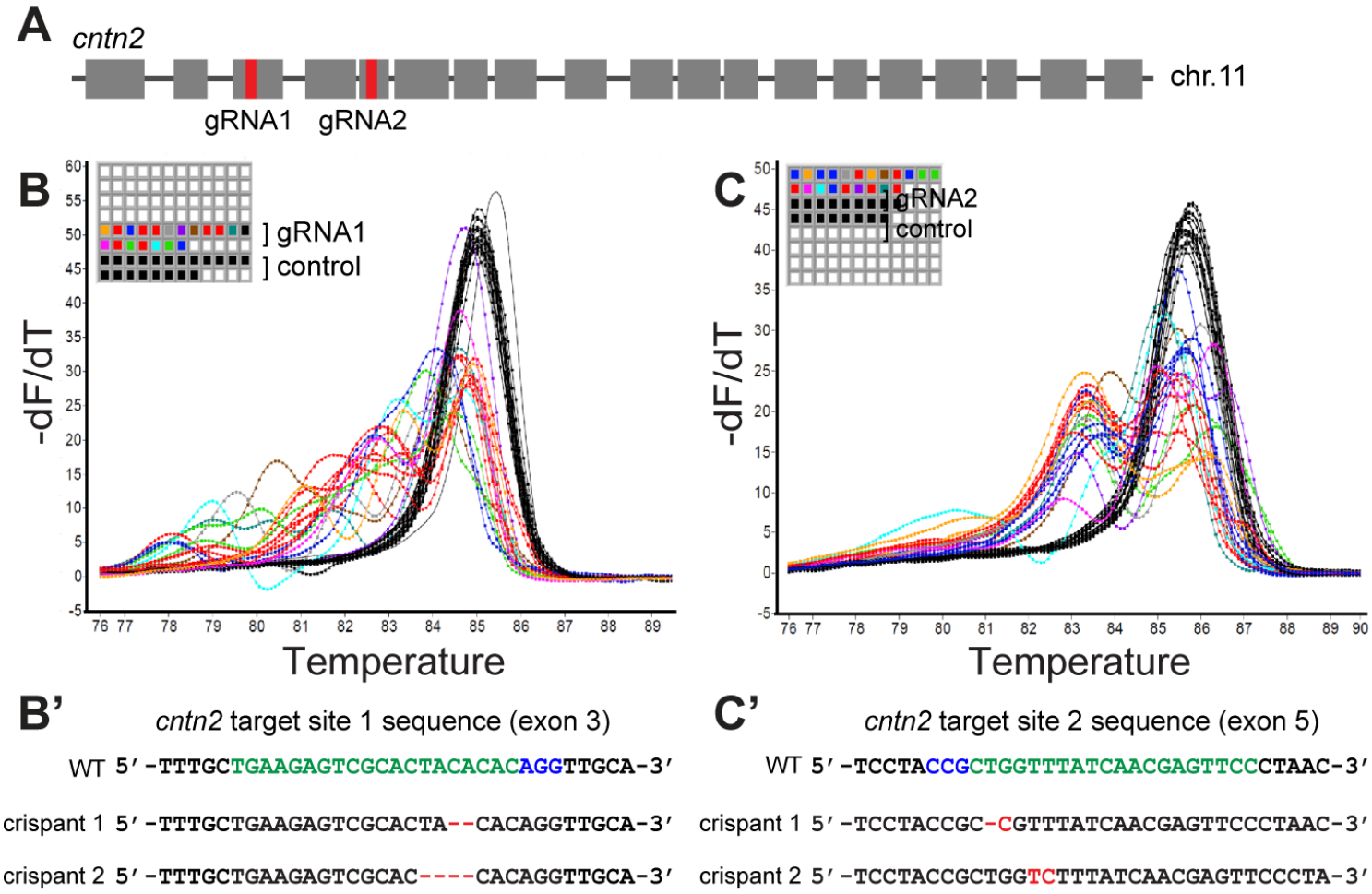

Figure 5.3: *Cntn2* RNP complexes induce mutations in G0 injected larvae. (**A**) Schematic representation of the *cntn2* gene on chromosome 11 (chr11:23,933,017-23,988,258 in GRCz11). Two independent target sequences were chosen in exon 3 (gRNA1) and exon 5 (gRNA2) (red bars). (**B,C**) HRMA detection of *cntn2* mutations in individual larvae injected with *cntn2* gRNAs (*cntn2* crispants) or with Cas9 only (control, back curves). Mutations are

Figure 5.3 (Continued): detected in 18/19 (94.7%) gRNA1-injected larvae and in 21/21 (100%) gRNA2-injected larvae. (B',C'). Sequences of mutations in *cntn2* crispants. The sequence of each target site is indicated in green (with PAM shown in blue). Two examples of mutated regions detected in individual larvae are shown.

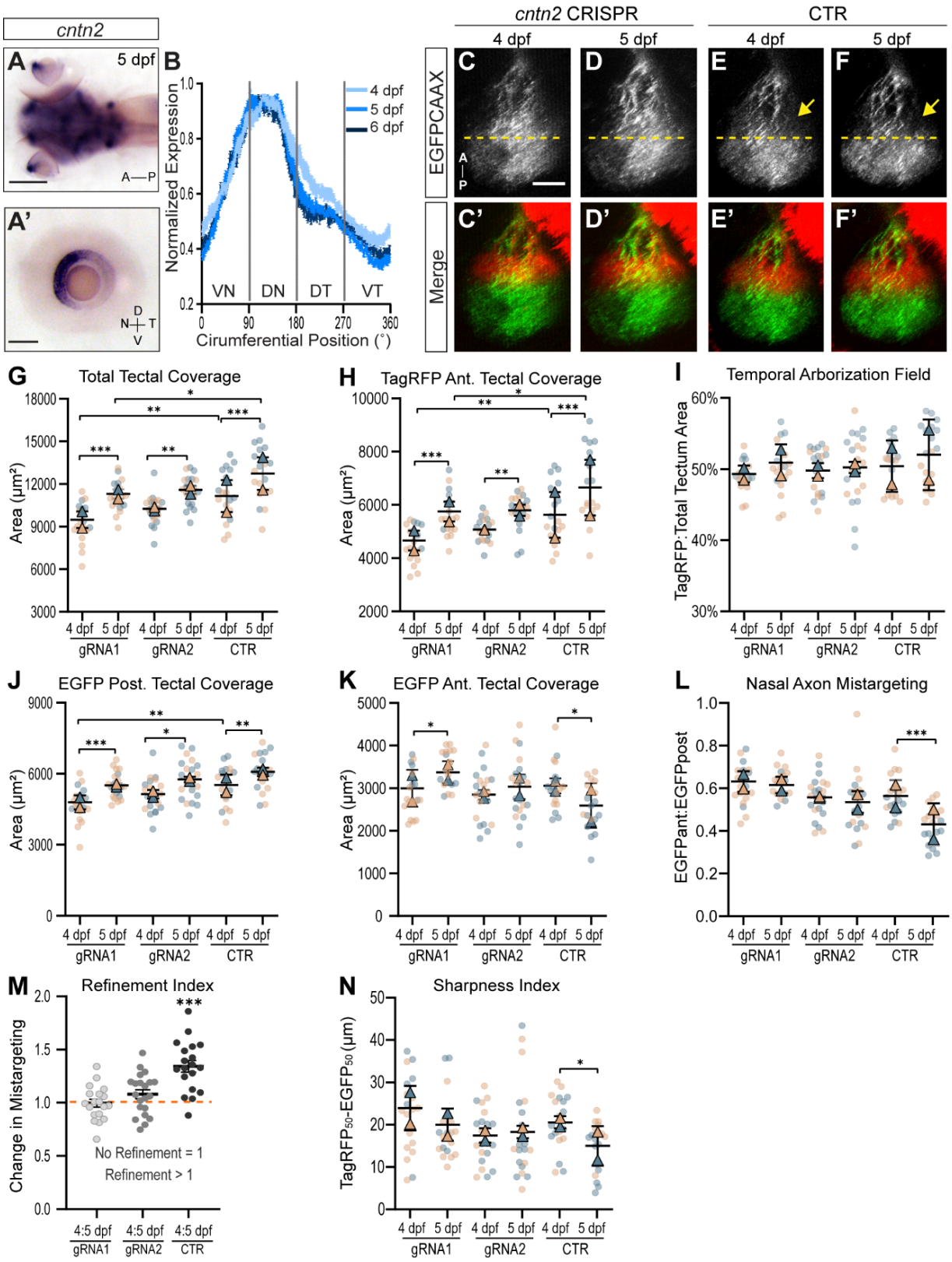

Figure 5.4: Cntn2 is required for the refinement of nasal projections and map sharpening. (**A,A'**) Larvae and dissected eye stained for *cntn2* by ISH at 5 dpf. *Cntn2* is strongly expressed in the nasal RGC layer. Scale bars: 100 µm (A), 50 µm (a'). (**B**) *Cntn2*

Figure 5.4 (Continued): expression is restricted to the nasal RGC layer at 4, 5 and 6 dpf. (**C-F'**) Development of the A/P retinotopic map in *cntn2* gRNA-injected (C-D') and Cas9-injected control larvae (E-F') from 4 to 5 dpf. The anterior tectal area covered by EGFP-positive nasal axons does not change between 4 and 5 dpf in *cntn2* crispants while it appears to decrease in control larvae (E-F, arrows). Confocal microscopy, scale bar: 50 μm. (**G**) The total tectal area significantly increases in crispants injected with gRNA1 or gRNA2 and in control larvae between 4 and 5 dpf. (**H**) The anterior area of the tectum covered by temporal axons significantly increases between 4 and 5 dpf in both crispants and controls. (**I**) The Temporal Arborization Field is similar between *cntn2* crispants and controls. (**J**) The area covered by nasal axons in the posterior half of the tectum significantly increases in *cntn2* crispants and controls. (**K**) The area covered by nasal axons in the anterior tectal half significantly decreases between 4 and 5 dpf in controls but not in crispants, indicating an absence of refinement in crispants. (**L**) The Nasal Axon Mistargeting Index decreases in controls but remains unchanged in crispants. (**M**) The Boundary Sharpness Index remains constant in *cntn2* crispants, indicating that the boundary between EGFP and TagRFP projection domains does not refine over time (see also Fig. S5). (**N**) The refinement Index is superior to 1 in controls but averages 1 in crispants, confirming the absence of refinement of the nasal projection domain. Means ± SEM. n = 19 gRNA1 crispants, 21 gRNA2 crispants, 19 controls. Statistical Analysis: (G-L, N) mixed effects one-way ANOVA with Tukey's posthoc test; (M) paired t-test compared to a control of one (1 representing no change); *$p < 0.05$, **$p < 0.01$, ***$p < 0.001$.

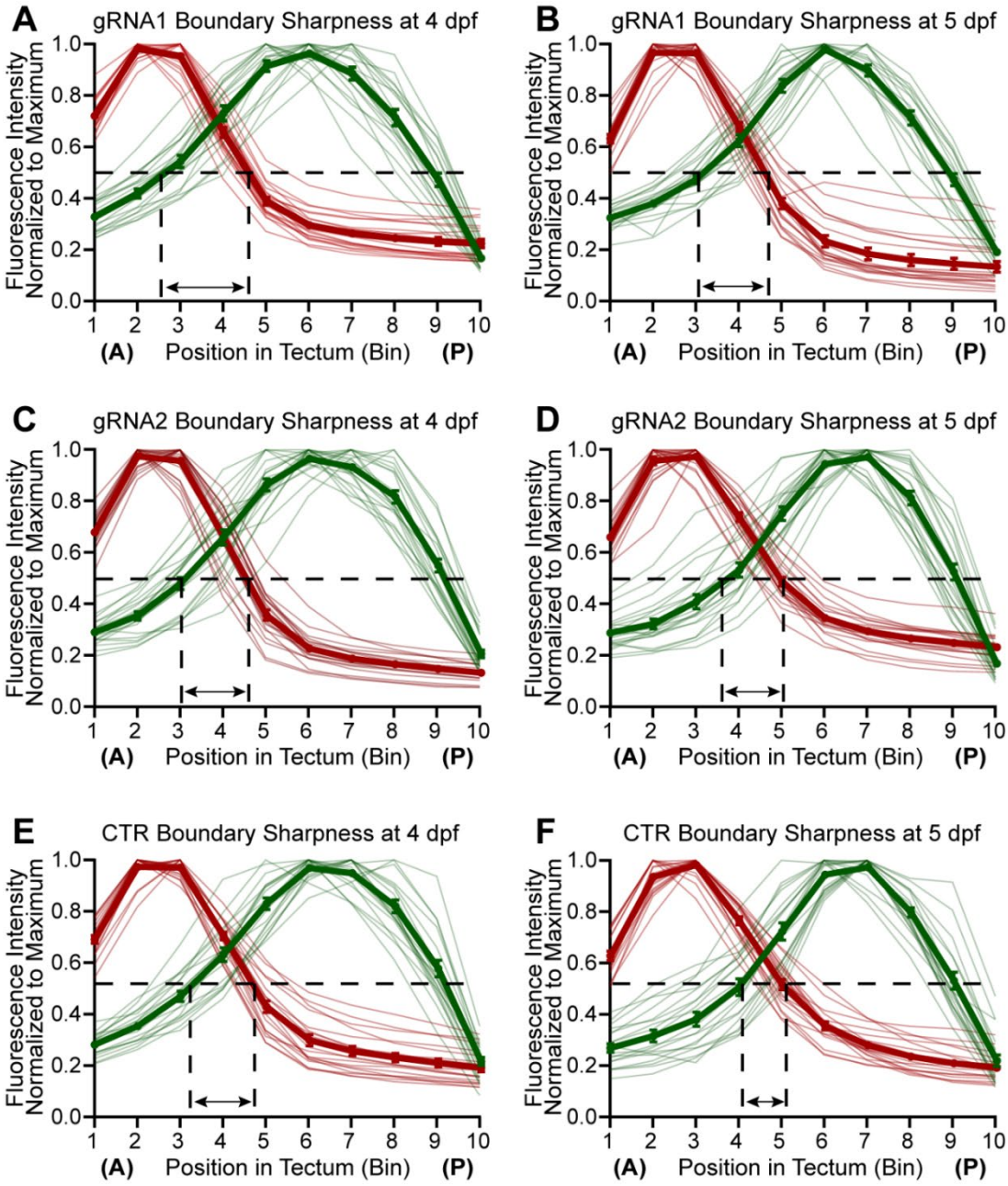

Figure 5.5: Cntn2 is necessary for the sharpening of the A/P retinotopic map. Mean fluorescence intensities of EGFP and TagRFP were normalized to their respective maximum value and plotted along the A/P axis of the tectum. (A-D) The boundary sharpness between the temporal and nasal arborization domains (shown as the distance between $EGFP_{50\%}$ and $TagRFP_{50\%}$) does not change significantly between 4 and 5 dpf in larvae injected with cntn2 gRNA1 (A,B) or gRNA2 (C,D). (**E,F**) The boundary sharpness significantly decreases between 4 and 5 dpf in Cas9-injected control larvae, indicating the formation of a more precise antero-posterior retinotopic map. Data represent mean ± SEM. n = 19 gRNA1-injected larvae, 21 gRNA2-injected larvae, 19 control larvae.

REFERENCES

1. Cang J, Feldheim DA. Developmental mechanisms of topographic map formation and alignment. *Annu Rev Neurosci*. Jul 8 2013;36:51-77. doi:10.1146/annurev-neuro-062012-170341

2. Dickson BJ. Molecular mechanisms of axon guidance. *Science*. Dec 6 2002;298(5600):1959-64. doi:10.1126/science.1072165

3. Missaire M, Hindges R. The role of cell adhesion molecules in visual circuit formation: from neurite outgrowth to maps and synaptic specificity. *Dev Neurobiol*. Jun 2015;75(6):569-83. doi:10.1002/dneu.22267

4. Carmeliet P, Ruiz de Almodovar C. VEGF ligands and receptors: implications in neurodevelopment and neurodegeneration. *Cell Mol Life Sci*. May 2013;70(10):1763-78. doi:10.1007/s00018-013-1283-7

5. Sánchez-Camacho C, Bovolenta P. Emerging mechanisms in morphogen-mediated axon guidance. *Bioessays*. Oct 2009;31(10):1013-25. doi:10.1002/bies.200900063

6. Yam PT, Charron F. Signaling mechanisms of non-conventional axon guidance cues: the Shh, BMP and Wnt morphogens. *Curr Opin Neurobiol*. Dec 2013;23(6):965-73. doi:10.1016/j.conb.2013.09.002

7. Tessier-Lavigne M, Goodman CS. The molecular biology of axon guidance. *Science*. Nov 15 1996;274(5290):1123-33. doi:10.1126/science.274.5290.1123

8. Luo L, Flanagan JG. Development of continuous and discrete neural maps. *Neuron*. Oct 25 2007;56(2):284-300. doi:10.1016/j.neuron.2007.10.014

9. McLaughlin T, O'Leary DD. Molecular gradients and development of retinotopic maps. *Annu Rev Neurosci*. 2005;28:327-55. doi:10.1146/annurev.neuro.28.061604.135714

10. Nishizumi H, Sakano H. Developmental regulation of neural map formation in the mouse olfactory system. *Dev Neurobiol*. Jun 2015;75(6):594-607. doi:10.1002/dneu.22268

11. Triplett JW. Molecular guidance of retinotopic map development in the midbrain. *Curr Opin Neurobiol*. Feb 2014;24(1):7-12. doi:10.1016/j.conb.2013.07.006

12. Plas DT, Lopez JE, Crair MC. Pretarget sorting of retinocollicular axons in the mouse. *J Comp Neurol*. Oct 31 2005;491(4):305-19. doi:10.1002/cne.20694

13. Imai T, Yamazaki T, Kobayakawa R, et al. Pre-target axon sorting establishes the neural map topography. *Science*. Jul 31 2009;325(5940):585-90. doi:10.1126/science.1173596

14. Spead O, Poulain FE. Trans-Axonal Signaling in Neural Circuit Wiring. *Int J Mol Sci*. Jul 21 2020;21(14)doi:10.3390/ijms21145170

15. Gestri G, Link BA, Neuhauss SC. The visual system of zebrafish and its use to model human ocular diseases. *Dev Neurobiol*. Mar 2012;72(3):302-27. doi:10.1002/dneu.20919

16. Poulain FE, Gaynes JA, Stacher Horndli C, Law MY, Chien CB. Analyzing retinal axon guidance in zebrafish. *Methods Cell Biol*. 2010;100:3-26. doi:10.1016/b978-0-12-384892-5.00001-3

17. Feldheim DA, O'Leary DD. Visual map development: bidirectional signaling, bifunctional guidance molecules, and competition. *Cold Spring Harb Perspect Biol*. Nov 2010;2(11):a001768. doi:10.1101/cshperspect.a001768

18. Erskine L, Herrera E. Connecting the retina to the brain. *ASN neuro*. 2014;6(6):1759091414562107.

19. Lee JS, von der Hardt S, Rusch MA, et al. Axon sorting in the optic tract requires HSPG synthesis by ext2 (dackel) and extl3 (boxer). *Neuron*. Dec 16 2004;44(6):947-60. doi:10.1016/j.neuron.2004.11.029

20. Lokmane L, Proville R, Narboux-Nême N, et al. Sensory map transfer to the neocortex relies on pretarget ordering of thalamic axons. *Current biology : CB*. 2013;23(9):810-816.

21. Pittman AJ, Law MY, Chien CB. Pathfinding in a large vertebrate axon tract: isotypic interactions guide retinotectal axons at multiple choice points. *Development*. Sep 2008;135(17):2865-71. doi:10.1242/dev.025049

22. Osterhout JA, El-Danaf RN, Nguyen PL, Huberman AD. Birthdate and outgrowth timing predict cellular mechanisms of axon target matching in the developing visual pathway. *Cell reports*. 2014;8(4):1006-1017.

23. Simon DK, O'Leary DD. Relationship of retinotopic ordering of axons in the optic pathway to the formation of visual maps in central targets. *J Comp Neurol*. May 15 1991;307(3):393-404. doi:10.1002/cne.903070305

24. Simon DK, O'Leary DD. Development of topographic order in the mammalian retinocollicular projection. *J Neurosci*. Apr 1992;12(4):1212-32. doi:10.1523/jneurosci.12-04-01212.1992

25. Stuermer CA. Retinotopic organization of the developing retinotectal projection in the zebrafish embryo. *J Neurosci*. Dec 1988;8(12):4513-30.

26. Holt CE, Harris WA. Order in the initial retinotectal map in Xenopus: a new technique for labelling growing nerve fibres. *Nature*. Jan 13 1983;301(5896):150-2. doi:10.1038/301150a0

27. Scholes JH. Nerve fibre topography in the retinal projection to the tectum. *Nature*. Apr 12 1979;278(5705):620-4.

28. Chan SO, Guillery RW. Changes in fiber order in the optic nerve and tract of rat embryos. *J Comp Neurol*. Jun 1 1994;344(1):20-32. doi:10.1002/cne.903440103

29. Karlstrom RO, Trowe T, Klostermann S, et al. Zebrafish mutations affecting retinotectal axon pathfinding. *Development (Cambridge, England)*. 1996;123:427-438.

30. Grant P, Rubin E. Ontogeny of the retina and optic nerve in Xenopus laevis. II. Ontogeny of the optic fiber pattern in the retina. *J Comp Neurol*. Feb 15 1980;189(4):671-98. doi:10.1002/cne.901890405

31. Silver J, Sapiro J. Axonal guidance during development of the optic nerve: the role of pigmented epithelia and other extrinsic factors. *J Comp Neurol*. Nov 10 1981;202(4):521-38. doi:10.1002/cne.902020406

32. Halfter W, Deiss S, Schwarz U. The formation of the axonal pattern in the embryonic avian retina. *J Comp Neurol*. Feb 22 1985;232(4):466-80. doi:10.1002/cne.902320405

33. Burrill JD, Easter SS, Jr. The first retinal axons and their microenvironment in zebrafish: cryptic pioneers and the pretract. *J Neurosci*. Apr 1995;15(4):2935-47.

34. Poulain FE, Chien CB. Proteoglycan-mediated axon degeneration corrects pretarget topographic sorting errors. *Neuron*. Apr 10 2013;78(1):49-56. doi:10.1016/j.neuron.2013.02.005

35. Trowe T, Klostermann S, Baier H, et al. Mutations disrupting the ordering and topographic mapping of axons in the retinotectal projection of the zebrafish, Danio rerio. *Development (Cambridge, England)*. 1996;123:439-450.

36. Esko JD, Selleck SB. Order out of chaos: assembly of ligand binding sites in heparan sulfate. *Annu Rev Biochem*. 2002;71:435-71. doi:10.1146/annurev.biochem.71.110601.135458

37. Poulain FE, Yost HJ. Heparan sulfate proteoglycans: a sugar code for vertebrate development? *Development*. Oct 15 2015;142(20):3456-67. doi:10.1242/dev.098178

38. Walz A, McFarlane S, Brickman YG, Nurcombe V, Bartlett PF, Holt CE. Essential role of heparan sulfates in axon navigation and targeting in the developing visual system. *Development*. Jun 1997;124(12):2421-30.

39. Irie A, Yates EA, Turnbull JE, Holt CE. Specific heparan sulfate structures involved in retinal axon targeting. *Development*. Jan 2002;129(1):61-70.

40. Bülow HE, Hobert O. Differential sulfations and epimerization define heparan sulfate specificity in nervous system development. *Neuron*. Mar 4 2004;41(5):723-36. doi:10.1016/s0896-6273(04)00084-4

41. Pratt T, Conway CD, Tian NM, Price DJ, Mason JO. Heparan sulphation patterns generated by specific heparan sulfotransferase enzymes direct distinct aspects of retinal axon guidance at the optic chiasm. *J Neurosci*. Jun 28 2006;26(26):6911-23. doi:10.1523/jneurosci.0505-06.2006

42. Hornberg H, Cioni JM, Harris WA, Holt CE. Hermes Regulates Axon Sorting in the Optic Tract by Post-Trancriptional Regulation of Neuropilin 1. *J Neurosci*. Dec 14 2016;36(50):12697-12706. doi:10.1523/jneurosci.2400-16.2016

43. Cioni JM, Wong HH, Bressan D, Kodama L, Harris WA, Holt CE. Axon-Axon Interactions Regulate Topographic Optic Tract Sorting via CYFIP2-Dependent WAVE Complex Function. *Neuron*. Mar 7 2018;97(5):1078-1093.e6. doi:10.1016/j.neuron.2018.01.027

44. Pittman AJ, Gaynes JA, Chien CB. nev (cyfip2) is required for retinal lamination and axon guidance in the zebrafish retinotectal system. *Dev Biol*. Aug 15 2010;344(2):784-94. doi:10.1016/j.ydbio.2010.05.512

45. Sperry RW. CHEMOAFFINITY IN THE ORDERLY GROWTH OF NERVE FIBER PATTERNS AND CONNECTIONS. *Proc Natl Acad Sci U S A*. Oct 1963;50:703-10.

46. Cang J, Niell CM, Liu X, Pfeiffenberger C, Feldheim DA, Stryker MP. Selective disruption of one Cartesian axis of cortical maps and receptive fields by deficiency in ephrin-As and structured activity. *Neuron*. 2008;57(4):511-523.

47. Cheng HJ, Nakamoto M, Bergemann AD, Flanagan JG. Complementary gradients in expression and binding of ELF-1 and Mek4 in development of the topographic retinotectal projection map. *Cell*. Aug 11 1995;82(3):371-81.

48. Drescher U, Kremoser C, Handwerker C, Löschinger J, Noda M, Bonhoeffer F. In vitro guidance of retinal ganglion cell axons by RAGS, a 25 kDa tectal protein related to ligands for Eph receptor tyrosine kinases. *Cell*. Aug 11 1995;82(3):359-70. doi:10.1016/0092-8674(95)90425-5

49. Cheng HJ, Flanagan JG. Identification and cloning of ELF-1, a developmentally expressed ligand for the Mek4 and Sek receptor tyrosine kinases. *Cell*. Oct 7 1994;79(1):157-68. doi:10.1016/0092-8674(94)90408-1

50. Nakamoto M, Cheng HJ, Friedman GC, et al. Topographically specific effects of ELF-1 on retinal axon guidance in vitro and retinal axon mapping in vivo. *Cell*. Sep 6 1996;86(5):755-66.

51. Frisen J, Yates PA, McLaughlin T, Friedman GC, O'Leary DD, Barbacid M. Ephrin-A5 (AL-1/RAGS) is essential for proper retinal axon guidance and topographic mapping in the mammalian visual system. *Neuron*. Feb 1998;20(2):235-43.

52. Feldheim DA, Kim YI, Bergemann AD, Frisen J, Barbacid M, Flanagan JG. Genetic analysis of ephrin-A2 and ephrin-A5 shows their requirement in multiple aspects of retinocollicular mapping. *Neuron*. Mar 2000;25(3):563-74.

53. McLaughlin T, Hindges R, O'Leary DD. Regulation of axial patterning of the retina and its topographic mapping in the brain. *Curr Opin Neurobiol*. Feb 2003;13(1):57-69.

54. Mui SH, Hindges R, O'Leary DD, Lemke G, Bertuzzi S. The homeodomain protein Vax2 patterns the dorsoventral and nasotemporal axes of the eye. *Development*. Feb 2002;129(3):797-804.

55. Schulte D, Furukawa T, Peters MA, Kozak CA, Cepko CL. Misexpression of the Emx-related homeobox genes cVax and mVax2 ventralizes the retina and perturbs the retinotectal map. *Neuron*. Nov 1999;24(3):541-53. doi:10.1016/s0896-6273(00)81111-3

56. Schulte D, Cepko CL. Two homeobox genes define the domain of EphA3 expression in the developing chick retina. *Development*. Dec 2000;127(23):5033-45.

57. Lambot MA, Depasse F, Noel JC, Vanderhaeghen P. Mapping labels in the human developing visual system and the evolution of binocular vision. *J Neurosci*. Aug 3 2005;25(31):7232-7. doi:10.1523/jneurosci.0802-05.2005

58. Rashid T, Upton AL, Blentic A, et al. Opposing gradients of ephrin-As and EphA7 in the superior colliculus are essential for topographic mapping in the mammalian visual system. *Neuron*. Jul 7 2005;47(1):57-69. doi:10.1016/j.neuron.2005.05.030

59. Feldheim DA, Nakamoto M, Osterfield M, et al. Loss-of-function analysis of EphA receptors in retinotectal mapping. *J Neurosci*. Mar 10 2004;24(10):2542-50. doi:10.1523/jneurosci.0239-03.2004

60. Brown A, Yates PA, Burrola P, et al. Topographic mapping from the retina to the midbrain is controlled by relative but not absolute levels of EphA receptor signaling. *Cell*. Jul 7 2000;102(1):77-88.

61. Bevins N, Lemke G, Reber M. Genetic dissection of EphA receptor signaling dynamics during retinotopic mapping. *J Neurosci*. Jul 13 2011;31(28):10302-10. doi:10.1523/jneurosci.1652-11.2011

62. Reber M, Burrola P, Lemke G. A relative signalling model for the formation of a topographic neural map. *Nature*. Oct 14 2004;431(7010):847-53. doi:10.1038/nature02957

63. Suetterlin P, Drescher U. Target-independent ephrina/EphA-mediated axon-axon repulsion as a novel element in retinocollicular mapping. *Neuron*. Nov 19 2014;84(4):740-52. doi:10.1016/j.neuron.2014.09.023

64. Lim YS, McLaughlin T, Sung TC, Santiago A, Lee KF, O'Leary DD. p75(NTR) mediates ephrin-A reverse signaling required for axon repulsion and mapping. *Neuron*. Sep 11 2008;59(5):746-58. doi:10.1016/j.neuron.2008.07.032

65. Brunet I, Weinl C, Piper M, et al. The transcription factor Engrailed-2 guides retinal axons. *Nature*. Nov 3 2005;438(7064):94-8. doi:10.1038/nature04110

66. Wizenmann A, Brunet I, Lam J, et al. Extracellular Engrailed participates in the topographic guidance of retinal axons in vivo. *Neuron*. Nov 12 2009;64(3):355-366. doi:10.1016/j.neuron.2009.09.018

67. Monnier PP, Sierra A, Macchi P, et al. RGM is a repulsive guidance molecule for retinal axons. *Nature*. 2002;419(6905):392-395.

68. Rajagopalan S, Deitinghoff L, Davis D, et al. Neogenin mediates the action of repulsive guidance molecule. *Nature cell biology*. 2004;6(8):756-762.

69. Niederkofler V, Salie R, Sigrist M, Arber S. Repulsive guidance molecule (RGM) gene function is required for neural tube closure but not retinal topography in the mouse visual system. *J Neurosci*. Jan 28 2004;24(4):808-18. doi:10.1523/jneurosci.4610-03.2004

70. Campbell DS, Regan AG, Lopez JS, Tannahill D, Harris WA, Holt CE. Semaphorin 3A elicits stage-dependent collapse, turning, and branching in Xenopus retinal growth cones. *J Neurosci*. Nov 1 2001;21(21):8538-47. doi:10.1523/jneurosci.21-21-08538.2001

71. Claudepierre T, Koncina E, Pfrieger FW, Bagnard D, Aunis D, Reber M. Implication of neuropilin 2/semaphorin 3F in retinocollicular map formation. *Dev Dyn*. Nov 2008;237(11):3394-403. doi:10.1002/dvdy.21759

72. Braisted JE, McLaughlin T, Wang HU, Friedman GC, Anderson DJ, O'Leary D D. Graded and lamina-specific distributions of ligands of EphB receptor tyrosine kinases in the developing retinotectal system. *Dev Biol*. Nov 1 1997;191(1):14-28. doi:10.1006/dbio.1997.8706

73. Hindges R, McLaughlin T, Genoud N, Henkemeyer M, O'Leary DDM. EphB forward signaling controls directional branch extension and arborization required for dorsal-ventral retinotopic mapping. *Neuron*. 2002;35(3):475-487.

74. Holash JA, Pasquale EB. Polarized expression of the receptor protein tyrosine kinase Cek5 in the developing avian visual system. *Dev Biol*. Dec 1995;172(2):683-93. doi:10.1006/dbio.1995.8039

75. Mann F, Ray S, Harris W, Holt C. Topographic mapping in dorsoventral axis of the Xenopus retinotectal system depends on signaling through ephrin-B ligands. *Neuron*. 2002;35(3):461-473.

76. Marcus RC, Gale NW, Morrison ME, Mason CA, Yancopoulos GD. Eph family receptors and their ligands distribute in opposing gradients in the developing mouse retina. *Dev Biol*. Dec 15 1996;180(2):786-9. doi:10.1006/dbio.1996.0347

77. Higenell V, Han SM, Feldheim DA, Scalia F, Ruthazer ES. Expression patterns of Ephs and ephrins throughout retinotectal development in Xenopus laevis. *Dev Neurobiol*. Apr 2012;72(4):547-63. doi:10.1002/dneu.20930

78. Thisse C, Thisse B. High-resolution in situ hybridization to whole-mount zebrafish embryos. *Nat Protoc*. 2008;3(1):59-69. doi:10.1038/nprot.2007.514

79. Thakar S, Chenaux G, Henkemeyer M. Critical roles for EphB and ephrin-B bidirectional signalling in retinocollicular mapping. *Nature communications*. 2011;2:431-431.

80. McLaughlin T, Lim YS, Santiago A, O'Leary DD. Multiple EphB receptors mediate dorsal-ventral retinotopic mapping via similar bi-functional responses to ephrin-B1. *Mol Cell Neurosci*. Nov 2014;63:24-30. doi:10.1016/j.mcn.2014.05.005

81. Schmitt AM, Shi J, Wolf AM, Lu C-C, King LA, Zou Y. Wnt-Ryk signalling mediates medial-lateral retinotectal topographic mapping. *Nature*. 2006;439(7072):31-37.

82. Buhusi M, Schlatter MC, Demyanenko GP, Thresher R, Maness PF. L1 interaction with ankyrin regulates mediolateral topography in the retinocollicular projection. *The Journal of neuroscience : the official journal of the Society for Neuroscience*. 2008;28(1):177-188.

83. Buhusi M, Demyanenko GP, Jannie KM, et al. ALCAM regulates mediolateral retinotopic mapping in the superior colliculus. *The Journal of neuroscience : the official journal of the Society for Neuroscience*. 2009;29(50):15630-15641.

84. Dai J, Dalal JS, Thakar S, et al. EphB regulates L1 phosphorylation during retinocollicular mapping. *Molecular and cellular neurosciences*. 2012;50(2):201-210.

85. Dai J, Buhusi M, Demyanenko GP, et al. Neuron glia-related cell adhesion molecule (NrCAM) promotes topographic retinocollicular mapping. *PLoS One*. 2013;8(9):e73000. doi:10.1371/journal.pone.0073000

86. Leamey CA, Merlin S, Lattouf P, et al. Ten_m3 regulates eye-specific patterning in the mammalian visual pathway and is required for binocular vision. *PLoS Biol*. Sep 2007;5(9):e241. doi:10.1371/journal.pbio.0050241

87. Dharmaratne N, Glendining KA, Young TR, Tran H, Sawatari A, Leamey CA. Ten-m3 is required for the development of topography in the ipsilateral retinocollicular pathway. *PloS one*. 2012;7(9):e43083-e43083.

88. Glendining KA, Liu SC, Nguyen M, et al. Downstream mediators of Ten-m3 signalling in the developing visual pathway. *BMC neuroscience*. 2017;18(1):78-78.

89. Harris WA, Holt CE, Bonhoeffer F. Retinal axons with and without their somata, growing to and arborizing in the tectum of Xenopus embryos: a time-lapse video study of single fibres in vivo. *Development*. Sep 1987;101(1):123-33.

90. Brennan C, Monschau B, Lindberg R, et al. Two Eph receptor tyrosine kinase ligands control axon growth and may be involved in the creation of the retinotectal map in the zebrafish. *Development*. Feb 1997;124(3):655-64.

91. O'Rourke NA, Fraser SE. Dynamic changes in optic fiber terminal arbors lead to retinotopic map formation: an in vivo confocal microscopic study. *Neuron*. Aug 1990;5(2):159-71. doi:10.1016/0896-6273(90)90306-z

92. O'Rourke NA, Cline HT, Fraser SE. Rapid remodeling of retinal arbors in the tectum with and without blockade of synaptic transmission. *Neuron*. Apr 1994;12(4):921-34. doi:10.1016/0896-6273(94)90343-3

93. Munz M, Gobert D, Schohl A, et al. Rapid Hebbian axonal remodeling mediated by visual stimulation. *Science*. May 23 2014;344(6186):904-9. doi:10.1126/science.1251593

94. Ruthazer ES, Li J, Cline HT. Stabilization of axon branch dynamics by synaptic maturation. *J Neurosci*. Mar 29 2006;26(13):3594-603. doi:10.1523/jneurosci.0069-06.2006

95. Ben Fredj N, Hammond S, Otsuna H, Chien CB, Burrone J, Meyer MP. Synaptic activity and activity-dependent competition regulates axon arbor maturation, growth arrest, and territory in the retinotectal projection. *J Neurosci*. Aug 11 2010;30(32):10939-51. doi:10.1523/jneurosci.1556-10.2010

96. Nakamura H, O'Leary DD. Inaccuracies in initial growth and arborization of chick retinotectal axons followed by course corrections and axon remodeling to develop topographic order. *J Neurosci*. Nov 1989;9(11):3776-95. doi:10.1523/jneurosci.09-11-03776.1989

97. Simon DK, O'Leary DD. Responses of retinal axons in vivo and in vitro to position-encoding molecules in the embryonic superior colliculus. *Neuron*. Nov 1992;9(5):977-89. doi:10.1016/0896-6273(92)90249-d

98. Sakurai T, Wong E, Drescher U, Tanaka H, Jay DG. Ephrin-A5 restricts topographically specific arborization in the chick retinotectal projection in vivo. *Proc Natl Acad Sci U S A*. Aug 6 2002;99(16):10795-800. doi:10.1073/pnas.162161499

99. Galli L, Maffei L. Spontaneous impulse activity of rat retinal ganglion cells in prenatal life. *Science*. Oct 7 1988;242(4875):90-1. doi:10.1126/science.3175637

100. Meister M, Wong RO, Baylor DA, Shatz CJ. Synchronous bursts of action potentials in ganglion cells of the developing mammalian retina. *Science*. May 17 1991;252(5008):939-43. doi:10.1126/science.2035024

101. Wong RO, Meister M, Shatz CJ. Transient period of correlated bursting activity during development of the mammalian retina. *Neuron*. Nov 1993;11(5):923-38. doi:10.1016/0896-6273(93)90122-8

102. Ackman JB, Crair MC. Role of emergent neural activity in visual map development. *Curr Opin Neurobiol*. Feb 2014;24(1):166-75. doi:10.1016/j.conb.2013.11.011

103. Zhang RW, Li XQ, Kawakami K, Du JL. Stereotyped initiation of retinal waves by bipolar cells via presynaptic NMDA autoreceptors. *Nat Commun*. Sep 2 2016;7:12650. doi:10.1038/ncomms12650

104. Ackman JB, Burbridge TJ, Crair MC. Retinal waves coordinate patterned activity throughout the developing visual system. *Nature*. Oct 11 2012;490(7419):219-25. doi:10.1038/nature11529

105. Kobayashi T, Nakamura H, Yasuda M. Disturbance of refinement of retinotectal projection in chick embryos by tetrodotoxin and grayanotoxin. *Brain Res Dev Brain Res*. Dec 1 1990;57(1):29-35. doi:10.1016/0165-3806(90)90181-w

106. Kaethner RJ, Stuermer CA. Growth behavior of retinotectal axons in live zebrafish embryos under TTX-induced neural impulse blockade. *J Neurobiol*. Jul 1994;25(7):781-96. doi:10.1002/neu.480250704

107. Gnuegge L, Schmid S, Neuhauss SC. Analysis of the activity-deprived zebrafish mutant macho reveals an essential requirement of neuronal activity for the development of a fine-grained visuotopic map. *J Neurosci*. May 15 2001;21(10):3542-8. doi:10.1523/jneurosci.21-10-03542.2001

108. Stuermer CA, Rohrer B, Münz H. Development of the retinotectal projection in zebrafish embryos under TTX-induced neural-impulse blockade. *J Neurosci*. Nov 1990;10(11):3615-26. doi:10.1523/jneurosci.10-11-03615.1990

109. Cohen-Cory S. BDNF modulates, but does not mediate, activity-dependent branching and remodeling of optic axon arbors in vivo. *J Neurosci*. Nov 15 1999;19(22):9996-10003. doi:10.1523/jneurosci.19-22-09996.1999

110. Reh TA, Constantine-Paton M. Eye-specific segregation requires neural activity in three-eyed Rana pipiens. *J Neurosci*. May 1985;5(5):1132-43. doi:10.1523/jneurosci.05-05-01132.1985

111. Hua JY, Smear MC, Baier H, Smith SJ. Regulation of axon growth in vivo by activity-based competition. *Nature*. Apr 21 2005;434(7036):1022-6. doi:10.1038/nature03409

112. Benjumeda I, Escalante A, Law C, et al. Uncoupling of EphA/ephrinA signaling and spontaneous activity in neural circuit wiring. *J Neurosci*. Nov 13 2013;33(46):18208-18. doi:10.1523/jneurosci.1931-13.2013

113. Kita EM, Scott EK, Goodhill GJ. Topographic wiring of the retinotectal connection in zebrafish. *Dev Neurobiol*. Jun 2015;75(6):542-56. doi:10.1002/dneu.22256

114. Simpson HD, Kita EM, Scott EK, Goodhill GJ. A quantitative analysis of branching, growth cone turning, and directed growth in zebrafish retinotectal axon guidance. *J Comp Neurol*. Apr 15 2013;521(6):1409-29. doi:10.1002/cne.23248

115. Kaethner RJ, Stuermer CA. Dynamics of terminal arbor formation and target approach of retinotectal axons in living zebrafish embryos: a time-lapse study of single axons. *J Neurosci*. Aug 1992;12(8):3257-71. doi:10.1523/jneurosci.12-08-03257.1992

116. Witte S, Stier H, Cline HT. In vivo observations of timecourse and distribution of morphological dynamics in Xenopus retinotectal axon arbors. *J Neurobiol*. Oct 1996;31(2):219-34. doi:10.1002/(sici)1097-4695(199610)31:2<219::aid-neu7>3.0.co;2-e

117. Campbell DS, Stringham SA, Timm A, et al. Slit1a inhibits retinal ganglion cell arborization and synaptogenesis via Robo2-dependent and -independent pathways. *Neuron*. Jul 19 2007;55(2):231-45. doi:10.1016/j.neuron.2007.06.034

118. Rajan I, Witte S, Cline HT. NMDA receptor activity stabilizes presynaptic retinotectal axons and postsynaptic optic tectal cell dendrites in vivo. *J Neurobiol*. Feb 15 1999;38(3):357-68. doi:10.1002/(sici)1097-4695(19990215)38:3<357::aid-neu5>3.0.co;2-#

119. Kesner P, Schohl A, Warren EC, Ma F, Ruthazer ES. Postsynaptic and Presynaptic NMDARs Have Distinct Roles in Visual Circuit Development. *Cell Rep*. Jul 28 2020;32(4):107955. doi:10.1016/j.celrep.2020.107955

120. Ruthazer ES, Akerman CJ, Cline HT. Control of axon branch dynamics by correlated activity in vivo. *Science*. Jul 4 2003;301(5629):66-70. doi:10.1126/science.1082545

121. Schmidt JT, Buzzard M, Borress R, Dhillon S. MK801 increases retinotectal arbor size in developing zebrafish without affecting kinetics of branch elimination and addition. *J Neurobiol*. Feb 15 2000;42(3):303-14.

122. Hiramoto M, Cline HT. Optic flow instructs retinotopic map formation through a spatial to temporal to spatial transformation of visual information. *Proc Natl Acad Sci U S A*. Nov 25 2014;111(47):E5105-13. doi:10.1073/pnas.1416953111

123. Burbridge TJ, Xu HP, Ackman JB, et al. Visual circuit development requires patterned activity mediated by retinal acetylcholine receptors. *Neuron*. Dec 3 2014;84(5):1049-64. doi:10.1016/j.neuron.2014.10.051

124. McLaughlin T, Torborg CL, Feller MB, O'Leary DD. Retinotopic map refinement requires spontaneous retinal waves during a brief critical period of development. *Neuron*. Dec 18 2003;40(6):1147-60. doi:10.1016/s0896-6273(03)00790-6

125. Cang J, Rentería RC, Kaneko M, Liu X, Copenhagen DR, Stryker MP. Development of precise maps in visual cortex requires patterned spontaneous activity in the retina. *Neuron*. Dec 8 2005;48(5):797-809. doi:10.1016/j.neuron.2005.09.015

126. Dhande OS, Hua EW, Guh E, et al. Development of single retinofugal axon arbors in normal and β2 knock-out mice. *J Neurosci*. Mar 2 2011;31(9):3384-99. doi:10.1523/jneurosci.4899-10.2011

127. Chandrasekaran AR, Plas DT, Gonzalez E, Crair MC. Evidence for an instructive role of retinal activity in retinotopic map refinement in the superior colliculus of the mouse. *J Neurosci*. Jul 20 2005;25(29):6929-38. doi:10.1523/jneurosci.1470-05.2005

128. Xu HP, Furman M, Mineur YS, et al. An instructive role for patterned spontaneous retinal activity in mouse visual map development. *Neuron*. Jun 23 2011;70(6):1115-27. doi:10.1016/j.neuron.2011.04.028

129. Xu HP, Burbridge TJ, Chen MG, et al. Spatial pattern of spontaneous retinal waves instructs retinotopic map refinement more than activity frequency. *Dev Neurobiol*. Jun 2015;75(6):621-40. doi:10.1002/dneu.22288

130. Butts DA, Kanold PO, Shatz CJ. A burst-based "Hebbian" learning rule at retinogeniculate synapses links retinal waves to activity-dependent refinement. *PLoS Biol*. Mar 2007;5(3):e61. doi:10.1371/journal.pbio.0050061

131. Rahman TN, Munz M, Kutsarova E, Bilash OM, Ruthazer ES. Stentian structural plasticity in the developing visual system. *Proc Natl Acad Sci U S A*. May 19 2020;117(20):10636-10638. doi:10.1073/pnas.2001107117

132. Zhang J, Ackman JB, Xu HP, Crair MC. Visual map development depends on the temporal pattern of binocular activity in mice. *Nat Neurosci*. Nov 18 2011;15(2):298-307. doi:10.1038/nn.3007

133. Cang J, Wang L, Stryker MP, Feldheim DA. Roles of ephrin-as and structured activity in the development of functional maps in the superior colliculus. *J Neurosci*. Oct 22 2008;28(43):11015-23. doi:10.1523/jneurosci.2478-08.2008

134. Pfeiffenberger C, Yamada J, Feldheim DA. Ephrin-As and patterned retinal activity act together in the development of topographic maps in the primary visual system. *J Neurosci*. Dec 13 2006;26(50):12873-84. doi:10.1523/jneurosci.3595-06.2006

135. Stellwagen D, Shatz CJ, Feller MB. Dynamics of retinal waves are controlled by cyclic AMP. *Neuron*. Nov 1999;24(3):673-85. doi:10.1016/s0896-6273(00)81121-6

136. Stellwagen D, Shatz CJ. An instructive role for retinal waves in the development of retinogeniculate connectivity. *Neuron*. Jan 31 2002;33(3):357-67. doi:10.1016/s0896-6273(02)00577-9

137. Cooper DM, Mons N, Karpen JW. Adenylyl cyclases and the interaction between calcium and cAMP signalling. *Nature*. Mar 30 1995;374(6521):421-4. doi:10.1038/374421a0

138. Ravary A, Muzerelle A, Hervé D, et al. Adenylate cyclase 1 as a key actor in the refinement of retinal projection maps. *J Neurosci*. Mar 15 2003;23(6):2228-38. doi:10.1523/jneurosci.23-06-02228.2003

139. Dhande OS, Bhatt S, Anishchenko A, et al. Role of adenylate cyclase 1 in retinofugal map development. *J Comp Neurol*. May 1 2012;520(7):1562-83. doi:10.1002/cne.23000

140. Nicol X, Muzerelle A, Rio JP, Métin C, Gaspar P. Requirement of adenylate cyclase 1 for the ephrin-A5-dependent retraction of exuberant retinal axons. *J Neurosci*. Jan 18 2006;26(3):862-72. doi:10.1523/jneurosci.3385-05.2006

141. Nicol X, Voyatzis S, Muzerelle A, et al. cAMP oscillations and retinal activity are permissive for ephrin signaling during the establishment of the retinotopic map. *Nat Neurosci*. Mar 2007;10(3):340-7. doi:10.1038/nn1842

142. Averaimo S, Assali A, Ros O, et al. A plasma membrane microdomain compartmentalizes ephrin-generated cAMP signals to prune developing retinal axon arbors. *Nat Commun*. Oct 3 2016;7:12896. doi:10.1038/ncomms12896

143. Dunn TA, Wang CT, Colicos MA, et al. Imaging of cAMP levels and protein kinase A activity reveals that retinal waves drive oscillations in second-messenger cascades. *J Neurosci*. Dec 6 2006;26(49):12807-15. doi:10.1523/jneurosci.3238-06.2006

144. Dunn TA, Storm DR, Feller MB. Calcium-dependent increases in protein kinase-A activity in mouse retinal ganglion cells are mediated by multiple adenylate cyclases. *PLoS One*. Nov 17 2009;4(11):e7877. doi:10.1371/journal.pone.0007877

145. Thies E, Davenport RW. Independent roles of Rho-GTPases in growth cone and axonal behavior. *J Neurobiol*. Feb 5 2003;54(2):358-69. doi:10.1002/neu.10135

146. Sahin M, Greer PL, Lin MZ, et al. Eph-dependent tyrosine phosphorylation of ephexin1 modulates growth cone collapse. *Neuron*. Apr 21 2005;46(2):191-204. doi:10.1016/j.neuron.2005.01.030

147. Roig-Puiggros S, Vigouroux RJ, Beckman D, et al. Construction and reconstruction of brain circuits: normal and pathological axon guidance. *J Neurochem*. Apr 2020;153(1):10-32. doi:10.1111/jnc.14900

148. McFadden K, Minshew NJ. Evidence for dysregulation of axonal growth and guidance in the etiology of ASD. *Front Hum Neurosci*. 2013;7:671. doi:10.3389/fnhum.2013.00671

149. Amaral DG, Schumann CM, Nordahl CW. Neuroanatomy of autism. *Trends Neurosci*. Mar 2008;31(3):137-45. doi:10.1016/j.tins.2007.12.005

150. Leinsinger GL, Heiss DT, Jassoy AG, Pfluger T, Hahn K, Danek A. Persistent mirror movements: functional MR imaging of the hand motor cortex. *Radiology*. May 1997;203(2):545-52. doi:10.1148/radiology.203.2.9114119

151. Srour M, Rivière JB, Pham JM, et al. Mutations in DCC cause congenital mirror movements. *Science*. Apr 30 2010;328(5978):592. doi:10.1126/science.1186463

152. Volk AE, Carter O, Fricke J, et al. Horizontal gaze palsy with progressive scoliosis: three novel ROBO3 mutations and descriptions of the phenotypes of four patients. *Mol Vis*. 2011;17:1978-86.

153. Nugent AA, Kolpak AL, Engle EC. Human disorders of axon guidance. *Curr Opin Neurobiol*. Oct 2012;22(5):837-43. doi:10.1016/j.conb.2012.02.006

154. Van Battum EY, Brignani S, Pasterkamp RJ. Axon guidance proteins in neurological disorders. *Lancet Neurol*. May 2015;14(5):532-46. doi:10.1016/s1474-4422(14)70257-1

155. Marsh APL, Edwards TJ, Galea C, et al. DCC mutation update: Congenital mirror movements, isolated agenesis of the corpus callosum, and developmental split brain syndrome. *Hum Mutat*. Jan 2018;39(1):23-39. doi:10.1002/humu.23361

156. Bellon A, Mann F. Keeping up with advances in axon guidance. *Curr Opin Neurobiol*. Dec 2018;53:183-191. doi:10.1016/j.conb.2018.09.004

157. Stoeckli ET. Understanding axon guidance: are we nearly there yet? *Development*. May 14 2018;145(10)doi:10.1242/dev.151415

158. Frei JA, Stoeckli ET. SynCAMs - From axon guidance to neurodevelopmental disorders. *Mol Cell Neurosci*. Jun 2017;81:41-48. doi:10.1016/j.mcn.2016.08.012

159. Bonanomi D. Axon pathfinding for locomotion. *Semin Cell Dev Biol*. Jan 2019;85:26-35. doi:10.1016/j.semcdb.2017.11.014

160. Howard LJ, Brown HE, Wadsworth BC, Evans TA. Midline axon guidance in the Drosophila embryonic central nervous system. *Semin Cell Dev Biol*. Jan 2019;85:13-25. doi:10.1016/j.semcdb.2017.11.029

161. Comer JD, Alvarez S, Butler SJ, Kaltschmidt JA. Commissural axon guidance in the developing spinal cord: from Cajal to the present day. *Neural Dev*. Sep 12 2019;14(1):9. doi:10.1186/s13064-019-0133-1

162. Komiyama T, Luo L. Development of wiring specificity in the olfactory system. *Curr Opin Neurobiol*. Feb 2006;16(1):67-73. doi:10.1016/j.conb.2005.12.002

163. Imai T. Positional information in neural map development: lessons from the olfactory system. *Development, growth & differentiation*. 2012;54(3):358-365.

164. Petrovic M, Schmucker D. Axonal wiring in neural development: Target-independent mechanisms help to establish precision and complexity. *BioEssays : news and reviews in molecular, cellular and developmental biology*. 2015;37(9):996-1004.

165. Wang L, Marquardt T. What axons tell each other: axon-axon signaling in nerve and circuit assembly. *Curr Opin Neurobiol*. Dec 2013;23(6):974-82. doi:10.1016/j.conb.2013.08.004

166. Landmesser L, Honig MG. Altered sensory projections in the chick hind limb following the early removal of motoneurons. *Dev Biol*. Dec 1986;118(2):511-31. doi:10.1016/0012-1606(86)90023-0

167. Honig MG, Lance-Jones C, Landmesser L. The development of sensory projection patterns in embryonic chick hindlimb under experimental conditions. *Dev Biol*. Dec 1986;118(2):532-48. doi:10.1016/0012-1606(86)90024-2

168. Swanson GJ, Lewis J. Sensory nerve routes in chick wing buds deprived of motor innervation. *J Embryol Exp Morphol*. Jun 1986;95:37-52.

169. Reh TA, Pitts E, Constantine-Paton M. The organization of the fibers in the optic nerve of normal and tectum-less Rana pipiens. *J Comp Neurol*. Aug 10 1983;218(3):282-96. doi:10.1002/cne.902180305

170. St John JA, Clarris HJ, McKeown S, Royal S, Key B. Sorting and convergence of primary olfactory axons are independent of the olfactory bulb. *J Comp Neurol*. Sep 15 2003;464(2):131-40. doi:10.1002/cne.10777

171. Hidalgo A, Brand AH. Targeted neuronal ablation: the role of pioneer neurons in guidance and fasciculation in the CNS of Drosophila. *Development*. Sep 1997;124(17):3253-62.

172. Pike SH, Melancon EF, Eisen JS. Pathfinding by zebrafish motoneurons in the absence of normal pioneer axons. *Development*. Apr 1992;114(4):825-31.

173. Pignata A, Ducuing H, Boubakar L, et al. A Spatiotemporal Sequence of Sensitization to Slits and Semaphorins Orchestrates Commissural Axon Navigation. *Cell Rep*. Oct 8 2019;29(2):347-362.e5. doi:10.1016/j.celrep.2019.08.098

174. Okumura M, Kato T, Miura M, Chihara T. Hierarchical axon targeting of Drosophila olfactory receptor neurons specified by the proneural transcription factors Atonal and Amos. *Genes to cells : devoted to molecular & cellular mechanisms*. 2016;21(1):53-64.

175. Whitlock KE, Westerfield M. A transient population of neurons pioneers the olfactory pathway in the zebrafish. *J Neurosci*. Nov 1 1998;18(21):8919-27. doi:10.1523/jneurosci.18-21-08919.1998

176. Bak M, Fraser SE. Axon fasciculation and differences in midline kinetics between pioneer and follower axons within commissural fascicles. *Development (Cambridge, England)*. 2003;130(20):4999-5008.

177. Šmít D, Fouquet C, Pincet F, Zapotocky M, Trembleau A. Axon tension regulates fasciculation/defasciculation through the control of axon shaft zippering. *eLife*. 2017;6:e19907.

178. Schwarting GA, Henion TR. Regulation and function of axon guidance and adhesion molecules during olfactory map formation. *J Cell Biochem*. Oct 2011;112(10):2663-71. doi:10.1002/jcb.23203

179. Siegenthaler D, Enneking E-M, Moreno E, Pielage J. L1CAM/Neuroglian controls the axon-axon interactions establishing layered and lobular mushroom body architecture. *The Journal of cell biology*. 2015;208(7):1003-1018.

180. Honig MG, Camilli SJ, Xue Q-S. Effects of L1 blockade on sensory axon outgrowth and pathfinding in the chick hindlimb. *Developmental biology*. 2002;243(1):137-154.

181. Honig MG, Rutishauser US. Changes in the segmental pattern of sensory neuron projections in the chick hindlimb under conditions of altered cell adhesion molecule function. *Dev Biol*. May 1 1996;175(2):325-37. doi:10.1006/dbio.1996.0118

182. Landmesser L, Dahm L, Schultz K, Rutishauser U. Distinct roles for adhesion molecules during innervation of embryonic chick muscle. *Dev Biol*. Dec 1988;130(2):645-70. doi:10.1016/0012-1606(88)90358-2

183. Thanos S, Bonhoeffer F, Rutishauser U. Fiber-fiber interaction and tectal cues influence the development of the chicken retinotectal projection. *Proc Natl Acad Sci U S A*. Mar 1984;81(6):1906-10. doi:10.1073/pnas.81.6.1906

184. Pollerberg GE, Mack TG. Cell adhesion molecule SC1/DMGRASP is expressed on growing axons of retina ganglion cells and is involved in mediating their extension on axons. *Dev Biol*. Oct 1994;165(2):670-87. doi:10.1006/dbio.1994.1284

185. Ott H, Bastmeyer M, Stuermer CA. Neurolin, the goldfish homolog of DM-GRASP, is involved in retinal axon pathfinding to the optic disk. *J Neurosci*. May 1 1998;18(9):3363-72. doi:10.1523/jneurosci.18-09-03363.1998

186. Thelen K, Maier B, Faber M, Albrecht C, Fischer P, Pollerberg GE. Translation of the cell adhesion molecule ALCAM in axonal growth cones - regulation and

functional importance. *J Cell Sci*. Feb 15 2012;125(Pt 4):1003-14. doi:10.1242/jcs.096149

187. Weiner JA, Koo SJ, Nicolas S, et al. Axon fasciculation defects and retinal dysplasias in mice lacking the immunoglobulin superfamily adhesion molecule BEN/ALCAM/SC1. *Mol Cell Neurosci*. Sep 2004;27(1):59-69. doi:10.1016/j.mcn.2004.06.005

188. Frei JA, Andermatt I, Gesemann M, Stoeckli ET. The SynCAM synaptic cell adhesion molecules are involved in sensory axon pathfinding by regulating axon-axon contacts. *Journal of cell science*. 2014;127(Pt 24):5288-5302.

189. Suter T, Blagburn SV, Fisher SE, Anderson-Keightly HM, D'Elia KP, Jaworski A. TAG-1 Multifunctionality Coordinates Neuronal Migration, Axon Guidance, and Fasciculation. *Cell Rep*. Jan 28 2020;30(4):1164-1177.e7. doi:10.1016/j.celrep.2019.12.085

190. Steimel A, Wong L, Najarro EH, Ackley BD, Garriga G, Hutter H. The Flamingo ortholog FMI-1 controls pioneer-dependent navigation of follower axons in C. elegans. *Development (Cambridge, England)*. 2010;137(21):3663-3673.

191. Hayashi S, Inoue Y, Kiyonari H, et al. Protocadherin-17 mediates collective axon extension by recruiting actin regulator complexes to interaxonal contacts. *Dev Cell*. Sep 29 2014;30(6):673-87. doi:10.1016/j.devcel.2014.07.015

192. Yoshida Y. Semaphorin signaling in vertebrate neural circuit assembly. *Front Mol Neurosci*. 2012;5:71. doi:10.3389/fnmol.2012.00071

193. Jongbloets BC, Pasterkamp RJ. Semaphorin signalling during development. *Development*. Sep 2014;141(17):3292-7. doi:10.1242/dev.105544

194. Yu L, Zhou Y, Cheng S, Rao Y. Plexin a-semaphorin-1a reverse signaling regulates photoreceptor axon guidance in Drosophila. *The Journal of neuroscience : the official journal of the Society for Neuroscience*. 2010;30(36):12151-12156.

195. Hsieh H-H, Chang W-T, Yu L, Rao Y. Control of axon-axon attraction by Semaphorin reverse signaling. *Proceedings of the National Academy of Sciences of the United States of America*. 2014;111(31):11383-11388.

196. Yu HH, Huang AS, Kolodkin AL. Semaphorin-1a acts in concert with the cell adhesion molecules fasciclin II and connectin to regulate axon fasciculation in Drosophila. *Genetics*. 2000;156(2):723-731.

197. Wolman MA, Regnery AM, Becker T, Becker CG, Halloran MC. Semaphorin3D regulates axon axon interactions by modulating levels of L1 cell adhesion molecule. *J Neurosci*. Sep 5 2007;27(36):9653-63. doi:10.1523/jneurosci.1741-07.2007

198. Castellani V, Chédotal A, Schachner M, Faivre-Sarrailh C, Rougon G. Analysis of the L1-deficient mouse phenotype reveals cross-talk between Sema3A and L1 signaling pathways in axonal guidance. *Neuron*. Aug 2000;27(2):237-49. doi:10.1016/s0896-6273(00)00033-7

199. Huettl RE, Soellner H, Bianchi E, Novitch BG, Huber AB. Npn-1 contributes to axon-axon interactions that differentially control sensory and motor innervation of the limb. *PLoS Biol*. Feb 2011;9(2):e1001020. doi:10.1371/journal.pbio.1001020

200. Luxey M, Jungas T, Laussu J, Audouard C, Garces A, Davy A. Eph:ephrin-B1 forward signaling controls fasciculation of sensory and motor axons. *Dev Biol*. Nov 15 2013;383(2):264-74. doi:10.1016/j.ydbio.2013.09.010

201. Jaworski A, Tessier-Lavigne M. Autocrine/juxtaparacrine regulation of axon fasciculation by Slit-Robo signaling. *Nat Neurosci*. Feb 5 2012;15(3):367-9. doi:10.1038/nn.3037

202. Shiau CE, Bronner-Fraser M. N-cadherin acts in concert with Slit1-Robo2 signaling in regulating aggregation of placode-derived cranial sensory neurons. *Development*. Dec 2009;136(24):4155-64. doi:10.1242/dev.034355

203. Boyer NP, Gupton SL. Revisiting Netrin-1: One Who Guides (Axons). *Front Cell Neurosci*. 2018;12:221. doi:10.3389/fncel.2018.00221

204. Islam SM, Shinmyo Y, Okafuji T, et al. Draxin, a repulsive guidance protein for spinal cord and forebrain commissures. *Science (New York, NY)*. 2009;323(5912):388-393.

205. Ahmed G, Shinmyo Y, Ohta K, et al. Draxin inhibits axonal outgrowth through the netrin receptor DCC. *J Neurosci*. Sep 28 2011;31(39):14018-23. doi:10.1523/jneurosci.0943-11.2011

206. Gao X, Metzger U, Panza P, et al. A Floor-Plate Extracellular Protein-Protein Interaction Screen Identifies Draxin as a Secreted Netrin-1 Antagonist. *Cell Rep*. Jul 28 2015;12(4):694-708. doi:10.1016/j.celrep.2015.06.047

207. Liu Y, Bhowmick T, Liu Y, et al. Structural Basis for Draxin-Modulated Axon Guidance and Fasciculation by Netrin-1 through DCC. *Neuron*. 2018;97(6):1261-1267.e4.

208. Berghuis P, Rajnicek AM, Morozov YM, et al. Hardwiring the brain: endocannabinoids shape neuronal connectivity. *Science*. May 25 2007;316(5828):1212-6. doi:10.1126/science.1137406

209. Mulder J, Aguado T, Keimpema E, et al. Endocannabinoid signaling controls pyramidal cell specification and long-range axon patterning. *Proc Natl Acad Sci U S A*. Jun 24 2008;105(25):8760-5. doi:10.1073/pnas.0803545105

210. Saez TM, Fernandez Bessone I, Rodriguez MS, et al. Kinesin-1-mediated axonal transport of CB1 receptors is required for cannabinoid-dependent axonal growth and guidance. *Development*. Apr 7 2020;doi:10.1242/dev.184069

211. Rash BG, Richards LJ. A role for cingulate pioneering axons in the development of the corpus callosum. *J Comp Neurol*. May 28 2001;434(2):147-57.

212. Bianco IH, Wilson SW. The habenular nuclei: a conserved asymmetric relay station in the vertebrate brain. *Philos Trans R Soc Lond B Biol Sci*. Apr 12 2009;364(1519):1005-20. doi:10.1098/rstb.2008.0213

213. Kowski AB, Veh RW, Weiss T. Dopaminergic activation excites rat lateral habenular neurons in vivo. *Neuroscience*. Jul 21 2009;161(4):1154-65. doi:10.1016/j.neuroscience.2009.04.026

214. Stamatakis AM, Jennings JH, Ung RL, et al. A unique population of ventral tegmental area neurons inhibits the lateral habenula to promote reward. *Neuron*. Nov 20 2013;80(4):1039-53. doi:10.1016/j.neuron.2013.08.023

215. Schmidt ERE, Brignani S, Adolfs Y, et al. Subdomain-mediated axon-axon signaling and chemoattraction cooperate to regulate afferent innervation of the lateral habenula. *Neuron*. 2014;83(2):372-387.

216. Molnar Z, Adams R, Blakemore C. Mechanisms underlying the early establishment of thalamocortical connections in the rat. *J Neurosci*. Aug 1 1998;18(15):5723-45.

217. Hevner RF, Miyashita-Lin E, Rubenstein JLR. Cortical and thalamic axon pathfinding defects in Tbr1, Gbx2, and Pax6 mutant mice: evidence that cortical and thalamic axons interact and guide each other. *The Journal of comparative neurology*. 2002;447(1):8-17.

218. Deck M, Lokmane L, Chauvet S, et al. Pathfinding of corticothalamic axons relies on a rendezvous with thalamic projections. *Neuron*. 2013;77(3):472-484.

219. Chen Y, Magnani D, Theil T, Pratt T, Price DJ. Evidence that descending cortical axons are essential for thalamocortical axons to cross the pallial-subpallial boundary in the embryonic forebrain. *PLoS One*. 2012;7(3):e33105. doi:10.1371/journal.pone.0033105

220. Wang L, Klein R, Zheng B, Marquardt T. Anatomical coupling of sensory and motor nerve trajectory via axon tracking. *Neuron*. 2011;71(2):263-277.

221. Grueber WB, Sagasti A. Self-avoidance and tiling: Mechanisms of dendrite and axon spacing. *Cold Spring Harb Perspect Biol*. Sep 2010;2(9):a001750. doi:10.1101/cshperspect.a001750

222. Peng J, Fabre PJ, Dolique T, et al. Sonic Hedgehog Is a Remotely Produced Cue that Controls Axon Guidance Trans-axonally at a Midline Choice Point. *Neuron*. Jan 17 2018;97(2):326-340.e4. doi:10.1016/j.neuron.2017.12.028

223. Araújo SJ, Tear G. Axon guidance mechanisms and molecules: lessons from invertebrates. *Nat Rev Neurosci*. Nov 2003;4(11):910-22. doi:10.1038/nrn1243

224. Yu HH, Araj HH, Ralls SA, Kolodkin AL. The transmembrane Semaphorin Sema I is required in Drosophila for embryonic motor and CNS axon guidance. *Neuron*. Feb 1998;20(2):207-20. doi:10.1016/s0896-6273(00)80450-x

225. Jeong S, Juhaszova K, Kolodkin AL. The Control of semaphorin-1a-mediated reverse signaling by opposing pebble and RhoGAPp190 functions in drosophila. *Neuron*. 2012;76(4):721-734.

226. Cho JY, Chak K, Andreone BJ, Wooley JR, Kolodkin AL. The extracellular matrix proteoglycan perlecan facilitates transmembrane semaphorin-mediated repulsive guidance. *Genes Dev*. Oct 1 2012;26(19):2222-35. doi:10.1101/gad.193136.112

227. Huang Z, Yazdani U, Thompson-Peer KL, Kolodkin AL, Terman JR. Crk-associated substrate (Cas) signaling protein functions with integrins to specify axon guidance during development. *Development*. Jun 2007;134(12):2337-47. doi:10.1242/dev.004242

228. Gallarda BW, Bonanomi D, Muller D, et al. Segregation of axial motor and sensory pathways via heterotypic trans-axonal signaling. *Science*. Apr 11 2008;320(5873):233-6. doi:10.1126/science.1153758

229. Nishikimi M, Oishi K, Tabata H, Torii K, Nakajima K. Segregation and pathfinding of callosal axons through EphA3 signaling. *The Journal of neuroscience : the official journal of the Society for Neuroscience*. 2011;31(45):16251-16260.

230. Zhou J, Wen Y, She L, et al. Axon position within the corpus callosum determines contralateral cortical projection. *Proc Natl Acad Sci U S A*. Jul 16 2013;110(29):E2714-23. doi:10.1073/pnas.1310233110

231. Molnar Z, Garel S, Lopez-Bendito G, Maness P, Price DJ. Mechanisms controlling the guidance of thalamocortical axons through the embryonic forebrain. *Eur J Neurosci*. May 2012;35(10):1573-85. doi:10.1111/j.1460-9568.2012.08119.x

232. Sakano H. Developmental regulation of olfactory circuit formation in mice. *Dev Growth Differ*. May 2020;62(4):199-213. doi:10.1111/dgd.12657

233. Imai T, Suzuki M, Sakano H. Odorant receptor-derived cAMP signals direct axonal targeting. *Science*. Oct 27 2006;314(5799):657-61. doi:10.1126/science.1131794

234. Chesler AT, Zou DJ, Le Pichon CE, et al. A G protein/cAMP signal cascade is required for axonal convergence into olfactory glomeruli. *Proc Natl Acad Sci U S A*. Jan 16 2007;104(3):1039-44. doi:10.1073/pnas.0609215104

235. Dang P, Fisher SA, Stefanik DJ, Kim J, Raper JA. Coordination of olfactory receptor choice with guidance receptor expression and function in olfactory sensory neurons. *PLoS Genet*. Jan 2018;14(1):e1007164. doi:10.1371/journal.pgen.1007164

236. Nakashima A, Takeuchi H, Imai T, et al. Agonist-independent GPCR activity regulates anterior-posterior targeting of olfactory sensory neurons. *Cell*. Sep 12 2013;154(6):1314-25. doi:10.1016/j.cell.2013.08.033

237. Kaneko M, Nighorn A. Interaxonal Eph-ephrin signaling may mediate sorting of olfactory sensory axons in Manduca sexta. *The Journal of neuroscience : the official journal of the Society for Neuroscience*. 2003;23(37):11523-11538.

238. Trowe T, Klostermann S, Baier H, et al. Mutations disrupting the ordering and topographic mapping of axons in the retinotectal projection of the zebrafish, Danio rerio. *Development*. Dec 1996;123:439-50.

239. Baudet ML, Zivraj KH, Abreu-Goodger C, et al. miR-124 acts through CoREST to control onset of Sema3A sensitivity in navigating retinal growth cones. *Nat Neurosci*. Dec 4 2011;15(1):29-38. doi:10.1038/nn.2979

240. Imai T, Sakano H. Axon-axon interactions in neuronal circuit assembly: lessons from olfactory map formation. *Eur J Neurosci*. Nov 2011;34(10):1647-54. doi:10.1111/j.1460-9568.2011.07817.x

241. Goyal G, Zierau A, Lattemann M, et al. Inter-axonal recognition organizes Drosophila olfactory map formation. *Sci Rep*. Aug 9 2019;9(1):11554. doi:10.1038/s41598-019-47924-9

242. Takeuchi H, Inokuchi K, Aoki M, et al. Sequential arrival and graded secretion of Sema3F by olfactory neuron axons specify map topography at the bulb. *Cell*. Jun 11 2010;141(6):1056-67. doi:10.1016/j.cell.2010.04.041

243. Sweeney LB, Couto A, Chou Y-H, et al. Temporal target restriction of olfactory receptor neurons by Semaphorin-1a/PlexinA-mediated axon-axon interactions. *Neuron*. 2007;53(2):185-200.

244. Sagasti A, Guido MR, Raible DW, Schier AF. Repulsive interactions shape the morphologies and functional arrangement of zebrafish peripheral sensory arbors. *Curr Biol*. May 10 2005;15(9):804-14. doi:10.1016/j.cub.2005.03.048

245. Gosse NJ, Nevin LM, Baier H. Retinotopic order in the absence of axon competition. *Nature*. Apr 17 2008;452(7189):892-5. doi:10.1038/nature06816

246. Triplett JW, Pfeiffenberger C, Yamada J, et al. Competition is a driving force in topographic mapping. *Proc Natl Acad Sci U S A*. Nov 22 2011;108(47):19060-5. doi:10.1073/pnas.1102834108

247. Senti K-A, Usui T, Boucke K, Greber U, Uemura T, Dickson BJ. Flamingo regulates R8 axon-axon and axon-target interactions in the Drosophila visual system. *Current biology : CB*. 2003;13(10):828-832.

248. Tomasi T, Hakeda-Suzuki S, Ohler S, Schleiffer A, Suzuki T. The transmembrane protein Golden goal regulates R8 photoreceptor axon-axon and axon-target interactions. *Neuron*. Mar 13 2008;57(5):691-704. doi:10.1016/j.neuron.2008.01.012

249. Hakeda-Suzuki S, Berger-Müller S, Tomasi T, et al. Golden Goal collaborates with Flamingo in conferring synaptic-layer specificity in the visual system. *Nat Neurosci*. Mar 2011;14(3):314-23. doi:10.1038/nn.2756

250. Millard SS, Flanagan JJ, Pappu KS, Wu W, Zipursky SL. Dscam2 mediates axonal tiling in the Drosophila visual system. *Nature*. Jun 7 2007;447(7145):720-4. doi:10.1038/nature05855

251. Katori S, Noguchi-Katori Y, Okayama A, et al. Protocadherin-αC2 is required for diffuse projections of serotonergic axons. *Sci Rep*. Nov 21 2017;7(1):15908. doi:10.1038/s41598-017-16120-y

252. Chen WV, Nwakeze CL, Denny CA, et al. Pcdhαc2 is required for axonal tiling and assembly of serotonergic circuitries in mice. *Science*. Apr 28 2017;356(6336):406-411. doi:10.1126/science.aal3231

253. Neukomm LJ, Freeman MR. Diverse cellular and molecular modes of axon degeneration. *Trends Cell Biol*. Sep 2014;24(9):515-23. doi:10.1016/j.tcb.2014.04.003

254. Bozza T, Vassalli A, Fuss S, et al. Mapping of class I and class II odorant receptors to glomerular domains by two distinct types of olfactory sensory neurons in the mouse. *Neuron*. Jan 29 2009;61(2):220-33. doi:10.1016/j.neuron.2008.11.010

255. Satoda M, Takagi S, Ohta K, Hirata T, Fujisawa H. Differential expression of two cell surface proteins, neuropilin and plexin, in Xenopus olfactory axon subclasses. *J Neurosci*. Jan 1995;15(1 Pt 2):942-55.

256. Johnson KG, Ghose A, Epstein E, Lincecum J, O'Connor MB, Van Vactor D. Axonal heparan sulfate proteoglycans regulate the distribution and efficiency of the repellent slit during midline axon guidance. *Curr Biol*. Mar 23 2004;14(6):499-504. doi:10.1016/j.cub.2004.02.005

257. Smart AD, Course MM, Rawson J, Selleck S, Van Vactor D, Johnson KG. Heparan sulfate proteoglycan specificity during axon pathway formation in the Drosophila embryo. *Dev Neurobiol*. Jul 2011;71(7):608-18. doi:10.1002/dneu.20854

258. Steigemann P, Molitor A, Fellert S, Jäckle H, Vorbrüggen G. Heparan sulfate proteoglycan syndecan promotes axonal and myotube guidance by slit/robo signaling. *Curr Biol*. Feb 3 2004;14(3):225-30. doi:10.1016/j.cub.2004.01.006

259. Gysi S, Rhiner C, Flibotte S, Moerman DG, Hengartner MO. A network of HSPG core proteins and HS modifying enzymes regulates netrin-dependent guidance of D-type motor neurons in Caenorhabditis elegans. *PLoS One*. 2013;8(9):e74908. doi:10.1371/journal.pone.0074908

260. Rhiner C, Gysi S, Fröhli E, Hengartner MO, Hajnal A. Syndecan regulates cell migration and axon guidance in C. elegans. *Development*. Oct 2005;132(20):4621-33. doi:10.1242/dev.02042

261. Wilson NH, Stoeckli ET. Sonic hedgehog regulates its own receptor on postcrossing commissural axons in a glypican1-dependent manner. *Neuron*. Aug 7 2013;79(3):478-91. doi:10.1016/j.neuron.2013.05.025

262. Matsumoto Y, Irie F, Inatani M, Tessier-Lavigne M, Yamaguchi Y. Netrin-1/DCC signaling in commissural axon guidance requires cell-autonomous expression of

heparan sulfate. *J Neurosci*. Apr 18 2007;27(16):4342-50. doi:10.1523/jneurosci.0700-07.2007

263. Corredor M, Bonet R, Moure A, et al. Cationic Peptides and Peptidomimetics Bind Glycosaminoglycans as Potential Sema3A Pathway Inhibitors. *Biophys J*. Mar 29 2016;110(6):1291-303. doi:10.1016/j.bpj.2016.01.033

264. De Wit J, De Winter F, Klooster J, Verhaagen J. Semaphorin 3A displays a punctate distribution on the surface of neuronal cells and interacts with proteoglycans in the extracellular matrix. *Mol Cell Neurosci*. May 2005;29(1):40-55. doi:10.1016/j.mcn.2004.12.009

265. Thacker BE, Seamen E, Lawrence R, et al. Expanding the 3-O-Sulfate Proteome--Enhanced Binding of Neuropilin-1 to 3-O-Sulfated Heparan Sulfate Modulates Its Activity. *ACS Chem Biol*. Apr 15 2016;11(4):971-80. doi:10.1021/acschembio.5b00897

266. Hindges R, McLaughlin T, Genoud N, Henkemeyer M, O'Leary D. EphB forward signaling controls directional branch extension and arborization required for dorsal-ventral retinotopic mapping. *Neuron*. Aug 1 2002;35(3):475-87.

267. Thakar S, Chenaux G, Henkemeyer M. Critical roles for EphB and ephrin-B bidirectional signalling in retinocollicular mapping. *Nat Commun*. Aug 16 2011;2:431. doi:10.1038/ncomms1445

268. Plas DT, Dhande OS, Lopez JE, et al. Bone morphogenetic proteins, eye patterning, and retinocollicular map formation in the mouse. *J Neurosci*. Jul 9 2008;28(28):7057-67. doi:10.1523/jneurosci.3598-06.2008

269. Chiang A, Priya R, Ramaswami M, Vijayraghavan K, Rodrigues V. Neuronal activity and Wnt signaling act through Gsk3-beta to regulate axonal integrity in mature

Drosophila olfactory sensory neurons. *Development*. Apr 2009;136(8):1273-82. doi:10.1242/dev.031377

270. Hayashi Y, Hirotsu T, Iwata R, et al. A trophic role for Wnt-Ror kinase signaling during developmental pruning in Caenorhabditis elegans. *Nat Neurosci*. Aug 2009;12(8):981-7. doi:10.1038/nn.2347

271. Lu M, Mizumoto K. Gradient-independent Wnt signaling instructs asymmetric neurite pruning in C. elegans. *Elife*. Dec 5 2019;8doi:10.7554/eLife.50583

272. Antinucci P, Nikolaou N, Meyer MP, Hindges R. Teneurin-3 specifies morphological and functional connectivity of retinal ganglion cells in the vertebrate visual system. *Cell Rep*. Nov 14 2013;5(3):582-92. doi:10.1016/j.celrep.2013.09.045

273. Leamey CA, Merlin S, Lattouf P, et al. Ten_m3 regulates eye-specific patterning in the mammalian visual pathway and is required for binocular vision. *PLoS biology*. 2007;5(9):e241-e241.

274. Beckmann J, Schubert R, Chiquet-Ehrismann R, Müller DJ. Deciphering teneurin domains that facilitate cellular recognition, cell-cell adhesion, and neurite outgrowth using atomic force microscopy-based single-cell force spectroscopy. *Nano Lett*. Jun 12 2013;13(6):2937-46. doi:10.1021/nl4013248

275. Hong W, Mosca TJ, Luo L. Teneurins instruct synaptic partner matching in an olfactory map. *Nature*. Mar 18 2012;484(7393):201-7. doi:10.1038/nature10926

276. Mosca TJ, Hong W, Dani VS, Favaloro V, Luo L. Trans-synaptic Teneurin signalling in neuromuscular synapse organization and target choice. *Nature*. Mar 18 2012;484(7393):237-41. doi:10.1038/nature10923

277. Young TR, Bourke M, Zhou X, et al. Ten-m2 is required for the generation of binocular visual circuits. *J Neurosci*. Jul 24 2013;33(30):12490-509. doi:10.1523/jneurosci.4708-12.2013

278. Berns DS, DeNardo LA, Pederick DT, Luo L. Teneurin-3 controls topographic circuit assembly in the hippocampus. *Nature*. Feb 15 2018;554(7692):328-333. doi:10.1038/nature25463

279. Kimmel CB, Ballard WW, Kimmel SR, Ullmann B, Schilling TF. Stages of embryonic development of the zebrafish. *Dev Dyn*. Jul 1995;203(3):253-310. doi:10.1002/aja.1002030302

280. Picker A, Brand M. Fgf signals from a novel signaling center determine axial patterning of the prospective neural retina. *Development*. Nov 2005;132(22):4951-62. doi:10.1242/dev.02071

281. Schindelin J, Arganda-Carreras I, Frise E, et al. Fiji: an open-source platform for biological-image analysis. *Nat Methods*. Jun 28 2012;9(7):676-82. doi:10.1038/nmeth.2019

282. Schneider CA, Rasband WS, Eliceiri KW. NIH Image to ImageJ: 25 years of image analysis. *Nat Methods*. Jul 2012;9(7):671-5. doi:10.1038/nmeth.2089

283. Parant JM, George SA, Pryor R, Wittwer CT, Yost HJ. A rapid and efficient method of genotyping zebrafish mutants. *Dev Dyn*. Dec 2009;238(12):3168-74. doi:10.1002/dvdy.22143

284. Kay JN, Finger-Baier KC, Roeser T, Staub W, Baier H. Retinal ganglion cell genesis requires lakritz, a Zebrafish atonal Homolog. *Neuron*. Jun 2001;30(3):725-36.

285. Kwan KM, Fujimoto E, Grabher C, et al. The Tol2kit: a multisite gateway-based construction kit for Tol2 transposon transgenesis constructs. *Dev Dyn*. Nov 2007;236(11):3088-99. doi:10.1002/dvdy.21343

286. McCormick C, Duncan G, Goutsos KT, Tufaro F. The putative tumor suppressors EXT1 and EXT2 form a stable complex that accumulates in the Golgi apparatus and catalyzes the synthesis of heparan sulfate. *Proc Natl Acad Sci U S A*. Jan 18 2000;97(2):668-73. doi:10.1073/pnas.97.2.668

287. Kawakami K, Shima A, Kawakami N. Identification of a functional transposase of the Tol2 element, an Ac-like element from the Japanese medaka fish, and its transposition in the zebrafish germ lineage. *Proc Natl Acad Sci U S A*. Oct 10 2000;97(21):11403-8. doi:10.1073/pnas.97.21.11403

288. Meijering EH, Niessen WJ, Viergever MA. Quantitative evaluation of convolution-based methods for medical image interpolation. *Med Image Anal*. Jun 2001;5(2):111-26. doi:10.1016/s1361-8415(00)00040-2

289. Gupta M, Brand M. Identification and expression analysis of zebrafish glypicans during embryonic development. *PLoS One*. 2013;8(11):e80824. doi:10.1371/journal.pone.0080824

290. Hofmeister W, Devine CA, Key B. Distinct expression patterns of syndecans in the embryonic zebrafish brain. *Gene Expr Patterns*. Mar-Apr 2013;13(3-4):126-32. doi:10.1016/j.gep.2013.02.002

291. Gosse NJ, Baier H. An essential role for Radar (Gdf6a) in inducing dorsal fate in the zebrafish retina. *Proc Natl Acad Sci U S A*. Feb 17 2009;106(7):2236-41. doi:10.1073/pnas.0803202106

292. French CR, Erickson T, French DV, Pilgrim DB, Waskiewicz AJ. Gdf6a is required for the initiation of dorsal-ventral retinal patterning and lens development. *Dev Biol*. Sep 1 2009;333(1):37-47. doi:10.1016/j.ydbio.2009.06.018

293. Varshney GK, Pei W, LaFave MC, et al. High-throughput gene targeting and phenotyping in zebrafish using CRISPR/Cas9. *Genome Res*. Jul 2015;25(7):1030-42. doi:10.1101/gr.186379.114

294. Chang N, Sun C, Gao L, et al. Genome editing with RNA-guided Cas9 nuclease in zebrafish embryos. *Cell Res*. Apr 2013;23(4):465-72. doi:10.1038/cr.2013.45

295. Koshiba-Takeuchi K, Takeuchi JK, Matsumoto K, et al. Tbx5 and the retinotectum projection. *Science*. Jan 7 2000;287(5450):134-7. doi:10.1126/science.287.5450.134

296. Zhang L, David G, Esko JD. Repetitive Ser-Gly sequences enhance heparan sulfate assembly in proteoglycans. *J Biol Chem*. Nov 10 1995;270(45):27127-35. doi:10.1074/jbc.270.45.27127

297. Cheung A, Trevers KE, Reyes-Corral M, Antinucci P, Hindges R. Expression and Roles of Teneurins in Zebrafish. *Front Neurosci*. 2019;13:158. doi:10.3389/fnins.2019.00158

298. Antinucci P, Suleyman O, Monfries C, Hindges R. Neural Mechanisms Generating Orientation Selectivity in the Retina. *Curr Biol*. Jul 25 2016;26(14):1802-15. doi:10.1016/j.cub.2016.05.035

299. Topczewski J, Sepich DS, Myers DC, et al. The zebrafish glypican knypek controls cell polarity during gastrulation movements of convergent extension. *Dev Cell*. Aug 2001;1(2):251-64. doi:10.1016/s1534-5807(01)00005-3

300. Lin X, Perrimon N. Dally cooperates with Drosophila Frizzled 2 to transduce Wingless signalling. *Nature*. Jul 15 1999;400(6741):281-4. doi:10.1038/22343

301. Song HH, Shi W, Xiang YY, Filmus J. The loss of glypican-3 induces alterations in Wnt signaling. *J Biol Chem*. Jan 21 2005;280(3):2116-25. doi:10.1074/jbc.M410090200

302. Yan D, Lin X. Drosophila glypican Dally-like acts in FGF-receiving cells to modulate FGF signaling during tracheal morphogenesis. *Dev Biol*. Dec 1 2007;312(1):203-16. doi:10.1016/j.ydbio.2007.09.015

303. Ohkawara B, Yamamoto TS, Tada M, Ueno N. Role of glypican 4 in the regulation of convergent extension movements during gastrulation in Xenopus laevis. *Development*. May 2003;130(10):2129-38. doi:10.1242/dev.00435

304. Desbordes SC, Sanson B. The glypican Dally-like is required for Hedgehog signalling in the embryonic epidermis of Drosophila. *Development*. Dec 2003;130(25):6245-55. doi:10.1242/dev.00874

305. Jackson SM, Nakato H, Sugiura M, et al. dally, a Drosophila glypican, controls cellular responses to the TGF-beta-related morphogen, Dpp. *Development*. Oct 1997;124(20):4113-20.

306. Capurro MI, Xu P, Shi W, Li F, Jia A, Filmus J. Glypican-3 inhibits Hedgehog signaling during development by competing with patched for Hedgehog binding. *Dev Cell*. May 2008;14(5):700-11. doi:10.1016/j.devcel.2008.03.006

307. Cano-Gauci DF, Song HH, Yang H, et al. Glypican-3-deficient mice exhibit developmental overgrowth and some of the abnormalities typical of Simpson-Golabi-Behmel syndrome. *J Cell Biol*. Jul 12 1999;146(1):255-64. doi:10.1083/jcb.146.1.255

308. Pilia G, Hughes-Benzie RM, MacKenzie A, et al. Mutations in GPC3, a glypican gene, cause the Simpson-Golabi-Behmel overgrowth syndrome. *Nat Genet*. Mar 1996;12(3):241-7. doi:10.1038/ng0396-241

309. Vuillaume ML, Moizard MP, Rossignol S, et al. Mutation update for the GPC3 gene involved in Simpson-Golabi-Behmel syndrome and review of the literature. *Hum Mutat*. Jun 2018;39(6):790-805. doi:10.1002/humu.23428

310. Mosca TJ, Luo L. Synaptic organization of the Drosophila antennal lobe and its regulation by the Teneurins. *Elife*. Oct 13 2014;3:e03726. doi:10.7554/eLife.03726

311. Leamey CA, Glendining KA, Kreiman G, et al. Differential gene expression between sensory neocortical areas: potential roles for Ten_m3 and Bcl6 in patterning visual and somatosensory pathways. *Cereb Cortex*. Jan 2008;18(1):53-66. doi:10.1093/cercor/bhm031

312. Drabikowski K, Trzebiatowska A, Chiquet-Ehrismann R. ten-1, an essential gene for germ cell development, epidermal morphogenesis, gonad migration, and neuronal pathfinding in Caenorhabditis elegans. *Dev Biol*. Jun 1 2005;282(1):27-38. doi:10.1016/j.ydbio.2005.02.017

313. O'Sullivan ML, de Wit J, Savas JN, et al. FLRT proteins are endogenous latrophilin ligands and regulate excitatory synapse development. *Neuron*. Mar 8 2012;73(5):903-10. doi:10.1016/j.neuron.2012.01.018

314. Silva JP, Lelianova VG, Ermolyuk YS, et al. Latrophilin 1 and its endogenous ligand Lasso/teneurin-2 form a high-affinity transsynaptic receptor pair with signaling capabilities. *Proc Natl Acad Sci U S A*. Jul 19 2011;108(29):12113-8. doi:10.1073/pnas.1019434108

315. Sando R, Jiang X, Südhof TC. Latrophilin GPCRs direct synapse specificity by coincident binding of FLRTs and teneurins. *Science*. Feb 22 2019;363(6429)doi:10.1126/science.aav7969

316. Boucard AA, Maxeiner S, Südhof TC. Latrophilins function as heterophilic cell-adhesion molecules by binding to teneurins: regulation by alternative splicing. *J Biol Chem*. Jan 3 2014;289(1):387-402. doi:10.1074/jbc.M113.504779

317. Vysokov NV, Silva JP, Lelianova VG, et al. Proteolytically released Lasso/teneurin-2 induces axonal attraction by interacting with latrophilin-1 on axonal growth cones. *Elife*. Nov 20 2018;7doi:10.7554/eLife.37935

318. Del Toro D, Carrasquero-Ordaz MA, Chu A, et al. Structural Basis of Teneurin-Latrophilin Interaction in Repulsive Guidance of Migrating Neurons. *Cell*. Jan 23 2020;180(2):323-339.e19. doi:10.1016/j.cell.2019.12.014

319. Tucker RP, Chiquet-Ehrismann R. Teneurins: a conserved family of transmembrane proteins involved in intercellular signaling during development. *Dev Biol*. Feb 15 2006;290(2):237-45. doi:10.1016/j.ydbio.2005.11.038

320. Oohashi T, Zhou XH, Feng K, et al. Mouse ten-m/Odz is a new family of dimeric type II transmembrane proteins expressed in many tissues. *J Cell Biol*. May 3 1999;145(3):563-77. doi:10.1083/jcb.145.3.563

321. Li J, Shalev-Benami M, Sando R, et al. Structural Basis for Teneurin Function in Circuit-Wiring: A Toxin Motif at the Synapse. *Cell*. Apr 19 2018;173(3):735-748.e15. doi:10.1016/j.cell.2018.03.036

322. Tucker RP, Beckmann J, Leachman NT, Schöler J, Chiquet-Ehrismann R. Phylogenetic analysis of the teneurins: conserved features and premetazoan ancestry. *Mol Biol Evol*. Mar 2012;29(3):1019-29. doi:10.1093/molbev/msr271

323. Zimmer M, Palmer A, Köhler J, Klein R. EphB-ephrinB bi-directional endocytosis terminates adhesion allowing contact mediated repulsion. *Nat Cell Biol*. Oct 2003;5(10):869-78. doi:10.1038/ncb1045

324. Marston DJ, Dickinson S, Nobes CD. Rac-dependent trans-endocytosis of ephrinBs regulates Eph-ephrin contact repulsion. *Nat Cell Biol*. Oct 2003;5(10):879-88. doi:10.1038/ncb1044

325. Scholz N, Guan C, Nieberler M, et al. Mechano-dependent signaling by Latrophilin/CIRL quenches cAMP in proprioceptive neurons. *Elife*. Aug 8 2017;6doi:10.7554/eLife.28360

326. Winkler J, Prömel S. The adhesion GPCR latrophilin - a novel signaling cascade in oriented cell division and anterior-posterior polarity. *Worm*. Apr-Jun 2016;5(2):e1170274. doi:10.1080/21624054.2016.1170274

327. Ovando-Zambrano JC, Arias-Montaño JA, Boucard AA. Alternative splicing event modifying ADGRL1/latrophilin-1 cytoplasmic tail promotes both opposing and dual cAMP signaling pathways. *Ann N Y Acad Sci*. Nov 2019;1456(1):168-185. doi:10.1111/nyas.14198

328. Martinez AF, Abe Y, Hong S, et al. An Ultraconserved Brain-Specific Enhancer Within ADGRL3 (LPHN3) Underpins Attention-Deficit/Hyperactivity Disorder Susceptibility. *Biol Psychiatry*. Dec 15 2016;80(12):943-954. doi:10.1016/j.biopsych.2016.06.026

329. Lange M, Norton W, Coolen M, et al. The ADHD-susceptibility gene lphn3.1 modulates dopaminergic neuron formation and locomotor activity during zebrafish development. *Mol Psychiatry*. Sep 2012;17(9):946-54. doi:10.1038/mp.2012.29

330. Filmus J, Capurro M, Rast J. Glypicans. *Genome Biol*. 2008;9(5):224. doi:10.1186/gb-2008-9-5-224

331. Capurro M, Martin T, Shi W, Filmus J. Glypican-3 binds to Frizzled and plays a direct role in the stimulation of canonical Wnt signaling. *J Cell Sci*. Apr 1 2014;127(Pt 7):1565-75. doi:10.1242/jcs.140871

332. Capurro MI, Shi W, Filmus J. LRP1 mediates Hedgehog-induced endocytosis of the GPC3-Hedgehog complex. *J Cell Sci*. Jul 15 2012;125(Pt 14):3380-9. doi:10.1242/jcs.098889

333. Gallet A, Staccini-Lavenant L, Thérond PP. Cellular trafficking of the glypican Dally-like is required for full-strength Hedgehog signaling and wingless transcytosis. *Dev Cell*. May 2008;14(5):712-25. doi:10.1016/j.devcel.2008.03.001

334. Christianson HC, Belting M. Heparan sulfate proteoglycan as a cell-surface endocytosis receptor. *Matrix Biol*. Apr 2014;35:51-5. doi:10.1016/j.matbio.2013.10.004

335. Minet AD, Rubin BP, Tucker RP, Baumgartner S, Chiquet-Ehrismann R. Teneurin-1, a vertebrate homologue of the Drosophila pair-rule gene ten-m, is a neuronal protein with a novel type of heparin-binding domain. *J Cell Sci*. Jun 1999;112 (Pt 12):2019-32.

336. Huberman AD, Feller MB, Chapman B. Mechanisms underlying development of visual maps and receptive fields. *Annu Rev Neurosci*. 2008;31:479-509. doi:10.1146/annurev.neuro.31.060407.125533

337. Assali A, Gaspar P, Rebsam A. Activity dependent mechanisms of visual map formation--from retinal waves to molecular regulators. *Semin Cell Dev Biol*. Nov 2014;35:136-46. doi:10.1016/j.semcdb.2014.08.008

338. Kutsarova E, Munz M, Ruthazer ES. Rules for Shaping Neural Connections in the Developing Brain. *Front Neural Circuits*. 2016;10:111. doi:10.3389/fncir.2016.00111

339. Leighton AH, Lohmann C. The Wiring of Developing Sensory Circuits-From Patterned Spontaneous Activity to Synaptic Plasticity Mechanisms. *Front Neural Circuits*. 2016;10:71. doi:10.3389/fncir.2016.00071

340. Thompson A, Gribizis A, Chen C, Crair MC. Activity-dependent development of visual receptive fields. *Curr Opin Neurobiol*. Feb 2017;42:136-143. doi:10.1016/j.conb.2016.12.007

341. Louail A, Sierksma MC, Chaffiol A, et al. cAMP-Dependent Co-stabilization of Axonal Arbors from Adjacent Developing Neurons. *Cell Rep*. Oct 6 2020;33(1):108220. doi:10.1016/j.celrep.2020.108220

342. Suetterlin P, Marler KM, Drescher U. Axonal ephrinA/EphA interactions, and the emergence of order in topographic projections. *Semin Cell Dev Biol*. Feb 2012;23(1):1-6. doi:10.1016/j.semcdb.2011.10.015

343. Weth F, Fiederling F, Gebhardt C, Bastmeyer M. Chemoaffinity in topographic mapping revisited--is it more about fiber-fiber than fiber-target interactions? *Seminars in cell & developmental biology*. 2014;35:126-135.

344. Förster D, Helmbrecht TO, Mearns DS, Jordan L, Mokayes N, Baier H. Retinotectal circuitry of larval zebrafish is adapted to detection and pursuit of prey. *Elife*. Oct 12 2020;9doi:10.7554/eLife.58596

345. Poulain FE, Gaynes JA, Stacher Hörndli C, Law MY, Chien CB. Analyzing retinal axon guidance in zebrafish. *Methods Cell Biol*. 2010;100:3-26. doi:10.1016/b978-0-12-384892-5.00001-3

346. Baier H, Klostermann S, Trowe T, Karlstrom RO, Nüsslein-Volhard C, Bonhoeffer F. Genetic dissection of the retinotectal projection. *Development*. Dec 1996;123:415-25.

347. Harvey BM, Baxter M, Granato M. Optic nerve regeneration in larval zebrafish exhibits spontaneous capacity for retinotopic but not tectum specific axon targeting. *PLoS One*. 2019;14(6):e0218667. doi:10.1371/journal.pone.0218667

348. Xiao T, Roeser T, Staub W, Baier H. A GFP-based genetic screen reveals mutations that disrupt the architecture of the zebrafish retinotectal projection. *Development*. Jul 2005;132(13):2955-67. doi:10.1242/dev.01861

349. Kawakami K, Asakawa K, Hibi M, Itoh M, Muto A, Wada H. Gal4 Driver Transgenic Zebrafish: Powerful Tools to Study Developmental Biology, Organogenesis, and Neuroscience. *Adv Genet*. 2016;95:65-87. doi:10.1016/bs.adgen.2016.04.002

350. Portugues R, Severi KE, Wyart C, Ahrens MB. Optogenetics in a transparent animal: circuit function in the larval zebrafish. *Curr Opin Neurobiol*. Feb 2013;23(1):119-26. doi:10.1016/j.conb.2012.11.001

351. Robles E. The power of projectomes: genetic mosaic labeling in the larval zebrafish brain reveals organizing principles of sensory circuits. *J Neurogenet*. Sep 2017;31(3):61-69. doi:10.1080/01677063.2017.1359834

352. Granato M, van Eeden FJ, Schach U, et al. Genes controlling and mediating locomotion behavior of the zebrafish embryo and larva. *Development*. Dec 1996;123:399-413.

353. Kishore S, Fetcho JR. Homeostatic regulation of dendritic dynamics in a motor map in vivo. *Nat Commun*. 2013;4:2086. doi:10.1038/ncomms3086

354. Eckardt D, Theis M, Döring B, Speidel D, Willecke K, Ott T. Spontaneous ectopic recombination in cell-type-specific Cre mice removes loxP-flanked marker cassettes in vivo. *Genesis*. Apr 2004;38(4):159-65. doi:10.1002/gene.20011

355. Luo L, Ambrozkiewicz MC, Benseler F, et al. Optimizing Nervous System-Specific Gene Targeting with Cre Driver Lines: Prevalence of Germline Recombination and Influencing Factors. *Neuron*. Apr 8 2020;106(1):37-65.e5. doi:10.1016/j.neuron.2020.01.008

356. Schmidt-Supprian M, Rajewsky K. Vagaries of conditional gene targeting. *Nat Immunol*. Jul 2007;8(7):665-8. doi:10.1038/ni0707-665

357. Wan Y, Otsuna H, Chien CB, Hansen C. FluoRender: An Application of 2D Image Space Methods for 3D and 4D Confocal Microscopy Data Visualization in Neurobiology Research. *IEEE Pac Vis Symp*. 2012:201-208. doi:10.1109/pacificvis.2012.6183592

358. Wan Y, Otsuna H, Holman HA, et al. FluoRender: joint freehand segmentation and visualization for many-channel fluorescence data analysis. *BMC Bioinformatics*. May 26 2017;18(1):280. doi:10.1186/s12859-017-1694-9

359. Lord SJ, Velle KB, Mullins RD, Fritz-Laylin LK. SuperPlots: Communicating reproducibility and variability in cell biology. *J Cell Biol*. Jun 1 2020;219(6)doi:10.1083/jcb.202001064

360. Boisset G, Schorderet DF. Zebrafish hmx1 promotes retinogenesis. *Exp Eye Res*. Dec 2012;105:34-42. doi:10.1016/j.exer.2012.10.002

361. Marcelli F, Boisset G, Schorderet DF. A dimerized HMX1 inhibits EPHA6/epha4b in mouse and zebrafish retinas. *PLoS One*. 2014;9(6):e100096. doi:10.1371/journal.pone.0100096

362. Takahashi H, Shintani T, Sakuta H, Noda M. CBF1 controls the retinotectal topographical map along the anteroposterior axis through multiple mechanisms. *Development*. Nov 2003;130(21):5203-15. doi:10.1242/dev.00724

363. Takahashi H, Sakuta H, Shintani T, Noda M. Functional mode of FoxD1/CBF2 for the establishment of temporal retinal specificity in the developing chick retina. *Dev Biol*. Jul 15 2009;331(2):300-10. doi:10.1016/j.ydbio.2009.05.549

364. Yoshiura K, Leysens NJ, Reiter RS, Murray JC. Cloning, characterization, and mapping of the mouse homeobox gene Hmx1. *Genomics*. May 15 1998;50(1):61-8.

365. Kwan KM, Otsuna H, Kidokoro H, Carney KR, Saijoh Y, Chien CB. A complex choreography of cell movements shapes the vertebrate eye. *Development*. Jan 2012;139(2):359-72. doi:10.1242/dev.071407

366. Adamska M, Wolff A, Kreusler M, Wittbrodt J, Braun T, Bober E. Five Nkx5 genes show differential expression patterns in anlagen of sensory organs in medaka: insight into the evolution of the gene family. *Dev Genes Evol*. Jul 2001;211(7):338-49. doi:10.1007/s004270100162

367. Wotton KR, Weierud FK, Juárez-Morales JL, Alvares LE, Dietrich S, Lewis KE. Conservation of gene linkage in dispersed vertebrate NK homeobox clusters. *Dev Genes Evol*. Oct 2009;219(9-10):481-96. doi:10.1007/s00427-009-0311-y

368. Deitcher DL, Fekete DM, Cepko CL. Asymmetric expression of a novel homeobox gene in vertebrate sensory organs. *J Neurosci*. Feb 1994;14(2):486-98. doi:10.1523/jneurosci.14-02-00486.1994

369. Bonn S, Zinzen RP, Girardot C, et al. Tissue-specific analysis of chromatin state identifies temporal signatures of enhancer activity during embryonic development. *Nat Genet*. Jan 8 2012;44(2):148-56. doi:10.1038/ng.1064

370. Heintzman ND, Stuart RK, Hon G, et al. Distinct and predictive chromatin signatures of transcriptional promoters and enhancers in the human genome. *Nat Genet*. Mar 2007;39(3):311-8. doi:10.1038/ng1966

371. Heintzman ND, Hon GC, Hawkins RD, et al. Histone modifications at human enhancers reflect global cell-type-specific gene expression. *Nature*. May 7 2009;459(7243):108-12. doi:10.1038/nature07829

372. Rada-Iglesias A, Bajpai R, Swigut T, Brugmann SA, Flynn RA, Wysocka J. A unique chromatin signature uncovers early developmental enhancers in humans. *Nature*. Feb 10 2011;470(7333):279-83. doi:10.1038/nature09692

373. Bogdanovic O, Fernandez-Minan A, Tena JJ, et al. Dynamics of enhancer chromatin signatures mark the transition from pluripotency to cell specification during embryogenesis. *Genome Res*. Oct 2012;22(10):2043-53. doi:10.1101/gr.134833.111

374. Moriyoshi K, Richards LJ, Akazawa C, O'Leary DD, Nakanishi S. Labeling neural cells using adenoviral gene transfer of membrane-targeted GFP. *Neuron*. Feb 1996;16(2):255-60. doi:10.1016/s0896-6273(00)80044-6

375. Irimia M, Tena JJ, Alexis MS, et al. Extensive conservation of ancient microsynteny across metazoans due to cis-regulatory constraints. *Genome Res*. Dec 2012;22(12):2356-67. doi:10.1101/gr.139725.112

376. Woolfe A, Goodson M, Goode DK, et al. Highly conserved non-coding sequences are associated with vertebrate development. *PLoS Biol*. Jan 2005;3(1):e7. doi:10.1371/journal.pbio.0030007

377. Hu M, Easter SS. Retinal neurogenesis: the formation of the initial central patch of postmitotic cells. *Dev Biol*. Mar 15 1999;207(2):309-21. doi:10.1006/dbio.1998.9031

378. Laessing U, Stuermer CA. Spatiotemporal pattern of retinal ganglion cell differentiation revealed by the expression of neurolin in embryonic zebrafish. *J Neurobiol*. Jan 1996;29(1):65-74. doi:10.1002/(sici)1097-4695(199601)29:1<65::aid-neu5>3.0.co;2-5

379. Schmitt EA, Dowling JE. Early retinal development in the zebrafish, Danio rerio: light and electron microscopic analyses. *J Comp Neurol*. Feb 22 1999;404(4):515-36.

380. Kawakami K. Tol2: a versatile gene transfer vector in vertebrates. *Genome Biol*. 2007;8 Suppl 1(Suppl 1):S7. doi:10.1186/gb-2007-8-s1-s7

381. Mosimann C, Kaufman CK, Li P, Pugach EK, Tamplin OJ, Zon LI. Ubiquitous transgene expression and Cre-based recombination driven by the ubiquitin promoter in zebrafish. *Development*. Jan 2011;138(1):169-77. doi:10.1242/dev.059345

382. Yoshikawa S, Kawakami K, Zhao XC. G2R Cre reporter transgenic zebrafish. *Dev Dyn*. Sep 2008;237(9):2460-5. doi:10.1002/dvdy.21673

383. Carmean V, Yonkers MA, Tellez MB, et al. pigk Mutation underlies macho behavior and affects Rohon-Beard cell excitability. *J Neurophysiol*. Aug 2015;114(2):1146-57. doi:10.1152/jn.00355.2015

384. Ohishi K, Inoue N, Maeda Y, Takeda J, Riezman H, Kinoshita T. Gaa1p and gpi8p are components of a glycosylphosphatidylinositol (GPI) transamidase that mediates attachment of GPI to proteins. *Mol Biol Cell*. May 2000;11(5):1523-33. doi:10.1091/mbc.11.5.1523

385. Ribera AB, Nüsslein-Volhard C. Zebrafish touch-insensitive mutants reveal an essential role for the developmental regulation of sodium current. *J Neurosci*. Nov 15 1998;18(22):9181-91. doi:10.1523/jneurosci.18-22-09181.1998

386. Neuhauss SC, Biehlmaier O, Seeliger MW, et al. Genetic disorders of vision revealed by a behavioral screen of 400 essential loci in zebrafish. *J Neurosci*. Oct 1 1999;19(19):8603-15. doi:10.1523/jneurosci.19-19-08603.1999

387. Schorderet DF, Nichini O, Boisset G, et al. Mutation in the human homeobox gene NKX5-3 causes an oculo-auricular syndrome. *Am J Hum Genet*. May 2008;82(5):1178-84. doi:10.1016/j.ajhg.2008.03.007

388. Stadler HS, Solursh M. Characterization of the homeobox-containing gene GH6 identifies novel regions of homeobox gene expression in the developing chick embryo. *Dev Biol*. Jan 1994;161(1):251-62. doi:10.1006/dbio.1994.1025

389. Wang W, Lo P, Frasch M, Lufkin T. Hmx: an evolutionary conserved homeobox gene family expressed in the developing nervous system in mice and Drosophila. *Mech Dev*. Dec 2000;99(1-2):123-37. doi:10.1016/s0925-4773(00)00488-3

390. Munroe RJ, Prabhu V, Acland GM, et al. Mouse H6 Homeobox 1 (Hmx1) mutations cause cranial abnormalities and reduced body mass. *BMC Dev Biol*. Apr 20 2009;9:27. doi:10.1186/1471-213x-9-27

391. Gillespie RL, Urquhart J, Lovell SC, et al. Abrogation of HMX1 function causes rare oculoauricular syndrome associated with congenital cataract, anterior segment dysgenesis, and retinal dystrophy. *Invest Ophthalmol Vis Sci*. Jan 8 2015;56(2):883-91. doi:10.1167/iovs.14-15861

392. Vaclavik V, Schorderet DF, Borruat FX, Munier FL. Retinal dystrophy in the oculo-auricular syndrome due to HMX1 mutation. *Ophthalmic Genet*. Jun 2011;32(2):114-7. doi:10.3109/13816810.2011.562955

393. Cowan CS, Renner M, De Gennaro M, et al. Cell Types of the Human Retina and Its Organoids at Single-Cell Resolution. *Cell*. Sep 17 2020;182(6):1623-1640.e34. doi:10.1016/j.cell.2020.08.013

394. Lukowski SW, Lo CY, Sharov AA, et al. A single-cell transcriptome atlas of the adult human retina. *Embo j*. Sep 16 2019;38(18):e100811. doi:10.15252/embj.2018100811

395. Voigt AP, Whitmore SS, Flamme-Wiese MJ, et al. Molecular characterization of foveal versus peripheral human retina by single-cell RNA sequencing. *Exp Eye Res*. Jul 2019;184:234-242. doi:10.1016/j.exer.2019.05.001

396. Connor RJ, Menzel P, Pasquale EB. Expression and tyrosine phosphorylation of Eph receptors suggest multiple mechanisms in patterning of the visual system. *Dev Biol*. Jan 1 1998;193(1):21-35. doi:10.1006/dbio.1997.8786

397. Feldheim DA, Vanderhaeghen P, Hansen MJ, et al. Topographic guidance labels in a sensory projection to the forebrain. *Neuron*. Dec 1998;21(6):1303-13. doi:10.1016/s0896-6273(00)80650-9

398. Scalia F, Currie JR, Feldheim DA. Eph/ephrin gradients in the retinotectal system of Rana pipiens: developmental and adult expression patterns. *J Comp Neurol*. May 1 2009;514(1):30-48. doi:10.1002/cne.21968

399. Biehlmaier O, Neuhauss SC, Kohler K. Onset and time course of apoptosis in the developing zebrafish retina. *Cell Tissue Res*. Nov 2001;306(2):199-207. doi:10.1007/s004410100447

400. Cole LK, Ross LS. Apoptosis in the developing zebrafish embryo. *Dev Biol*. Dec 1 2001;240(1):123-42. doi:10.1006/dbio.2001.0432

401. Alsina B, Vu T, Cohen-Cory S. Visualizing synapse formation in arborizing optic axons in vivo: dynamics and modulation by BDNF. *Nat Neurosci*. Nov 2001;4(11):1093-101. doi:10.1038/nn735

402. Meyer MP, Smith SJ. Evidence from in vivo imaging that synaptogenesis guides the growth and branching of axonal arbors by two distinct mechanisms. *J Neurosci*. Mar 29 2006;26(13):3604-14. doi:10.1523/jneurosci.0223-06.2006

403. Xu HP, Burbridge TJ, Ye M, et al. Retinal Wave Patterns Are Governed by Mutual Excitation among Starburst Amacrine Cells and Drive the Refinement and

Maintenance of Visual Circuits. *J Neurosci*. Mar 30 2016;36(13):3871-86. doi:10.1523/jneurosci.3549-15.2016

404. Kent WJ, Sugnet CW, Furey TS, et al. The human genome browser at UCSC. *Genome Res*. Jun 2002;12(6):996-1006. doi:10.1101/gr.229102

405. Tucker RP. Teneurins: Domain Architecture, Evolutionary Origins, and Patterns of Expression. *Front Neurosci*. 2018;12:938. doi:10.3389/fnins.2018.00938

406. Nunes SM, Ferralli J, Choi K, Brown-Luedi M, Minet AD, Chiquet-Ehrismann R. The intracellular domain of teneurin-1 interacts with MBD1 and CAP/ponsin resulting in subcellular codistribution and translocation to the nuclear matrix. *Exp Cell Res*. Apr 15 2005;305(1):122-32. doi:10.1016/j.yexcr.2004.12.020

407. Li J, Xie Y, Cornelius S, et al. Alternative splicing controls teneurin-latrophilin interaction and synapse specificity by a shape-shifting mechanism. *Nat Commun*. May 1 2020;11(1):2140. doi:10.1038/s41467-020-16029-7

408. Simon DJ, Weimer RM, McLaughlin T, et al. A caspase cascade regulating developmental axon degeneration. *J Neurosci*. Dec 5 2012;32(49):17540-53. doi:10.1523/jneurosci.3012-12.2012

409. Yang J, Weimer RM, Kallop D, et al. Regulation of axon degeneration after injury and in development by the endogenous calpain inhibitor calpastatin. *Neuron*. Dec 4 2013;80(5):1175-89. doi:10.1016/j.neuron.2013.08.034

410. Cusack CL, Swahari V, Hampton Henley W, Michael Ramsey J, Deshmukh M. Distinct pathways mediate axon degeneration during apoptosis and axon-specific pruning. *Nat Commun*. 2013;4:1876. doi:10.1038/ncomms2910

411. Spead O, Verreet T, Donelson CJ, Poulain FE. Characterization of the caspase family in zebrafish. *PLoS One*. 2018;13(5):e0197966. doi:10.1371/journal.pone.0197966

412. Geden MJ, Romero SE, Deshmukh M. Apoptosis versus axon pruning: Molecular intersection of two distinct pathways for axon degeneration. *Neurosci Res*. Feb 2019;139:3-8. doi:10.1016/j.neures.2018.11.007

413. Simon DJ, Pitts J, Hertz NT, et al. Axon Degeneration Gated by Retrograde Activation of Somatic Pro-apoptotic Signaling. *Cell*. Feb 25 2016;164(5):1031-45. doi:10.1016/j.cell.2016.01.032

414. Ghosh AS, Wang B, Pozniak CD, Chen M, Watts RJ, Lewcock JW. DLK induces developmental neuronal degeneration via selective regulation of proapoptotic JNK activity. *J Cell Biol*. Sep 5 2011;194(5):751-64. doi:10.1083/jcb.201103153

415. Chen M, Maloney JA, Kallop DY, et al. Spatially coordinated kinase signaling regulates local axon degeneration. *J Neurosci*. Sep 26 2012;32(39):13439-53. doi:10.1523/jneurosci.2039-12.2012

416. Campbell DS, Holt CE. Apoptotic pathway and MAPKs differentially regulate chemotropic responses of retinal growth cones. *Neuron*. Mar 27 2003;37(6):939-52. doi:10.1016/s0896-6273(03)00158-2

417. Campbell DS, Okamoto H. Local caspase activation interacts with Slit-Robo signaling to restrict axonal arborization. *J Cell Biol*. Nov 25 2013;203(4):657-72. doi:10.1083/jcb.201303072

418. Ladilov Y, Appukuttan A. Role of soluble adenylyl cyclase in cell death and growth. *Biochim Biophys Acta*. Dec 2014;1842(12 Pt B):2646-55. doi:10.1016/j.bbadis.2014.06.034

419. de Rooij J, Zwartkruis FJ, Verheijen MH, et al. Epac is a Rap1 guanine-nucleotide-exchange factor directly activated by cyclic AMP. *Nature*. Dec 3 1998;396(6710):474-7. doi:10.1038/24884

420. Li M, Wang X, Meintzer MK, Laessig T, Birnbaum MJ, Heidenreich KA. Cyclic AMP promotes neuronal survival by phosphorylation of glycogen synthase kinase 3beta. *Mol Cell Biol*. Dec 2000;20(24):9356-63. doi:10.1128/mcb.20.24.9356-9363.2000

421. Suzuki S, Yokoyama U, Abe T, et al. Differential roles of Epac in regulating cell death in neuronal and myocardial cells. *J Biol Chem*. Jul 30 2010;285(31):24248-59. doi:10.1074/jbc.M109.094581

422. Mohebiany AN, Harroch S, Bouyain S. New insights into the roles of the contactin cell adhesion molecules in neural development. *Adv Neurobiol*. 2014;8:165-94. doi:10.1007/978-1-4614-8090-7_8

423. Gurung S, Asante E, Hummel D, et al. Distinct roles for the cell adhesion molecule Contactin2 in the development and function of neural circuits in zebrafish. *Mech Dev*. Aug 2018;152:1-12. doi:10.1016/j.mod.2018.05.005

424. Lang DM, Warren JT, Jr., Klisa C, Stuermer CA. Topographic restriction of TAG-1 expression in the developing retinotectal pathway and target dependent reexpression during axon regeneration. *Mol Cell Neurosci*. Feb 2001;17(2):398-414. doi:10.1006/mcne.2000.0936

425. Warren JT, Jr., Chandrasekhar A, Kanki JP, Rangarajan R, Furley AJ, Kuwada JY. Molecular cloning and developmental expression of a zebrafish axonal glycoprotein similar to TAG-1. *Mech Dev*. Feb 1999;80(2):197-201. doi:10.1016/s0925-4773(98)00215-9

426. Jacobi AM, Rettig GR, Turk R, et al. Simplified CRISPR tools for efficient genome editing and streamlined protocols for their delivery into mammalian cells and mouse zygotes. *Methods*. May 15 2017;121-122:16-28. doi:10.1016/j.ymeth.2017.03.021

427. Nakano Y, Fujita M, Ogino K, et al. Biogenesis of GPI-anchored proteins is essential for surface expression of sodium channels in zebrafish Rohon-Beard neurons to respond to mechanosensory stimulation. *Development*. May 2010;137(10):1689-98. doi:10.1242/dev.047464

428. Chen ZY, Sun C, Reuhl K, Bergemann A, Henkemeyer M, Zhou R. Abnormal hippocampal axon bundling in EphB receptor mutant mice. *J Neurosci*. Mar 10 2004;24(10):2366-74. doi:10.1523/jneurosci.4711-03.2004

429. Kazarinova-Noyes K, Malhotra JD, McEwen DP, et al. Contactin associates with Na+ channels and increases their functional expression. *J Neurosci*. Oct 1 2001;21(19):7517-25. doi:10.1523/jneurosci.21-19-07517.2001

430. Liu CJ, Dib-Hajj SD, Black JA, Greenwood J, Lian Z, Waxman SG. Direct interaction with contactin targets voltage-gated sodium channel Na(v)1.9/NaN to the cell membrane. *J Biol Chem*. Dec 7 2001;276(49):46553-61. doi:10.1074/jbc.M108699200

431. McEwen DP, Isom LL. Heterophilic interactions of sodium channel beta1 subunits with axonal and glial cell adhesion molecules. *J Biol Chem*. Dec 10 2004;279(50):52744-52. doi:10.1074/jbc.M405990200

432. McEwen DP, Meadows LS, Chen C, Thyagarajan V, Isom LL. Sodium channel beta1 subunit-mediated modulation of Nav1.2 currents and cell surface density is dependent on interactions with contactin and ankyrin. *J Biol Chem*. Apr 16 2004;279(16):16044-9. doi:10.1074/jbc.M400856200

433. Rush AM, Craner MJ, Kageyama T, Dib-Hajj SD, Waxman SG, Ranscht B. Contactin regulates the current density and axonal expression of tetrodotoxin-resistant but not tetrodotoxin-sensitive sodium channels in DRG neurons. *Eur J Neurosci*. Jul 2005;22(1):39-49. doi:10.1111/j.1460-9568.2005.04186.x

434. Shah BS, Rush AM, Liu S, et al. Contactin associates with sodium channel Nav1.3 in native tissues and increases channel density at the cell surface. *J Neurosci*. Aug 18 2004;24(33):7387-99. doi:10.1523/jneurosci.0322-04.2004

435. Alnemri ES, Livingston DJ, Nicholson DW, et al. Human ICE/CED-3 protease nomenclature. *Cell*. 1996:171. vol. 2.

436. McIlwain DR, Berger T, Mak TW. Caspase functions in cell death and disease. *Cold Spring Harb Perspect Biol*. Apr 1 2013;5(4):a008656. doi:10.1101/cshperspect.a008656

437. Fuchs Y, Steller H. Programmed cell death in animal development and disease. *Cell*. Nov 11 2011;147(4):742-58. doi:10.1016/j.cell.2011.10.033

438. Yamaguchi Y, Miura M. Programmed cell death in neurodevelopment. *Dev Cell*. Feb 23 2015;32(4):478-90. doi:10.1016/j.devcel.2015.01.019

439. Kuida K, Zheng TS, Na S, et al. Decreased apoptosis in the brain and premature lethality in CPP32-deficient mice. *Nature*. Nov 28 1996;384(6607):368-72. doi:10.1038/384368a0

440. Kuida K, Haydar TF, Kuan CY, et al. Reduced apoptosis and cytochrome c-mediated caspase activation in mice lacking caspase 9. *Cell*. Aug 7 1998;94(3):325-37. doi:10.1016/s0092-8674(00)81476-2

441. Pompeiano M, Blaschke AJ, Flavell RA, Srinivasan A, Chun J. Decreased apoptosis in proliferative and postmitotic regions of the Caspase 3-deficient embryonic central nervous system. *J Comp Neurol*. Jul 17 2000;423(1):1-12.

442. Hakem R, Hakem A, Duncan GS, et al. Differential requirement for caspase 9 in apoptotic pathways in vivo. *Cell*. Aug 7 1998;94(3):339-52. doi:10.1016/s0092-8674(00)81477-4

443. Kuranaga E. Caspase signaling in animal development. *Dev Growth Differ*. Feb 2011;53(2):137-48. doi:10.1111/j.1440-169X.2010.01237.x

444. Hyman BT, Yuan J. Apoptotic and non-apoptotic roles of caspases in neuronal physiology and pathophysiology. *Nat Rev Neurosci*. May 18 2012;13(6):395-406. doi:10.1038/nrn3228

445. Connolly PF, Jäger R, Fearnhead HO. New roles for old enzymes: killer caspases as the engine of cell behavior changes. *Front Physiol*. 2014;5:149. doi:10.3389/fphys.2014.00149

446. Unsain N, Barker PA. New Views on the Misconstrued: Executioner Caspases and Their Diverse Non-apoptotic Roles. *Neuron*. Nov 4 2015;88(3):461-74. doi:10.1016/j.neuron.2015.08.029

447. Fischer H, Koenig U, Eckhart L, Tschachler E. Human caspase 12 has acquired deleterious mutations. *Biochem Biophys Res Commun*. May 3 2002;293(2):722-6. doi:10.1016/s0006-291x(02)00289-9

448. Xue Y, Daly A, Yngvadottir B, et al. Spread of an inactive form of caspase-12 in humans is due to recent positive selection. *Am J Hum Genet*. Apr 2006;78(4):659-70. doi:10.1086/503116

449. Eckhart L, Ballaun C, Uthman A, et al. Identification and characterization of a novel mammalian caspase with proapoptotic activity. *J Biol Chem*. Oct 21 2005;280(42):35077-80. doi:10.1074/jbc.C500282200

450. Eckhart L, Ballaun C, Hermann M, et al. Identification of novel mammalian caspases reveals an important role of gene loss in shaping the human caspase repertoire. *Mol Biol Evol*. May 2008;25(5):831-41. doi:10.1093/molbev/msn012

451. Sakamaki K, Satou Y. Caspases: evolutionary aspects of their functions in vertebrates. *J Fish Biol*. Mar 2009;74(4):727-53. doi:10.1111/j.1095-8649.2009.02184.x

452. Pérez-Garijo A. When dying is not the end: Apoptotic caspases as drivers of proliferation. *Semin Cell Dev Biol*. Oct 2018;82:86-95. doi:10.1016/j.semcdb.2017.11.036

453. Bell RAV, Megeney LA. Evolution of caspase-mediated cell death and differentiation: twins separated at birth. *Cell Death Differ*. Aug 2017;24(8):1359-1368. doi:10.1038/cdd.2017.37

454. Burgon PG, Megeney LA. Caspase signaling, a conserved inductive cue for metazoan cell differentiation. *Semin Cell Dev Biol*. Oct 2018;82:96-104. doi:10.1016/j.semcdb.2017.11.009

455. Keller N, Ozmadenci D, Ichim G, Stupack D. Caspase-8 function, and phosphorylation, in cell migration. *Semin Cell Dev Biol*. Oct 2018;82:105-117. doi:10.1016/j.semcdb.2018.01.009

456. Salvesen GS, Walsh CM. Functions of caspase 8: the identified and the mysterious. *Semin Immunol*. Jun 2014;26(3):246-52. doi:10.1016/j.smim.2014.03.005

457. Bergmann A, Steller H. Apoptosis, stem cells, and tissue regeneration. *Sci Signal*. Oct 26 2010;3(145):re8. doi:10.1126/scisignal.3145re8

458. Hollville E, Deshmukh M. Physiological functions of non-apoptotic caspase activity in the nervous system. *Semin Cell Dev Biol*. Oct 2018;82:127-136. doi:10.1016/j.semcdb.2017.11.037

459. Mukherjee A, Williams DW. More alive than dead: non-apoptotic roles for caspases in neuronal development, plasticity and disease. *Cell Death Differ*. Aug 2017;24(8):1411-1421. doi:10.1038/cdd.2017.64

460. Fernando P, Brunette S, Megeney LA. Neural stem cell differentiation is dependent upon endogenous caspase 3 activity. *Faseb j*. Oct 2005;19(12):1671-3. doi:10.1096/fj.04-2981fje

461. Oomman S, Strahlendorf H, Finckbone V, Strahlendorf J. Non-lethal active caspase-3 expression in Bergmann glia of postnatal rat cerebellum. *Brain Res Dev Brain Res*. Dec 7 2005;160(2):130-45. doi:10.1016/j.devbrainres.2005.07.010

462. Oomman S, Strahlendorf H, Dertien J, Strahlendorf J. Bergmann glia utilize active caspase-3 for differentiation. *Brain Res*. Mar 17 2006;1078(1):19-34. doi:10.1016/j.brainres.2006.01.041

463. Dash PK, Blum S, Moore AN. Caspase activity plays an essential role in long-term memory. *Neuroreport*. Aug 21 2000;11(12):2811-6. doi:10.1097/00001756-200008210-00040

464. Gulyaeva NV, Kudryashov IE, Kudryashova IV. Caspase activity is essential for long-term potentiation. *J Neurosci Res*. Sep 15 2003;73(6):853-64. doi:10.1002/jnr.10730

465. Stepanichev MY, Kudryashova IV, Yakovlev AA, et al. Central administration of a caspase inhibitor impairs shuttle-box performance in rats. *Neuroscience*. 2005;136(2):579-91. doi:10.1016/j.neuroscience.2005.08.010

466. Huesmann GR, Clayton DF. Dynamic role of postsynaptic caspase-3 and BIRC4 in zebra finch song-response habituation. *Neuron*. Dec 21 2006;52(6):1061-72. doi:10.1016/j.neuron.2006.10.033

467. Li Z, Jo J, Jia JM, et al. Caspase-3 activation via mitochondria is required for long-term depression and AMPA receptor internalization. *Cell*. May 28 2010;141(5):859-71. doi:10.1016/j.cell.2010.03.053

468. Westphal D, Sytnyk V, Schachner M, Leshchyns'ka I. Clustering of the neural cell adhesion molecule (NCAM) at the neuronal cell surface induces caspase-8- and -3-dependent changes of the spectrin meshwork required for NCAM-mediated neurite outgrowth. *J Biol Chem*. Dec 31 2010;285(53):42046-57. doi:10.1074/jbc.M110.177147

469. Rotschafer SE, Allen-Sharpley MR, Cramer KS. Axonal Cleaved Caspase-3 Regulates Axon Targeting and Morphogenesis in the Developing Auditory Brainstem. *Front Neural Circuits*. 2016;10:84. doi:10.3389/fncir.2016.00084

470. Ohsawa S, Hamada S, Kuida K, Yoshida H, Igaki T, Miura M. Maturation of the olfactory sensory neurons by Apaf-1/caspase-9-mediated caspase activity. *Proc Natl Acad Sci U S A*. Jul 27 2010;107(30):13366-71. doi:10.1073/pnas.0910488107

471. Kuo CT, Zhu S, Younger S, Jan LY, Jan YN. Identification of E2/E3 ubiquitinating enzymes and caspase activity regulating Drosophila sensory neuron dendrite pruning. *Neuron*. Aug 3 2006;51(3):283-90. doi:10.1016/j.neuron.2006.07.014

472. Williams DW, Kondo S, Krzyzanowska A, Hiromi Y, Truman JW. Local caspase activity directs engulfment of dendrites during pruning. *Nat Neurosci*. Oct 2006;9(10):1234-6. doi:10.1038/nn1774

473. Nikolaev A, McLaughlin T, O'Leary DD, Tessier-Lavigne M. APP binds DR6 to trigger axon pruning and neuron death via distinct caspases. *Nature*. Feb 19 2009;457(7232):981-9. doi:10.1038/nature07767

474. Unsain N, Higgins JM, Parker KN, Johnstone AD, Barker PA. XIAP regulates caspase activity in degenerating axons. *Cell Rep*. Aug 29 2013;4(4):751-63. doi:10.1016/j.celrep.2013.07.015

475. Dinkel H, Van Roey K, Michael S, et al. ELM 2016--data update and new functionality of the eukaryotic linear motif resource. *Nucleic Acids Res*. Jan 4 2016;44(D1):D294-300. doi:10.1093/nar/gkv1291

476. Campanella JJ, Bitincka L, Smalley J. MatGAT: an application that generates similarity/identity matrices using protein or DNA sequences. *BMC Bioinformatics*. Jul 10 2003;4:29. doi:10.1186/1471-2105-4-29

477. Kumar S, Stecher G, Tamura K. MEGA7: Molecular Evolutionary Genetics Analysis Version 7.0 for Bigger Datasets. *Mol Biol Evol*. Jul 2016;33(7):1870-4. doi:10.1093/molbev/msw054

478. Edgar RC. MUSCLE: multiple sequence alignment with high accuracy and high throughput. *Nucleic Acids Res*. 2004;32(5):1792-7. doi:10.1093/nar/gkh340

479. Waterhouse AM, Procter JB, Martin DM, Clamp M, Barton GJ. Jalview Version 2--a multiple sequence alignment editor and analysis workbench. *Bioinformatics*. May 1 2009;25(9):1189-91. doi:10.1093/bioinformatics/btp033

480. Whelan S, Goldman N. A general empirical model of protein evolution derived from multiple protein families using a maximum-likelihood approach. *Mol Biol Evol*. May 2001;18(5):691-9. doi:10.1093/oxfordjournals.molbev.a003851

481. Masumoto J, Zhou W, Chen FF, et al. Caspy, a zebrafish caspase, activated by ASC oligomerization is required for pharyngeal arch development. *J Biol Chem*. Feb 7 2003;278(6):4268-76. doi:10.1074/jbc.M203944200

482. Eimon PM, Kratz E, Varfolomeev E, et al. Delineation of the cell-extrinsic apoptosis pathway in the zebrafish. *Cell Death Differ*. Oct 2006;13(10):1619-30. doi:10.1038/sj.cdd.4402015

483. Sakata S, Yan Y, Satou Y, et al. Conserved function of caspase-8 in apoptosis during bony fish evolution. *Gene*. Jul 1 2007;396(1):134-48. doi:10.1016/j.gene.2007.03.010

484. Sakamaki K, Imai K, Tomii K, Miller DJ. Evolutionary analyses of caspase-8 and its paralogs: Deep origins of the apoptotic signaling pathways. *Bioessays*. Jul 2015;37(7):767-76. doi:10.1002/bies.201500010

485. Wilson KP, Black JA, Thomson JA, et al. Structure and mechanism of interleukin-1 beta converting enzyme. *Nature*. Jul 28 1994;370(6487):270-5. doi:10.1038/370270a0

486. Martinon F, Tschopp J. Inflammatory caspases and inflammasomes: master switches of inflammation. *Cell Death Differ*. Jan 2007;14(1):10-22. doi:10.1038/sj.cdd.4402038

487. Huang WB, Ren HL, Gopalakrishnan S, Xu DD, Qiao K, Wang KJ. First molecular cloning of a molluscan caspase from variously colored abalone (Haliotis

diversicolor) and gene expression analysis with bacterial challenge. *Fish Shellfish Immunol*. Apr 2010;28(4):587-95. doi:10.1016/j.fsi.2009.12.016

488. Xu L, Yuan S, Li J, et al. The conservation and uniqueness of the caspase family in the basal chordate, amphioxus. *BMC Biol*. Sep 21 2011;9:60. doi:10.1186/1741-7007-9-60

489. Inohara N, Nuñez G. Genes with homology to mammalian apoptosis regulators identified in zebrafish. *Cell Death Differ*. May 2000;7(5):509-10. doi:10.1038/sj.cdd.4400679

490. Amores A, Catchen J, Ferrara A, Fontenot Q, Postlethwait JH. Genome evolution and meiotic maps by massively parallel DNA sequencing: spotted gar, an outgroup for the teleost genome duplication. *Genetics*. Aug 2011;188(4):799-808. doi:10.1534/genetics.111.127324

491. Glasauer SM, Neuhauss SC. Whole-genome duplication in teleost fishes and its evolutionary consequences. *Mol Genet Genomics*. Dec 2014;289(6):1045-60. doi:10.1007/s00438-014-0889-2

492. Takle H, McLeod A, Andersen O. Cloning and characterization of the executioner caspases 3, 6, 7 and Hsp70 in hyperthermic Atlantic salmon (Salmo salar) embryos. *Comp Biochem Physiol B Biochem Mol Biol*. Jun 2006;144(2):188-98. doi:10.1016/j.cbpb.2006.02.006

APPENDIX A

CHARACTERIZATION OF THE CASPASE FAMILY IN ZEBRAFISH[4]

[4] Spead O, Verreet T, Donelson CJ, Poulain FE. 2018. *PLOS ONE.* 13(5):e0197966
Reprinted here with permission from the publisher.

A.1 ABSTRACT

First discovered for their role in mediating programmed cell death and inflammatory responses, caspases have now emerged as crucial regulators of other cellular and physiological processes including cell proliferation, differentiation, migration, and survival. In the developing nervous system, for instance, the non-apoptotic functions of caspases have been shown to play critical roles in the formation of neuronal circuits by regulating axon outgrowth, guidance and pruning. How caspase activity is spatially and temporally maintained at sub-lethal levels within cells remains however poorly understood, especially in vivo. Thanks to its transparency and accessibility, the zebrafish offers the unique ability to directly visualize caspase activation in vivo. Yet, detailed information about the caspase family in zebrafish is lacking. Here, we report the identification and characterization of 19 different caspase genes in zebrafish, and show that caspases have diverse expression profiles from cleavage to larval stages, suggesting highly specialized and/or redundant functions during embryonic development.

A.2 INTRODUCTION

Caspases are highly conserved intracellular cysteine-dependent proteases best known for their critical role in mediating apoptosis and inflammatory responses [435, 436]. As transducers and executioners of programmed cell death, caspases are especially important during development, when the elimination of unnecessary cells contributes to tissue morphogenesis [437]. In the nervous system, for instance, apoptosis has been detected in neural precursor cells, postmitotic neurons and glial cells [438], and a lack of caspase-3 or -9 has been shown to cause brain hyperplasia and neural overgrowth in mice [439-442]. More

recently, caspases have also emerged as central mediators of non-apoptotic signaling pathways regulating a large variety of cellular and physiological functions [443-446]. How caspase activation is induced and maintained at sublethal levels within cells remains however poorly characterized.

Caspases are synthesized as zymogens that become activated upon oligomerization or cleavage at specific aspartate residues. They comprise an N-terminal prodomain of varying size and a catalytic CASc domain that includes a large P20 and a small P10 subunits. So far, 12 caspases have been identified in human (Caspases-1 to 10, -12, and -14, with -12 being inactive due to deleterious mutations), and additional caspases including Caspases-11 and -13 (murine and bovine orthologs of human Caspase-4, respectively), -15, -16, -17 and -18 have been detected in other vertebrates [447-451]. Based on their functional and structural similarities, caspases have generally been classified as inflammatory (Caspases-1, -4, -5 and -12) and initiators (Caspases-2, -8, -9 and -10) or executioners of apoptosis (Caspases-3, -6 and -7). However, this subdivision has progressively become obsolete with the discovery of functions in additional processes including cell proliferation [452], differentiation [453, 454], motility and migration [445, 455], survival [456] and tissue regeneration and repair [457].

Essential non-apoptotic functions of caspases have especially been demonstrated in the developing and mature nervous system [444, 446, 458, 459]. Caspase-3, for instance, has been implicated in the regulation of neural stem cell differentiation [460], Bergman glia differentiation [461, 462] synaptic plasticity, learning and memory [463-467]. More recently, caspases have also been identified as important regulators of axon outgrowth and pathfinding. The role of caspase activity in axon guidance was first suggested by the

observation that growth cone responses to netrin or lysophosphatidic acid were blocked in the presence of caspase inhibitors in vitro [416]. Since then, caspases have been shown to regulate NCAM-dependent axon outgrowth [468], axon targeting in the auditory brainstem and the olfactory bulb [469, 470], and retinal axon arborization [417]. Caspases have also emerged as playing a crucial role in the refinement of neuronal connectivity by regulating axonal and dendritic pruning [408-410, 471-473]. For instance, pruning of retinal axons projecting to the superior colliculus is delayed in mice lacking caspase-3 or -6 [408, 409].

How the non-apoptotic activity of caspases is spatially and temporally induced and restricted in cells or axons is not yet well understood. Several mechanisms have been proposed, including subcellular regulation by inhibitors such as XIAP [474] or post-translational modifications [446]. Yet, our understanding of when, where and how caspases are locally activated and controlled in vivo remains rudimentary due to a limited number of models suitable for high resolution in vivo imaging. Thanks to their advantageous accessibility and transparency, zebrafish embryos offer the unique ability to directly visualize axon development and degeneration in vivo and address these questions [16, 34]. The recent use of genetically encoded biosensors to detect caspase activation in real time in this model has revealed an important function of Caspases-3 and -9 in axon remodeling [417], and will likely provide new insight into the fine spatio-temporal activation of caspases in other contexts. Yet, detailed information about caspases in zebrafish is surprisingly lacking. To gain insight into the functions of caspases during axon guidance and pruning in vivo, we first carried out a comprehensive analysis of the caspase family in zebrafish. We report here the identification and characterization of 19 different caspase genes including known orthologs of human caspases as well as new members of this

family. We also show that zebrafish caspases have distinct expression patterns during development, suggesting both specific and conserved functions among vertebrates.

A.3 Materials and Methods

Zebrafish husbandry

This research was approved by the University of South Carolina Institutional Animal Care and Use Committee (IACUC) (protocol number: 2398-101289-111717). Wild type (WT) embryos (Tubingen and AB strains) were obtained from natural matings, raised at 28.5°C in E3 medium (5 mM NaCl, 0.17 mM KCl, 0.33 mM CaCl2, and 0.33 mM MgSO4) in the presence of 150 mM of 1-phenyl-2-thiourea (PTU) (Sigma) to prevent pigment formation, and staged by ge and morphology [279]. Embryos were anaesthetized in tricaine (Western Chemicals) before fixation or RNA extraction.

Identification and cloning of caspase coding sequences

GenBank and the Ensembl *Danio rerio* (GRCz10) databases were used to identify genomic loci for all zebrafish caspase genes. *Mus musculus, Homo sapiens, Bos taurus*, and *Gallus gallus* caspase gene sequences were blasted against the databases and the zebrafish sequences identified were confirmed for the presence of a CASc domain (SMART accession number SM00115). Zebrafish mRNA was isolated from embryos at cleavage, blastula sphere, gastrula shield, gastrula bud, pharyngula prim-5 (24 hours-post-fertilization (hpf)), long-pec (48 hpf), protruding mouth (72 hpf) and larval day 4 (96 hpf) stages using Trizol and the RNeasy mini kit (Qiagen), and cDNA was prepared from RNA using the SuperScriptIII First-Strand Synthesis system (Invitrogen). Full length primers **(Figure A.1**) were used to amplify zebrafish caspase cDNAs. Amplicons

were subcloned into PCRII-TOPO (Invitrogen) and sequenced to verify gene identity and confirm sequence orientation for the generation of sense and antisense RNA probes. Protein sequences were analyzed using the Eukaryotic Linear Motif (ELM) resource prediction tool and Motif Scan (MyHits, SIB, Switzerland) to identify and annotate functional domains [475].

Sequence comparison and phylogeny

Zebrafish caspase protein sequences were compared to the following protein sequences using the MatGAT (Matrix Global Alignment Tool) software [476] with a BLOSUM 62 scoring matrix (gap opening and gap extending penalties of 4): *Homo sapiens* Caspase-1 (NP_150634), Caspase-2 (NP_116764), Caspase-3 (NP_116786), Caspase-4 (NP_001216), Caspase-5 (NP_001129584), Caspase-6 (NP_001217), Caspase-7 (NP_001253986), Caspase-8 (NP_001073594), Caspase-9 (NP_001220), Caspase-10 (NP_116759), Caspase-12 (NP_001177945), and Caspase-14 (NP_036246), *Bos Taurus* Caspase-15 (NP_001029681), *Mus musculus* Caspase-16 (XP_003945628), *Gallus gallus* Caspase-17 (UniProt A9YDV3), and Caspase-18 (NP_001038154). Phylogenetic analyses were conducted using the Mega 7 software [477] and included the following additional sequences: *Gallus gallus* Caspase-1 (XP_003642432.2), Caspase-2 (NP_001161173), Caspase-3 (NP_990056.1), Caspase-6 (NP_990057), Caspase-7 (UniprotF1NV61), Caspase-8 (NP_989923.1), Caspase-9 (Uniprot F1NL59), Caspase-10 (XP_421936.4), *Latimeria chalumnae* Caspase-1 (Uniprot H3B2V3), Caspase-2 (Uniprot H3A019), Caspase-3 (Uniprot H3ACL5), Caspase-6 (Uniprot H2ZXX5), Caspase-7 (Uniprot M3XIX0), Caspase-8 (Uniprot H3A526), Caspase-9 (Uniprot H3BFW5), Caspase-10 (Uniprot H2ZXE8), Caspase-14l (XP_014344655.1), Caspase-17 (Uniprot

H3AXG0), Caspase-18 (H3A2R2), *Oryzias latipes* Caspase-1 (Uniprot H2LPF5), Caspase-2 (XP_011483724.1), Caspase-3a (NP_001098168.1), Caspase-3b (NP_001098140.1), Caspase-6 (Uniprot H2MXM9), Caspase-6l1 (XP_023813211.1), Caspase-6l2 (XP_023813213.1), Caspase-7 (XP_023805391.1), Caspase-8 (NP_001098258.1), Caspase-9 (Uniprot H2LBD7), Caspase-17 (Augustus g31162.t1), Caspase-20 (XP_023820994.1), *Takifugu rubripes* Caspase-1 (Uniprot H2SKU3), Caspase-1l (Uniprot H2UDK1), Caspase-2 (H2UKY4), Caspase-3 (NP_001027871t), Caspase-6 (Augustus g16014.t2), Caspase-7 (Uniprot H2U497 and H2U498), Caspase-8 (Uniprot H2TIG5), Caspase-9 (Uniprot H2V836), Caspase-10 (Uniprot H2V630 and H2V635), Caspase-17 (Uniprot H2VEU2), Caspase-20 (Uniprot H2THL4), *Gasterosteus aculeatus* Caspase-1 (Uniprot G3P6H8), Caspase-1l (Augustus g16792.t3), Caspase-2 (Uniprot G3P808), Caspase-3a (Augustus g8732.t3), Caspase-3b (Uniprot G3Q4K5), Caspase-3c (Uniprot G3Q4L2 and BT027477), Caspase-6 (Uniprot G3PZL5), Caspase-7 (Augustus g18074.t1), Caspase-8 (NP_001254591), Caspase-9 (Augustus g27457.t1), Caspase-10 (NP_001254593), Caspase-17 (Augustus g16285.t1) and Caspase-20 (Augustus g4015.t1). Multiple alignment of 90 caspase protein sequences was generated with Muscle [478] and visualized with Jalview software [479]. The evolutionary history was inferred by using the Maximum Likelihood method based on the Whelan And Goldman + Freq. model [480]. Initial trees for the heuristic search were obtained by applying the Neighbor-Joining method to a matrix of pairwise distances estimated using a JTT model. A discrete Gamma distribution was used to model evolutionary rate differences among sites (5 categories (+G, parameter = 1.4388)). 500 bootstrap replications were used as a

test of phylogeny, with values indicated next to the branch. The tree is drawn to scale, with branch lengths measured in the number of substitutions per site.

RT-PCR

cDNA was prepared from different developmental stages as mentioned above and used for RT-PCR. Full length primers (**Figure A.1**) were used to amplify *casp1*, *casp3a*, *casp3b*, *casp6a*, *casp6b*, *casp7*, *casp17*, *casp19a*, *casp19b*, *casp21* and *casp22*. Different primers were used for the following caspases: *casp2*_fw: TAATGTGAGGTTCGACTCAG; *casp6c*_rv: TCCAGTTGTGAACGATAACG; *casp8a*_fw: CTACGATGTGATAATTCTCGT; *casp8b*_fw: ACAGATGAACCGAAGAGG; *casp9*_fw: AATACAGAGCAAGGCAACC; *casp10*_fw: CACGAGACCTCAACACTG; *casp10*_rv: GTGAATGTCTGAGGAAACAC; *casp20*_fw: TGACTACAATAACCTCTCTGATG; and *casp23*_fw: TCCAATTCTGAAGTGCAACT. The following primers were used to amplify *actin* as a control: *actin_fw*: ATCCCAAAGCCAACAGAGAG; *actin_rv*: CAACGGAAACGCTCATTGC.PCR reactions were conducted using 30 to 36 cycles.

In situ hybridization

In vitro transcription of digoxigenin-labeled probes was performed using the RNA Labeling Kit (Roche Diagnostics Corporation) according to manufacturer's instructions. Embryos were dechorionated at the appropriate developmental stages and fixed in 4% paraformaldehyde in phosphate buffered saline (pH 7.4) for 2 hours at room temperature and overnight at 4°C.

Whole-mount in situ hybridization was performed as previously described [78]. Sense probes were used as controls for all caspases and did not reveal any staining. After staining, embryos were cleared in 80% glycerol for imaging. Images were acquired using an Olympus SZX16 stereomicroscope equipped with an Olympus DP80 dual color camera and Cellsens standard software. Digital images were cropped and aligned using Adobe Photoshop.

A.4 Results and Discussion

Identification of zebrafish caspases

13 caspase genes (*casp*) have been identified in human, including *casp*1 to 10, 12, 14 and 16p (*casp16p* being a pseudogene) [450, 451]. Additional caspases have been detected in other vertebrates and include mammalian *casp15* (absent in the human and mouse genomes) [449], *casp17* (present in all vertebrate lineages except for therian mammals), and *casp18* (present in chicken but absent in placental mammals) [450]. We blasted these sequences against GenBank and Ensembl *Danio rerio* (GRCz10) EST databases to identify corresponding zebrafish caspases and found 19 *casp* genes (**Figure A.2**). Some of these genes were reported previously but were not always named according to the accepted caspase nomenclature [450, 481-484]. Other genes we identified have never been described before. We named all caspase genes according to their similarity to the vertebrate orthologs, and attributed new numbers based on the taxonomy proposed in previous studies [450]. The accession numbers of all genes from the different databases are shown in **Figure A.2**, and new GenBank accession numbers were obtained for all sequences.

For simplicity, we analyzed zebrafish caspases based on the initial classification of caspases into inflammatory, initiator and executioner groups (**Figure A.6**). In human, genes encoding inflammatory caspases include *casp1*, *casp4*, *casp5*, and *casp12* and are clustered on chromosome 11, suggesting they may have originated from gene duplication events. In contrast, we found zebrafish casp1, casp19a, casp19b and casp23 genes on three different chromosomes (**Figure A.2**) and did not observe any conserved chromosomal synteny with human caspases (data not shown). Surprisingly, we could only find one or two inflammatory caspase genes in other teleost species (casp1 in medaka and casp1/1l in stickleback and fugu) and did not identify any casp23 ortholog. Phylogenetic analysis of caspase sequences across vertebrates revealed that zebrafish inflammatory caspases cluster in a separate group, suggesting the occurrence of duplication events specific to that lineage (**Figure A.7)**. Interestingly, comparison of caspase protein sequences shows that zebrafish Caspase-1 (previously known as Caspy [481]) is the most similar to human Caspase-1, sharing 38% identity and 56% homology (**Figure A.3**). Analysis of the conserved catalytic CASc domain also indicates that zebrafish Caspase-1 has a His at position 318 that is not conserved in Caspases-19a, -19b and -23 (**Figure A.8**). His 318 is similar to His 342 in human Caspase-1 that binds the specific P3 alanine residue of Caspase-1 substrates [485], suggesting functional conservation. Caspases-19a and 19b are 70% identical (**Figure A.4**) and phylogenetically cluster together, indicating they are recent duplicated isoforms. While mammalian inflammatory caspases are characterized by the presence of a caspase-recruitment domain (CARD) in their N-terminal region [486], Caspases-1, -19a and -19b share a pyrin (PYR) domain in its place. Interestingly, these PYR domains appear specific to zebrafish caspases, as Caspases-1

and -11 in other teleosts possess a CARD domain similar to mammals. Although in the same group, Caspase-23 differs from the other inflammatory caspases by the absence of a PYR or CARD domain in its N-terminal region (**Figure A.6)**. Caspase-23 also possesses an unusual QSCRG cysteine active site (positions 340-344) in its CASc domain instead of the conserved QACRG pentapeptide found in other caspases (**Figure A.8**). Interestingly, a similar QSCRG is found in amphoxius and sea snail caspases [487, 488], suggesting an ancient origin.

Genes encoding initiator caspases in mammals include *casp2*, *casp9*, and the subfamily of *casp8* and *casp10*. Another caspase belonging to the caspase-8 subfamily, *casp18*, has been detected in chicken and opossum but is not present in eutherian mammals [450]. As previously reported [451, 483, 484, 489], we identified orthologs for *casp2*, *casp9*, *casp8* (as *casp8a* and *casp8b*), and *casp10* but not for *casp18* in zebrafish (**Figures A.2, A.3, A.7**). We also detected additional caspase genes belonging to the caspase-8 subfamily that we named *casp20* and *casp22*. Like in mammals, zebrafish Caspase-2 and Caspase-9 are characterized by the presence of a CARD in their N-terminal region (**Figure A.6**). Caspase-8a and Caspase-10, on the other hand, possess two death-effector domains (DEDs). Interestingly, the N-terminal pro-domain of Caspase-8b is much shorter and lacks these DED motifs. It notably includes two nuclear localization signals not detected in Caspase-8a (**Figure A.6**). Despite these differences, the CASc domains of Caspase-8a and Caspase-8b are very similar (62% identity and 77% homology) and possess the QACQG active site characteristic of human Caspase-8 (**Figure A.8**), indicating that both caspases are duplicated isoforms. The adjacent localization of *casp8a* and *casp8b* genes on chromosome 6 further suggests a common origin from a recent

gene duplication event. This duplication appears specific to the zebrafish lineage, as no *casp8b* could be identified in other teleosts including fugu, medaka and stickleback (**Figure A.15**). In addition to *casp8a* and *casp8b*, we detected another paralog on chromosome 6 that we named *casp20*. This paralog has been described in previous studies as CARD-Casp8 due to the presence of a CARD in the N-terminal pro-domain instead of the two DED domains present in Caspases-8, -10 and -18 [483, 484] (**Figure A.6)**. Interestingly, comparative genomics and phylogenetic analyses suggest that *casp8*, *casp10*, *casp18* originate from a common ancestor during vertebrate evolution (**Figure A.7**) [484]. *Casp8*, *casp18* and *casp10* genes are clustered on the same chromosome in chicken, coelacanth and spotted gar genomes (**Figure A.15** and [484]).

While *casp18* has been lost in the human genome (and in other eutherian mammals), *casp8* and *casp10* remain clustered on chromosome 2 (**Figure A.15**). In contrast, *casp8* and *casp10* have been segregated on different chromosomes in the teleost lineage after extensive chromosomal rearrangements during evolution (**Figure A.15**). Similarly to *casp18* in other species, *casp20* is found in close proximity to *casp8* in all teleost genomes (*casp8b* in zebrafish) but could not be identified in other vertebrates including shark, lamprey and gar. The clustering of *casp8*, *casp18* and *casp10* in the genome of spotted gar, whose lineage represents the unduplicated sister taxon of teleosts [490], suggests that *casp8*, *casp18* and *casp10* genes formed an ancestral cluster in vertebrates that has been dispersed during teleost evolution. *Casp20* might have derived from *casp18* by domain shuffling from DED to CARD or might have arisen as a new gene after duplication in teleosts. In addition to *casp20*, we discovered a previously unknown caspase on chromosome 5 that we named *casp22* (**Figure A.2, A.7**). Surprisingly, we could not identified any *casp22* ortholog in other teleost genomes. Analysis of the

chromosomal synteny around the *casp22* locus revealed a partial conservation among teleosts, with *casp22* neighboring genes being dispersed on different chromosomes in species other than zebrafish (data not shown). Like Caspase-20, Caspase-22 possesses a CARD in its N-terminal region (**Figure A.6**). Phylogenetic analysis revealed that *casp20* and *casp22* segregate together (**Figure A.7**), suggesting they might originate from a duplication event unique to the zebrafish lineage.

The last classical functional group of caspases in vertebrates includes apoptosis executioners Caspases-3, -6 and -7 that are characterized by a short pro-domain. Another caspase sharing a similar structure, Caspase-17, has been identified in vertebrates other than therian mammals [450], but its function in programmed cell death has not been defined. We identified two orthologs for *caspase-3* (*casp3a* and *casp3b*), three orthologs for *caspase-6* (*casp6a*, *casp6b* and *casp6c*), and one ortholog each for *caspase*-7 (*casp7*) and *caspase-17* (*casp17*) (**Figure A.3, A7**). We also discovered a novel uncharacterized caspase on chromosome 21 that we named *casp21* (**Figure A.2**). Protein sequence comparison revealed a high level of conservation between human and zebrafish Caspase-3, -6 and -7 (**Figure A.3**). *Casp3a* and *casp3b* are located on different chromosomes, suggesting they have arisen from the whole genome duplication that occurred in the teleost lineage [491]. Supporting that hypothesis, several *casp3* genes were also found on different chromosomes in medaka and stickleback and clustered in two distinct groups in our phylogenetic analysis (**Figure A.7**). We could only identify one *casp3* in fugu and tetraodon, suggesting a specific gene loss in the pufferfish lineage. In contrast to *casp3a* and *casp3b*, *casp6a*, *casp6b* and *casp6c* were found in adjacent positions on chromosome 3. Interestingly, we only identified one *casp6* gene in stickleback, fugu or tetraodon, but three potential *casp6* paralogs on independent

scaffolds in medaka. Phylogenetic analysis showed that zebrafish and medaka *casp6* paralogs cluster in separate groups, suggesting independent gene duplication events in these two lineages. Analysis of the chromosomal synteny at the casp6 locus further revealed a conservation of *casp6* flanking genes among teleosts except in zebrafish, suggesting extensive chromosomal rearrangements in addition to duplications (**Figure A.16**). Interestingly, the three zebrafish Caspase-6s share a Traf2 (TNF receptor associated factor 2) binding site in their pro-domain that is also found in Caspases-8a, -8b and -2 but not in other executioner caspases (**Figure A.6**), suggesting they might participate in the regulation of tumor necrosis factor (TNF) signaling. As reported previously [450], we also identified *casp17* as a distinct caspase that does not phylogenetically segregate with the group of executioner caspases (**Figure A.7**). Remarkably, Caspase-17 has a Met in its CASc domain at position 197 instead of the Arg conserved in all other caspases that is involved in substrate binding (**Figure A.8**). Finally, we discovered a novel caspase, Caspase-21, that segregates with the group defined by Caspases-3 and -7 in our phylogenetic analysis (**Figure A.7**). *Casp21* appears specific to the zebrafish lineage, as we could not identify any *casp21* ortholog in other teleost genomes. Protein sequence comparison between Caspase-21 and the other zebrafish caspases further showed a higher similarity with Caspase-3a and Caspase-3b (**Figure A.4),** suggesting they might share common functional properties.

Spatiotemporal expression of caspases during development

To characterize the expression of caspases during development, we analyzed the temporal and spatial expression of all caspase genes from cleavage to larval stages using reverse transcription PCR (RT-PCR) and in situ hybridization (ISH).

Inflammatory caspases. RT-PCR analysis revealed that *casp1*, *casp19a*, *casp19b* and *casp23* have different temporal expression profiles during development (**Figure A.9**). Expression of *casp1* and *casp19a* begins at the pharyngula stage (24 hpf) and is maintained at 48, 72 and 96 hpf. In contrast, *casp19b* expression was only weakly detected at 48 and 72 hpf and became clearly visible at 96 hpf. Remarkably, *casp23* expression could only be detected at cleavage and sphere stages, indicating that *casp23* is only maternally expressed. ISH further revealed common and specific expression domains for *casp1* and *casp19a* at 48, 72 and 96 hpf (**Figure A.10**). While both caspases were detected in the pharyngeal arches as previously described [481], *casp1*, but not *casp19a*, was also found in the intestinal bulb at 72 and 96 hpf (**Figure A.10C, A.10D, A.10G and A.10H**). In contrast, *casp19a* was specifically detected in the epidermis at 48 and 72 hpf as well as in the proctodeum at 48 hpf (**Figure A.10J-A.10O**), suggesting distinct functions in these specific organs. *Casp19a* expression became notably restricted to the pharyngeal arches at 96 hpf (**Figure A.10L and A.10P**). Our attempts to detect *casp19b* with probes directed against the coding sequence or the 5'UTR of the transcript were unfortunately unsuccessful, suggesting that *casp19b* expression levels might be below the detection threshold of ISH.

Initiator caspases. Initiator caspases including *casp2*, *casp9*, and the members of the caspase-8 subfamily *casp8a*, *casp8b*, *casp10*, *casp20* and *casp22* share a similar temporal expression profile during development, as shown by RT-PCR (**Figure A.9**). Expression of *casp2*, *casp9*, *casp8a*, *casp8b* and *casp10* was detected throughout

embryonic development from cleavage to larval stages, indicating both maternal and zygotic expression. *Casp8a* and *casp8b* expression appeared notably stronger at maternal stages, suggesting an important function for these caspases during early development. *Casp20* expression was not detected at cleavage stage but was observed at very low levels at sphere and shield stages. It was then strongly detected from bud stage to 96 hpf. In contrast, *Casp22* expression was only observed at lower levels from 24 to 96 hpf.

ISH revealed distinct expression patterns for *casp2* and *casp9* from 24 to 96 hpf (**Figure A.11**). While *casp2* appeared selectively expressed in the midbrain and hindbrain at 24 hpf **(Figure A.11A**), *casp9* expression was strongly detected in the olfactory placode and was observed at lower levels in the gut and proctodeum (**Figure A.11D**). *Casp2* continued to be expressed in the midbrain and hindbrain at 48 and 72 hpf and was also detected in the retina and pharyngeal arches at these stages (**Figure A.11B and A.11C**). Expression in the intestinal bulb appeared at 72 hpf (F**igure A.11C**). Compared to *casp2*, *casp9* appeared ubiquitously expressed at low levels at 48 and 72 hpf (**Figure A.11E and A.11F**). Stronger expression was detected in the retina and different regions of the brain including the diencephalon, midbrain and hindbrain, which is consistent with the reported role of Caspase-9 in retinal axon arbor dynamics [417]. At 96 hpf, *casp2* and *casp9* became more similarly expressed and were strongly detected in the intestinal bulb, the nervous system and the retina (**Figure A.11D and A.11H**). C*asp2*, but not *casp9*, was notably observed in the liver at that stage (**Figure A.11D**).

Members of the caspase-8 subfamily demonstrated a different spatial expression compared to *casp2* and *casp9* (**Figure A.12**). While we were unable to detect *casp8b* and *casp22* despite using multiple probes directed against the coding sequence, 3'UTR, or

5'UTR of both transcripts, we observed a strong expression of *casp8a* in the muscles, retina and nervous system at 24, 48 and 72 hpf (**Figure A.12A-A.12C**). *Casp8a* expression decreased in the muscles but remained high in the nervous system and retina at 96 hpf and became prominent in the intestinal bulb (**Figure A.12D**). *Casp10* appeared to be expressed at lower levels and was notably detected at the floorplate at 24 and 48 hpf (**Figure A.12E and A.12F**). Its expression became apparent in the pharyngeal arches at 48 and 72 hpf (**Figure A.12F and A.12G**) and was strongly detected in the muscles and intestinal bulb at 72 hpf (**Figure A.12G**). Similarly to *casp8a*, *casp10* expression decreased in the muscles and became strongly detected in the intestinal bulb at 96 hpf (**Figure A.12H**). In contrast to the low expression of *casp10* at 24 hpf, *casp20* was strongly detected in the nervous system, throughout the gut and in the proctodeum at that stage (**Figure A.12I**). Interestingly, *casp20* expression was also observed in the vascular system at this time point. At 48 hpf, however, *casp20* expression became restricted to the pharyngeal arches and the intestinal bulb (**Figure A.12J**), where it remained strongly detected at 72 and 96 hpf (**Figure A.12K and A.12L**).

Executioner caspases. Known as the principal mediators of apoptosis in all tissues, executioner caspases appeared to have variable spatiotemporal patterns of expression during development. *Casp3a*, *casp6a*, *casp6b* and *casp6c* were detected at relatively constant levels from maternal to late stages of development by RT-PCR (**Figure A.9**). In contrast, only low levels of expression were observed for *casp3b* and *casp17* from 24 to 96 hpf. *Casp7* expression was detected at low levels from cleavage to bud stages but increased from 24 to 96 hpf. Interestingly, a shorter *casp7* transcript was detected at all stages by RT-PCR and appeared to encode a protein with a shorter pro-

domain. The functional significance of this isoform remains however unclear. *Casp21* was barely detected at shield and bud stages but became clearly expressed from 24 to 96 hpf.

ISH analysis revealed specific and complementary expression patterns of executioner caspases at 24, 48, 72 and 96 hpf (**Figure A.13**). While *casp3b* could not be clearly detected at 24 hpf (**Figure A.13E**), strong expression of *casp3a* was observed in the olfactory placodes, diencephalon, midbrain and hindbrain at that stage (**Figure A.13A**). As reported in previous studies [417], *casp3a* remained strongly expressed in the brain and retina at 48, 72 and 96 hpf, but was not detected in the trunk (**Figure A.13B-A.13D)**. In contrast, *casp3b* appeared ubiquitously expressed, albeit at low levels, at 48 hpf, with a higher expression in the pharyngeal arches (**Figure A.13F**). Expression levels appeared to increase at 72 hpf, being higher in the pharyngeal arches, muscles and intestinal bulb (**Figure A.13G**). Both *casp3a* and *casp3b* became expressed at high levels in the intestinal bulb at 96 hpf (**Figure A.13D and A.13H**). While we have not been able to detect *casp6b* and *cas6c*, we observed a specific and dynamic expression of *casp6a* at 24, 48, 72 and 96 hpf. *Casp6a* expression was detected in the lens, gut, proctodeum and to a lower extent in the epidermis at 24 hpf (**Figure A.13I**). It became restricted to the pharyngeal arches at 48 hpf (**Figure A.13J**), but then expanded and was strongly visible in the liver and intestinal bulb at 72 and 96 hpf (**Figure A.13K and A.13L**). While *casp3a*, *casp3b* and *cas6a* are expressed in several tissues and organs, *casp7* was exclusively detected in the lens at 48 and 72 hpf (**Figure A.13N and A.13O**). Although surprising, such restricted expression has also been observed in the salmon embryo [492], suggesting a highly specific and conserved function among teleosts. Like *casp3a*, *casp3b* and *casp6a*, *casp7* expression became also detected in the intestinal bulb at 96 hpf

(**Figure A.13P**. *Casp21* expression was not detected at 24 hpf (**Figure A.13O** but became visible in the primary head sinus (phs at 48 hpf (**Figure A.13R**. Expression was maintained in the phs at 72 hpf and became also visible in the primordial hindbrain channel and the muscles (**Figure A.13S**. It became detected in the pharyngeal arches and intestinal bulb at 96 hpf (**Figure A.13T**. Finally, *casp17* expression could not be observed by ISH at 24, 48 or 72 hpf (**Figure A.14A, A.14C, A.14E and A.14G** but was strongly and exclusively detected in the liver and intestinal bulb at 96 hpf (**Figure A.14D and A.14H**. Previous studies have also detected *casp17* in the liver of chicken[450], suggesting functional conservation among vertebrates.

A.5 CONCLUSIONS

Our study reveals that the zebrafish caspase family is much larger than anticipated, including 19 distinct caspase genes. As summarized in **Figure A.5**, zebrafish caspases have both shared and specific expression profiles that suggest distinct and complementary functions during development. It is interesting to note that only a restricted number of caspases including *casp2*, *casp3a*, *casp8a*, *casp9* and *casp20* are strongly expressed in the developing nervous system. Other caspases may not be expressed there or may be expressed at such low levels in normal conditions that they would escape detection by ISH. We also discovered that some caspases such as *casp6a* or *casp19a* have dynamic expression patterns that change over time, while others such as *casp7* are unexpectedly expressed in a restricted number of structures or tissues. Altogether, our analysis offers a starting point for future studies investigating the functions of caspases during embryonic development. Our characterization of zebrafish caspases will be especially useful for the generation of new caspase mutants or the

development of genetically encoded biosensors expressed in a cell- or tissue-specific manner.

Gene name	forward primer	reverse primer
casp1	ATGGCCAAATCTATCAAGG	TCAGAGTCCGGGGAA
casp19a	ATGGAGGATATTACCCAG	TCACAGTCCAGGAAAC
casp19b	ATGGAGGATATTACCAAGTTG	TCACTGTCCAGGGAAC
casp23	AATCGTCGTTTAGCGCTTTAG	GCAGATATATATTGCACTTGCTATG
casp2	ATGTTGGGAGAGTGC	TTAGTTGCTGGGGTAG
casp9	ATGGAGCAGAAACACAG	TCATGACTGTGAAGACTG
casp8a	ATGGATCCTCAGATCTTTCACG	TCAGTCTATGGGCAGCACT
casp8b	ATGGATAAAACTAGTAATCCTA	TTAGGAGACTCCATTCAT
casp10	GACATGGACATGTGTTTTCAGAG	GAGCATCATCAAGGAAGCC
casp20	ATGAGTAAAAAGGAATCAACTC	TCAGTTATTCACTGGCG
casp22	ATGGCAGATCAACTTTTGG	CTGTTTAAGAGAACCGGC
casp3a	ATGAACGGAGACTGTGTG	TTAAGGAGTGAAGTACATCTCTTTG
casp3b	ATGTCGCACGTGAAACCA	TTATTTAGGGAAGTAGAGTTCTTTGG
casp6a	ATGGCAAGTCACACT	TTACTTTTTGGGCCTG
casp6b	ATGGCAACTAACACCAGAAGC	CTATTGGATCTGAGTATTGTCTCTG
casp6c	ATGCACCACAACAAATCAATAATG	GTAGGGATTAGGTATGGATTAG
casp7	ATGAATAAAGAAGCCCTTACTTCC	TCAGTTGAAGTAGAGCTCTTTAG
casp21	ATGAGTTTACAAGCTTCTAAAGAC	TTACAATTTCTTATTCTTCTCTGCAAC
casp17	CAACACAAGCACTAATGTCAG	TCCTCATTTCTGTGATCTTCAG

Figure A.1: Primers used for caspase cloning.

Gene name	other / previous names	GRCz10 chromosome location (strand)	Ensembl Gene ID	Genbank Acc # (old)	Genbank Acc # (new)
casp1	*caspase-a*, *caspy*, *zgc:109869*	chr16:42,043,825–42,054,428 (-)	ENSDARG00000008165	BC095022	MG957992
*casp19a**	*caspase-b*, *caspy2*, *zgc:109807* *caspase-1A*, *si:ch211-233g6.8*	chr1:57,315,773–57,323,452 (-)	ENSDARG00000052039 ENSDARG00000075270	BC095000, DQ022755	MG958005
*casp19b**	*caspase-bl*, *caspase-b1*, *si:ch211-15j1.6*	chr1:57,370,656–57,376,144 (-)	ENSDARG00000094433	-	MG958006
*casp23**	*caspase-c*, *zgc:113326*, *zgc:171731*	chr7:19,348,435–19,352,383 (+)	ENSDARG00000014657	BC151948	MG958010
casp2	*caspase-2*	chr16:17,643,307–17,669,604 (-)	ENSDARG00000062052	BC163115	MG957993
casp9	*im:7136887*, *zgc:101776*	chr23:25,047,448–25,058,524 (+)	ENSDARG00000004325	BC097103	MG958002
casp8a	*zgc:92075*	chr6:12,811,868–12,821,422 (+)	ENSDARG00000058325	BC081583	MG958000
casp8b	*caspase-8l1*	chr6:12,862,945–12,867,126 (+)	ENSDARG00000058341	DQ812121	MG958001
casp10	*caspase-8l2*, *caspase-8b*	chr9:1,343,221–1,355,521 (+)	ENSDARG00000070272	DQ812123 (partial)	MG958003
*casp20**	*caspxa*,*caspxb*, *zgc:194469*, *CARD-Casp8*	chr6:12,878,158–12,881,286 (-)	ENSDARG00000058347	BC163666	MG958007
*casp22**	*si:dkey-103e21.5*	chr5:22,081,469–22,086,320 (-)	ENSDARG00000091926	BC133883	MG958009
casp3a	*caspase-3a*, *zgc:100890*	chr1:16,835,237–16,841,582 (+)	ENSDARG00000017905	BC078310	MG957994
casp3b	*caspase-3b*	chr14:4,022,953–4,036,126 (-)	ENSDARG00000055045	DQ812120	MG957995
casp6a	*caspase-6a*, *zgc:112960*	chr3:32,830,371–32,834,050 (-)	ENSDARG00000093405	BC094299	MG957996
casp6b	*caspase-6b*, *zgc:103604*	chr3:32,822,780–32,826,756 (-)	ENSDARG00000025608	BC083437	MG957997
casp6c	*caspase-6c*, *zgc:136946*	chr3:32,837,963–32,841,789 (-)	ENSDARG00000070368	BC114318	MG957998
casp7	*zgc:110595*	chr12:30,456,171–30,467,659 (-)	ENSDARG00000091836	BC095327	MG957999
*casp21**	*CABZ01041682.1; FO834888.1*	chr21:8,440,994–8,445,761 (+)	ENSDARG00000055550	-	MG958008
casp17	*CU467905.1*	chr10:42,334,831–42,350,374 (+)	ENSDARG00000086266 (partial)	-	MG958004

* new number attributed

Figure A.2: Nomenclature and accession numbers for zebrafish caspases.

	Hs. CASP1	Hs. CASP2	Hs. CASP3	Hs. CASP4	Hs. CASP5	Hs. CASP6	Hs. CASP7	Hs. CASP8	Hs. CASP9	Hs. CASP10	Hs. CASP12	Hs. CASP14	Bt. CASP15	Mm. CASP16	Gg. CASP17	Gg. CASP18
Casp1	**38/55**	29/47	27/45	35/56	33/51	24/42	25/48	26/42	30/49	23/40	32/51	28/42	26/47	23/47	19/33	26/44
Casp19a	33/56	25/49	25/41	32/54	30/53	19/41	26/51	24/42	27/49	24/45	30/50	23/39	26/46	25/48	20/36	24/46
Casp19b	32/52	26/49	27/42	33/55	31/49	21/39	26/49	24/42	27/46	23/42	33/50	25/41	27/48	25/50	19/34	27/47
Casp23	33/50	26/46	23/38	31/50	31/51	20/35	22/41	21/42	23/41	22/44	28/44	20/34	24/42	22/40	18/33	24/48
Casp2	26/47	**48/65**	27/40	26/47	28/51	25/40	26/45	27/44	32/52	27/45	26/42	24/36	27/43	26/45	22/32	24/48
Casp9	25/47	30/52	29/42	24/45	25/45	27/41	31/49	30/47	**49/67**	30/49	22/42	23/38	27/45	26/44	20/35	30/52
Casp8a	27/46	28/49	27/39	27/45	27/47	26/38	29/45	**38/55**	32/50	37/56	23/41	22/34	25/42	25/41	21/34	40/60
Casp8b	28/46	25/42	31/53	27/48	25/41	31/49	30/48	**30/43**	27/46	29/43	25/46	26/43	25/45	25/39	22/39	32/46
Casp10	24/43	25/46	25/37	23/41	24/47	22/36	30/44	35/57	30/46	**37/60**	22/39	22/33	23/41	24/42	19/33	33/52
Casp20	28/47	30/44	34/48	28/46	27/43	28/44	30/51	29/43	31/51	32/46	26/47	28/42	28/47	23/44	21/38	29/46
Casp22	31/50	27/48	29/46	28/50	27/46	29/46	32/51	32/46	34/52	33/48	30/51	29/43	27/47	25/49	27/42	31/52
Casp3a	27/40	25/40	**56/71**	29/42	24/37	38/58	41/54	24/36	28/45	23/36	28/42	33/47	27/45	23/41	29/48	26/38
Casp3b	27/42	23/40	**56/70**	29/42	25/39	38/54	45/57	26/36	27/44	24/36	27/46	31/49	26/43	20/38	28/50	26/37
Casp6a	26/38	24/38	41/61	28/42	24/40	**65/77**	33/48	25/37	29/44	23/34	26/45	29/50	27/45	24/42	27/42	25/38
Casp6b	19/36	23/34	37/60	25/40	20/35	**53/68**	29/43	20/32	26/42	21/33	21/42	30/54	25/42	22/40	29/51	22/34
Casp6c	22/36	23/35	39/59	25/40	22/34	**54/67**	29/41	25/32	26/42	22/34	22/43	32/54	25/41	23/40	28/50	25/36
Casp7	28/45	28/45	46/60	29/48	29/45	37/51	**54/67**	30/45	30/50	28/42	27/47	29/45	26/47	23/43	27/45	31/44
Casp21	25/41	23/38	38/60	29/42	25/37	37/51	32/46	20/33	24/40	24/35	28/44	31/47	26/41	22/37	32/53	26/39
Casp17	20/37	21/35	28/49	21/38	19/36	27/49	28/44	21/34	21/36	21/35	21/39	28/44	22/40	22/35	**37/54**	21/37

Highest percentages of identity and similarity are highlighted in grey.

Identity and similarity between orthologs are indicated in bold.

Hs: *Homo sapiens*; Mm: *Mus musculus*; Bt: *Bos Taurus*; Gg: *Gallus gallus*

Figure A.3: Protein sequence identity (%) and similarity (%) with other vertebrate caspases.

	Casp1																		
Casp1	**100**	**Casp19a**																	
Casp19a	41/61	**100**	**Casp19b**																
Casp19b	42/60	**70/82**	**100**	**Casp23**															
Casp23	36/52	33/52	34/53	**100**	**Casp2**														
Casp2	26/48	26/50	27/45	26/46	**100**	**Casp9**													
Casp9	28/48	27/45	27/48	24/46	30/54	**100**	**Casp8a**												
Casp8a	26/45	25/46	25/45	23/46	31/52	29/49	**100**	**Casp8b**											
Casp8b	25/50	25/47	23/44	22/39	29/44	30/46	40/53	**100**	**Casp10**										
Casp10	23/40	28/45	26/44	25/46	29/46	30/49	35/53	28/39	**100**	**Casp20**									
Casp20	29/47	24/46	23/45	25/43	28/46	31/50	34/47	35/56	31/43	**100**	**Casp22**								
Casp22	29/51	24/51	26/51	26/45	30/49	31/52	33/50	33/54	33/47	38/55	**100**	**Casp3a**							
Casp3a	26/42	23/39	22/40	24/35	26/41	27/42	28/40	31/51	25/38	32/48	32/47	**100**	**Casp3b**						
Casp3b	26/45	25/42	26/40	23/34	26/40	26/41	25/39	32/52	23/37	32/49	33/49	**61/77**	**100**	**Casp6a**					
Casp6a	25/43	20/40	24/41	23/37	26/40	27/42	26/38	31/48	24/36	31/49	30/45	38/57	39/59	**100**	**Casp6b**				
Casp6b	22/38	21/39	18/38	21/34	24/36	26/35	25/36	30/46	20/35	31/46	28/43	37/57	36/54	**66/77**	**100**	**Casp6c**			
Casp6c	25/40	20/39	20/38	22/31	24/36	27/40	26/35	32/46	23/35	31/45	31/45	36/55	36/54	**63/73**	**80/89**	**100**	**Casp7**		
Casp7	25/48	27/49	26/47	25/42	27/44	32/47	30/46	33/56	30/44	35/54	33/52	47/62	49/63	37/53	35/48	35/47	**100**	**Casp21**	
Casp21	27/42	26/41	24/39	25/37	24/37	25/39	21/36	33/51	22/36	30/45	28/44	42/60	40/60	34/52	37/56	37/56	37/52	**100**	**Casp17**
Casp17	20/37	20/37	20/37	19/35	23/38	21/34	22/35	28/48	20/34	28/42	26/43	31/52	29/53	28/50	31/47	31/45	27/49	34/53	**100**

Identity and similarity between duplicated isoforms are highlighted in grey and bold.

Figure A.4: Protein sequence identity (%) and similarity (%) among zebrafish caspases.

			ep	op/ob	di	mb	hb	fp	r	ln	mp/ms	phs/phbc	vs	pa	lv	ib	g	pr
INFLAMMATORY	*casp1*	24 hpf																
		48 hpf												+++				
		72 hpf												+++		+++		
		96 hpf												+++		+++		
	casp19a	24 hpf																
		48 hpf	+++								+++			+++				+++
		72 hpf	+											+++				
		96 hpf												+++				
INITIATOR	*casp2*	24 hpf				++	++											
		48 hpf				++	++		++					++				
		72 hpf				+++	+++		+++					++		+++		
		96 hpf				+++	+++		+++					+++	+++	+++	+	
	casp9	24 hpf		+++													+++	+++
		48 hpf		+++	+++	+++	+++		+++		+						+++	
		72 hpf		+++	+++	+++	+++		+++		+						+++	
		96 hpf			++	++	++		+++					+		++	++	
	casp8a	24 hpf			+	+	+++	+++	+		+							
		48 hpf			+++	+++	+++		+++		+++							
		72 hpf				+	+		+++		+++					+++		
		96 hpf				++	++		+++					++		+++		
	casp10	24 hpf						++										
		48 hpf									+			+++				
		72 hpf									+++			+++		+++		
		96 hpf				++	++							+++		++		
	casp20	24 hpf		+++	+++	+++	+++						++				+++	+++
		48 hpf												+++		+++		
		72 hpf												+++		+++		
		96 hpf			++	++	++							+++		+++	+	

Figure A.5: Developmental expression patterns of zebrafish caspases.

EXECUTIONER	*casp3a*	24 hpf		+++	+++	+++	+++											
		48 hpf		+++	+++	+++	++		+++									
		72 hpf		++	+++	+++	++		+++									
		96 hpf		++	+++	+++	++		+++						+++	++	++	
	casp3b	24 hpf																
		48 hpf									+			+				
		72 hpf									++			++		+++		
		96 hpf												++		+++		
	casp6a	24 hpf	+							++							+++	+++
		48 hpf												+++				
		72 hpf									+			+++	+++	+++		
		96 hpf												+	++	+++		
	casp7	24 hpf																
		48 hpf								+++								
		72 hpf								+++								
		96 hpf								+++				+++		+++		
	casp21	24 hpf																
		48 hpf									+	+						
		72 hpf									+	+++						
		96 hpf				+	+							++		++		
OTHER	*casp17*	24 hpf																
		48 hpf																
		72 hpf																
		96 hpf													+++	+++		

Figure A.5: Developmental expression patterns of zebrafish caspases (Continued) Expression levels detected by ISH are indicated by +, ++, or +++. ep: epidermis, op/ob: olfactory placodes/bulb; di: diencephalon; mb: midbrain; hb: hindbrain; fp: floorplate; r: retina; ln: lens; mp/ms: muscle pioneers/muscles; phs/phbc: primary head sinus/primordial hindbrain channel; vs: vascular system; pa: pharyngeal arches; lv: liver; ib: intestinal bulb; g: gut; pr: proctodeum

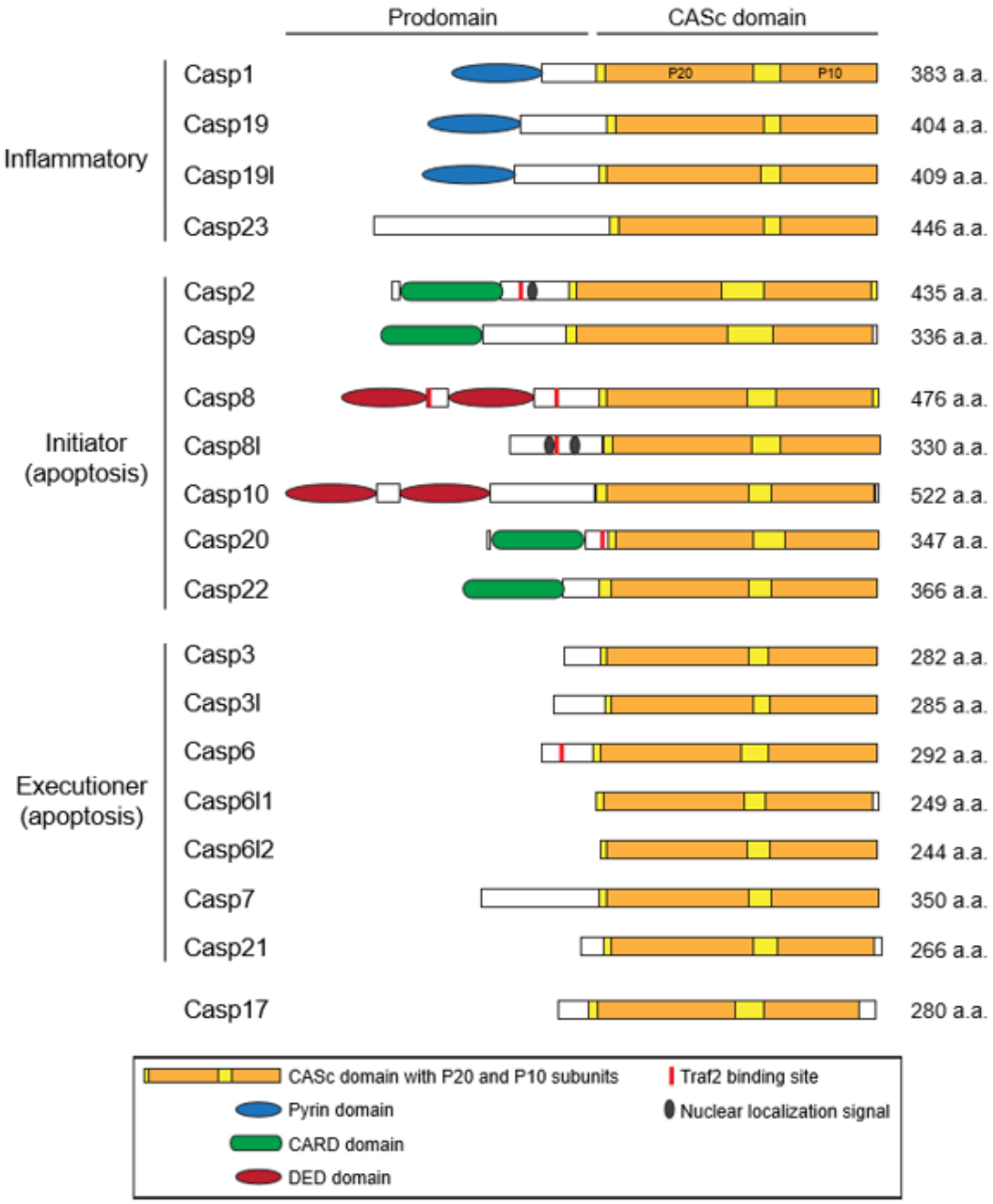

Figure A.6: Domain structure of zebrafish caspases. Caspases are presented based on the classical classification of caspases as inflammatory, initiator, or executioner. The catalytic CASc domain is indicated in yellow, with large and small subunits in orange. CARD: caspase recruitment domain; DED: death-effector domains.

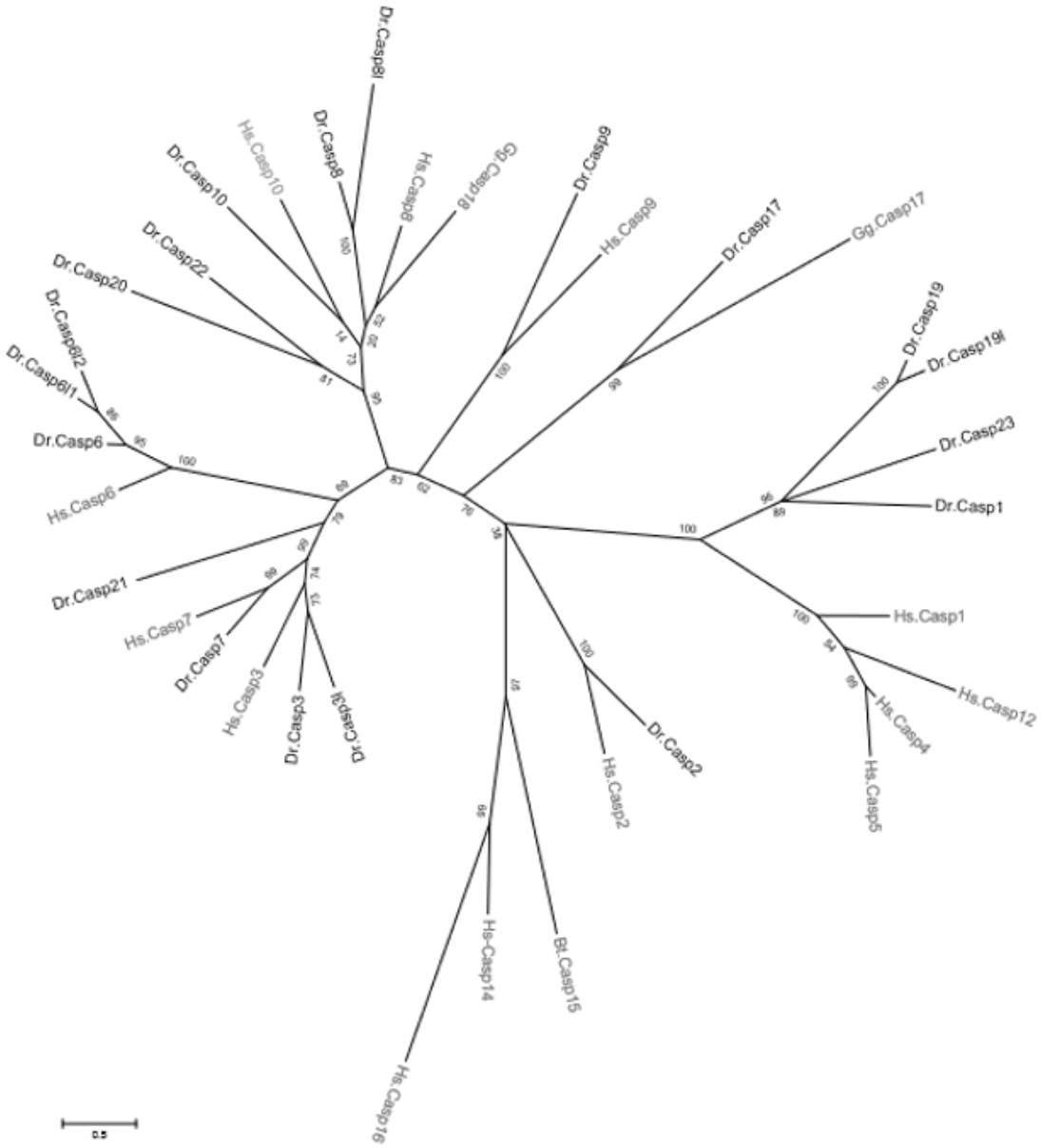

Fig A.7: Phylogenetic tree of zebrafish and other relevant vertebrate caspases. A phylogenetic comparison was conducted for caspase protein sequences from zebrafish (Dr), human (Hs), mouse (Ms, used for Casp16), cow (Bt, used for Casp15), chicken (Gg), coelacanth (Lc), medaka (Ol), stickleback (Ga) and fugu (Tr). Teleost species are indicated in blue, with zebrafish in bold. 500 bootstrap replications were used as a test of phylogeny, with values indicated next to the branch.

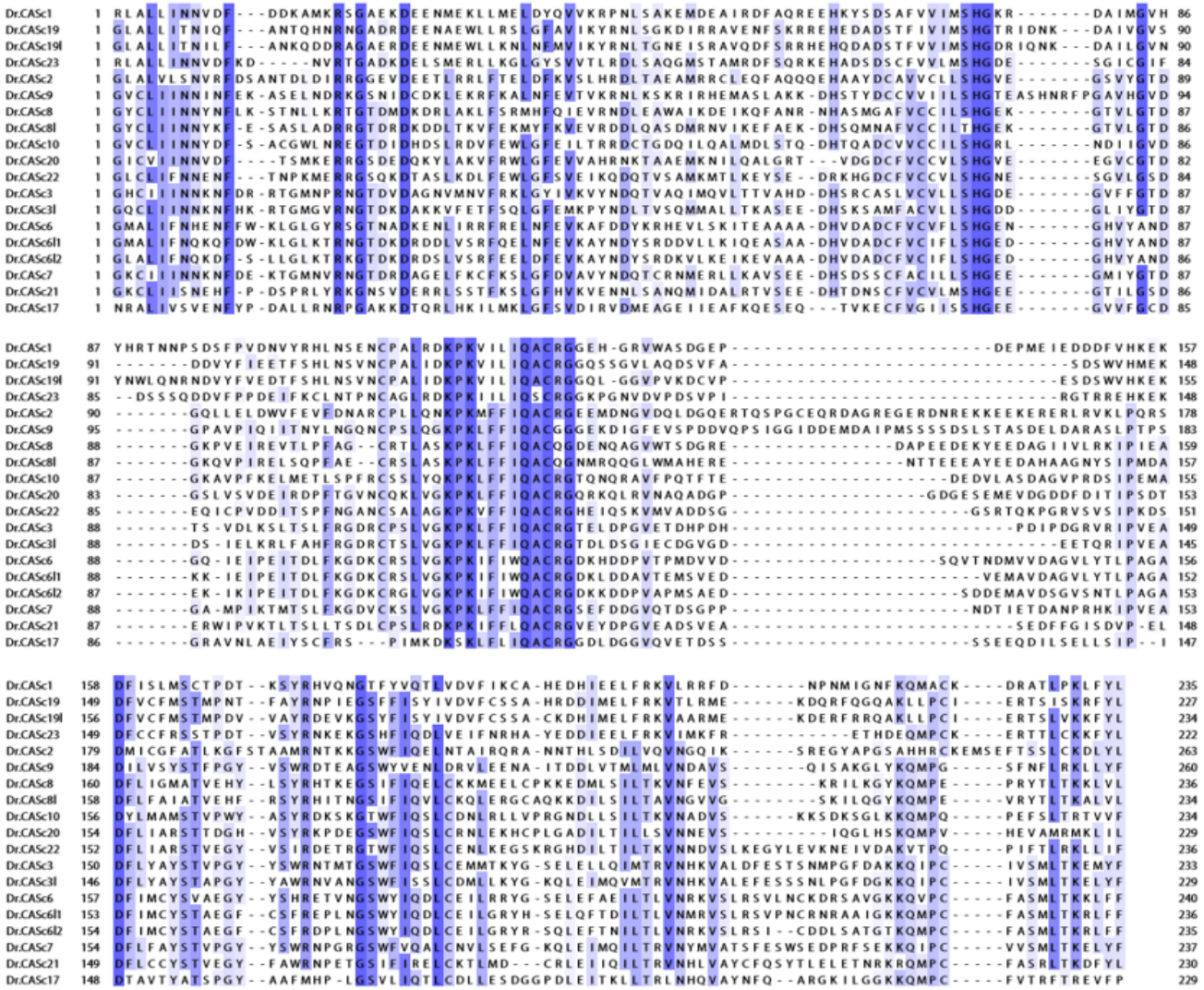

Figure A.8: Multiple protein sequence alignment of zebrafish caspase CASc catalytic domains. Residues highlighted in blue are conserved across caspases.

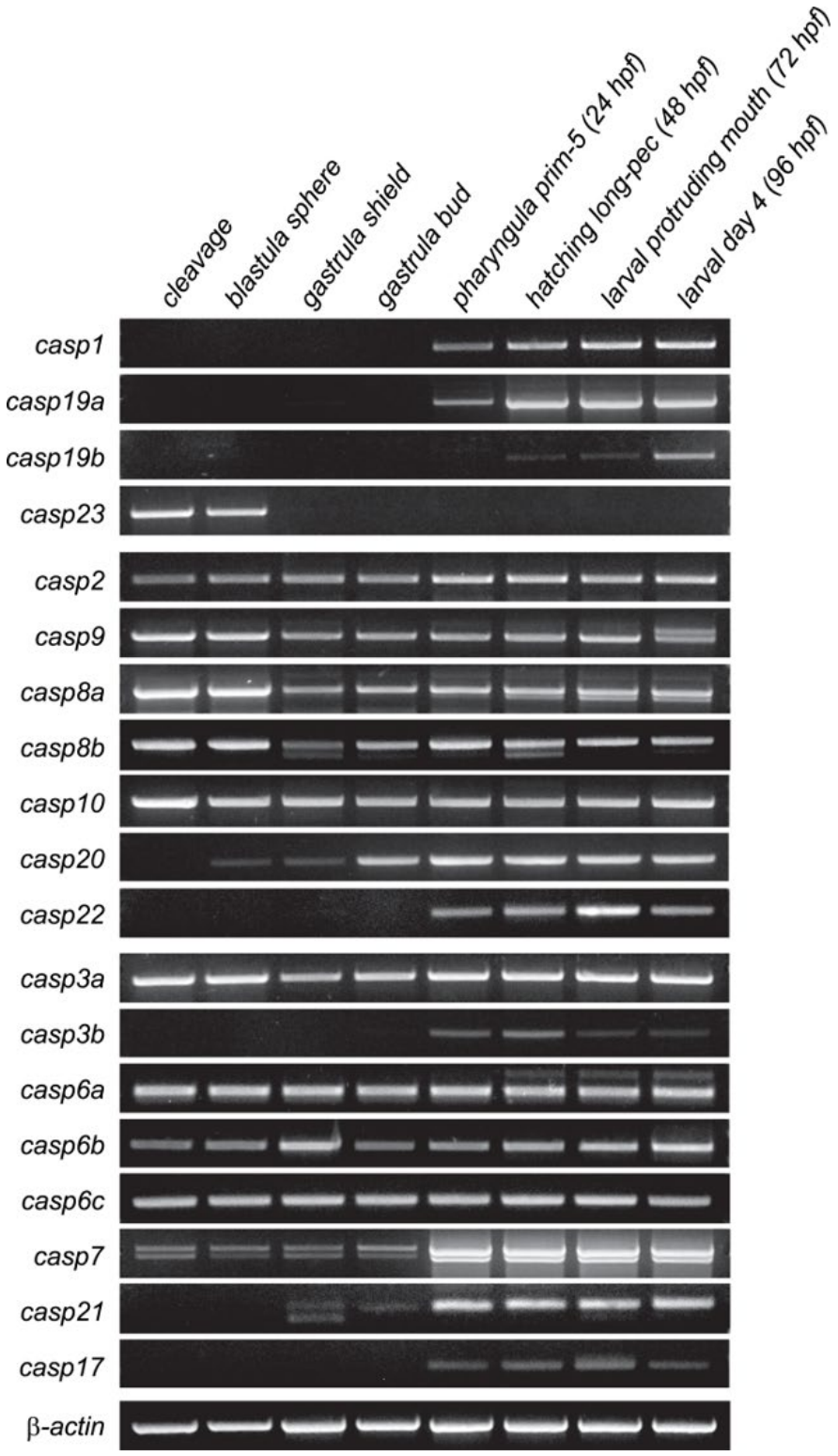

Figure A.9: Temporal mRNA expression of caspases during embryonic development. RT-PCR was performed for all 19 caspase genes using cDNA from specified developmental stages. β-actin was used as a control.

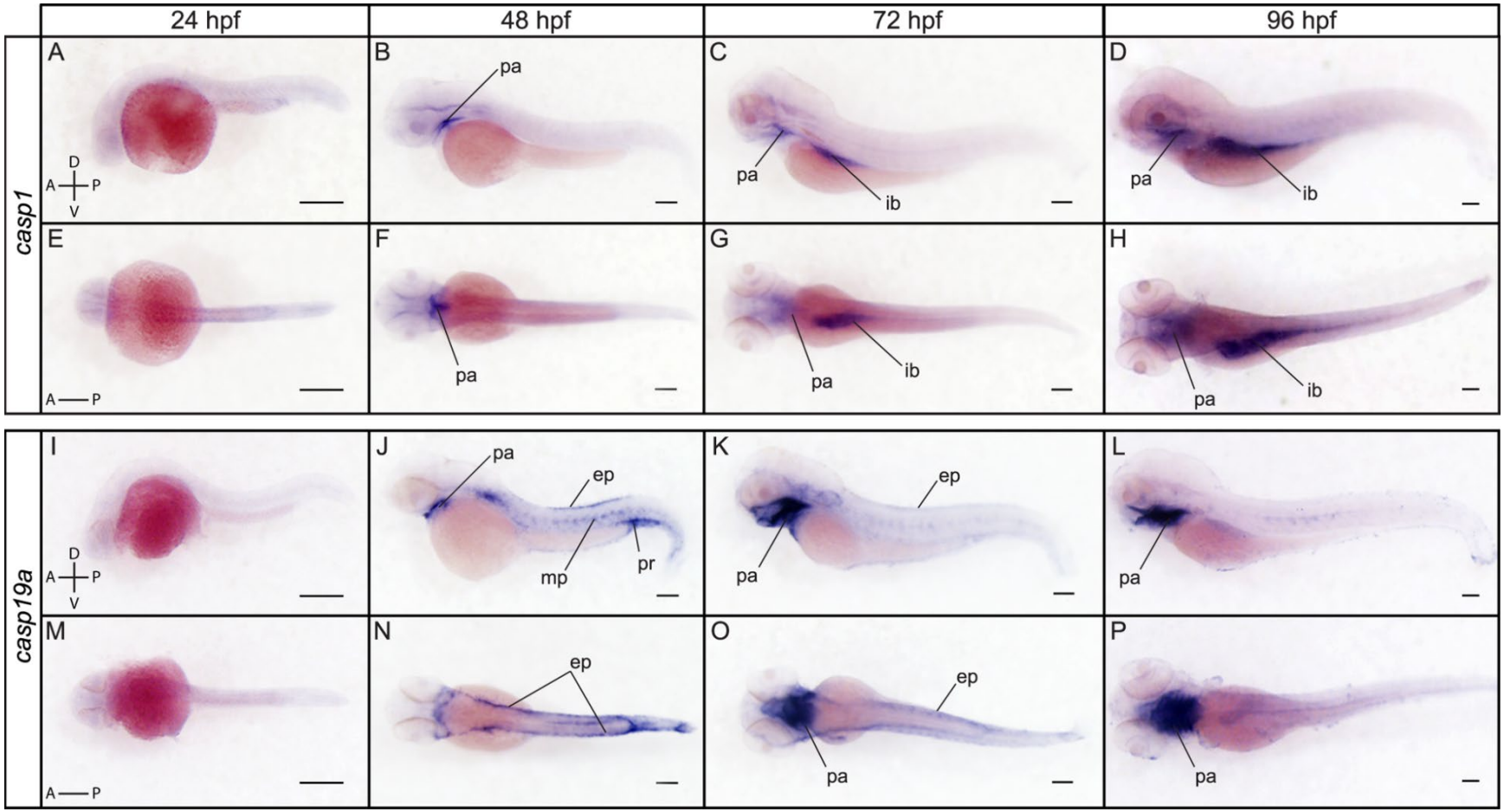

Figure A.10: Spatial expression of *casp1* and *casp19a* at 24, 48, 72 and 96 hpf. Lateral (A-D) and dorsal (E-H) views of whole embryos stained for *casp1* by ISH show expression in the pharyngeal arches (pa) at 48, 72 and 96 hpf and in the intestinal bulb (ib) at 72 and 96 hpf. *Casp19a* expression is strongly detected in the pharyngeal arches (pa) at 48, 72 and 96 hpf, and is also seen in the epidermis (ep) at 48 and 72 hpf (lateral views in J and K, dorsal views in N and O). Expression is also observed in the proctodeum (pr) and at lower levels in the muscles pioneers (mp) at 48 hpf. Scale bar: 200 µm.

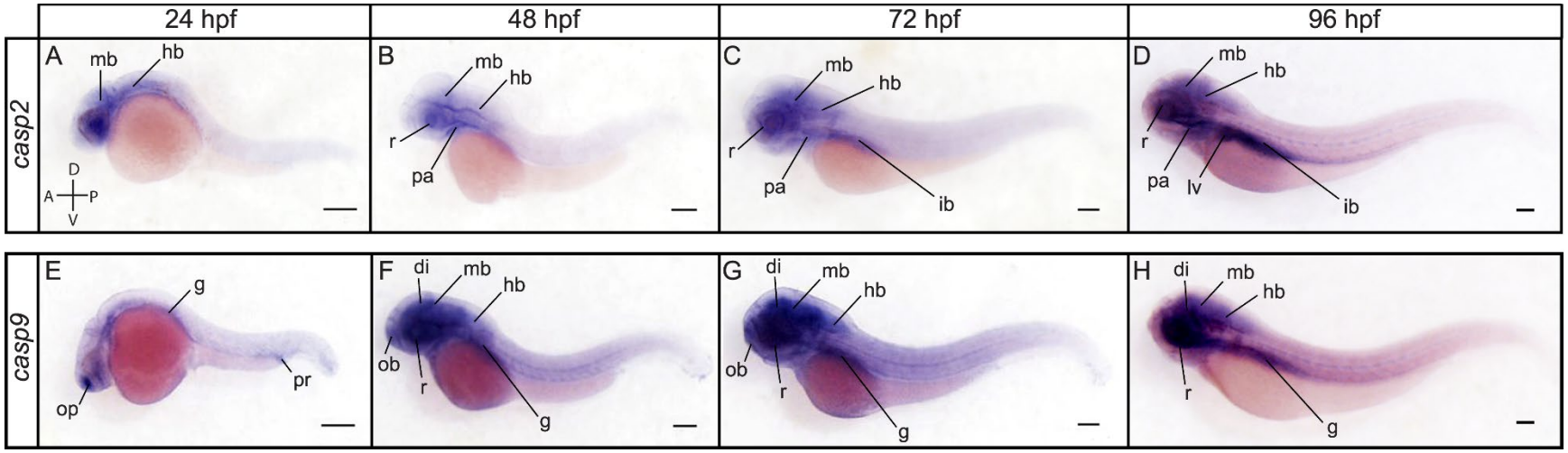

Figure A.11: Spatial expression of *casp2* and *casp9* at 24, 48, 72 and 96 hpf. Lateral views of whole embryos stained for *casp2* (A-D) and *casp9* (E-H) by ISH. *Casp2* is expressed in the midbrain (mb) and hindbrain (hb) at all stages analyzed. Expression is also observed in the pharyngeal arches (pa) and retina (r) at 48, 72 and 96 hpf (B-D), and in the intestinal bulb (ib) at 72 and 96 hpf (C, D). *Casp2* becomes strongly detected in the liver (lv) at 96 hpf (D). *Casp9* is expressed at high levels in the olfactory placodes (op) and at levels in the gut (g) and proctodeum (pr) at 24 hpf (E). *Casp9* appears ubiquitously expressed at low levels at 48 and 72 hpf and is strongly detected in the retina, diencephalon (di), midbrain, hindbrain and gut from 48 to 96 hpf (F-H). Scale bar: 200 μm.

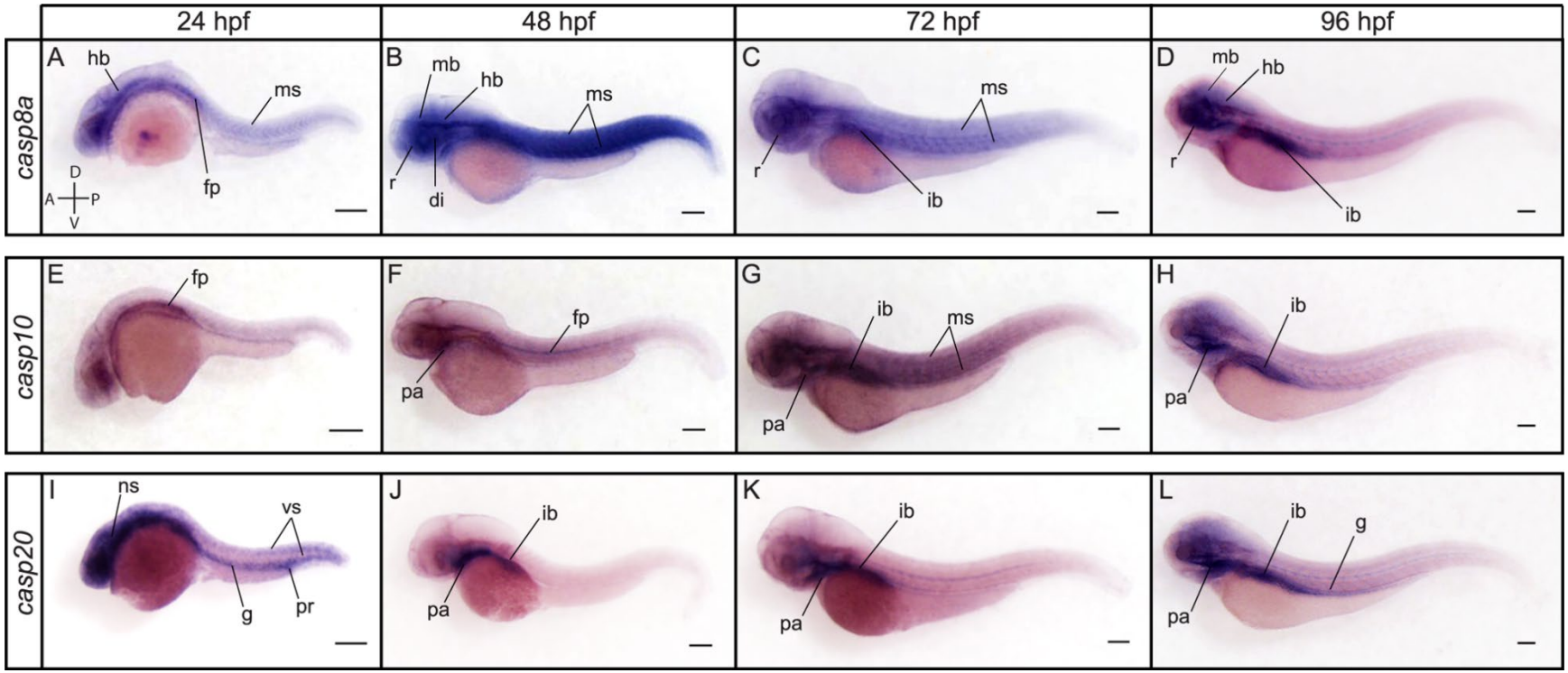

Figure A.12: Spatial expression of the caspase-8 family members *casp8a*, *casp10* and *casp20* at 24, 48, 72 and 96 hpf. Lateral views of whole embryos stained for *casp8a* (A-D), *casp10* (E-H) and *casp20* (I-L) by ISH. *Casp8a* is expressed in the hindbrain (hb), muscles (ms) and at the floorplate (fp) at 24 hpf (A). Its expression is then strongly detected in the retina (r), diencephalon (di), midbrain (mb), hindbrain and muscles (ms) at 48 hpf (B). Additional expression in the intestinal bulb (ib) is observed at 72 and 96 hpf (C, D). *Casp10* expression is detected at the floorplate at 24 and 48 hpf (E, F) and in the pharyngeal arches (pa) at 48 hpf (F). A strong expression is detected in the pharyngeal arches, muscles and intestinal bulb at 72 hpf (G). *Casp10* remains highly detected in the pharyngeal arches and intestinal bulb at 96 hpf (H). *Casp20* is strongly expressed in the nervous system (ns), vascular system (vs), proctodeum (pr) and throughout the gut (g) at 24 hpf (I). Its expression ecomes restricted to the pharyngeal arches and the intestinal bulb at 48, 72 and 96 hpf (J-L). Scale bar: 200 µm.

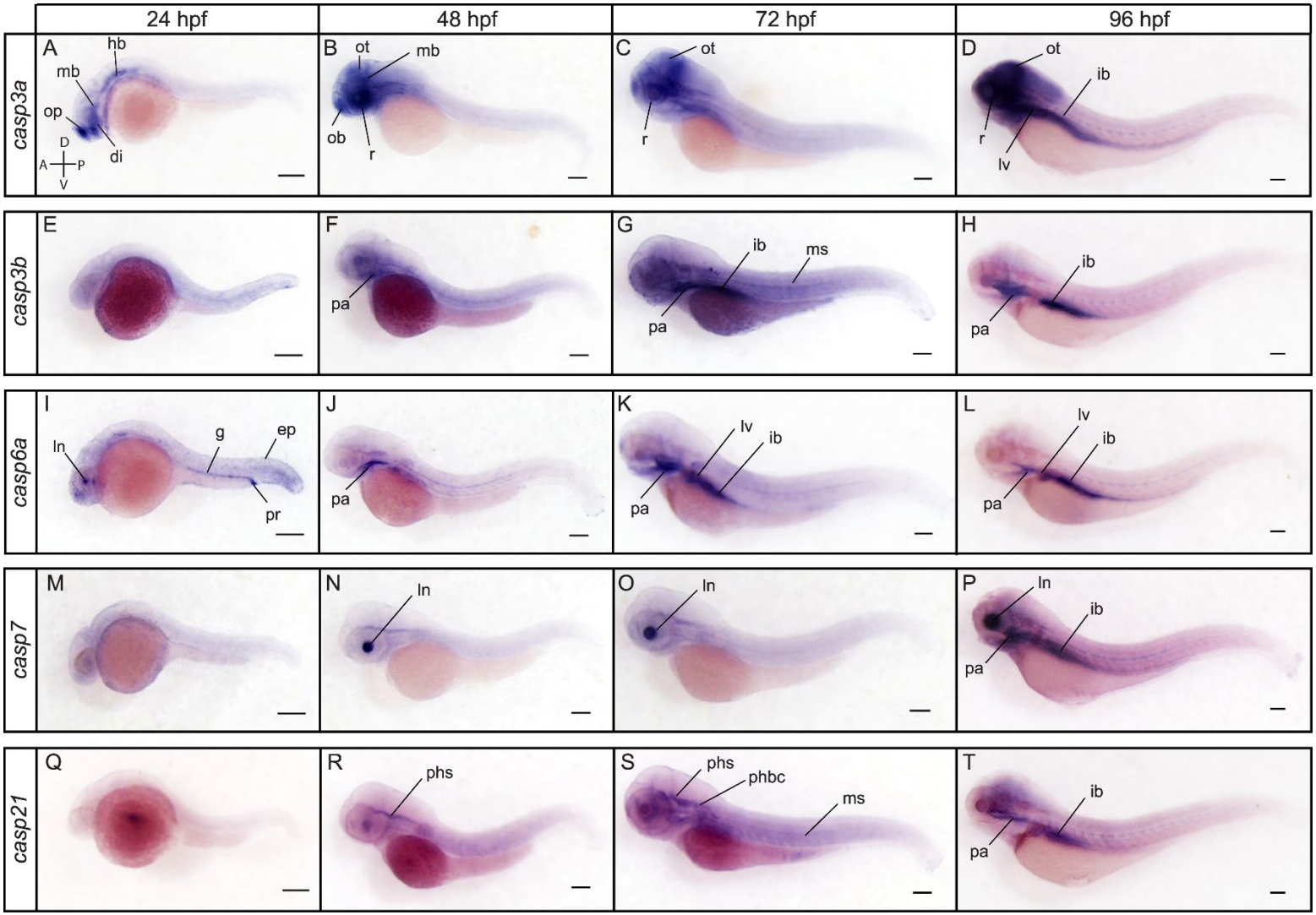

Figure A.13: Spatial expression of the executioner caspases *casp3a, casp3b, casp6a, casp7* and *casp21* at 24, 48, 72 and 96 hpf. Lateral views of whole embryos stained for *casp3a* (A-D), *casp3b* (E-H), *casp6a* (I-L), *casp7* (M-P), and *casp21*

Figure A.13 (Continued): (Q-T) by ISH. *Casp3a* is expressed in the olfactory placodes (op), diencephalon (di), midbrain (mb) and hindbrain (hb) at 24 hpf (A). Expression remains high in the nervous system at 48, 72 and 96 hpf and is strongly detected in the olfactory bulb (ob), retina (r), and optic tectum (ot) (B-D). *Casp3a* becomes strongly expressed in the intestinal bulb and liver at 96 hpf (D). *Casp3b* expression is not detected at 24 hpf (E) but becomes visible at 48 and 72 hpf, notably in the pharyngeal arches (pa), muscles (ms) and intestinal bulb (ib) (F, G). Expression becomes restricted to the pharyngeal arches and intestinal bulb at 96 hpf (H). *Casp6a* expression is mostly detected in the lens (ln), gut (g) proctodeum (pr) and epidermis (ep) at 24 hpf (I). It becomes restricted to the pharyngeal arches at 48 hpf (J), and is strongly detected in the pharyngeal arches, intestinal bulb and liver (lv) at 72 and 96 hpf (K, L). *Casp7* expression appears restricted to the lens at 48 and 72 hpf (N, O). It expands to the intestinal bulb at 96 hpf (P). *Casp21* expression is not visible at 24 hpf (Q) but is detected in the primary head sinus (phs) at 48 hpf (R). It is maintained in the primary head sinus and is also observed in the primordial hindbrain channel (phbc) and the muscles at 72 hpf (S). *Casp21* expression becomes visible in the nervous system, pharyngeal arches and intestinal bulb at 96 hpf (T). Scale bar: 200 μm.

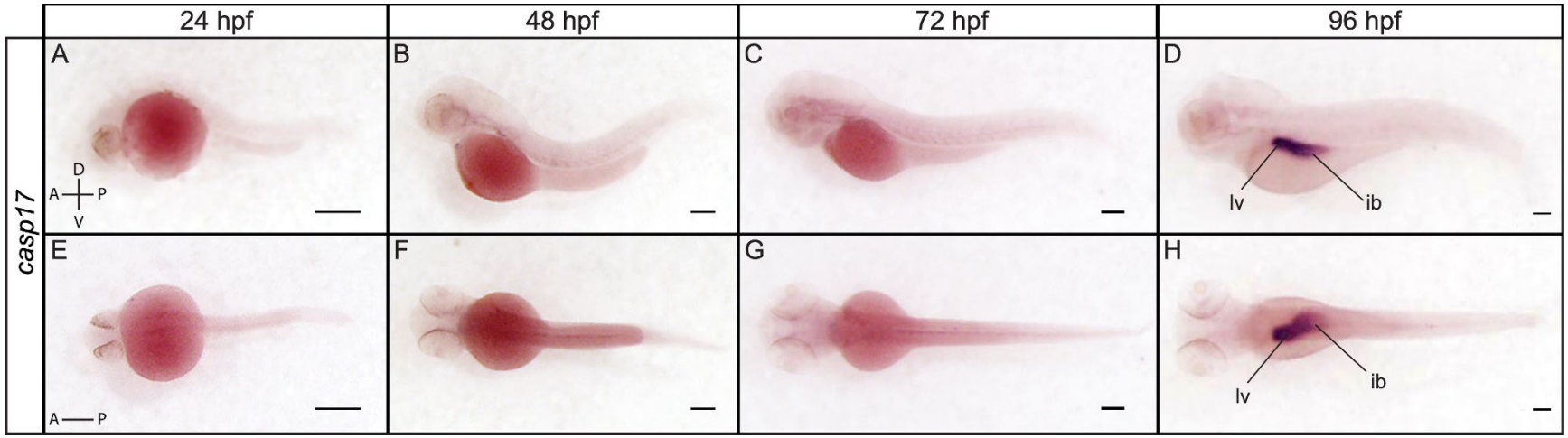

Figure A.14: Spatial expression of *casp17* at 24, 48, 72 and 96 hpf. Lateral (A-D) and dorsal (E-H) views of a whole embryo stained for *casp17* by ISH show a strong and specific expression of *casp17* in the liver (lv) and intestinal bulb (ib) at 96 hpf (D, H). Scale bar: 200 µm.

S1 Figure

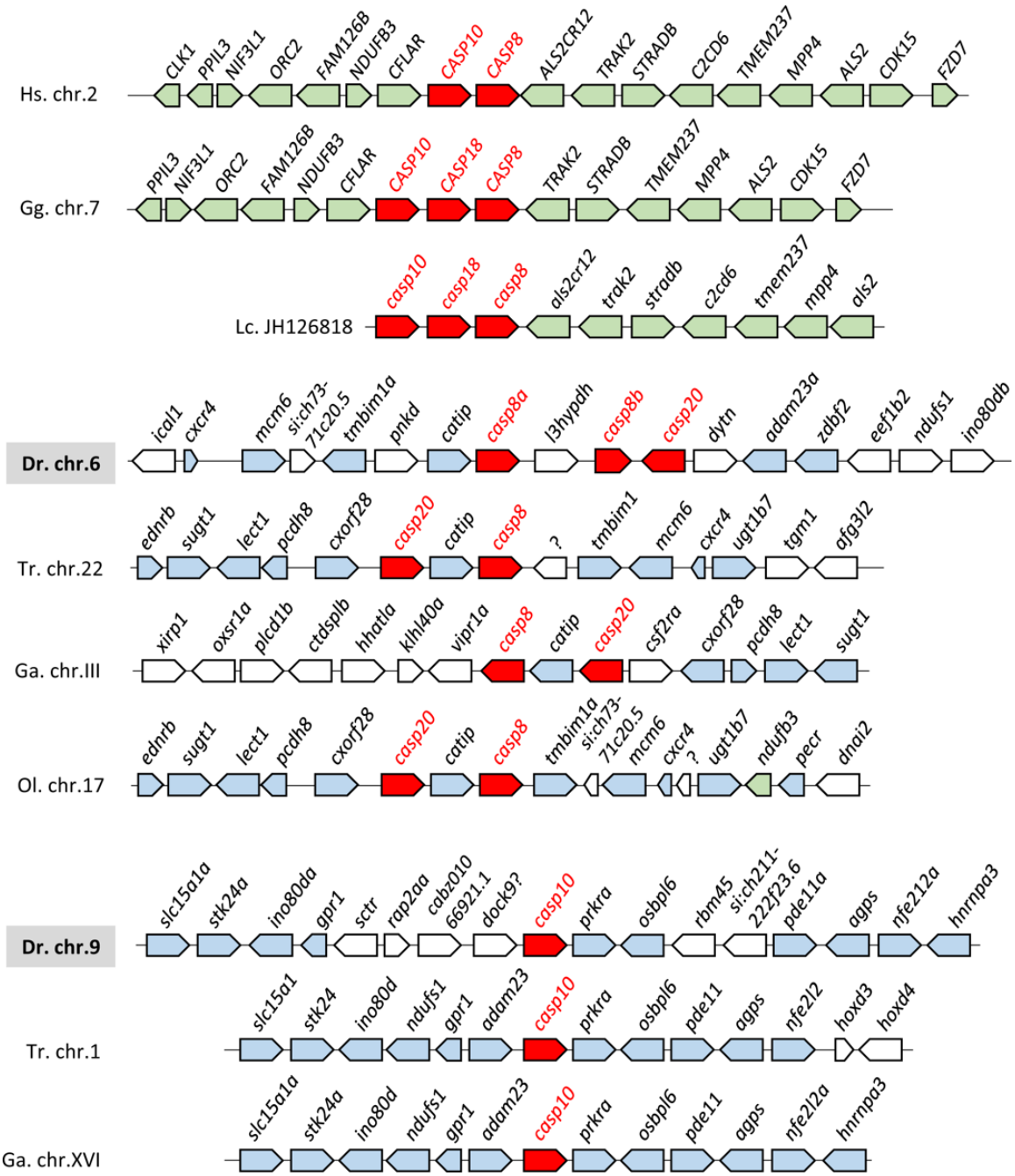

Figure A.15: Syntenic conservation between *casp8*, *casp10*, *casp18* and *casp20* orthologs. Caspase genes are represented in red. Genes conserved among coelacanth and tetrapods are represented in green while genes conserved among teleosts are shown in blue. Non-conserved genes are in white. Chromosomes are indicated on the left for each species, with zebrafish chromosomes highlighted in grey. Hs: *Homo sapiens*, Gg: *Gallus gallus*; Lc: *Latimeria chalumnae*, Dr: *Danio rerio*, Tr: *Takifugu rubripes*, Ga: *Gasterosteus aculeatus*, Ol: *Oryzias latipes*.

S2 Figure

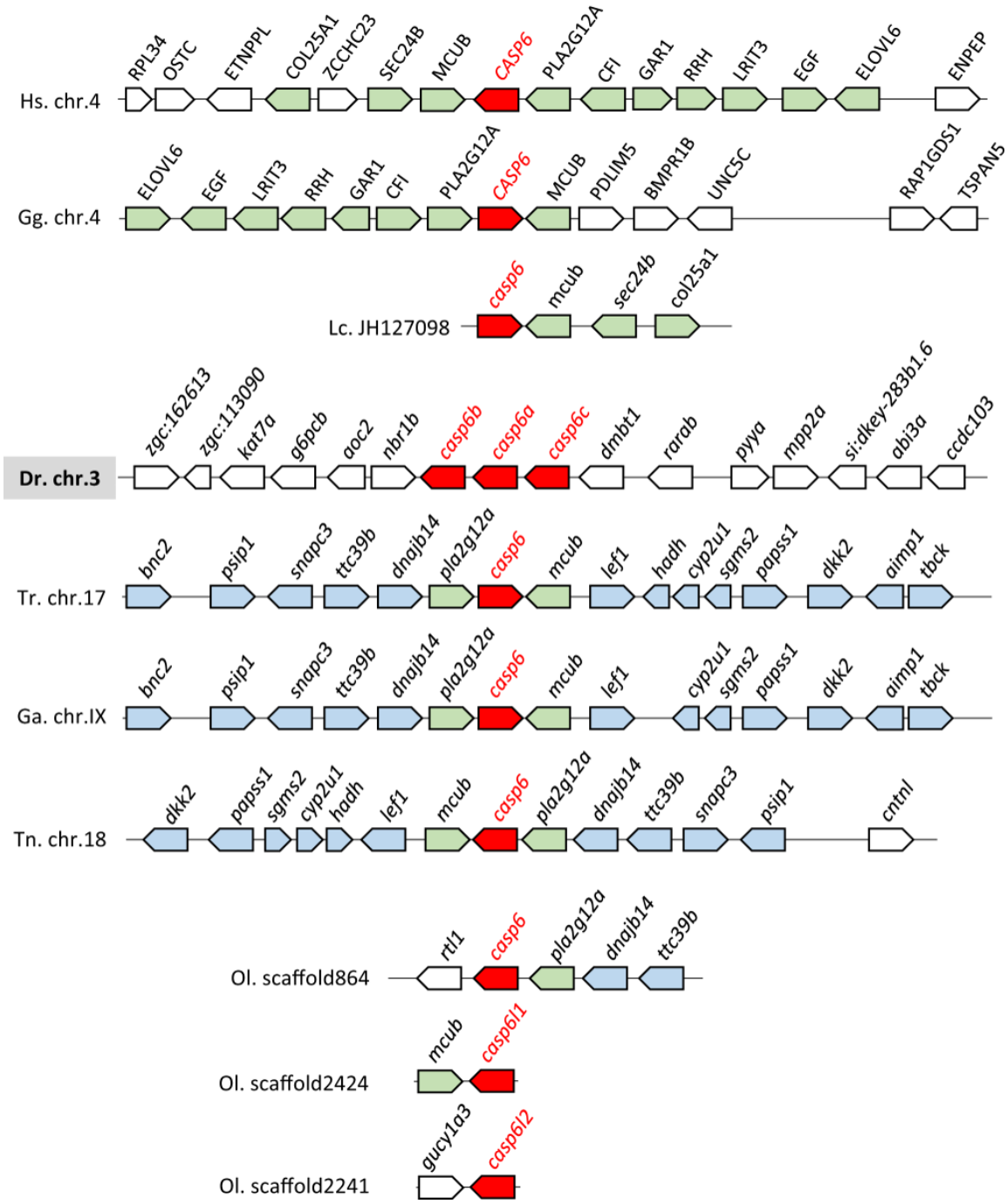

Figure A.16: Syntenic conservation between *casp6* orthologs. Caspase-6 genes are represented in red. Genes conserved among coelacanth and tetrapods are represented in green while those conserved among teleosts are shown in blue. Non-conserved genes are in white. Chromosomes are indicated on the left for each species, with zebrafish chromosomes highlighted in grey. Hs: *Homo sapiens*, Gg: *Gallus gallus*; Lc: *Latimeria chalumnae*, Dr: *Danio rerio*, Tr: *Takifugu rubripes*, Ga: *Gasterosteus aculeatus*, Ol: *Oryzias latipes*, Tn: *Tetraodon nigroviridis*.

APPENDIX B

PERMISSIONS TO REPRINT

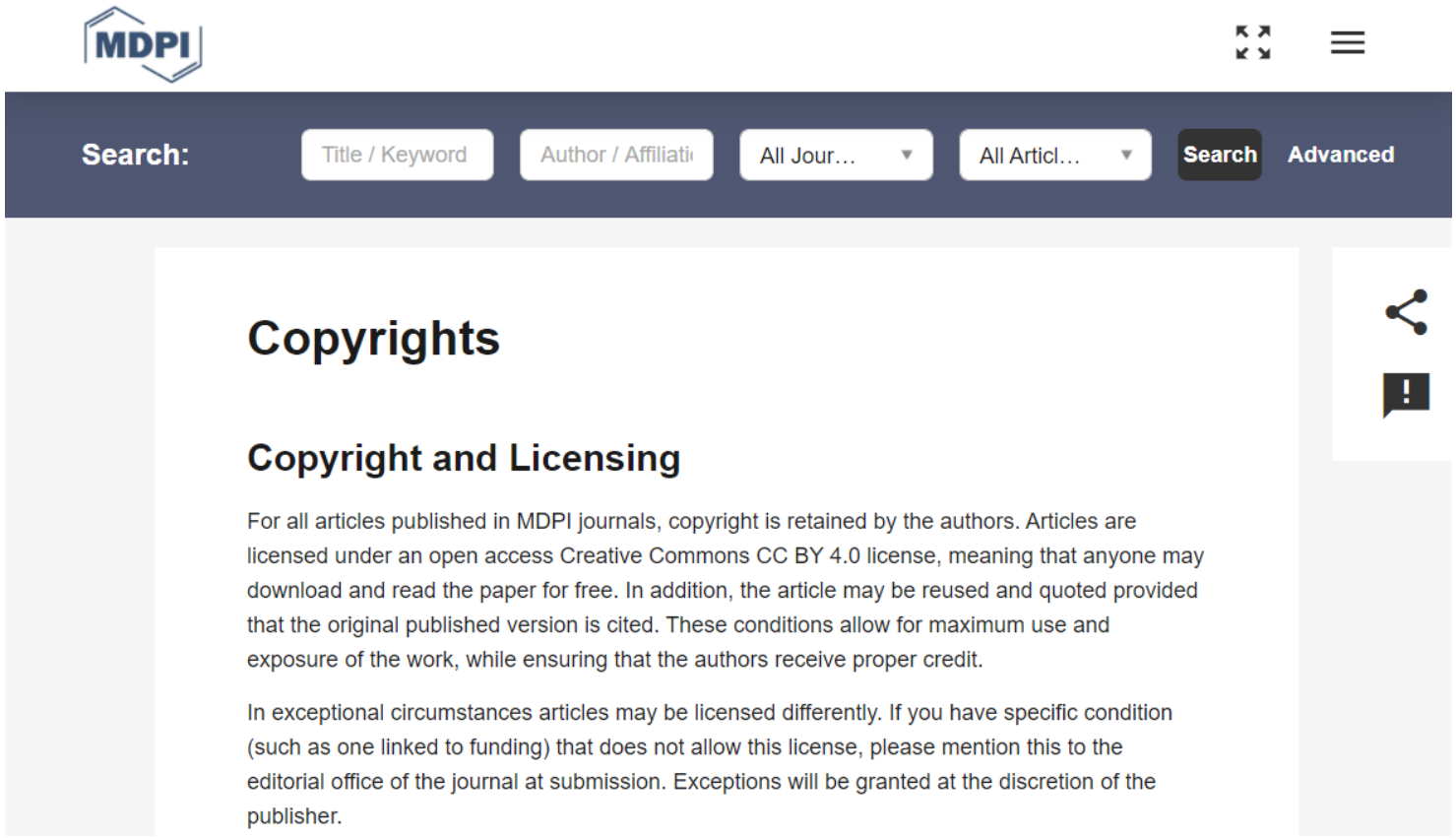

Figure B.1: IJMS Reprint Guidelines (Chapter 2)

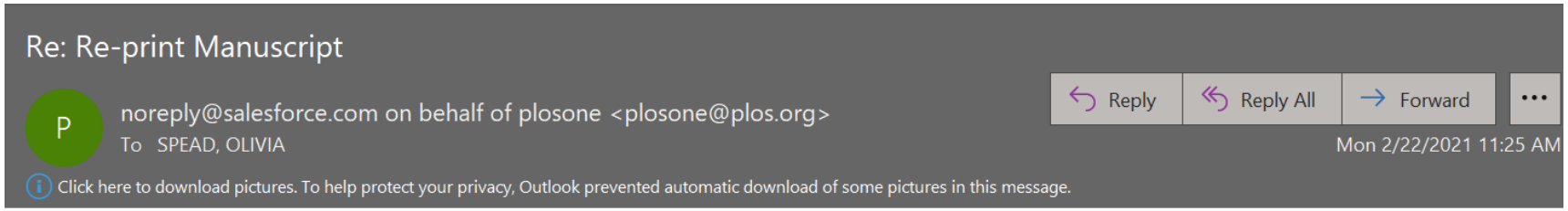

Dear Olivia Spead,

Thank you for your message. PLOS ONE publishes all of the content in the articles under an open access license called "CC-BY." This license allows you to download, reuse, reprint, modify, distribute, and/or copy articles or images in PLOS journals, so long as the original creators are credited (e.g., including the article's citation and/or the image credit). Additional permissions are not required. You can read about our open access license here: http://journals.plos.org/plosone/s/licenses-and-copyright

There are many ways to access our content, including HTML, XML, and PDF versions of each article. Higher resolution versions of figures can be downloaded directly from the article.

Thank you for your interest in PLOS ONE and for your continued support of the Open Access model. Please do not hesitate to be in touch with any additional questions.

Kind regards,
Vicky Stabler
Editorial Office
PLOS | plos.org
Empowering researchers to transform science
1160 Battery Street, Suite 225, San Francisco, CA 94111

Case Number: 07028190
ref:_00DU0Ifis._5004P1RBKxw:ref

Figure B.2: PLOS ONE Permission to Reprint (Appendix A)